



HAL
open science

Transport properties in biomimetic tissues

Manon Valet

► **To cite this version:**

Manon Valet. Transport properties in biomimetic tissues. Biological Physics [physics.bio-ph]. Sorbonne Université, 2019. English. NNT : 2019SORUS397 . tel-03001263

HAL Id: tel-03001263

<https://theses.hal.science/tel-03001263v1>

Submitted on 12 Nov 2020

HAL is a multi-disciplinary open access archive for the deposit and dissemination of scientific research documents, whether they are published or not. The documents may come from teaching and research institutions in France or abroad, or from public or private research centers.

L'archive ouverte pluridisciplinaire **HAL**, est destinée au dépôt et à la diffusion de documents scientifiques de niveau recherche, publiés ou non, émanant des établissements d'enseignement et de recherche français ou étrangers, des laboratoires publics ou privés.

THÈSE DE DOCTORAT
DE SORBONNE UNIVERSITÉ

Spécialité : Physique
École Doctorale 534 : Physique en Île de France

Présentée par

MANON VALET

Pour obtenir le grade de :
DOCTEUR DE SORBONNE UNIVERSITÉ

Sujet de la thèse :

**TRANSPORT PROPERTIES IN
BIOMIMETIC TISSUES**

Présentée et soutenue publiquement le 6 septembre 2019
Devant un jury composé de :

M. Fabien MONTEL	Rapporteur
M. Christophe YBERT	Rapporteur
M. Jean-Baptiste FOURNIER	Examinateur
Mme Cécile SYKES	Examinatrice
Mme Dora TANG	Examinatrice
M. Alexis PREVOST	Directeur de thèse
M. Elie WANDERSMAN	Membre invité
Mme Léa-Laetitia PONTANI	Membre invité

ABSTRACT - EN

In this thesis work, we develop an experimental model biomimetic of cell-cell communication. It consists in networks of aqueous droplets bathing in oil and connected by lipid bilayers decorated with ion channels. To produce these droplet networks, we first develop an original printing method based on the periodic extraction through an oil/air interface of a capillary in which the aqueous phase is injected. When the bilayers are decorated with the ion channel hemolysin, we then study the diffusion of a fluorescent probe in 1D nanoporous networks, using epifluorescence microscopy. We establish that the characteristic diffusion time depends non-linearly on the nanopores concentration. We show that our results are well captured within a first passage time theoretical description, in which nanopores are clustered rather than being independent. In the last part, we use cell-free reactions to express directly within the droplets the previously used hemolysin or the mechanosensitive ion channel MscL. We successfully demonstrate the insertion and functionality of synthesized hemolysin using both confocal microscopy and electrophysiological measurements. These results pave the way to the study of diffusive transport properties in mechanosensitive networks under mechanical stress.

ABSTRACT - FR

Dans ce travail nous développons un modèle expérimental biomimétique de la communication cellule-cellule. Il s'agit de réseaux de gouttelettes aqueuses baignant dans l'huile et reliées par des bicouches lipidiques ornées de canaux ioniques. Pour produire ces réseaux de gouttelettes, nous développons d'abord une méthode d'impression originale basée sur l'extraction périodique à travers une interface huile/air d'un capillaire dans lequel la phase aqueuse est injectée. Nous incorporons ensuite aux bicouches un canal ionique – l'hémolysine - pour étudier la diffusion d'une sonde fluorescente dans des réseaux nanoporeux 1D par microscopie d'épifluorescence. Nous établissons que le temps de diffusion caractéristique dépend de façon non linéaire de la concentration introduite en nanopores. Nous montrons que nos résultats peuvent être compris par le biais d'une description théorique basée sur les temps de premier passage, dans laquelle les nanopores sont regroupés dans la membrane plutôt qu'isolés. Dans la dernière partie, nous utilisons des réactions cell-free pour exprimer directement dans les gouttelettes l'hémolysine précédemment utilisée ou le canal ionique mécanosensible MscL. Nous avons démontré dans ce cadre l'insertion et la fonctionnalité de l'hémolysine ainsi synthétisée par microscopie confocale et mesures électrophysiologiques. Ces résultats permettront d'entreprendre l'étude des propriétés de transport diffusives dans les réseaux mécanosensibles sous contrainte mécanique.

CONTENTS

List of Figures	ix
List of Tables	xi
Acronyms	xii

I FRENCH SUMMARY / RÉSUMÉ FRANÇAIS

Résumé Français	xv
1.1 Introduction	xv
1.2 Modèle biomimétique de tissu cellulaire	xv
Droplet Interface Bilayers	xv
Production microfluidique de gouttes	xvi
Modèle Quasistatique	xix
1.3 Transport passif dans des tissus artificiels connectés par des nanopores protéiques	xxi
L'hémolysine : un canal de communication	xxi
Transport dans des lignes de gouttes connectées	xxiii
Cinétique de transport	xxv
1.4 Expression <i>in situ</i> de protéines membranaires	xxvii
Synthèse <i>in vitro</i> de protéines	xxvii
Composition et fabrication de la réaction	xxviii
Localisation des protéines synthétisées	xxx
Fonctionnalité des protéines synthétisées <i>in situ</i>	xxxii
1.5 Conclusion	xxxv

Introduction

Introduction	1
--------------	---

I DESIGN OF BIOMIMETIC TISSUES

1 DROPLET INTERFACE BILAYERS AS ANALOGS OF CELLULAR MEMBRANES	6
1 Model membranes: history	6
1.1 Liposomes	6
1.2 Planar artificial membranes	8
2 Physico-chemistry of droplet interface bilayers	10
2.1 Solvent effects	10
2.2 Lipids-out	11
2.3 Lipids-in	11
3 Towards DIB networks ?	12
2 PRODUCTION OF MICRODROPLETS	13
1 Emulsification	13
2 Microfluidic on a chip production	14
2.1 State of the art	14
2.2 Methods	15
3 The capillary trap method	15
3.1 Chemicals	15
3.2 Microfluidics and setup motorization	16
3.3 Imaging	16

4	Analysis of the capillary trap method	18
4.1	Volume of detached droplets	18
4.2	Fast imaging	19
3	MODELING THE QUASI-STATIC DETACHMENT PROCESS	21
1	Surface energies model	21
1.1	Free energies computation	21
1.2	Surface free energies in the final states	23
1.3	Analytical resolution	24
2	Capillary forces resolution	24
2.1	Computing the meniscus shape	26
2.2	Computing the droplet shape	28
2.3	Resolution	29
3	Partial conclusion	30
II DIFFUSIVE TRANSPORT IN AN ARTIFICIAL TISSUE		
4	CONNECTING DROPLETS WITH HEMOLYSIN PORES	33
1	Inserting hemolysin in bilayers	33
2	Chemical model for pore equilibration	34
2.1	Previous studies of hemolysin insertion	34
2.2	Model exposition	34
3	Diffusion through hemolysin	35
4	Mean First-Passage Time	36
5	Continuous Time Random Walks	37
5.1	Translationally invariant random walks	37
5.2	Waiting-Time Density	38
5.3	One-Dimensional Case	39
5	MOLECULAR TRANSPORT IN LINES OF DROPLETS	42
1	Layering connected droplets	43
1.1	Chemical composition of the two phases	43
1.2	Droplet production	43
1.3	Networks fabrication	44
1.4	Microfabrication of patterned substrates	44
1.5	Timelapse Acquisition	44
2	Fluorescence quantification	45
2.1	Image analysis	45
2.2	Possible Artifacts	46
3	The number of pores tunes diffusion	47
6	TUNING THE DIFFUSION PROCESS	49
1	Mean-First Passage Time	49
2	Comparing the model to our experimental data	51
2.1	Extracting the timescale of the problem	51
2.2	Derivation of a cluster size	52
2.3	Edge and Finite Effects	53
2.4	Long-time behavior	54
3	Improving the transport kinetics	55
7	ENGINEERING 2D NETWORKS	57
1	Theoretical Modeling	57
1.1	Square lattice	57
1.2	Triangular lattice	58
2	2D compact networks	58

2.1	Experimental networks	58
2.2	Voronoi segmentation	60
3	2D diffusion at a glance	61
4	Partial Conclusion	61
III IN SITU SYNTHESIS OF A TRANSMEMBRANE PROTEIN THROUGH DNA PROGRAMMING		
8	CELL-FREE EXPRESSION SYSTEMS TO PRODUCE PROTEINS <i>in situ</i>	65
1	Cell-free systems - state of the art	65
2	Membrane protein insertion	65
3	Characterization of the production dynamics	67
9	TXTL COMPOSITION AND FABRICATION	70
1	Cell-free reaction	70
2	Plasmid Templates	71
3	Reporter Proteins	73
4	Bulk Expression	74
10	LOCALIZATION OF CELL-FREE SYNTHESIZED PROTEINS	78
1	Materials and methods	78
1.1	TXTL and lipid composition	78
1.2	Liposome encapsulation	78
1.3	Stability Analysis	79
1.4	Fluorescence Measurements on DIBs	80
2	In situ Expression	80
2.1	Liposome encapsulation	80
2.2	Encapsulation in DIBs	81
3	Membrane Stabilization	83
3.1	Dilution	83
3.2	Size	84
3.3	Lipid Mix	84
4	Localization of membrane proteins in droplet interface bilayers	85
4.1	Bilayer intensity contrast analysis	85
4.2	Results	86
11	FUNCTIONALITY OF TXTL PRODUCED PROTEINS	89
1	An electrokinetic model for the membrane	89
1.1	Pure bilayers	89
1.2	Channel insertion in pure bilayers	90
2	Materials and Methods	90
2.1	Droplet formation	90
2.2	Electrode recording	90
2.3	Electrophysiology setup	91
2.4	Organic solvent composition	92
2.5	TXTL composition	92
3	Hemolysin Conductance	92
3.1	Lipid noise study	92
3.2	Compatibility of TXTL reactions with chloride ions	94
3.3	Average conductance measurement	94
3.4	Combinatorial insertion	96
Conclusion		100
A	MICROFABRICATION TECHNIQUES	102

1	Micromilling	102
2	Design of microfluidic chips	102
3	Droplet compaction out of the chip	102
4	Droplet compaction in the chip	103
B	CHEMICAL POTENTIAL CALCULUS	104
C	CELL-FREE PROTOCOLS	106
1	Energy Buffer composition	106
2	Plasmid constructs	106
3	Extract dilution data	107
D	ADDITIONAL RESULTS REGARDING CELL-FREE REACTIONS	108
1	Production in SUVs	108
E	PUBLICATIONS	111
	BIBLIOGRAPHY	125

LIST OF FIGURES

Figure i	Illustration de la formation d'une DIB	xvii
Figure ii	Schéma de fonctionnement et analyse en caméra rapide de la méthode du piège capillaire.	xix
Figure iii	Modèle a minima de détachement	xx
Figure iv	Expérience de diffusion sur un réseau 1D connecté par l'hémolysine	xxv
Figure v	Analyse de l'échelle de temps du phénomène diffusif	xxvii
Figure vi	Composition et cinétique de la réaction TXTL	xxx
Figure vii	Quantification de l'insertion de protéines membranaires synthétisées <i>in situ</i> dans les DIBs	xxxii
Figure viii	Dispositif expérimental pour réaliser des mesures électrophysiologiques	xxxiii
Figure ix	Analyse d'événements discrets résultant de l'insertion de plusieurs pores	xxxiv
Figure x	Prédiction de la conductance individuelle du pore en fonction des sauts attendus	xxxv
Figure 1.1	Organization of lipids in biological membranes.	7
Figure 1.2	Development of droplet interface bilayers configurations.	9
Figure 1.3	A few examples of DIB realizations in the last decade.	10
Figure 1.4	Lipids-in and out implementation.	11
Figure 2.1	Sketch of a bilayer network assembly.	13
Figure 2.2	Techniques to produce water-in-oil emulsions.	14
Figure 2.3	Capillary trap setup.	17
Figure 2.4	Dependence of the radius of the emulsion on the flow rate and the speed of extraction.	18
Figure 2.5	Lower limit on the mean radius of water-in-oil emulsions.	20
Figure 3.1	Quasistatic model of the droplet detachment.	23
Figure 3.2	Minimal detached droplet radius as a function of the introduced SDS concentration.	25
Figure 3.3	Full meniscus parametrization.	26
Figure 3.4	Numerical resolution of the oil meniscus and of the oil/water interface	29
Figure 3.5	Production of small DIB networks	30
Figure 4.1	Hemolysin crystal structure with characteristic dimensions	33
Figure 4.2	Modeling of a 1D Continuous Time Random Walk.	40
Figure 5.1	Typical diffusion experiment in a line of droplets connected with hemolysin nanopores.	42
Figure 5.2	Droplet layering and timelapse acquisition	45
Figure 5.3	Morphological operations to detect droplet contours.	46
Figure 5.4	Transport Kinetics	47
Figure 6.1	Mean First Passage Times graphical representations.	49
Figure 6.2	Analysis of the timescales	52

Figure 6.3	Random walk with a reflective boundary.	53
Figure 7.1	Examples of lattices	58
Figure 7.2	Experimental 2D compaction	59
Figure 7.3	Diffusion in 2D networks of DIBs.	59
Figure 7.4	Power Diagram results.	60
Figure 7.5	Occupancy probability map on Power Diagram Cells	61
Figure 8.1	Comparison between cell-free protein synthesis and traditional recombinant synthesis.	69
Figure 9.1	Example of genetic constructs and characterization on agarose gel.	73
Figure 9.2	Quantifying kinetics and yielding of TXTL production in bulk.	75
Figure 9.3	SDS Page of TXTL reaction products.	76
Figure 10.1	Emulsion Transfer Technique.	79
Figure 10.2	Formation of small droplet networks for stability assays.	80
Figure 10.3	TXTL reactions encapsulated in GUVs.	81
Figure 10.4	In situ TXTL expression of eGFP.	82
Figure 10.5	Stability analysis of DIBs in the context of TXTL production.	83
Figure 10.6	Increasing DIB stability with extract dilution and lipid mix optimization.	85
Figure 10.7	Measure of protein insertion.	86
Figure 10.8	Insertion of MscL and MscLeGFP in the bilayer.	87
Figure 10.9	Insertion of α HL and α HLeGFP in the bilayer.	87
Figure 10.10	Graphical representation and scoring of protein localization at the membrane.	88
Figure 11.1	Experimental setup for bilayer electrophysiology recording.	91
Figure 11.2	Comparison between the DPhPC and the Dupin mix.	93
Figure 11.3	TXTL expression in presence of increasing [KCl] concentration.	94
Figure 11.4	Description of electrophysiological recordings.	95
Figure 11.5	Expected Current Jumps.	96
Figure 11.6	First available configurations for hemolysin insertion	97
Figure 11.7	Determining the experimental conductance of hemolysin.	99
Figure A.1	Microfluidic chip conception for emulsion production	102
Figure C.1	Extract Dilution Data, Source V. Noireaux Lab, Jon Garamella	107
Figure D.1	Protein solubilization, dilution TXTL 25%	109

LIST OF TABLES

Table 9.1	Reaction assembly, 90 μ L final volume, no dilution	71
Table 11.1	Expected Current Jumps.	97
Table C.1	Energy Buffer Composition	106
Table C.2	Plasmid types	106
Table D.1	Reaction assembly, 50% extract	108
Table D.2	Reaction assembly, 25% extract	109

$\text{}^3\text{PGA}$ 3-phosphoglycerate
BLM Black Lipid Membrane
s-BLM *Metal-supported* Bilayer Lipid Membrane
sb-BLM *Agar salt-bridge-supported* Bilayer Lipid Membrane
CFPS Cell-Free Protein Synthesis
CTRW Continuous Time Random Walk
FPT First-Passage Time
IVTT In Vitro Translation Transcription
MscL Mechanosensitive Channel of Large Conductance
NET Narrow-Escape Time
PDMS Polydimethylsiloxane
PMMA Poly(methyl methacrylate)
SDS Sodium dodecyl sulfate
UTR Untranslated Region

Part I

FRENCH SUMMARY / RÉSUMÉ FRANÇAIS

RÉSUMÉ FRANÇAIS

1.1 INTRODUCTION

Les canaux protéiques intégrés dans les membranes biologiques sont l'un des modes de communication utilisés par les cellules pour intégrer l'information sur leur environnement et envoyer des signaux. Afin d'étudier de manière quantitative et reproductible le fonctionnement de ces pores, on peut les insérer dans des membranes artificielles de type Droplet Interface Bilayer (DIB). L'hémolysine a par exemple largement été utilisée comme canal ionique modèle sans qu'un lien quantitatif entre la dynamique du transport et le nombre de pores insérés n'ait été établi. Nous avons donc décidé de mettre en place une étude quantitative du transport dans des réseaux de bicouches connectés par des nanopores protéiques. Dans un premier temps nous montrerons comment optimiser la production d'émulsions monodisperses eau-dans-huile pour former des réseaux compacts de bicouches. Nous avons développé pour cela une méthode d'impression originale où nous superposons les gouttelettes en réseaux 1D ou 2D de manière simple et économique. Dans un second temps, nous développons un protocole pour insérer l'hémolysine dans des réseaux membranaires où une goutte source contenant un fluorophore est connectée à des gouttes réceptrices initialement non fluorescentes. Nous relierons l'augmentation du signal des premiers voisins de la source à la concentration introduite en pores grâce à une description microscopique de la disposition des pores dans la bicouche. Pour être capable de modifier le transport passif de la sonde sous contrainte mécanique, nous cherchons enfin à remplacer l'hémolysine par un canal protéique mécanosensible, MscL. Cette protéine hydrophobe doit être produite directement dans les réseaux de bicouches pour permettre son adsorption dans la membrane. Nous insérons donc dans ces réseaux une réaction *cell-free* de transcription traduction développée sous le nom TXTL. Nous démontrons dans ce nouveau cadre que nous sommes capables d'insérer dans une bicouche de l'hémolysine synthétisée *in situ* et fonctionnelle.

1.2 MODÈLE BIOMIMÉTIQUE DE TISSU CELLULAIRE

Droplet Interface Bilayers

Les membranes cellulaires fournissent un support physique aux protéines membranaires assurant des fonctions essentielles pour la communication entre la cellule et son environnement. En particulier, les protéines transmembranaires - y compris les canaux ioniques - transmettent des signaux entre le milieu intérieur et extérieur. Pour étudier la fonction de ces protéines en dehors du reste du contexte cellulaire, il peut être nécessaire de les reconstituer dans des membranes artificielles [1], également appelées biomimétiques. Ces membranes modèles sont de deux types : les liposomes et les membranes planes.

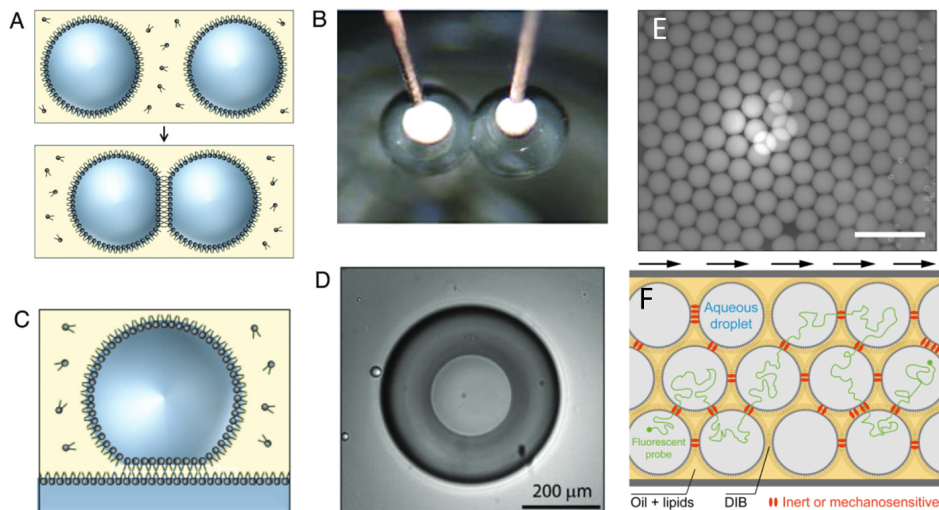
Les liposomes sont très efficaces pour la reconstitution des protéines membranaires, mais il peut être difficile d'y évaluer la fonctionnalité de ces protéines. Par exemple dans le cas de protéines mécanosensibles, la gamme de stimuli mé-

caniques disponibles est limitée par la fragilité et la taille de ces vésicules. Pour la même raison il est difficile d'y réaliser des mesures électrophysiologiques. Les membranes artificielles planes à base de phospholipides ont donc été développées comme alternative, avec comme aboutissement récent une méthode appelée *Droplet Interface Bilayers* [2]. Cette technique permet de former des bicouches robustes et stables sur lesquelles une grande variété de stimuli peut être appliquée. Ces bicouches peuvent de plus être assemblées en réseaux et permettent de nouvelles approches biomimétiques à l'échelle du tissu cellulaire. Publiée initialement en 1968 [3], la technique a été redécouverte par Bayley et al. en 2005 [2]. Deux configurations possibles pour générer une DIB sont décrites dans cette dernière référence [2]. Dans le premier cas, la bicouche lipidique est formée entre une goutte enrobée d'une monocouche de phospholipides et un plan hydrogel sur lequel une autre monocouche est adsorbée. Cette géométrie est appelée Droplet on a Hydrogel Bilayer (DHB) - Fig i, C et D. Dans le second cas, deux gouttes sont mises en contact et forment une bicouche à leur interface - approche que l'on nommera par extension DIB dans le reste du manuscrit - Fig i, A et B. Les DHBs ont été développées en premier [4, 5, 6, 7]. Le principal avantage de cette variante est optique : la bicouche se trouvant dans le plan d'observation, la dynamique des protéines membranaires y est facilement visible. Au contraire dans la configuration DIB, la bicouche est assemblée entre deux gouttelettes aqueuses qui sont soit suspendues soit posées sur un substrat. La bicouche se trouve donc dans le plan perpendiculaire au plan d'observation. Le grand avantage de cette dernière version par rapport à la configuration DHB est que les gouttelettes peuvent facilement être compactées en réseaux. Une méthode complète pour les deux configurations a été publiée en 2013 dans *Nature Methods* [5].

PHYSICO-CHIMIE : Le paramètre important dans la constitution de bicouches via la technique DIB est la bonne équilibration des monocouches de phospholipides. Si les monocouches autour des gouttelettes aqueuses ne sont pas équilibrées, les gouttelettes fusionnent lorsqu'elles sont mises en contact. La bonne équilibration des monocouches dépend de la vitesse d'adsorption des lipides. Cette cinétique dépend de trois paramètres : la concentration introduite en lipides, la méthode de fabrication des gouttes et le solvant utilisé pour dissoudre les lipides. Dans la méthode dite *Lipids-out* [8], les lipides sont habituellement dissous dans le solvant organique à une concentration entre 5 et 10 mg/mL, jusqu'à 20 mg/mL dans certains cas. Un mélange d'hexadécane et d'huile de silicone AR20 (1:1 v/v) semble être le meilleur compromis entre un bon et un mauvais solvant pour assurer la stabilité de la bicouche. Nous utilisons le DPhPC (1,2-diphytanoyl-sn-glycero-3-phosphocholine) comme phospholipide constitutif de la membrane. Nous présentons maintenant une méthode originale permettant de fabriquer de manière reproductible et stable des réseaux de bicouches.

Production microfluidique de gouttes

Nous cherchons à produire une émulsion eau-dans-huile stable que nous assemblerons ensuite en un réseau compact et monodisperse quasi-cristallin. Pour cela nous avons développé une technique nommée "piège capillaire" pour produire des réseaux de bicouches [9].



Présentation de la technique dite DIB dans différentes configurations A) Assemblage d'une membrane entre deux gouttes enrobées d'une monocouche de phospholipides B) Illustration expérimentale d'une mesure électrophysiologique sur une DIB, les deux électrodes sont plantées dans les gouttes et permettent de les amener facilement en contact. C) Variante dite DHB où la bicouche est formée entre un plan d'hydrogel et la goutte D) Image du plan de la bicouche dans la configuration DHB. A) à D) tirés de [4]. E) Compaction d'une émulsion eau-dans-huile stabilisée par un surfactant dans le plan, barre d'échelle ? F) Schéma de principe d'un réseau de DIB où des protéines membranaires sont insérées. Dans cette configuration il est possible de suivre le déplacement d'une sonde fluorescente d'une goutte à l'autre.

Figure 1: Illustration de la formation d'une DIB

ÉMULSIFIÉ Ce procédé nécessite de disperser une phase fluide dans une autre sans que ces deux phases soient miscibles entre elles. La surface de contact entre les deux phases est augmentée dans ce processus et nécessite donc généralement un apport d'énergie externe. Plusieurs techniques ont été documentées dans [10]. Nous ne résumerons brièvement ici que quatre de ces procédés. On peut d'abord fragmenter une phase dans une autre en tirant parti de la turbulence, en cisillant ou en vortexant les deux phases. Une telle émulsion, généralement polydispense, peut ensuite être re-calibrée en utilisant des homogénéisateurs haute pression comme c'est le cas dans les procédés industriels. En deuxième approche, l'émulsion peut être forcée à travers un poreux de manière à détacher la phase fragmentée [11], généralement avec une polydispensité assez élevée comparée aux autres méthodes. Dans les techniques de production de type imprimante à jet d'encre, la phase à disperser est fragmentée en utilisant par exemple une tête piézoélectrique. Cette méthode a donné des résultats impressionnants dans la constitution de réseaux de DIBs 3D [12, 13]. Enfin, l'émulsification peut être réalisée sur puce microfluidique, selon un procédé miniaturisé très efficace pour produire des émulsions monodisperses.

Nous avons d'abord essayé de produire des émulsions en utilisant des puces microfluidiques (détails en [Appendix A](#)). Avec cette approche il est difficile de positionner avec précision les gouttes sur des emplacements pré-définis. Il est également compliqué d'accéder au système à posteriori pour injecter par exemple la sonde fluorescente. Nous avons donc développé la technique de piège capillaire en nous inspirant plutôt des approches de type "imprimante à la demande".

PRODUCTION DE GOUTTES À LA DEMANDE Cette technique tire parti de la compétition entre les différentes tensions de surface en présence pour détacher les gouttes *à la demande*. La phase aqueuse est injectée continuellement dans un capillaire qui traverse l'interface entre un bain d'huile lipidique et l'air de manière périodique. Lors de la phase de rétraction, le ménisque d'huile détache une goutte au bout de la pointe - Fig ii A. Une méthode similaire a été publiée deux ans avant par Liao et al. [14] mais les auteurs n'y analysent pas l'effet des tensions de surface sur le mécanisme de détachement et ne proposent pas une caractérisation complète et quantitative de la méthodologie de production. Nous exposons dans ce qui suit les caractéristiques précises de notre technique de piège capillaire.

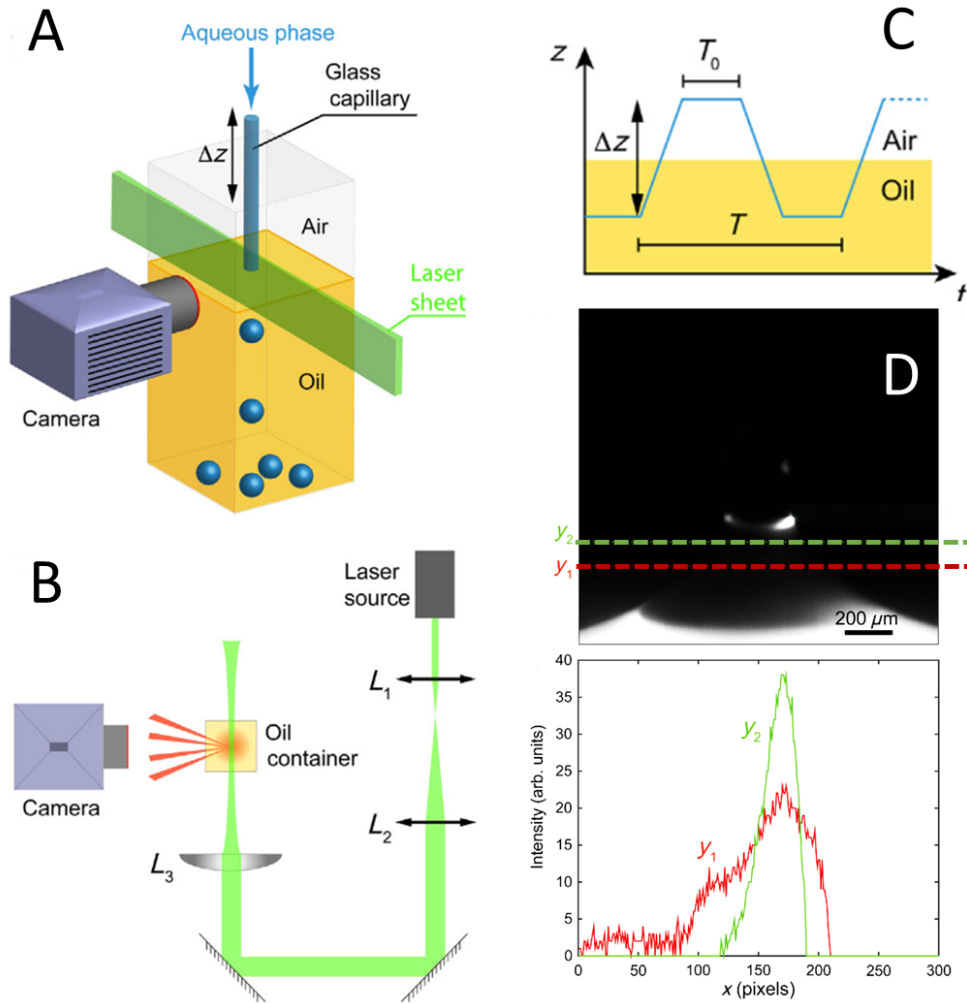
MATÉRIEL ET MÉTHODES Nous analysons l'effet de la tension de surface sur les caractéristiques de l'émulsion produite en variant les tensions de surface air/eau γ_{ao} et huile/eau γ_{ow} via la concentration introduite en SDS dans la phase aqueuse. Nous regardons également comment varie le rayon minimal des gouttes produites avec le rayon interne R_0 du capillaire utilisé ($R_0 \in [20 - 700] \mu\text{m}$). Ces capillaires sont reliés à un pousse-seringue KDS Scientific Legato 270 permettant d'avoir un contrôle fin sur le débit volumique injecté. La tête du capillaire est motorisée en z et le réservoir d'huile en x/y via une routine Labview. Ce programme nous permet de changer de manière dynamique la période d'extraction au cours de la phase de production des gouttes - Fig ii C).

Nous imageons le détachement de la goutte grâce à une caméra rapide (3000 images/s) afin de capturer la localisation des deux phases aqueuses et huileuses lorsque la goutte se détache. Pour imager la phase huile, nous élaborons un montage de type "feuille de lumière" afin d'éclairer sélectivement l'huile fluorescente dans le plan du détachement - Fig ii B (marquage Nile Red et éclairage laser COMPASS 315 M $\lambda = 532 \text{ nm}$).

CARACTÉRISATION DES PERFORMANCES DE LA MÉTHODE Grâce à l'imagerie de fluorescence, nous pouvons conclure qu'il n'y a pas démouillage de l'huile sur le ménisque lorsque le capillaire s'arrache à la surface. Des coupes transverses sur l'image réalisée dans le plan confirment qu'il reste un film fin d'huile au cours du procédé - Fig ii D.

Nous analysons ensuite la distribution de taille R_d des émulsions produites. Expérimentalement, le rayon de la goutte détachée $R_d \geq 2 \text{ à } 3 R_0$. Nous avons vérifié que le volume injecté par période d'extraction correspond bien au volume de la goutte détachée, ce qui signifie que le système d'injection n'est pas compressible et fonctionne dans un régime permanent. Il existe un débit volumique limite Q^* en dessous duquel on ne détache plus une goutte à chaque période. Nous associons à Q^* le rayon minimal de détachement noté R_d^* . Pour $Q > Q^*$, $R_d = f(Q)$ est convenablement ajusté par $R_d \propto (QT)^{\frac{1}{3}}$. Nous déduisons donc que R_d est facilement contrôlé soit en changeant T la période d'extraction soit Q le débit volumique d'injection. La méthode produit une émulsion avec une polydispersité inférieure à 1% dans ce régime de production.

Nous avons vérifié que la taille de la goutte produite ne changeait pas avec la vitesse d'extraction du capillaire, ce qui nous permet de conclure que la méthode fonctionne visiblement de manière quasistatique. Nous proposons donc de décrire le détachement des gouttes avec un modèle comparant les énergies associées à un état initial et un état final sans inclure de description hydrodynamique.



A) Dispositif de caractérisation du piège capillaire B) Montage optique pour l'imagerie par feuille de lumière de l'huile colorée par le Nile Red C) Schéma du principe d'extraction périodique à travers un bain d'huile D) Imagerie par fluorescence de l'huile sur le ménisque avec coupes transversales correspondantes en y_1 et y_2 . Il y a un signal significatif par rapport à la ligne de base en y_2 , ce qui signifie qu'il n'y a pas démoillage de l'huile au niveau du pincement de la gouttelette.

Figure ii: Schéma de fonctionnement et analyse en caméra rapide de la méthode du piège capillaire.

Modèle Quasistatique

Expérimentalement lorsque la concentration introduite en SDS augmente, les tensions de surface γ_{aw} et γ_{ow} décroissent [15]. Nous observons que R_d^* décroît également.

Dans une version *a minima* de notre modèle nous imposons la forme du ménisque et de la goutte au cours du détachement pour calculer les énergies de surface associées à 1) l'état goutte attachée 2) l'état goutte détachée. Lorsque la pointe du capillaire est immergée, la goutte est initialement attachée au capillaire et a la forme d'une calotte sphérique de hauteur h et de rayon R . Quand le capillaire remonte, la partie émergée de la goutte change de forme (on postule une forme parabolique) et les contributions des énergies de surface eau/huile et huile/air augmentent. La calotte sphérique est finalement coupée à un rayon $R = R_1$. La goutte détachée forme alors une sphère de rayon R_d dans l'huile.

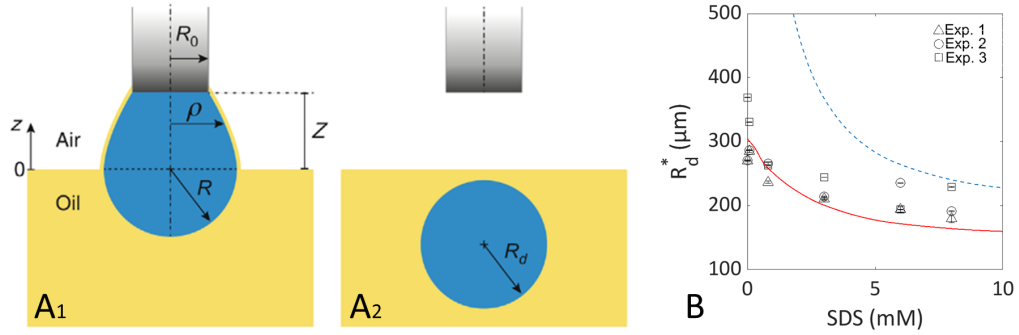
CALCUL DES ÉTATS INITIAUX ET FINAUX On calcule l'énergie libre F_A (resp. F_B) associée à l'état 1 (resp 2) voir Fig iii A1 et A2. Le volume et l'aire du paraboloïde associé à $\rho(z)$ sont calculés en utilisant comme conditions au bord la continuité de la dérivée en $z = 0$ et la continuité de la parabole au raccordement $\rho(Z) = R_0$.

On écrit F_A et F_B comme des fonctions des différents paramètres géométriques et des trois tensions de surface γ_{ow} , γ_{ao} et γ_{aw} .

$$\mathcal{F}_A = \gamma_{ow}(\mathcal{A}_p + \mathcal{A}_c) + \gamma_{ao}\mathcal{A}_p \quad (1.1)$$

$$\mathcal{F}_D = \pi R_0^2 \gamma_{aw} + 4\pi R_d^2 \gamma_{ow} + \gamma_{ao}\pi R_1^2 \quad (1.2)$$

On résoud numériquement l'égalité $F_A = F_B$ en utilisant la conservation entre le volume initial V_0 et la somme des volumes correspondant au paraboloïde (V_p) et à la calotte sphérique coupée en R_1 (V_c). Le couple (h, Z) correspondant nous permet de déterminer R_d^* .



A 1) Goutte attachée à la pointe du capillaire. La connexion entre la calotte sphérique immergée et la pointe du capillaire se fait avec un paraboloïde d'équation $\rho(z)$. En A 2) la gouttelette est détachée et complètement immergée dans le bain d'huile. Dans ce modèle, nous supposons que le ménisque d'huile est extrêmement mince et que sa forme correspond à la ligne parabolique du haut de la gouttelette. B) Résolution numérique pour le rayon minimal R_d^* détaché, γ_{ao} est fixé à 18 mN/m et $R_0 = 100 \mu\text{m}$. La résolution analytique complète est tracée en pointillés bleus. Nous devons postuler une tension $\gamma_{ao} = 36 \text{ mN/m}$ (ligne rouge) pour capturer correctement les données expérimentales (symboles noirs). Le rayon détaché dépend faiblement de la concentration introduite en SDS.

Figure iii: Modèle a minima de détachement

À partir de considérations géométriques on peut déduire que le rayon minimal R_1 auquel la gouttelette est coupée en traversant l'interface est en fait le rayon de courbure de la calotte sphérique. Si on injecte alors $R_1 = R$ et $a(Z) = 0$ dans la résolution numérique, on obtient le même résultat qu'en l'absence de cette simplification. Avec cette modification, R_d^* peut être résolu de façon analytique via Mathematica. Nous posons les variables réduites suivantes $z^* = \frac{Z}{R_0}$, $r^* = \frac{R}{R_0}$, $f_A = \frac{F_A}{R_0^2}$ et $f_D = \frac{F_D}{R_0^2}$ afin d'obtenir une expression compacte pour la hauteur minimale z^* à laquelle la goutte est coupée. Avec l'approximation supplémentaire $r^* \ll 1$, on obtient une expression très simplifiée pour r^* :

$$r^* = \frac{\sqrt{5\gamma_{ao} + 12\gamma_{aw} + 5\gamma_{ow}}}{2\sqrt{2\gamma_{ao} - \gamma_{ow}}} \quad (1.3)$$

Ce résultat est tracé Fig iii B. Il faut postuler une tension superficielle plus élevée $\gamma_{oa} = 36 \text{ mN/m}$ (ligne rouge continue) que la tension superficielle réelle $\gamma_{oa} = 18 \text{ mN/m}$ (ligne bleue pointillée) pour capturer la dépendance des données

expérimentales avec la concentration introduite en SDS. Ceci est probablement dû au fait que nous sous-estimons la surface du ménisque d’huile dans notre modèle géométrique rudimentaire. Malgré cette approximation brutale nous parvenons à décrire la relation entre R_d^* et la concentration introduite en SDS avec un modèle d’ordre zéro. Avec ce résultat, nous démontrons que le phénomène peut être décrit via un cadre théorique simplifié comparant simplement l’énergie des deux états finaux.

1.3 TRANSPORT PASSIF DANS DES TISSUS ARTIFICIELS CONNECTÉS PAR DES NANOPORES PROTÉIQUES

L’hémolysine : un canal de communication

INSERTION DE L’HÉMOLYSINE DANS UNE BICOUCHE L’alpha-hémolysine est une protéine multimérique de 293 acides aminés produite par la bactérie *Staphylococcus aureus* pour lyser les érythrocytes (ou globules rouges) via perforation de leur membrane [16]. Ses monomères constitutifs sont solubles dans l’eau et s’oligomérisent en heptamères dans les membranes. La structure du pore a été caractérisée en 1996 par Song et al. [17]. Le diamètre interne du pore varie entre 1.4 nm et 2.5 nm, ce qui permet le passage de molécules de taille inférieure à 1-4 kDa [18]. L’hémolysine est également capable de s’insérer dans des bicouches de synthèse, ce qui permet de postuler que le mécanisme de base permettant son insertion repose sur des interactions hydrophobes seulement [19]. Bayley et al. ont par ailleurs démontré que dans la configuration DIB l’oligomérisation se produisait en moins de 5 ms [7].

Suite à ces données, nous ferons l’hypothèse que l’assemblage du pore peut se décrire à l’aide d’une seule équation d’équilibre (Eq 1.4). Nous utiliserons le modèle classique d’adsorption de Langmuir [20] pour établir la relation entre la concentration en pores dans la bicouche C_s et la concentration introduite en monomères C_i .



La constante d’équilibre d’adsorption K peut s’écrire en fonction de C_i (concentration introduite en monomères) et C_s (concentration en pores adsorbés), avec C_0 et $C_{0,s}$ des constantes de normalisation. Les détails du modèle sont reproduits [Appendix B](#).

$$K = 7 \ln C_i / C_0 - \ln C_s / C_{0,s} \quad (1.5)$$

A partir de l’équation 1.5 nous pouvons écrire la proportionnalité entre C_i et C_s , ce qui nous permet d’utiliser le seul paramètre $c = C_i$ pour décrire la composition en pores de la bicouche.

$$C_s = \frac{N_a^p}{\mathcal{A}_D} \propto c^7 \quad (1.6)$$

DIFFUSION À TRAVERS L’HÉMOLYSINE La communication d’une goutte à l’autre est permise par la transmission d’une molécule à travers le pore. L’hémolysine a été largement utilisée pour démontrer la fonctionnalisation d’une bicouche, que ce soit dans des liposomes ou des DIBs. En revanche, très peu d’études ont réellement

étudié la relation entre ce transport et le nombre de pores présent. Dupin et Simmel [21] proposent un modèle décrivant la diffusion à travers l'hémolysine à l'aide d'un coefficient de diffusion effectif prenant en compte le nombre de pores dans la bicouche. Nous proposons d'engager plutôt la réflexion sur la manière dont l'arrangement spatial des pores dans la bicouche change le temps pris par une sonde pour traverser cette paroi. En effet, la sonde peut être caractérisée comme un marcheur aléatoire qui doit trouver sa cible par hasard tout en explorant l'intérieur de la goutte. Une fois l'hémolysine atteinte, la sonde peut traverser le pore et visiter le compartiment voisin. Ce problème est décrit théoriquement dans le cadre du *Narrow Escape Problem*.

TEMPS DE PREMIER PASSAGE En considérant un objet diffusif et une cible, le temps de premier passage (FPT) décrit combien de temps il faut attendre avant que cet objet atteigne la cible pour la première fois. Nous considérons un domaine fermé avec limites réfléchissantes. Dans le cas d'une cible de petite taille devant celle du domaine [22], le FPT est aussi appelé le Narrow Escape Time (NET). Une sonde brownienne avec un coefficient de diffusion D s'échappera d'une cavité sphérique de rayon R pourvue d'une sortie de taille a en un temps caractéristique typique $\langle T \rangle = \frac{R^3}{aD}$ [23]. Une dérivation exacte est faite pour les domaines de forme arbitraire, d'abord dans [24] puis via une approche unifiée dans [25]. En supposant un pore de diamètre a , diffusant sur la surface d'une sphère d'un rayon R , comme illustré Fig v A1, le temps moyen $\langle T \rangle$ nécessaire pour qu'une sonde à l'intérieur de la gouttelette atteigne le pore est :

$$\langle T \rangle = \frac{V}{2Da} \quad (1.7)$$

Nous adaptons cette description au cas de plusieurs gouttes connectées par ces pores de taille a . Au lieu de modéliser la diffusion dans ces réseaux par un coefficient de diffusion effectif D_{eff} , nous utiliserons le cadre des marches aléatoires en temps continu (CTRW). Grâce à ce formalisme nous établirons un lien entre $\langle T \rangle$ et la marche aléatoire discrète sur les sites $\{\mathbf{r}_0, \mathbf{r}_1, \dots, \mathbf{r}_N\}$.

MARCHE ALÉATOIRE EN TEMPS CONTINU Toute la section qui suit est une application directe du livre de B.D. Hughes, *Random Walks* [26]. Nous adoptons les notations suivantes pour la fonction $f(\mathbf{r}, t)$.

- La transformée de Laplace par rapport à la variable t est notée $\hat{f}(\mathbf{r}, s) = \int_0^\infty f(\mathbf{r}, t) \exp(-s.t) dt$.
- La transformée de Fourier discrète par rapport à la variable \mathbf{r} est notée $\tilde{f}(\mathbf{k}, t) = \sum_{\mathbf{r}} \exp(i\mathbf{k}\mathbf{r}) \cdot f(\mathbf{r}, t)$.

Nous considérons une marche aléatoire sur un réseau discret de dimension $d = 1$. $P_n(x)$ est la probabilité de trouver le marcheur en x après n pas de temps. La probabilité de se trouver au bout d'un pas en x sachant qu'on était avant en x_0 s'écrit $p(x - x_0)$. Dans le cas où tous les déplacements sont autorisés pareillement, on peut établir la relation de récurrence :

$$P_{n+1}(x) = \sum_{x-x_0} p(x - x_0) P_n(x_0) \quad (1.8)$$

Dans l'espace de Fourier on peut introduire le facteur de structure $\Lambda(k) = \sum_x e^{ikx} p(x)$. Avec ce nouvel outil, on écrit de manière compacte $\tilde{P}_n(k) = \Lambda(k)^n$, ce qui donne la forme suivante pour $P_n(x)$:

$$P_n(x) = \frac{1}{2\pi} \int \exp(ikx) \Lambda(k)^n dk \quad (1.9)$$

Cette expression peut être utilisée dans le développement asymptotique de la fonction génératrice $P(\mathbf{r}, \xi)^1$

$$P(x, \xi) = \sum_n P_n(x) \xi^n = \frac{1}{2\pi} \int \frac{\exp(ikx)}{1 - \xi \Lambda(k)} dk \quad (1.10)$$

A partir de cette relation, nous proposons de garder le caractère discret spatial de la marche aléatoire, dont les sites correspondent aux centres des gouttes connectées. Nous considérerons en revanche une distribution continue $\psi(t)$ de temps d'attente entre chaque pas. Dans le cas canonique, cette *waiting time density* est exponentielle décroissante $\psi(t) = \lambda \exp(-\lambda t)$. Ce choix est motivé dans notre cas par le cadre particulier du *Narrow Escape Problem* [27]. L'échelle de temps $\lambda = \frac{1}{\tau}$ qui caractérise la densité de temps d'attente est en fait l'inverse du NET.

Lorsqu'on peut découpler probabilité spatiale et temporelle, le théorème de Montroll et Weiss relie la probabilité spatiale de présence sur le réseau et la densité de temps d'attente :

Considérons $P(x|x_0, \xi) = \sum P_n(x|x_0) \xi^n$ la fonction génératrice pour la probabilité d'occupation des sites sur une marche aléatoire discrète. La transformée de Laplace de la probabilité $p(x|x_0, t)$ de trouver le marcheur en t et x sachant qu'il est parti de x_0 à $t = 0$ s'écrit:

$$\hat{p}(x|x_0, s) = s^{-1} \{1 - \hat{\psi}(s)\} P(x|x_0, \hat{\psi}(s)) \quad (1.11)$$

En combinant Eq 1.11 et $\Lambda(k) = \sum_x \exp(ikx) \frac{1}{2} (\delta_{0,-1} + \delta_{0,1})$ (le marcheur démarre en $x = 0$ à $t = 0$) on obtient :

$$p(x|x_0, t) = \frac{1}{2\pi} \int \exp(ikx) \exp(-\lambda (-\cos k) t) dk \quad (1.12)$$

Pour $x = n$ entier introduisons $\mathcal{I}_n(\lambda t) = \frac{1}{\pi} \int_0^\pi \cos kn \exp(\lambda t \cos k) dk$, la fonction de Bessel modifiée du premier type :

$$p(x, t) = e^{-\lambda t} \mathcal{I}_x(\lambda t)$$

Dans le chapitre suivant nous allons relier précisément la cinétique du transport au nombre de pores adsorbés dans la membrane grâce à des mesures optiques moyennées. Nous lions cette cinétique à une description microscopique de l'arrangement des pores dans la membrane.

Transport dans des lignes de gouttes connectées

FABRICATION DES LIGNES Pour assurer la reproductibilité des réseaux d'une expérience à l'autre, nous déposons les gouttes dans des emplacements pré-définis

¹ Les fonctions génératrices sont un outil commode permettant d'écrire les fonctions sous forme de série entière.

à l'aide de la technique du piège capillaire. Ces emplacements sont des rainures hémicylindriques de 100 μm de profondeur, 200 μm de largeur et 5 mm de longueur. Les gouttes sont contraintes en lignes dans ces rainures. Pour la phase huile de l'émulsion, nous dissolvons le DPhPC dans un mélange hexadécane/huile de silicone AR20 (v/v 1:1) à une concentration finale de 6,5 mg/mL. Des échantillons d'hémolysine dans le tampon KCl 100 mM HEPES 10 mM sont préparés à différentes concentrations, de 100 à 300 $\mu\text{g}/\text{mL}$. Les gouttes aqueuses de diamètre 200 à 250 μm de diamètre sont produites à l'aide d'un piège capillaire et disposées dans les rainures. Nous injectons ensuite une gouttelette contenant de la carboxyfluorescéine à 20 μM préparée dans le même tampon. L'expérience est représentée Fig iv A, avec un schéma expliquant comment les gouttes sont reliées par l'hémolysine. Nous représentons un exemple où la goutte source commence à se vider dans le premier voisin, accompagné d'une image typique du réseau en lumière blanche, barre d'échelle 200 μm . Nous mesurons la diffusion d'un fluorophore par microscopie d'épifluorescence, en prenant des images au $\times 10$ toutes les 10 à 20 min avec un temps d'exposition de 500 ms. Une expérience typique dure de 12 à 16 heures. Nous utilisons cet ensemble de données pour quantifier l'augmentation de la fluorescence chez les voisins de la gouttelette source.

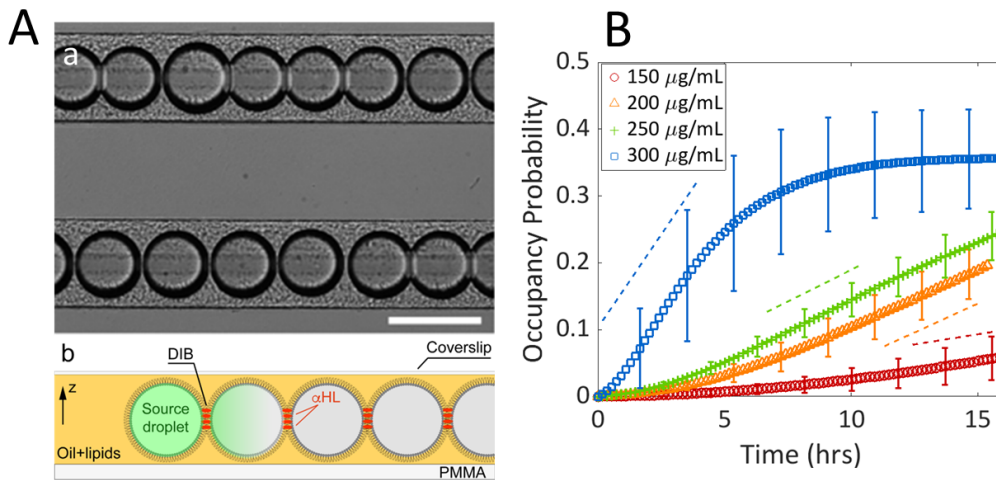
ANALYSE D'IMAGE Nous quantifions l'augmentation de fluorescence dans les premiers voisins. Après avoir détecté les contours des gouttes sur les images en visible, nous ajustons ces contours par des cercles en utilisant une transformée de Hough. L'intensité est moyennée dans un disque dont le diamètre fait la moitié du disque initialement détecté qui circonscrit la goutte. Nous définissons comme probabilité d'occupation de la goutte i l'intensité ainsi mesurée normalisée par toutes les intensités sur la ligne. Avec cette convention, la somme des probabilités sur une ligne connectée vaut 1. La source étant décrite par l'indice s , la probabilité P_i vaut:

$$P_i(t) = \frac{I_i(t) + (\delta_{i,s} - 1)I_i(0)}{\sum_k I_k(t) + (\delta_{k,s} - 1)I_k(0)} \quad (1.13)$$

Les lignes formées ont entre 3 et 10 gouttes connectées. Le signal augmente chez le premier voisin puis le deuxième, mais il n'est pas possible de s'éloigner davantage de la source dans l'analyse. La diffusion est en effet trop lente par rapport à la durée moyenne de l'expérience, d'environ 12 heures. Nous étudions donc l'évolution de la probabilité d'occupation chez le premier voisin de la source. Le signal est légèrement parasité par l'évaporation dans la goutte (tendance à la surconcentration) et le photoblanchiment (perte de signal). En moyenne, on constate que l'augmentation de la fluorescence due à la diffusion est plus forte que la concentration en fluorophore due à l'évaporation. Elle est également plus forte que la baisse d'intensité due au photoblanchiment.

LE NOMBRE DE PORES ADSORBÉS CHANGE LA DYNAMIQUE DU SIGNAL Nous sélectionnons d'abord la plage de concentration introduite en pores où nous détectons la diffusion de la carboxyfluorescéine de la source vers le premier voisin. Nous utilisons comme seuil de détection une probabilité d'occupation supérieure à 1% chez le premier voisin à la fin de l'expérience. Nous n'avons effectué aucune sélection préalable d'expériences avant analyse, ce qui signifie que les chocs osmotiques qui peuvent produire un faux positif sont également inclus dans l'analyse. Il y a une séparation claire entre les expériences à 0 et 100 $\mu\text{g}/\text{mL}$ et le reste. Nous décidons

donc d'analyser la cinétique de diffusion sur la plage d'expériences comprise entre $c = 150 \mu\text{g/mL}$ et $c = 300 \mu\text{g/mL}$ (concentration introduite en hémolysine).



A) Lignes de DIBs connectées par l'hémolysine a) Photo BF, barre d'échelle 200 μm b) Schéma de principe de la diffusion avec la sonde fluorescente utilisée B) Probabilité d'occupation pour les premiers voisins, $c = 150, 200, 250$ et $300 \mu\text{g/mL}$. On observe en majorité le régime transitoire pour ces conditions.

Figure iv: Expérience de diffusion sur un réseau 1D connecté par l'hémolysine

De cet ensemble de données, nous retirons les expériences où l'intensité de la source augmentait avec le temps en raison d'une évaporation anormalement élevée, et celles où la cinétique ultra-rapide montrait un déséquilibre osmotique. Nous avons moyennés les courbes pour chaque concentration introduite c dans cet ensemble restreint (Fig iv B). On voit que la concentration introduite en pores modifie la cinétique de transport de la source vers son premier voisin. Nous observons un régime transitoire linéaire par rapport au temps - pour les concentrations de 150, 200 et 250 μg/mL. Pour la concentration la plus élevée, 300 μg/mL, un plateau apparaît lorsque la concentration commence à s'équilibrer chez le premier voisin. Nous atteignons plus rapidement le plateau en raison d'un effet de bord (les lignes à haute concentration sont en moyenne plus courtes). Lorsque c augmente, la pente du régime transitoire augmente également. Nous allons maintenant discuter comment cette relation peut être quantifiée à l'aide des temps de premier passage.

Cinétique de transport

TEMPS DE PREMIER PASSAGE Nous cherchons l'origine microscopique de l'échelle de temps. Dans notre expérience, la sonde fluorescente ne sort de la source que si sa trajectoire aboutit sur la cible, ici l'hémolysine dans la bicouche. Ce cadre conceptuel correspond au temps de premier passage abordé quelques paragraphes en amont.

L'hémolysine a un diamètre interne d'environ 10 nm et elle est insérée en surface d'une goutte de rayon $R = 100 \mu\text{m}$. Prenant comme coefficient de diffusion de la fluorescéine dans l'eau $D = 4.10^{-6} \text{ cm}^2 \cdot \text{s}^{-1}$ [28], nous pouvons estimer $\langle T \rangle \simeq 5.10^5 \text{ s}$ à partir de 1.7. Ce temps est largement diminué par le fait que plusieurs pores sont insérés dans la bicouche. Lorsque N pores de diamètre a sont distribués en

bordure du domaine, deux limites coexistent selon que les pores sont considérés indépendants ou dépendants.

Dans le premier cas, le NET pour N pores varie comme le NET pour un seul pore divisé par N , (Fig v A2) : $\langle T \rangle = \frac{V}{2DNa}$

Lorsque N devient très grand, les pores forment des clusters d'aire $S = Na^2$ et de taille typique $\sqrt{S} = \sqrt{Na}$. Le NET devient donc: $\langle T \rangle = \frac{V}{2D\sqrt{Na}}$ (Fig v A3).

Connaissant le rapport entre la concentration introduite en pores et la concentration adsorbée, nous pouvons maintenant relier l'échelle de temps à c le paramètre de contrôle du problème.

Dans le régime où les pores sont indépendants :

$$\langle T \rangle \propto \frac{1}{N} \propto c^{-7} \quad (1.14)$$

Dans le régime où les pores sont agglomérés :

$$\langle T \rangle \propto \frac{1}{\sqrt{N}} \propto c^{-\frac{7}{2}} \quad (1.15)$$

Dans le cadre théorique de la marche en temps continu, le premier voisin situé à la coordonnée $x = 1$ a la probabilité d'occupation suivante (linéaire au premier ordre par rapport au temps) :

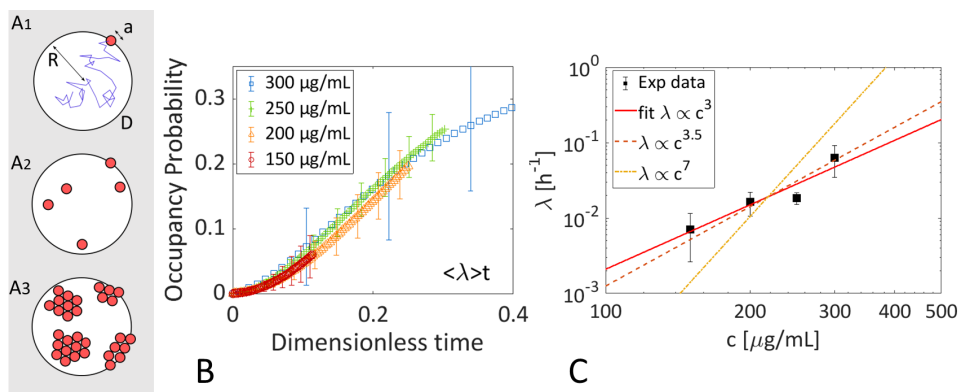
$$p(1, t) = \mathcal{I}_1(\lambda t)e^{-\lambda t} \simeq \frac{\lambda t}{2} - \frac{(\lambda t)^2}{2} + \frac{5(\lambda t)^3}{16} - \frac{7(\lambda t)^4}{48} + o(t^5) \quad (1.16)$$

TRANSPOSITION AUX DONNÉES EXPÉRIMENTALES Nous utilisons le développement limité de la probabilité d'occupation au site 1 pour calculer la pente des différentes courbes dans le régime linéaire et obtenir $\tau = \frac{1}{\lambda}$. Nous ajustons le régime transitoire des courbes individuelles dans le régime linéaire avec un modèle linéaire $a.x + b$, $a = \frac{\lambda}{2}$. Les courbes ne sont pas linéaires pendant les premiers instants de l'expérience ($t \leq 1$ h), probablement car le système n'est pas encore totalement équilibré. Nous recherchons donc les régimes linéaires en ajustant les courbes autour de leur point d'inflexion.

Nous vérifions d'abord que λ est la seule échelle de temps de l'expérience en renormalisant chaque cinétique moyennée sur une concentration par la moyenne λ extraite des courbes individuelles correspondant à cette concentration. Fig v B nous voyons que les courbes s'alignent bien sur une seule tendance. Les différents λ sont tracés Fig v C.

Nous cherchons une loi de puissance qui décrive la dépendance entre λ et la concentration introduite. Après ajustement, nous obtenons $\lambda \propto c^{3 \pm 1}$. Ce résultat nous permet de faire la distinction entre deux régimes, celui dans lequel $\lambda \propto c^{7/2}$ (pores indépendants) et celui dans lequel $\lambda \propto c^7$ (clusters). La valeur inférée de l'exposant nous montre que le cas $\lambda \propto c^{7/2}$ est le régime le plus probable. Nous confirmons cette hypothèse en traçant les asymptotes des deux régimes - ligne pointillée orange pour le régime *pores indépendants* et ligne pointillée rouge pour le régime *pores dépendants*. Le régime *pores dépendants* est bien à l'intérieur des barres d'erreur alors que la limite opposée est sans aucun doute hors de l'intervalle de confiance.

De cette analyse, nous concluons que les pores sont très probablement agglomérés à l'intérieur de la bicouche.



A1) Exemple d'une trajectoire avec coefficient diffusif D conduisant à la cible de diamètre a dans la goutte de rayon R A2) Cas où sont présents plusieurs pores indépendants A3) Cas où les pores sont agglomérés (*clusters*) B) Renormalisation des courbes correspondant aux différentes concentrations par leurs échelles de temps $\frac{1}{\lambda}$ respectives C) Représentations des différents λ s avec lois de puissance associées (ligne rouge continue ajustement avec $\lambda \propto c^3$, ligne rouge pointillée variation en $\lambda \propto c^{7/2}$ et ligne jaune variation en $\lambda \propto c$). On peut écarter la loi de puissance en c^7 à partir de cette analyse.

Figure v: Analyse de l'échelle de temps du phénomène diffusif

1.4 EXPRESSION *in situ* DE PROTÉINES MEMBRANAIRES

Synthèse in vitro de protéines

CONTEXTE La synthèse protéique *in vitro* de type *cell free* détourne la machine de transcription/traduction d'un organisme hôte pour synthétiser directement dans un tube à essai la protéine d'intérêt [29]. Par rapport à la synthèse recombinante traditionnelle des bactéries, elle dissocie le cycle bactérien de la synthèse protéique elle-même. Cela permet de multiplier les expériences sur une échelle de temps plus courte dans le cadre d'une étude fonctionnelle des protéines.

Deux approches distinctes cohabitent aujourd'hui dans la production de type *cell free*. L'approche *bottom up* est symbolisée par le système PURE dans lequel tous les constituants sont extraits séparément, purifiés et réassemblés pour former la réaction [30]. Dans l'approche *top down*, le lysat bactérien est partiellement purifié et combiné avec de l'ADN exogène, des acides aminés, des nucléotides et un système de régénération de l'ATP [31] [32]. Nous utilisons un système développé dans cette seconde tendance.

Ces systèmes sont utilisés aujourd'hui pour produire différents types de protéines, en particulier des protéines transmembranaires dans des membranes reconstituées [33].

INSERTION DE PROTÉINE MEMBRANAIRE α HL présente l'avantage d'être hydrosoluble sous sa forme monomérique ce qui permet de reconstituer l'heptamère facilement dans une membrane. Ce n'est pas le cas de beaucoup de canaux ioniques comme MscL, le pore mécanosensible pentamérique à large conductance présent chez *E. coli*. Les monomères de MscL ne sont pas solubles dans l'eau. En revanche, si on peut synthétiser cette protéine *in situ* dans le voisinage immédiat d'une membrane, on peut espérer qu'elle s'y replie dans sa conformation fonctionnelle [34], comme cela a été démontré dans le cas des liposomes [35]. Les vésicules unilamel-

lares géantes² (GUV) peuvent être préparées à l'aide d'une technique d'émulsion inverse [37, 38]. Les liposomes fournissent la membrane nécessaire pour l'insertion d'une protéine membranaire et ils améliorent également le maintien de la réaction *cell free* en jouant le rôle de micro-réacteur.

Les systèmes de type *cell free* ont également été intégrés à des gouttes destinées à former des DIBs, en exprimant les protéines avant formation de l'émulsion [39] ou directement *in situ* [40, 41, 42, 43, 44, 21]. En particulier, Bayley et Holden ont publié en 2008 une étude précurseur dans laquelle ils ont directement produit de l'hémolysine avec deux systèmes dits In Vitro Translation Transcription (IVTT, PURE ou Promega) dans des gouttes contenant des liposomes [45]. Dans ces différents travaux, lorsque les protéines membranaires produites étaient des canaux ioniques, leur fonctionnalité a été démontrée par des mesures optiques et/ou électrophysiologiques.

CARACTÉRISATION DE LA PRODUCTION En dépit du développement de sondes optiques performantes pour imager les flux ioniques, l'électrophysiologie demeure un outil puissant pour étudier l'insertion et la fonctionnalité d'un seul pore par sa résolution temporelle de l'ordre du MHz et sa sensibilité [46]. Les bicouches lipidiques supportées ont été développées pour mesurer des courants à travers des canaux ioniques uniques [47]. Dans ce cadre, les membranes biologiques sont généralement représentées par un circuit électronique équivalent avec une résistance et une capacité en parallèle [48]. L'élément capacitif provient de la capacité des membranes à maintenir des charges ségréguées de part et d'autre du double feuillet lipidique (têtes polaires des lipides). Le résistance en parallèle permet de tenir compte de la perméabilité de la membrane à certains solutés. La résistance de la bicouche pure a été estimée par Montal et Mueller [49] entre 10^6 et $10^8 \Omega/\text{cm}^2$.

Wallace, Bayley et al. ont démontré par des mesures électrophysiologiques que l'hémolysine s'insérait bien dans des DIBs [5]. La conductance de l'hémolysine est asymétrique comme montré dans [50, 51]. On retiendra comme valeur de référence la conductance $\sigma_{\alpha HL}$ donnée dans [51] : sous une tension appliquée de ± 100 ms et une concentration en sel $[KCl] = 1$ M, $\sigma_{\alpha HL} = 1,09 \pm 0,04 \cdot 10^{-9} \text{ S} = 1090 \pm 40 \text{ pS}$ et dans l'état inversé $\sigma_{\alpha HL} = 720 \pm 61 \text{ pS}$.

Composition et fabrication de la réaction

TXTL Nous utilisons un système d'expression de protéines TXTL³ développé par V. Noireaux (UMN, USA). Dans le cadre de ma thèse j'ai passé plusieurs semaines dans ce laboratoire (Minneapolis) afin d'y apprendre les bases expérimentales permettant d'utiliser les réactions TXTL. J'ai pu ensuite transposer ces compétences au laboratoire Jean Perrin. Ce système à base d'extrait cellulaire d'*E. coli* a subi plusieurs étapes d'optimisation [52, 53, 32]. Le mélange réactionnel peut être décomposé en trois composants principaux : l'extrait cellulaire lui-même, le mélange d'acides aminés et le mélange énergétique. Ces trois ingrédients nous sont fournis par le Noireaux lab.

1. L'extrait fournit toutes la machinerie moléculaire nécessaire à la production de protéines, y compris l'ARN polymérase qui assemble les ARNm à partir

² Ces liposomes géants ont un diamètre de d supérieur au micron et sont comparables en dimensions aux cellules vivantes [36].

³ abréviation pour Transcription-Traduction

du modèle d'ADN et les ribosomes qui assemblent les acides aminés en protéines.

2. Le mélange d'acides aminés (AA) contient les 20 acides aminés canoniques à 17 mM afin d'obtenir une concentration finale de 3 mM dans la réaction.
3. La dernière partie de la réaction est le mix énergétique abrégé 3PGA, dont la composition exacte est donnée dans la [Table C.1](#). En plus de contenir les ribonucléotides nécessaires pour alimenter la réaction, le mix énergétique comprend plusieurs métabolites et enzymes importants dans la régénération de l'ATP, le principal étant le 3PGA, 3-phosphoglycérate [54].

À ces trois éléments essentiels de la réaction (extrait cellulaire/mélange d'acides aminés/mix énergétique) nous ajoutons des sels (Glutamate de magnésium et de potassium) à la concentration finale respective $[MgGlu] = 5 \text{ mM}$ et $[KGlu] = 90 \text{ mM}$. Nous ajoutons également de la maltodextrine à la concentration finale de 30 mM, le plasmide codant pour la séquence protéique et du polyéthylène glycol (concentration finale 4,5% w/v). Les proportions volumétriques des différents composés pour préparer une réaction finale de 90 μL sont résumées Fig [vi A](#).

PLASMIDE Un plasmide est une construction circulaire à double brin d'ADN. Cette information génétique relativement petite (enchainement d'environ 10^3 à 10^6 paires de bases) est physiquement séparée du génome bactérien et répliquée indépendamment par l'hôte. Les différents plasmides que nous utilisons sont listés [Table C.2](#). Pour l'hémolysine en particulier, nous utilisons un plasmide P28 α HL couplant le promoteur spécifique au facteur de transcription σ_{28} à la séquence codant l'hémolysine.

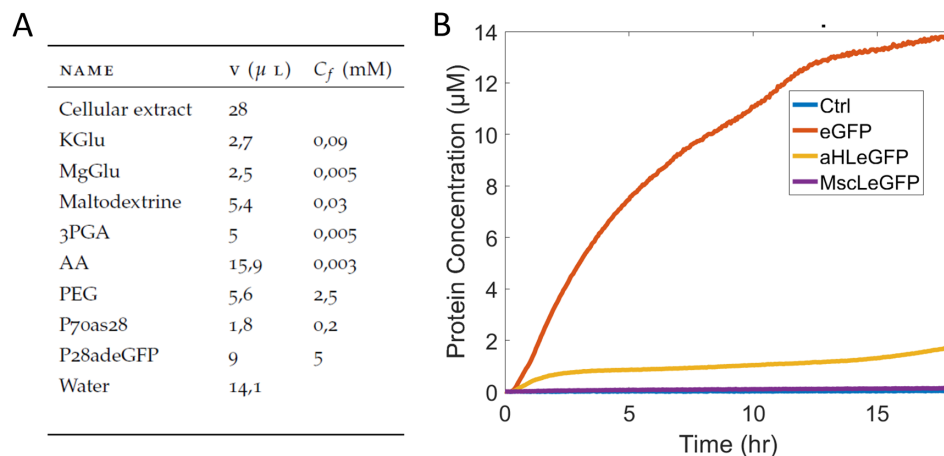
PROTÉINE FLUORESCENTE Il est courant d'utiliser des protéines fluorescentes pour caractériser la production de la réaction TXTL. La référence que nous utilisons est eGFP (Enhanced GFP), un dérivé de la protéine GFP conçu pour renforcer ses propriétés fluorescentes. Cette protéine absorbe à 488 nm et émet à 509 nm ⁴. Pour pouvoir quantifier de façon similaire la quantité de protéines transmembranaires que nous produisons, nous utilisons des protéines de fusion associant eGFP à la protéine transmembranaire d'intérêt, dans notre cas l'hémolysine (plasmide associé P28 α HLeGFP) ou MscL (P28MscLeGFP).

La cinétique de fluorescence est réalisée dans une plaque de 96 puits, 2 μL par puits, Biotek Synergy 2 Plate Reader (Minneapolis) ou dans un RotorQ Quiagen, 10 μL par réaction (Paris). Dans les deux cas, la réaction est maintenue à 29 °C, la température optimale pour l'expression TXTL.

RÉACTION DE 2 μL La cinétique d'expression TXTL à 29 °C pour une réaction sur Plate Reader est caractérisée Fig [vi B](#). Contrairement à la production d'eGFP ou d' α HLeGFP, la production de MscLeGFP ne dépasse pas le niveau de base du contrôle (réaction TXTL sans plasmide). La fluorescence MscLeGFP ne peut pas être mesurée en fluorimétrie volumique, probablement parce que la protéine n'est pas soluble dans la réaction et que le chromophore n'est donc pas bien replié.

Pour vérifier que les protéines MscL, α HL et MscLeGFP sont effectivement produites, nous avons réalisé un gel SDS Page qui confirme la présence de ces trois

⁴ <https://www.biotek.com/resources/technical-notes/excitation-and-emission-of-green-fluorescent-proteins/>



A) Table résumant les différents composés de la réaction pour un volume final de 90 μ L. NB: *Cellular extract* = Extrait cellulaire. B) Cinétiques de production pour eGFP et les protéines de fusion α HLeGFP et MscLeGFP, 2 μ L par réaction, réaction contrôle sans plasmide. MscLeGFP ne se distingue pas du contrôle car la protéine n'est pas dans sa conformation fonctionnelle, probablement en raison de son hydrophobicité.

Figure vi: Composition et cinétique de la réaction TXTL

protéines. Nous allons maintenant montrer comment nous avons réussi à exprimer directement ces protéines dans les DIBs.

Localisation des protéines synthétisées

Nous démontrons d'abord que l'expression de MscLeGFP produit un signal de fluorescence lorsque la réaction est encapsulée dans un liposome. Il est donc possible d'insérer directement une protéine membranaire dans une bicouche modèle si elle est exprimée *in situ*. Nous montrons ensuite que l'expression TXTL fonctionne dans les émulsions eau-dans-huile qui servent à faire les DIBs. Troisièmement, nous montrons comment nous pouvons stabiliser les membranes tout en exprimant MscLeGFP dans la configuration DIB. Enfin, nous démontrons l'insertion de protéines membranaires dans les DIBs.

FABRICATION DE LIPOSOMES Nous avons d'abord encapsulé les réactions TXTL dans des liposomes afin de démontrer qu'une protéine membranaire hydrophobe pouvait s'insérer dans une membrane si elle était exprimée *in situ* [38]. Les liposomes sont formés par émulsion inverse. On émulsionne la réaction TXTL produisant MscLeGFP dans de l'huile contenant des lipides EggPC (mélange de phospholipides extraits de l'oeuf du gallinacé). Les gouttes sont ensuite transférées dans la solution externe par centrifugation, ce qui permet de former la membrane séparant la réaction TXTL de la solution externe.

MESURES DE FLUORESCENCE La cinétique de la réaction TXTL dans les émulsions est quantifiée par épifluorescence pour démontrer la compatibilité de l'expression avec la configuration DIB. Nous avons également réalisé des mesures confocales pour quantifier l'insertion préférentielle des protéines membranaires fluorescentes dans les membranes. Les gouttes ($R = 20\text{-}30 \mu\text{m}$) sont formées dans des lames de

microscope à fond creux. Les bicouches sont imagées à l'aide d'un module confocal à spinning disk (résolution en z de 0.5 μm et objectif motorisé x20 Nikon Apo Plan).

EXPRESSION IN SITU

ENCAPSULATION DANS DES LIPOSOMES Nous montrons que bien qu'aucune fluorescence n'était visible lorsque MscLeGFP était exprimée dans des réactions de 2 ou 10 μL , il y a production d'une protéine fluorescente qui va à la membrane lorsque la même réaction est encapsulée dans un liposome (Fig [vii A](#)). Il est donc possible d'insérer une protéine membranaire hydrophobe directement dans une membrane via expression TXTL *in situ*.

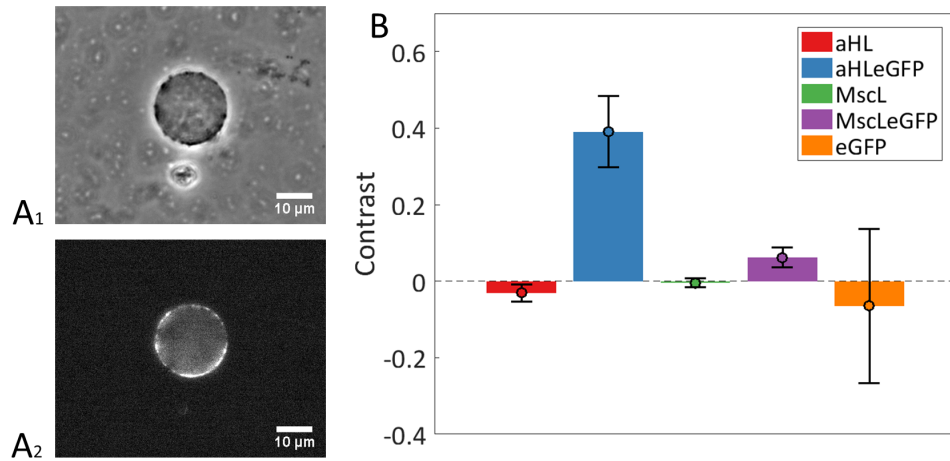
EXPRESSION EN DIB Nous avons d'abord quantifié la production d'eGFP dans une émulsion eau-dans-huile. La dynamique est un peu différente de ce qui est observé dans des réactions de 10 μL . On voit typiquement une expression allant jusqu'à produire 10 μM d'eGFP en 2 heures. Ensuite la réaction commence à ralentir, probablement en raison d'un apport limité en oxygène au niveau des gouttes.

STABILISATION DE LA MEMBRANE A partir de la littérature nous pouvons isoler trois paramètres importants pour la stabilité des bicouches lipidiques. La réaction en gouttes est diluée et/ou supplémentée avec une solution de liposomes. On peut également diminuer la taille des gouttes, les membranes plus petites étant plus stables. Enfin, la composition en lipides de la phase organique peut être optimisée.

Le DPhPC utilisé pour les expériences avec l'hémolysine ne permettait pas d'obtenir des membranes suffisamment stables en présence du TXTL, y compris lorsque nous avons dilué 2 fois ou 4 fois la réaction avec une solution de liposomes. Nous avons donc utilisé un mix de lipides plus stable proposé récemment par Dupin et Simmel [[21](#)] : 0.25 mM cholestérol, 0.25 mM DOPG, 4 mM DOPC and 0.5 mM DPhPC dans un mélange 1:1 hexadécane:Silicone AR20. Nous désignons ce mélange sous le nom de "Dupin mix" pour le reste de cette thèse.

LOCALISATION DES PROTÉINES MEMBRANAIRES DANS LES BICOUCHES Nous démontrons optiquement l'insertion de protéines membranaires dans les DIBs à partir de mesures au microscope confocal. Nous mesurons le contraste entre le signal au niveau de la bicouche et le centre des gouttes, moyenné sur une épaisseur de longueur $\Delta z = 5 \mu\text{m}$. Cette quantité est renormalisée par rapport au background. Nous comparons les contrastes moyennés sur plusieurs cas de DIBs pour MscL, MscLeGFP, αHL , αHLeGFP et eGFP (Fig [vii B](#)). Nous obtenons des valeurs négatives pour les protéines membranaires non fluorescentes et des valeurs positives pour les protéines membranaires fluorescentes. Pour les protéines membranaires non fluorescentes, l'autofluorescence de bulk⁵ domine par rapport au signal à la membrane, ce qui n'est pas le cas pour les protéines membranaires fluorescentes. Dans le cas d'eGFP, nous obtenons également un contraste négatif car la fluorescence de bulk domine largement. Dans le cas des protéines membranaires fluorescentes (αHLeGFP et MscLeGFP), un contraste positif montre quantitativement que la bicouche émet un signal supérieur à celui du bulk.

⁵ *bulk* est ici pris au sens de "en volume".



A1) Liposome contenant la réaction TXTL exprimant MscLeGFP au bout de 7 heures d'incubation, visible A2) Le même liposome en microscopie de fluorescence, on voit nettement la présence de la protéine membranaire fluorescente à la membrane B) Quantification des différents contrastes pour les membranes contenant α HL, α HLeGFP, MscL, MscLeGFP et eGFP dans la configuration DIB. $N(\alpha$ HL)=12, $N(\alpha$ HLeGFP)=13, $N(\text{MscL})=11$, $N(\text{MscLeGFP})=14$ and $N(\text{eGFP})=16$

Figure vii: Quantification de l'insertion de protéines membranaires synthétisées *in situ* dans les DIBs

Fonctionnalité des protéines synthétisées *in situ*

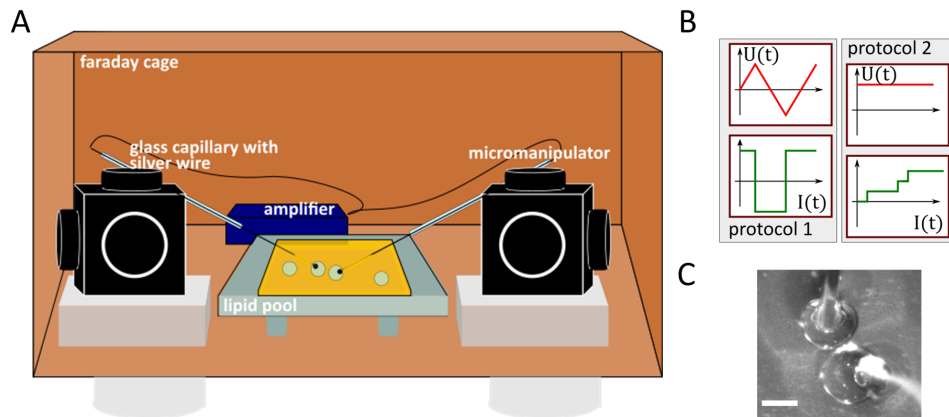
Après avoir démontré la localisation des protéines membranaires dans la bicouche par des mesures confocales, nous allons confirmer que l'hémolysine ainsi synthétisée est fonctionnelle grâce à des mesures électrophysiologiques.

MODÈLE ÉLECTROCINÉTIQUE DE MEMBRANE BIOLOGIQUE La capacitance C d'une bicouche peut être mesurée par une entrée de tension périodique, qui peut être soit la somme de deux sinusoides ou un signal triangulaire. Dans le cas d'une entrée triangulaire de tension, la réponse d'une bicouche de résistance infinie est un signal carré (réponse capacitive pure). Ce signal étalonné pour une capacité connue⁶ nous permet de mesurer *in situ* la capacitance de la DIB et de vérifier que la membrane est correctement formée. La conductance est le ratio entre l'intensité mesurée et le voltage appliqué. α HL étant un pore rempli d'eau, sa conductance est proportionnelle à la salinité de la solution [55]. S'il est possible d'extraire de la trace de l'intensité enregistrée un saut individuel imputable à un seul pore alors $\sigma_{\alpha HL} = A \frac{\Delta I}{\Delta U}$ (A étant le coefficient de proportionnalité tenant compte de la concentration en sel de la solution). En raison de cette conductance fixe $\sigma_{\alpha HL}$, lorsque plusieurs pores s'insèrent à la suite la trace enregistrée doit montrer de multiples sauts quantifiés. Ces sauts proviennent d'une augmentation de la conductance G de la membrane par multiples entiers $\Delta G = n \cdot \sigma_{\alpha HL}$.

MESURE DE COURANTS À TRAVERS UNE DIB Nous avons développé un protocole basé sur [5] pour caractériser l'insertion de l'hémolysine dans une bicouche grâce à des mesures électrophysiologiques. Après avoir produit des gouttes contenant la réaction TXTL exprimant α HL, nous utilisons deux électrodes Ag/AgCl

⁶ composant électrocinetique de valeur $C = 100$ pF.

pour enregistrer les courants de part et d'autre de la membrane entre deux gouttes. Ces mêmes électrodes sont utilisées pour mettre deux gouttes en contact afin de former la bicouche, via deux micromanipulateurs Narishige - Fig viii A.



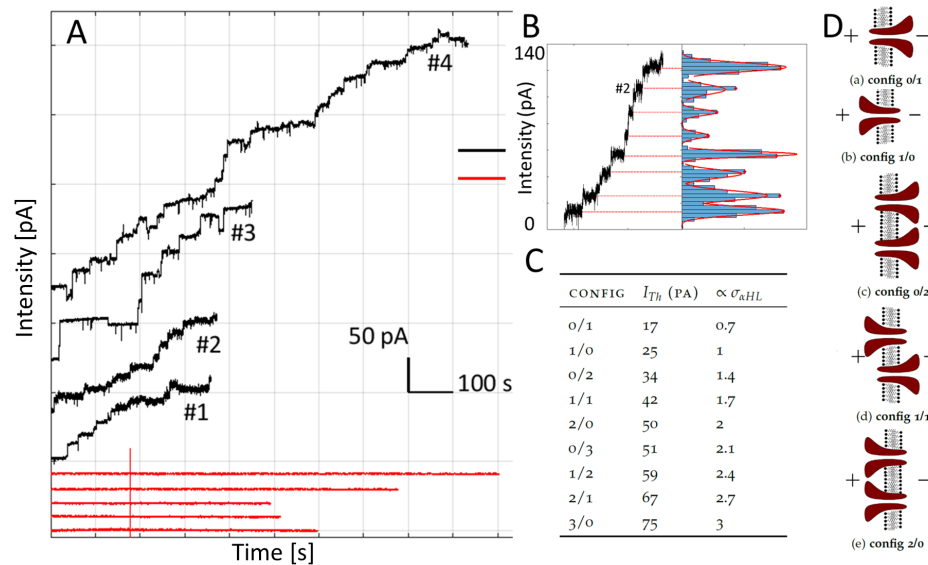
A) Schéma du dispositif électrique pour les mesures sur DIB. Les électrodes (*glass capillary with silver wire*) sont connectées à un amplificateur de courant (*amplifier*). L'ensemble ainsi que la cuve contenant les gouttes aqueuses dans le bain de phospholipides sont isolés du bruit électrique dans une cage de Faraday. B) Protocoles de mesure de capacitance (protocol 1, input sous la forme d'une tension triangle périodique, réponse en intensité sous la forme d'un créneau) et enregistrement d'événements d'insertion de pores individuels (protocol 2, on impose une tension constante et on mesure les sauts de courant résultants). En C) Vue de deux gouttes mises en contact, échelle = 200 μm

Figure viii: Dispositif expérimental pour réaliser des mesures électrophysiologiques

Les courants à travers la membrane sont enregistrés avec un amplificateur de courant Element Amplifier eONE. Le montage complet est isolé du bruit électrique ambiant par une cage de Faraday en cuivre. Dans cette enceinte nous mesurons typiquement un niveau de bruit de l'ordre de 1 pA. Les signaux sont acquis à 1.25 kHz. On peut faire deux choix pour la composition lipidique du solvant organique, le DPhPC ou le mix Dupin. Le DPhPC a traditionnellement été utilisé pour les mesures électrophysiologiques sur les membranes planes. Le mix Dupin donne des résultats extrêmement stables mais seules des mesures optiques ont pour l'instant été publiées. Nous avons choisi de comparer les caractéristiques électriques des membranes formées avec les deux types de mélange de lipides en utilisant un tampon KCl 500 mM. Après avoir vérifié que la capacité mesurée est de l'ordre de 100 pF, nous mesurons le bruit résultant de l'application d'une tension de 50 mV. Le DPhPC donne de meilleurs résultats que le mix Dupin en terme de bruit et d'intensité résiduelle, les membranes résultantes semblant moins permissives pour les défauts tels que la présence de pores transients. Nous avons donc choisi le DPhPC pour réaliser les mesures sur des DIBs contenant l'hémolysine.

CONDUCTANCE DE L'HÉMOLYSINE Pour réaliser des mesures à l'aide d'électrodes Ag/AgCl sur les réactions TXTL il faut des ions chlorure en solution. Nous avons donc d'abord regardé comment le niveau d'expression de αHLeGFP variait lors de l'introduction progressives de sels. Avec une concentration introduite de 100 mM en KCl, le niveau d'expression est comparable à celui de la réaction non salée. En revanche, si la concentration introduite en sel vaut 500 mM alors le niveau d'expression redescend au niveau de celui du contrôle. Afin de détecter des sauts de courant au dessus du niveau de bruit (1 pA) avec une bonne résolution en

intensité et une tension appliquée de 50 mV nous avons donc choisi d'exprimer d'abord α HL avec une réaction TXTL à 100% puis de diluer la réaction 500 fois dans un tampon KCl 500 mM. Avec ces paramètres, chaque saut individuel dû à l'hémolysine doit mesurer 25 pA. Les traces résultantes sont lissées à l'aide d'un filtre en ondelettes [56]. Les traces résultantes sont montrées Fig. ix A. A côté des expériences positives où la réaction TXTL a exprimé pendant 5 heures avant d'être diluée, nous montrons les contrôles où la même réaction est diluée à $t = 0$, avant d'avoir eu le temps de produire l'hémolysine.



A) Traces enregistrées pour les expériences comprenant de l'hémolysine (noir) et les contrôles (rouges). Des événements discrets sont visibles sur les traces noires. B) Analyse des sauts discrets à partir d'histogrammes résultants C) et D) Expression combinatoire des conductances attendues suivant le sens d'insertion des protéines de part et d'autre de la membrane

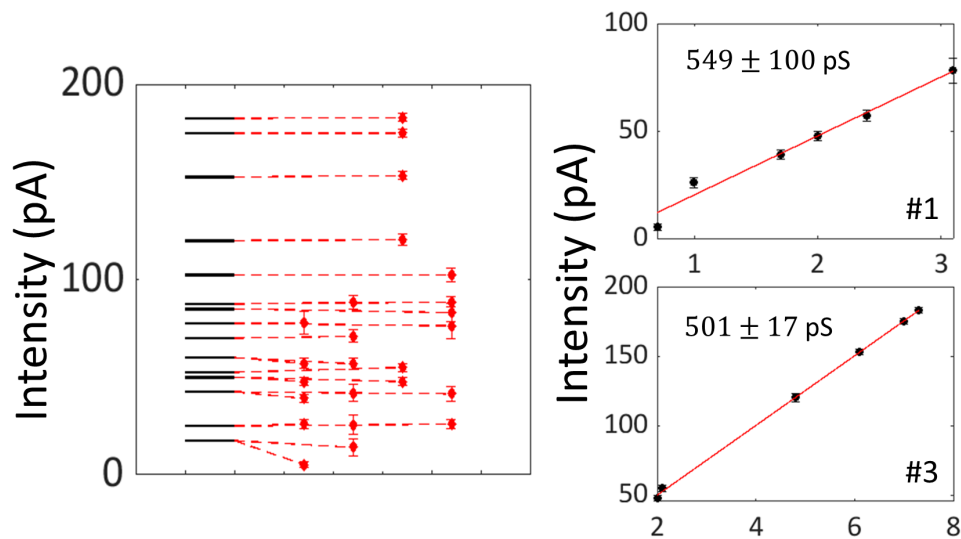
Figure ix: Analyse d'événements discrets résultant de l'insertion de plusieurs pores

Fig ix B, nous montrons comment sont mesurés les sauts de courant sur chaque trace individuelle. Si on moyenne les sauts résultants pour chacune des traces, les valeurs résultantes sont trop dispersées pour pouvoir considérer que les sauts ont en moyenne une valeur constante. Nous postulons que ces différences proviennent de l'asymétrie en conductance du pore selon qu'il s'insère dans la bicouche depuis la goutte de droite ou celle de gauche. Un pore inséré donne deux possibilités, une insertion à droite ou une à gauche (*config 1/0 ou 0/1*). Deux pores insérés donnent trois possibilités, deux à droite, un à droite et un à gauche et deux à gauche (*config 2/0, 1/1 ou 0/2*). Les différentes configurations disponibles allant jusqu'à trois pores insérés sont représentées Fig ix C et D⁷.

Ces sauts de courant attendus peuvent être représentés par *niveaux d'intensité* par analogie avec les niveaux d'énergie discrets atomiques (Fig x A). Pour les 6 premiers niveaux de chaque trace, nous associons chaque saut de courant expérimental $I_{exp,k}$ au niveau théorique le plus proche $I_{th,i}$ en minimisant $\frac{|I_{th,i} - I_{exp,k}|}{I_{th,i}}$. Les points expérimentaux avec leurs barres d'erreur (rouges) sont alignés dans les colonnes 1,2,3 et 4 correspondant à la trace dont ils sont dérivés. Ils sont reliés à leur plus proche voisin théorique par une ligne rouge pointillée. Cet alignement

⁷ Se lit ainsi : pour 1 pore depuis la gouttelette 1 et 2 pores depuis la gouttelette 2, on devrait voir une augmentation du courant de 59 pA, ce qui est proportionnel à $1 + 2 * 0.7 = 2.4\sigma_{\alpha HL}$.

permet d'attribuer à chaque point expérimental la proportionnalité attendue à la conductance (Fig ix C). Ces sauts de courant sont ensuite représentés en fonction de leur proportionnalité par rapport à la conductance attendue pour en déduire la conductance expérimentale. Cela donne 4 ajustements Fig x B pour les 4 traces individuelles avec une conductance inférée en pS. La première trace donne une énorme erreur sur la conductance attendue à cause du décalage de l'origine. Les trois autres donnent une estimation raisonnable de la valeur de conductance par rapport à ce qui a été publié précédemment [51]. Nous présentons ici un début de preuve expérimentale de l'insertion fonctionnelle d'hémolysine synthétisée par voie TXTL dans une bicouche de type DIB. Un nombre de traces individuelles plus important nous permettra de confirmer ce résultat.



A) Attribution des différents niveaux d'intensité attendus aux niveaux mesurés expérimentaux pour en déduire la proportionnalité à la conductance de l'hémolysine B) Pour chaque trace avec hémolysine, représentation des différents sauts expérimentaux avec leur proportionnalité à la conductance de l'hémolysine et ajustement linéaire pour prédire la conductance individuelle $\sigma_{\alpha HL}$ en pS.

Figure x: Prédiction de la conductance individuelle du pore en fonction des sauts attendus

1.5 CONCLUSION

Nous avons présenté dans ce résumé une étude quantitative du transport passif moléculaire dans des tissus biomimétiques. Nous avons construit un modèle de tissu cellulaire par le biais d'une nouvelle technique d'assemblage de membranes synthétiques de type DIB. Nous démontrons au passage qu'il est possible de produire et de compacter facilement des émulsions eau-dans-huile en tirant partie des différences en énergies de surface des trois phases en présence, eau/huile/air. Pour compléter notre modèle expérimental et décrire de manière simplifiée une communication cellule à cellule, nous insérons dans les membranes des nanopores protéiques inertes comme portes communicantes de goutte à goutte. Nous relierons le temps moyen pris par une sonde fluorescente pour aller d'une goutte à une autre au nombre et à l'arrangement des pores grâce à une description microscopique tirant parti des temps de premier passage. Le cadre théorique des marches aléatoires à temps continu nous permet de relier la description expérimentale en temps continu de l'augmentation de signal de fluorescence dans les premiers voisins au

caractère spatial discret du réseau. Enfin, nous essayons d'étendre notre modèle expérimental au cas d'un pore mécanosensible MscL qui n'est pas soluble dans l'eau. Pour produire cette protéine, nous implémentons une réaction *cell free* dans les réseaux de gouttes afin de pouvoir produire MscL et l'insérer dans sa conformation native dans la membrane. Nous démontrons dans le cas de l'hémolysine que notre méthodologie nous permet bien de produire et d'insérer un pore. Nous montrons en particulier la localisation de l'hémolysine à la membrane par des mesures confocales de fluorescence et sa fonctionnalité par des mesures de courant. Une des perspectives à court terme de ce travail est de créer des réseaux mécanosensibles contenant MscL synthétisé par voie TXTL, où les propriétés de diffusion pourraient par exemple être modifiées via un stimulus mécanique.

INTRODUCTION

INTRODUCTION

Engineering compartments mimicking functions in biological networks has multiple appeals [57, 58]. Fundamentally, it is a bottom-up approach that consists in deconstructing complex phenomena into simple block functions to get a better understanding of how each separate function works. This decomposition is best illustrated in the quest for artificial life [59].

The first type of decomposition consists in deconstructing the dynamics of biological responses into blocks as it is done in electronics - an approach that is described as *modular design*. The individual blocks are genetic circuits that can be oscillators [60], logic gates [61] or switches [62]. When combined, these genetic circuits produce sophisticated responses, ultimately designed to exhibit robust outputs to a large variety of inputs. Purnick and Weiss describe the assembly of these blocks into more complex systems as the "second wave" of synthetic biology [63]. However, the study of these genetic regulation networks alone does not recapitulate the functions of a living system. The output of DNA programs has to be organized on several scales, from the molecular to the multi-cellular level. This organization relies on mechanisms rooted in soft matter physics. To quote a few of these mechanisms, self-assembly of large structures [64], molecular crowding [65] and membrane trafficking are all non genetic processes that play a prominent role in the cell organization. That is why the second type of decomposition involves the functional separation of what makes a unicellular entity a living thing, for instance functions such as DNA replication, lipid synthesis or division [59]. These functions are structured using biological bilayers, gel scaffolds or microreactors to provide physical support to their dynamics. Particular emphasis has been put on compartmentalization [66].

In this thesis, we will work on cell-cell communication, an extremely important function in multicellular assemblies. Engineering a biomimetic model of inter-cellular communication brings us back to compartmentalization. Compartments are used to create local concentration areas to maximize enzyme efficiency, to retain reagents and limit toxicity as well as to avoid competition between several parallel reactions [67]. Organelles are one of the most striking example of compartmentalized functions in a living cell. Cellular assemblies such as epithelial tissues are another type of compartmentalization on a submillimetric scale. Several strategies can be implemented to reproduce lipid compartmentalization in biomimetic systems. Lipid vesicles and lipid-stabilized water-in-oil emulsions have been widely used to encapsulate specific functions. This compartmentalization presents several advantages. It is highly dynamic by itself [68]. It is also a physical native scaffold for protein activity such as membrane protein function [69] and it can be selectively permeabilized. On the engineering side, compartmentalization gives way to biosensors engineering [35] and drug delivery optimization [70, 71].

We will focus on a particular type of compartmentalization relying on water-in-oil emulsions. Droplet Interface Bilayers have been extensively used since 2005 to develop compartmentalization tools through the use of compact water-in-oil emulsions, in general stabilized with phospholipids [4]. Since then, they have been increasingly introduced as analogs of artificial tissues [13] and have even been used to print cells in 3D scaffolds, bridging the gap between biomimetic devices

and cell cultures in tissue engineering approaches [72]. Because they phenocopy multicellular assemblies in a simplified and elegant way, they offer numerous perspectives in fundamental studies of morphogenesis, wound healing and other mechanisms relying on the physical transmission of forces at the tissue scale. They were used to study protein function [73] because they provide the lipid environment that is required. In particular, it was demonstrated that pore insertion was possible in these systems, paving the way for intercellular communication study. Protein channels embedded in biological membranes are indeed one of the communication modes that cells use to integrate information on their surroundings and send signals, in particular through the use of gap junction channels or paracrine communication. In DIB systems hemolysin was first used as a model nanopore, followed by more complex ion channels such as mechanosensitive proteins or active transporters. The transport of small solutes through hemolysin was evidenced but no quantitative link between the dynamics of this transport and the number of inserted pores was provided. Yet, we know that during physiological responses to environmental stress, cells modulate their internal protein concentration to adapt to the timeline of their environment. From this consideration, it would not be surprising that the speed of communication of the cell with its environment is modulated by an increased protein channel synthesis. This points towards the need of understanding better the relationship between the number of embedded pores in a bilayer and the transport kinetics through one or several bilayers if one considers multicellular assemblies.

To tackle this question, we implemented a quantitative study of transport in nanoporous connected bilayer networks. This thesis work is organized in three main parts. First, we focus on the generation of monodisperse water-in-oil emulsions. Keeping in mind the final objective - the fabrication of bilayer arrays organized in pre-designed geometries with a controlled connectivity - we develop an original printing method where we layer the droplets in 1D or 2D arrays in a simple and cost-effective way.

Secondly, we develop a protocol for pore insertion in these arrays. We use hemolysin like many researchers working in the field of synthetic membranes, but this time we explore the quantitative link between the introduced pore concentration and the transport kinetics of a fluorescent probe through the pore. To do so we make linear arrays of bilayers comprising a source droplet connected to receiver droplets. We link the increase in fluorescence of the source first neighbors to the introduced concentration in pores using first passage processes.

To eventually mechanically tune diffusion in these bilayer arrays, we aim at replacing hemolysin with MscL, a mechanosensitive pore. Due to its high hydrophobicity, this protein has to be synthesized directly in the droplet. We thus couple Droplet Interface Bilayers to cell-free protein expression, using an *E. coli* based system [32]. We demonstrate that we are able to insert cell-free synthesized hemolysin and to prove its functionality through electrophysiological measurements.

Each part is divided in several chapters. Due to the diversity of the techniques we used, we have chosen to distribute the material and methods at the beginning of each relevant chapter to ease the reading. State of the art in the corresponding areas is typically detailed in the first chapter of each part. Microfluidic and bilayer assembly techniques will be presented in [Chapter 2](#), production of bilayer arrays will be exposed in [Chapter 5](#), TXTL assembly and production in [Chapter 9](#) and electrophysiological measurements in [Chapter 11](#). With this arrangement, we hope we managed to increase the reader's comfort.

We add that we are very grateful to several collaborations and thank C. Josserand⁸ and S. Neukirch⁹ (capillary modeling and numerics [Part i](#)), R. Voituriez¹⁰ (modeling [Part ii](#)) as well as J. Mathé¹¹ (electrophysiology [Part iii](#)) and V. Noireaux¹² (cell-free systems [Part iii](#)) for their help.

8 LadHyX, Polytechnique, Paris - France

9 MISES, Institut Jean le Rond d'Alembert, Paris - France

10 Laboratoire Jean Perrin, Paris - France

11 LAMBE, Evry - France

12 University of Minnesota, Minneapolis - USA

Part I

DESIGN OF BIOMIMETIC TISSUES

In the following chapters ([Part i](#)), we introduce the system used to assemble biomimetic tissues. We take advantage of a recently developed system called Droplet Interface Bilayer [\[4\]](#) to produce aqueous compartments separated by bilayers. We introduce these model membranes in [Chapter 1](#). In [Chapter 2](#), we expose an original production of water-in-oil emulsions with the final objective of layering reproducible arrays of bilayers. We model in [Chapter 3](#) the water droplets detachment process in a quasistatic framework. This work was published in [\[9\]](#), see [Appendix E](#).

DROPLET INTERFACE BILAYERS AS ANALOGS OF CELLULAR MEMBRANES

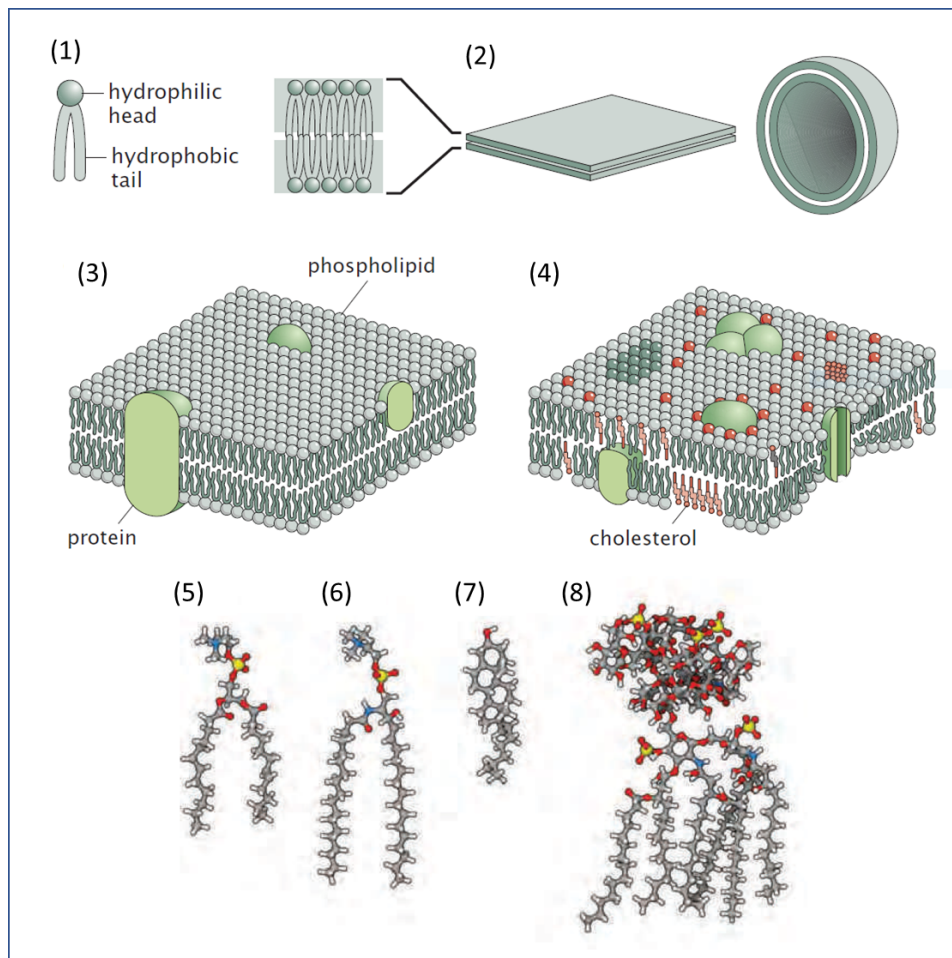
1 MODEL MEMBRANES: HISTORY

Lipids are one of the four main building blocks of living structures. These molecules are amphiphile structures made of polar heads and long hydrophobic carbon chains (Fig 1.1). Lipids at a concentration above the critical micellar concentration (cmc) spontaneously form organized structures in aqueous environments [74]. This behavior minimizes hydrophobic and hydrophilic repulsions. Depending on their shape, lipids can form micelles around a hydrophobic core, with their carbon tails pointing inside and hydrophilic heads outside. They can also adopt more intricate structures such as bilayers - a double layer of lipids with hydrophobic tails inside and polar heads outside - and vesicles, a closed version of bilayers. Their tendency to adopt a conformation rather than another one depends on the nature and size of the tail and the head. The packing ratio of lipids is a geometrical measure that predicts the most probable structure adopted by these molecules.

Living organisms are made of cells that are individually delimited by bilayers. Inside a cell, subcompartments are also membrane enclosed - a typical example of a membrane-bound organelle is the Golgi apparatus. Each cell type has a different membrane composition in lipids but some average considerations can be summarized. In the plasma membrane the major lipid component is the phospholipid, with a glycerol group linking two carbon chains to the polar head. Cholesterol is another type of lipids that disrupts the lipid packing in the membrane due to its planar hydrophobic structure. The last category is composed of sphingolipids. In addition to these three categories, living species exhibit specific types of lipids, such as lipopolysaccharides in bacteria (Fig 1.1). Membranes are not only boundaries that separate functions in the cell. They provide a physical support for membrane protein functions, in particular the function of communication between the cell and its environment [75]. For this reason, investigating the role of the lipid composition in the functionality of these proteins has been an increasing research field [76]. Proteins can be simply bound or anchored to the membrane but transmembrane proteins - including ion channels - are deeply embedded in their lipidic environment. They span all the membrane with hydrophilic parts on both sides of the bilayer leaflets. To investigate precisely the function of these membrane proteins, it is often necessary to reconstitute them in artificial membranes [1], also called biomimetic bilayers. These model membranes are mainly of two types: liposomes and planar membranes.

1.1 *Liposomes*

Membrane proteins have been reconstituted in liposomes, by mechanical means (sonication), solvent methods (solvent injection/reversed-phase evaporation), freeze-thawing or detergent-mediated solubilization [1] which is the most popular approach. Detergents are amphiphile molecules that provide hydrophobic cores for



(1) Generic structure of the lipid molecule (2) Self-organization in bilayers and vesicles (3) Insertion of proteins in phospholipid homogeneous membranes (4) Insertion of proteins in heterogeneous membranes with cholesterol domains (shown in red) (5) Phospholipid (6) Sphingolipid (7) Cholesterol (8) Lipo polysaccharide. Atomistic color code for (5), (6), (7) and (8): H (white), C (grey), O (red), N (blue) and P (yellow). [75] *Reproduced with permission of Taylor and Francis.*

Figure 1.1: Organization of lipids in biological membranes.

membrane-bound domains in membrane proteins. They greatly improve protein solubilization in aqueous buffers. With detergent-mediated solubilization, purified membrane proteins are mixed with detergents before being added to a lipid solution. The detergent can then be removed through dialysis or other filtration processes. It is however not always necessary to purify the protein before its insertion inside a model membrane. Due to the recent developments of In Vitro Translation Transcription (IVTT) systems it is now possible to synthesize directly the membrane protein in the bilayer vicinity. We will detail this technique later in [Chapter 8](#).

Model bilayers can be used to emulate the membrane protein environment. Liposomes are for instance very efficient at membrane protein reconstitution. However, performing electrophysiological measurements on these objects can be technically challenging [77]. Indeed, patch clamp recordings have a very low output efficiency and are difficult to couple to mechanical stimuli, even if micropipette aspiration gives access to a limited range of mechanical stimuli. An alternative to liposomes has thus been developed in the form of planar membranes. These bilayers are usually larger than liposomes with typical sizes ranging from 10 to 100 μm . They

were primarily developed as supported bilayers for electrophysiological recordings. Recently, a new configuration coined "Droplet Interface Bilayers" was developed [2]. It offers robust and stable bilayers on which a wide variety of stimuli can be applied. Droplet interface bilayers are also easily integrated in networks and offer analogs of living tissues. In that sense, they pave the way for collective approaches that are harder to tackle with liposomes [78].

1.2 Planar artificial membranes

Historically, these bilayers were made with phosphatidylcholine mixtures extracted from a living organism, for example the hen egg. Problems in reproducibility arose because of the mixture variations due to its natural origin, as well as because of oxidization problems. These phosphatidylcholine lipids have indeed many insaturations that make them sensitive to oxygen-mediated oxidization. With technical improvements in pure lipid synthesis and purification, important progress were made in the constitution of robust and stable planar lipid bilayers. The most used lipid in this configuration is the 1 – 2-diphytanoyl-3-sn-glycero-3-phosphocholine (DPhPC). This lipid was first synthesized in 1971 [79]. It is easily purified and remains insensitive to autoxidation.

1.2.1 Black Lipid Bilayers

Black Lipid Membrane (BLM), also called planar lipid bilayer membranes, were developed conjointly to liposomes to provide a platform for drug screening and protein functionality investigations [47]. BLMs have this historical name due to the optical techniques first used to characterize their formation. The thinning of the bilayer was indeed optically seen as a black spot due to destructive interferences. Mueller and coworkers reported in 1962 [80] the successful realization of a bimolecular lipid structure that is sensitive to pH and exhibits reproducible resistance and capacitance over several experimental realizations. They used a septum with a Teflon coated aperture to form a bilayer between two aqueous compartments [81]. To strengthen the bilayer stability, *Metal-supported* Bilayer Lipid Membrane (s-BLM) and *Agar salt-bridge-supported* Bilayer Lipid Membrane (sb-BLM) were developed. The mechanical support provided by either a metal or a hydrogel substrate stabilizes further the membrane. The hydrogel is required to monitor ion fluxes through the BLM. Despite this improvement, these types of bilayers remain fragile in particular to mechanical inputs. They are not stable over a long period of time and their production remains tedious and almost impossible to parallelize [2]. Droplet Interface Bilayers were developed to overcome this challenge.

1.2.2 Droplet Interface Bilayers

The first account of a droplet interface bilayer was published in 1966 [3]. In this paper, the authors produced a synthetic membrane through the contact of two volumes of aqueous buffer in a bath of oil containing lipids. Phospholipids from the brain were dissolved in heptane and egg albumen was added to the aqueous phase. A droplet of the protein solution was brought on top of the interface between the same aqueous phase and the bath of phospholipids (Fig 1.2 A). This technique was proposed as a way of introducing proteins in synthetic bilayers which were supposed to be too densely packed for this use in the former configurations (s-BLM).

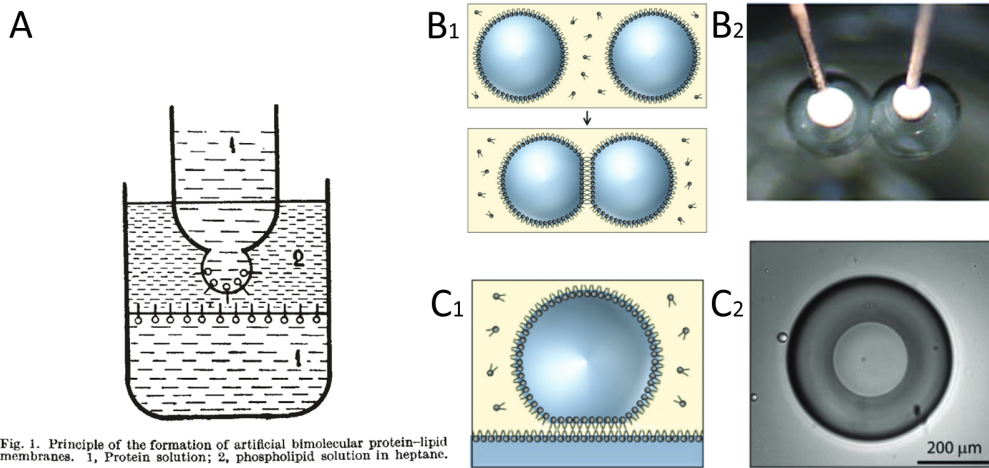


Fig. 1. Principle of the formation of artificial bimolecular protein-lipid membranes. 1, Protein solution; 2, phospholipid solution in heptane.

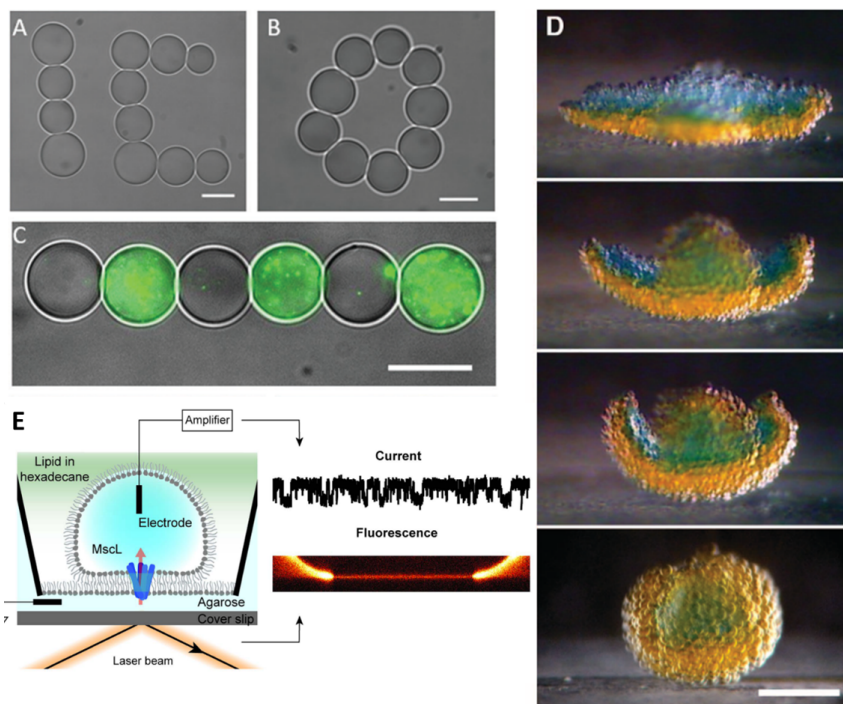
(A) First Interface Bilayer, *Reprinted by permission from Springer Nature [3] ©1968* with (1) Protein solution in an aqueous buffer (2) Phospholipid solution in heptane. (B1) to (C2) *Reproduced and adapted from [4] with permission from the Royal Society of Chemistry* - scale bars 200 μm . (B1) and (B2) Droplet Interface Bilayer configuration, aqueous droplets mounted on electrodes. (C1) and (C2) Droplet on Hydrogel Bilayer configuration, top view for the bright field image.

Figure 1.2: Development of droplet interface bilayers configurations.

The technique was rediscovered by Bayley and coworkers in 2005, following an idea of Needham [2]. Ten years later, the authors published an updated version of their review [4] in which they described two possible configurations for the modern "droplet interface bilayer". In the first case, the bilayer is formed between a lipid monolayer coated droplet and a hydrogel plane, also coated (Fig 1.2 C1). This geometry is called Droplet on a Hydrogel Bilayer. In the second case, two droplets are brought in contact and make a bilayer at their interface (Fig 1.2 B1).

DROPLET/HYDROGEL CONFIGURATION Droplets on Hydrogel Bilayers were firstly developed by Bayley and coworkers then conjointly with Wallace and coauthors [4, 5, 6, 7]. Fig 1.2 C1 and C2 show a sketch of the bilayer formation principle. The main advantage of this method is that the bilayer is in the plane of observation. It means that the dynamics of membrane proteins in the bilayer can be easily acquired, in particular with Total Internal Reflection Fluorescence (TIRF) microscopy [82], providing the thickness of the hydrogel is small enough. DHBs were also originally proposed as a way to screen protein activity on purification protein gels [2]. The droplet would then be used to scan the gel surface and investigate several protein bands obtained in a migration assay while displacing the bilayer in the horizontal plane. It could also in theory be parallelized on multi-well plates, in particular for electrophysiological measurements, even if until now this type of parallelization has not been achieved yet. Later on, the DHB configuration has been used extensively by Martinac to study MscL functionality - see [39] and very recently Piezo 1 activity [83], two mechanosensitive proteins identified respectively in *E. coli* and in human. The development of the DIB platform promoted *in vitro* studies to investigate MscL and Piezo sensitiveness to mechanical stresses.

DROPLET/DROPLET CONFIGURATION The works of Leo [84] and Sarles [85] are also to be mentioned in the area of mechanosensitivity studies relying on DIB technology. They were rather developed in the droplet/droplet configuration. In this case, the bilayer is constituted between two aqueous droplets that are either



(A) to (C): Opti-DIB networks assembled using optical tweezers. Scale bars=15 μm , 10 μm and 15 μm *Reproduced from [86] Creative Commons License 3.0.* (D) 3D DIBs tissue folding upon osmotic changes. The orange droplets contain 80 mM KCl and the blue ones 8 mM. Scale bar 200 μm , timelapse 8 hours, reproduced from [13]. *Reprinted with permission from AAAS.* (E) DHB setup to record MscL activity. The use of simultaneous TIRF and electrophysiological recording is eased in this configuration. *Reproduced from [39] Creative Commons License 4.0.*

Figure 1.3: A few examples of DIB realizations in the last decade.

suspended or resting on a substrate (Fig 1.2 B1 and B2). The great advantage of this method compared to the DHB configuration is that droplets can be compacted in 1D, 2D and 3D arrays. This stacking has extensive engineering applications, reviewed in [4].

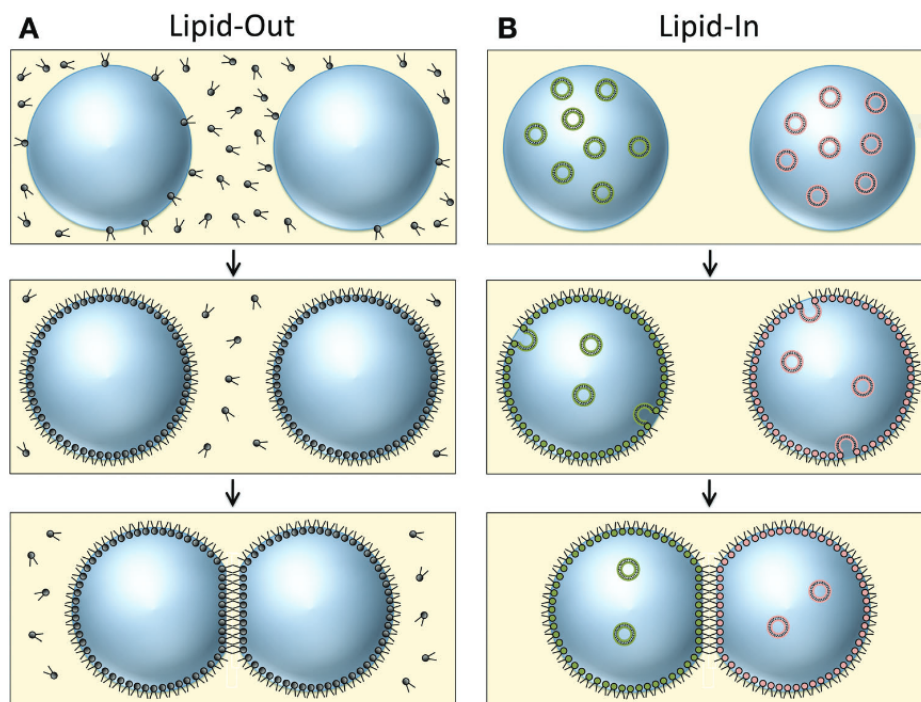
A full method for both configurations was published in 2013 in Nature Methods [5]. We present some key realizations in the new field of DIBs Fig 1.3.

2 PHYSICO-CHEMISTRY OF DROPLET INTERFACE BILAYERS

Stabilizing droplet interface bilayers requires to incubate firstly the aqueous droplets in the phospholipid bath. If the monolayers around the aqueous droplets are not equilibrated, the droplets fuse when they are brought in contact. We will see that the solvent composition as well as the method used to bring lipids in the system are important parameters for DIB stability.

2.1 Solvent effects

The first solvents used to dissolve lipids were alkanes such as hexadecane or heptane [2]. Squalene was sometimes used [87]. Solvent mixtures were then experimented with addition of silicone oil AR20 [4, 12] which is a poor solvent for the lipids. This ingredient thus probably favors lipid assembly in a bilayer rather than monolayer homogenization around the droplet. A mixture of hexadecane and



DIB formation, reproduced from [4] with permission from the Royal Society of Chemistry. (A) In the *Lipids-out* configuration lipids are dissolved in the oil bath (aggregates) and can adsorb in monolayers around the aqueous droplets. (B) In the *Lipids-in* configuration, lipids are in the aqueous droplets in the form of liposomes. These liposomes adsorb to the interface to transfer from the bilayers to the monolayers.

Figure 1.4: Lipids-in and out implementation.

silicone oil AR20 1:1 v/v seems to be the best actual trade-off between a good and a bad solvent to ensure DIB stability.

2.2 *Lipids-out*

Lipids are usually dissolved in the organic solvent at a concentration between 5 and 10 mg/mL, even up to 20 mg/mL in some cases. This method has been coined *Lipids-out* [8]. The main advantage of this approach is that lipid mixtures are easily prepared and do not require freeze-thawing and extrusion. It provides also more flexibility to insert reactive components in the aqueous compartments as it leaves the droplets free of reactions involving liposomes.

2.3 *Lipids-in*

In the *Lipids-in* method, liposomes are added to the aqueous phase as a source of lipids [8] (Fig 1.4a, Panel B). This method has several advantages. It is possible to produce asymmetric bilayers by changing the content of one droplet compared to the other one. Also, some lipids are not properly dissolved in typical alkanes such as hexadecane and it can be easier to incorporate them as liposomes [88]. The assembly of the monolayers in the *Lipids-in* case has been reported to occur much faster than in the *Lipids-Out* configuration. Kinetics were measured through surface tension measurement with the assumption that when the monolayer adsorption is complete, the surface tension stabilizes around an equilibrium value. It occurs

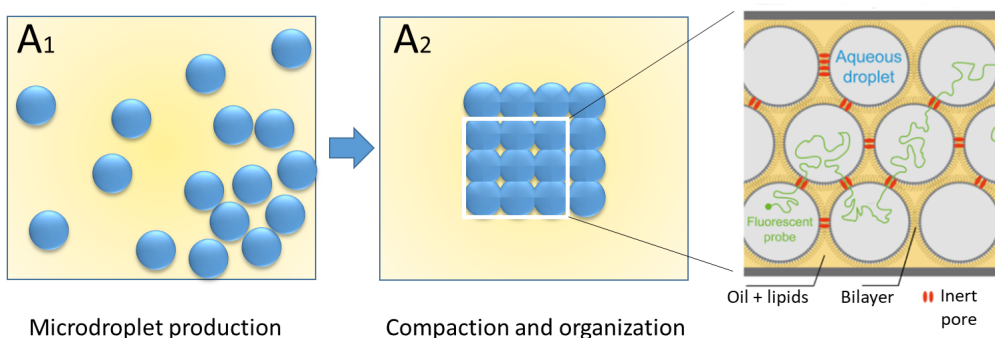
in typically 5 min - to be compared to the half hour incubation required for the *Lipids-out* case. Ventasekan et al. [8] attribute this difference to an adsorption barrier that exists in the *Lipids-out* case due to the presence of micellar structures close to the bilayer.

3 TOWARDS DIB NETWORKS ?

Droplet interface bilayers were originally made with DPhPC but other types of lipids have been used since then, either pure or mixed in different proportions. From a single membrane, researchers developed arrays of bilayers while miniaturizing the produced droplets. Complex proteins have been inserted in these membranes with a recent success involving Piezo 1 [83]. As in the individual bilayer case, these multiple membranes have to be stabilized to yield a compact and monodisperse network. We have thus developed a particular method to ensure reproducible assembly of bilayers in networks.

PRODUCTION OF MICRODROPLETS

In this chapter, we will present how we managed to implement a method called capillary trap to produce reproducible networks of lipid bilayers. The logical reasoning we follow to develop this method is sketched on Fig 2.1.



(A1) Production of a loose water-in-oil emulsion stabilized with phospholipids. (A2) If the emulsion is monodisperse, it can be assembled into a compact network in a reproducible way. Zoom in on the bilayers containing inert transmembrane pores. We monitor the motion of a probe in this network. The probe goes from one droplet to another one through the pores.

Figure 2.1: Sketch of a bilayer network assembly.

1 EMULSIFICATION

Emulsification requires the dispersion of one fluid phase into another one without any miscibility between both phases. This process yields an increase in the surface of contact between the two phases. It thus usually requires an external energy input. Several emulsification techniques have been documented in [10]. We will only summarize here four of these processes:

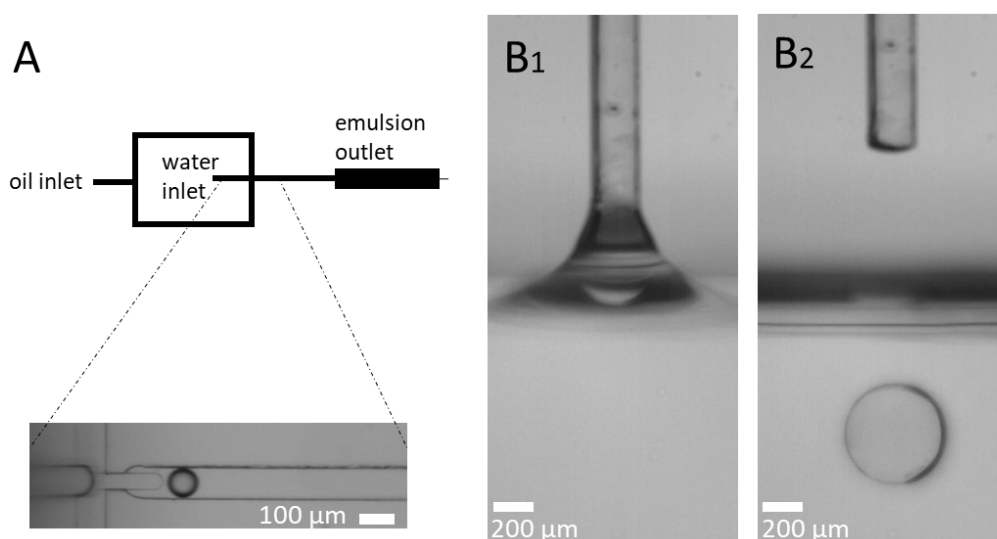
1. **Fragmentation through turbulent inertial and turbulent viscous forces.** This can be obtained for instance through syringe shearing or vortexing. The resulting emulsion is usually polydisperse.
2. **Emulsification through membrane filtration.** It consists in forcing the dispersed phase through a porous material. The continuous flow is flushed parallel to the membrane to collect and detach the fragmented phase [11].
3. **Inkjet printing.** The dispersed phase is fragmented using a piezoelectric actuator. This method has been used to engineer monodisperse spherical particles (see for instance [89]). Recently, this technique has been used by Bayley and coworkers to print DIB networks [12, 13].
4. **Emulsification in microchannels.** It is probably the most successful process in fundamental research. Microchannels offer a convenient miniaturization of fabrication processes and deliver monodisperse emulsions very easily, although with a rather poor yield.

In this PhD work, two of the latter methods were implemented to constitute DIB arrays, namely microchannel emulsification and inkjet printing. As described further down, inkjet printing is the most adapted technique to bilayer networks requirements.

2 MICROFLUIDIC ON A CHIP PRODUCTION

2.1 State of the art

We will briefly present here a state of the art of water-in-oil emulsion production on a microfluidic chip. Anna et al. described in 2003 the production of a water-in-oil emulsion using a flow focusing device [90], shortly after the development of T-junctions to produce this type of emulsions [91]. Both devices are used for the production of monodisperse emulsions of various sizes.



(A) Flow focusing device to produce a water-in-oil emulsion. Oil and water can be injected using syringe pumps or a pressure-driven device. Competition between surface tension and viscous forces detaches droplets with a periodicity fixed by the ratio between the two flow rates of injection. Zoom in on the chip constriction where the droplets are produced. (B1) and (B2) Pictures of the capillary trap. An aqueous flow is enforced in a capillary. (B1) The water forms a spherical cap in the oil and is captured by the oil meniscus. (B2) When the capillary has crossed the interface, the droplet detaches. The extraction period sets the radius of the detached droplets.

Figure 2.2: Techniques to produce water-in-oil emulsions.

Droplet Interface Bilayers production on-a-chip has been published by different teams. Thutupalli and coworkers outlined in [92] a proof of concept of membrane production in microfluidic chips using step emulsification¹ [93]. They produced densely packed water droplets stabilized with DPhPC and cholesterol in squalene. Ces and coworkers proposed a junction geometry to mix different droplet populations [94], enabling the production of asymmetric bilayers made of DPhPC on one leaflet and of DOPC on the other leaflet. Lipids were added as liposomes to the aqueous phase (*lipids-in*). By coupling the microfluidic junction with a tube of different dimensions they were able to produce 3D arrays of droplets. However these authors pinpointed the difficulty to assemble the droplets on modular ge-

¹ Droplet formation when the interface between the two phases (here oil and water) meets a step in the height of the microfluidic channel.

ometries with this mode of production. To note, permeability assays have also been implemented on chips. Microfluidics are in these cases rather used as a way of finely tuning the contact area between two droplets. They also conveniently favor the parallelization of experiments [95].

2.2 Methods

In this work we have tried firstly to implement microfluidic on-a-chip production to make bilayer networks.

To assemble these arrays, droplets can be packed in the outlet of the microfluidic chip as they are produced [96] or trapped directly on the chip using adequate geometries. The main issue regarding this method is the production rate of such chips. We observed in our case that stable production usually occurred around $f \geq 100$ Hz. This rate implies downstream packing of the droplets at high speed, which can lead to multiple droplet fusions if the monolayers are not well equilibrated. Even if dynamic fluid layers motion around the droplets usually facilitates the adsorption of the monolayer coating [97], we still observed many fusions with this method of production. We also highlight here three other main restrictions of microfluidic on-a-chip droplet generation:

1. Because the channel geometry is difficult to change, it can be tricky to mix different droplet populations. It is also challenging to have a controlled network connectivity.
2. Channels in microfluidic chips are usually made of Polydimethylsiloxane (PDMS), which is not compatible with some organic solvents. In particular, silicone based solvents are good solvents for PDMS and induce swelling of the channels. This effect eventually deteriorates the geometry of the channel, impairing the quality of the emulsion production.
3. Last, because droplets are produced in a sealed chip, it is difficult to access the network after its production to inject a probe or perform electrophysiological measurements.

Because of the drawbacks listed above, we decided to develop a different approach based on an inkjet printing inspired method. Details about the experimental procedure for on-chip production are given in [Appendix A](#).

3 THE CAPILLARY TRAP METHOD

We present now an original method we have designed to produce arrays of DIBs. This technique relies on surface tension competition to produce the droplets *on demand* and was published in *Physical Review Applied* [9]. Briefly, the aqueous phase is forced to flow through a capillary that crosses periodically the interface between the air and a bath of oil (Fig 2.3 A). When the tip of the capillary retracts through the interface, the droplet detaches.

3.1 Chemicals

Pure water droplets could be produced with our method. We used two types of oil, silicone oil (viscosity 5 mPa.s, purchased from Sigma Aldrich) and hexadecane (Sigma

Aldrich). To investigate the effect of surface tension in the droplet detachment, we added surfactants molecules to the oil phase or the water phase. We used as surfactants, Sodium dodecyl sulfate (**SDS**) (configuration 1) and Span 80 (configuration 2). In configuration 1, the surfactant is anionic and soluble in water. SDS was dissolved from 0.08 mM to 8 mM - its critical micellar concentration - in the aqueous buffer. We also used silicone oil as the oil phase. In configuration 2, we used a nonionic surfactant, soluble in the oil phase. Span 80 was dissolved in hexadecane at a mass concentration of 2% wt. In that case the aqueous buffer was pure water. We performed additional fluorescence imaging by using fluorescein in pure deionized water or Nile Red in hexadecane.

3.2 *Microfluidics and setup motorization*

We used different types of capillaries to form the droplets. Glass capillaries with inner diameters ranging from 20 μm to 100 μm were first purchased from Drummond as calibrated micropipettes (25 μL). They were then pulled in a laser-based micropipette puller (P-2000, Sutter Instrument). After that, each capillary was cut and adjusted to the right inner diameter using a microforge (Narishige). Another type of capillaries was bought from Molex (Polymicro Technologies capillary tubing). In that case, we removed the polymer coating by burning it and gently rubbing it out. We then cut the capillary using a ceramic cutter to obtain a flat tip. Capillaries were treated to become hydrophobic with a 2 h exposure to a vapor of 1H,1H,2H,2H-perfluorodecyltrichlorosilane (Alpha Aesar, Thermo Fisher Scientific) under a medium vacuum. These capillaries were connected to Tygon tubing (PHYMEP) using either superglue for the Molex capillaries or a fluidic plastic frame for the Drummond micropipettes. Aqueous flow in the capillary was enforced with a KDS Scientific Legato 270 Syringe Pump. We alternated this flow-rate driven mode with a pressure-driven injection system (Fluigent) to prove the versatility of the used technique.

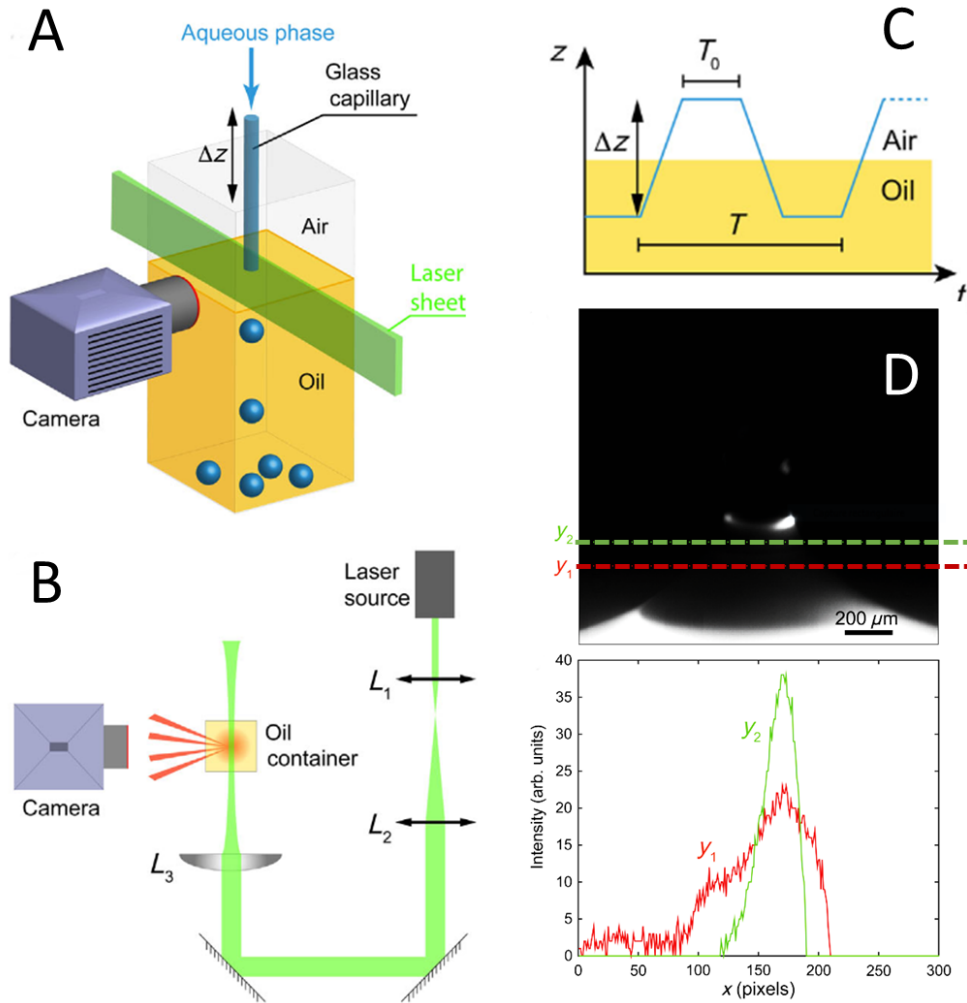
We motorized the capillary using a Newport motorized translation stage with a controller (M-ILS250 CCL series). The controller was interfaced with Labview and the period of extraction T with the vertical distance of translation Δz could be tuned by the operator (Fig 2.3 C).

3.3 *Imaging*

We first characterized the efficiency of the method, i.e. its ability to produce monodisperse droplets of a required radius in a reproducible way. We also imaged the dynamics of the detachment process to understand what is happening between the three different phases at the detachment instant.

3.3.1 *Size statistics*

To perform stastical analysis on the produced emulsions, we recorded pictures of the detached droplets on hundreds of cycles using a Point Grey Chameleon3 USB camera with a high-magnification Navitar objective. Illumination was performed with an LED Panel. We triggered the camera on the motor displacement to record one frame per detached droplet (Labview routine).



(A) Capillary trap setup for fast camera imaging with light sheet illumination. (B) Optical setup for light sheet imaging of the stained oil. (C) Scheme of periodical extraction through a bath of oil. (D) Fluorescence imaging of the Nile Red stained oil on top of the meniscus with the corresponding transverse cuts in y_1 and y_2 . There is fluorescence signal from the stained oil on both cuts.

Figure 2.3: Capillary trap setup.

3.3.2 Fast-Camera imaging

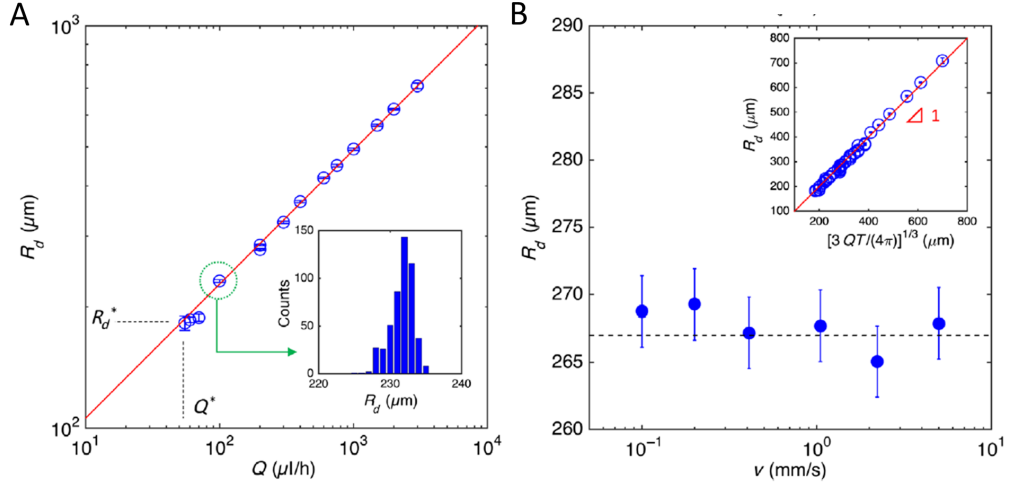
To capture the dynamics of the detachment, we used a fast camera PhotronFastcam APRX RS with a Schneider Optics objective. The frequency of acquisition was set at 3000 frames/s. In bright field we used the transmitted light from an LED panel. In fluorescence imaging, we used two types of illumination systems depending on whether it was the oil or the water that we stained. If we were imaging fluorescein-stained water, we used a Prior Lumen 200 in transmission combined with a set of excitation/emission filters (475 ± 35 nm/ 530 ± 43 nm, Thorlabs). The small size of the water droplet did not require a planar illumination, contrary to the oil case.

If the oil was imaged, we needed to avoid bulk fluorescence imaging that was lowering the resolution on the spatial localization of the oil in the meniscus area. We thus implemented a light sheet illumination with a Green Laser COMPASS 315 M - $\lambda = 532$ nm (Fig 2.3). The beam was expanded by a combination of two lenses L_1 and L_2 to a diameter of $950 \mu\text{m}$. We used after the expander a cylindrical lens L_3 of focal length $f = 30$ mm.

4 ANALYSIS OF THE CAPILLARY TRAP METHOD

4.1 Volume of detached droplets

We first checked that the injected volume per period of time T (Fig 2.3 C) corresponded to the actual volume of the detached droplet. Indeed, this would not be the case if our system was compressible and if the capillary trap was working in a transitory regime. We observed that there was a lower boundary on the flow rate Q for which we did not detach a droplet at each extraction period. This limit flow rate Q^* set the lower cutoff for the radius of the detached droplet R_d^* . For $Q > Q^*$, we fitted $R_d \simeq (QT)^{1/3}$ (Fig 2.4 A). In this experiment we used the same capillary of inner radius $R_0 = 98.5 \mu\text{m}$. We found a good agreement between R_d and $R_{d,th} = (\frac{3}{4\pi}QT)^{1/3}$. We confirmed this by plotting $R_d = f(R_{d,th})$ and found a slope 1 [9], meaning that in our setup we can control R_d by changing T the period of extraction or Q the flow-rate of injection. The method proved moreover to produce monodisperse droplets when Q was above Q^* . The polydispersity was lower than 1% in this regime (*insert* Fig 2.4 A).



(A) R_d the radius of the detached droplet is plotted as a function of the injected flow-rate Q . We kept the period constant in this experiment and changed the value of Q to check that we eventually get what we inject in the process. Experimental points in blue for a capillary inner radius R_0 are well adjusted by a power law $Q^{1/3}$, plotted in red. (B) We plot the radius of the detached droplet as a function of the speed of extraction v . We see that the process seems quasistatic over two decades, from 0.1 mm/s up to 10 mm/s.

Figure 2.4: Dependence of the radius of the emulsion on the flow rate and the speed of extraction.

Several capillary numbers can be considered as we have three phases: air/oil/water. We can compute the oil/water associated capillary number $C_{A,w}$ for a flow rate $Q = 100 \mu\text{L/h}$, a capillary inner radius of $100 \mu\text{m}$, the water viscosity $\eta_w \simeq 1 \text{ mPa}\cdot\text{s}$, the surface tension between oil and water $\gamma_{ow} = 10 \text{ mN/m}$ and an extraction speed $v = 5 \text{ mm/s}$. The absolute speed of the flow during extraction is $v_a = 2 \text{ mm/s}$:

$$C_{A,w} = \frac{\eta_w v_a}{\gamma_{ow}} = 2.10^{-4} \ll 1 \quad (2.1)$$

The other capillary number that would be associated to the oil phase in air ($\eta_o = 5 \text{ mPa}\cdot\text{s}$ and $\gamma_{oa} = 18 \text{ mN/m}$) is also $\ll 1$:

$$C_{A,o} = \frac{\eta_o v}{\gamma_{oa}} \simeq 1.10^{-4} \ll 1 \quad (2.2)$$

Overall it means we can probably neglect viscous effects with respect to capillarity in our theoretical description of the phenomenon. In agreement with this, we also checked the dependency of the size of the detached droplet on the speed of extraction. We changed the speed of extraction while keeping $2Q \left(T_0 + \frac{\Delta z}{v}\right)$ constant. We scanned 2 decades in speed, from $v = 0.1$ mm/s up to $v = 10$ mm/s Fig 2.4 B. We did not measure a significant effect of the extraction speed on the radius of the detached droplet.

In addition, we can compute the capillary length for the oil and water phases $l_{c,ow} = \sqrt{\frac{\gamma_{ow}}{(\rho_w - \rho_o)g}} \simeq 3$ mm to compare the effects of gravity with surface tensions.

This capillary length is approximately ten times larger than the capillary typical dimensions. These first assessments weight in favor of a zeroth-order model where we would not take into account neither viscous effects nor gravity. We concluded from this that the capillary trap works in a quasistatic way in the range of extraction speeds that we explored.

We then checked whether the mean radius of the emulsions changes with the production technique. We experimentally saw that the radius of the detached droplet R_d was always larger than 2 to $3R_0$, R_0 the inner radius of the capillary. This effect was seen in all the different conditions, whether we used a syringe pump or a pressure-driven device, in configuration 1 (SDS) or configuration 2 (Span 80) (Fig 2.5). This observation remains true for capillary inner radii going from 20 μm up to 400 μm .

We propose in the following chapter a model where we compare two plausible states with an energy balance. The only ingredients of this model are the surface tensions.

4.2 Fast imaging

We investigated the shape of the interface when the droplet detaches (Fig 2.2 B) to conclude if there was dewetting of the oil on top of the water or not. We could not extract the shape of the droplet from fluorescence imaging of the water phase because the surrounding oil was diffusing and absorbing the light emitted by fluorescein. From fluorescence imaging of the oil, we concluded that the oil remained on top of the droplet until the last moment of detachment and we did not observe any dewetting within our time resolution. A transverse cut performed in the neck of the attached droplet confirmed that there was still a thin film of oil emitting light from Nile Red fluorescence (Fig 2.3 D). These observations suggest that the water droplet never sees the air between the instant where it is formed under the surface and the detachment time point.

ADDITIONAL REMARKS ON THE ORIGINALITY OF THE METHOD When we published our method, we were unaware of the work of Liao and coworkers that was very similar to the capillary trap. These authors had indeed published a method called Dynamic Interfacial Printing in 2016 [14]. The authors describe a dynamic nozzle with a periodic translational motion between air and oil. They analyzed the droplet detachment as the result of two competing effects:

- a capillary force that holds the aqueous phase in the capillary,
- a shearing force that detaches the droplet from the nozzle.

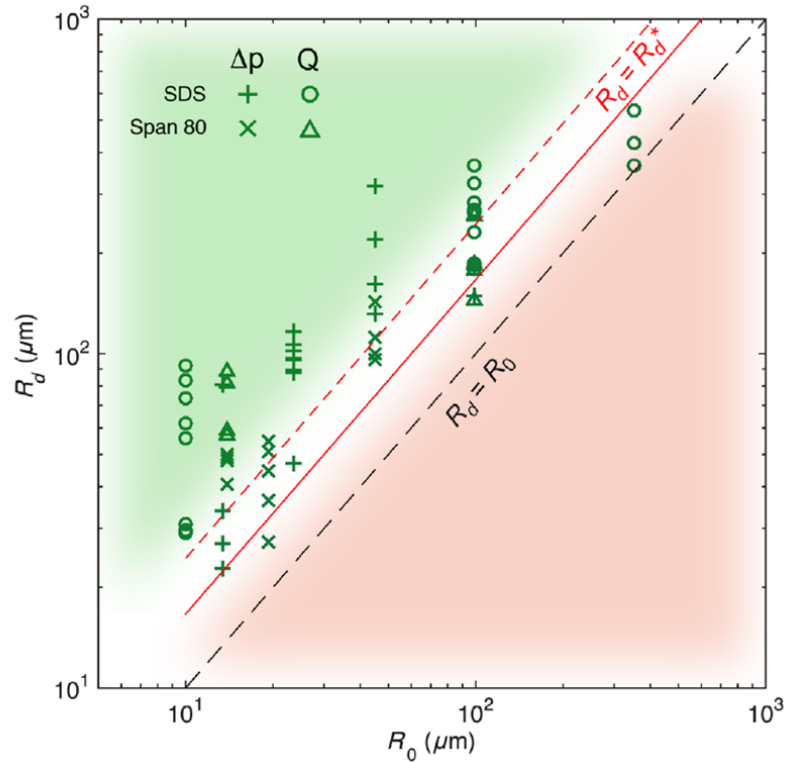


Diagram showing the mean radius of emulsions obtained with the capillary trap. We either use configuration 1 (SDS) with a pressure driven injection (*plus*) or a flow-rate driven injection (*circle*) or configuration 2 (Span 80) with a pressure driven injection (*cross*) or a flow-rate driven injection (*triangle*). All the experiments yield a minimal mean radius $R_d^* > R_0$. We plot the lower boundary $R_d = R_0$ (dashed dark). We also draw the model prediction detailed in [Chapter 3](#) for $R_d = R_d^*$ with $\gamma_{ao} = 36$ mN/m (red solid line) and $\gamma_{ao} = 18$ mN/m (red dashed line).

Figure 2.5: Lower limit on the mean radius of water-in-oil emulsions.

Despite these considerations, they do not quantify the effect of the surface tensions on the diameter of the produced droplets. On our side, we have provided a deeper understanding of the underlying mechanisms by demonstrating that the process is quasi-static and by studying its dependence with surface tensions.

COST-EFFECTIVE CAPILLARY TRAP Finally, we also developed a cost-effective version of our setup, involving an Arduino controller, a motorized microscope stage with a low cost stepper motor and a simple hydrostatic control of the pressure. Details about it can be found in [Appendix E](#) ([9]).

MODELING THE QUASI-STATIC DETACHMENT PROCESS

1 SURFACE ENERGIES MODEL

Experimentally, we observe that the introduced concentration in SDS changes the minimal radius of the detached droplet R_d^* . When the concentration in SDS increases, the two surface tensions γ_{aw} (air/water) and γ_{ow} (oil/water) decrease [15]. We observe that R_d^* also slightly decreases (Fig 3.2).

We heuristically model the detachment of the droplet by taking into account capillary interactions only. We impose the shape of both the meniscus and the droplet in the detachment process and compute the resulting surface energies between the attached and the detached state. We investigate if this *a minima* model can describe the weak dependency of R_d^* with the change in surface tension induced by a varying SDS concentration. We assume in this situation that the droplet is attached to the capillary and shaped as a spherical cap with a height h and a radius R (Fig 3.1 A). When the capillary moves up, the shape of the droplet changes: the droplet is cut at $R = R_1$. We postulate a parabolic shape for the neck line between the spherical cap and the tip of the capillary (Fig 3.1 B). The oil/water interface and the oil/air interface increase until the neck of the droplet breaks at the level of the tip, forming a droplet of radius R_d inside the oil (Fig 3.1 C). At this step, the height of the tip of the capillary is called Z . It is the critical height at which the droplet detaches.

1.1 Free energies computation

We compare the free energies of the two possible states:

1. The droplet remains attached to the tip of the capillary (Fig 3.1 B).
2. The droplet detaches from the tip of the capillary (Fig 3.1 C).

For the spherical cap of curvature radius R , height h , cut in R_0 , the three parameters are not independent and linked by the relation $h = R + R\sqrt{1 - \frac{R_0^2}{R^2}}$. The area \mathcal{A}_c and volume \mathcal{V}_c of the spherical cap can be computed:

$$\mathcal{A}_c = 2\pi R h = \pi(R_0^2 + h^2) \quad (3.1)$$

$$\mathcal{V}_c = \frac{\pi}{6} h(3R_0^2 + h^2) \quad (3.2)$$

The paraboloid shape of the neck can be parameterized with $\rho(z)$:

$$\rho(z) = c + az + bz^2 \quad (3.3)$$

Boundary conditions are given by imposing the continuity of the derivative of the water droplet shape at the interface between the bath of oil and the air and the continuity of the paraboloid at the tip of the capillary. It can be written as follow:

$$\lim_{z \rightarrow 0^-} \frac{d\rho}{dz} = \lim_{z \rightarrow 0^+} \frac{d\rho}{dz} \quad (3.4)$$

$$\rho(z = Z) = R_0 \quad (3.5)$$

The spherical shape minimizes the surface at a given volume and the model implies $h > R$. We can thus deduce that the minimal radius R_1 at which the droplet is cut when crossing the interface is actually the radius of curvature of the spherical cap. We thus have $R_1 = R$ and the paraboloid equation becomes:

$$\begin{cases} a = 0 \\ b = \frac{R_0 - R}{Z^2} \\ \rho(z) = R + \frac{R_0 - R}{Z^2} z^2 \end{cases} \quad (3.6)$$

We get the total surface \mathcal{A}_p and volume \mathcal{V}_p of the paraboloid with the following equations:

$$\begin{aligned} \mathcal{A}_p &= 2\pi \int_0^Z \rho(z) dz \\ &= 2\pi \left(R + \frac{R_0 - R}{3} \right) Z \\ \mathcal{V}_p &= \int_0^Z dz \pi \rho^2(z) \\ &= \pi \left(R^2 + \frac{(R - R_0)^2}{5} + 2R \frac{R_0 - R}{3} \right) Z \end{aligned}$$

We have the volume conservation between the initial volume V_0 and the sum of V_p the paraboloid volume and V_c the spherical cap volume cut in R :

$$\begin{aligned} V_0 &= V_p + V_c \\ \frac{\pi}{6} h (3R_0^2 + h^2) &= \frac{2}{3} \pi R^3 + \pi \left(R^2 Z + \frac{(R - R_0)^2}{5} + 2R \frac{R_0 - R}{3} \right) Z \end{aligned} \quad (3.7)$$

Using Eq 3.7:

$$Z = \frac{\frac{1}{6} \left(R + \sqrt{R^2 - R_0^2} \right) \left(\left(R + \sqrt{R^2 - R_0^2} \right)^2 + 3R_0^2 \right) - \frac{2R^3}{3}}{R^2 + \frac{2}{3}R(R_0 - R) + \frac{1}{5}(R_0 - R)^2} \quad (3.8)$$

This expression developed to the 1st order in $\frac{R_0}{R}$ yields:

$$Z = R \left(\frac{5}{4} - \frac{5}{8} \frac{R_0}{R} \right) \quad (3.9)$$

We give a more pedestrian approach in [9]. Assuming $\frac{R_0}{R} \ll 1$ we indeed have the volume of the initial spherical cap:

$$V_c \simeq \frac{4}{3} \pi R^3 \quad (3.10)$$

Injecting 3.10 in 3.7 we get;

$$Z = \frac{\frac{2}{3}R^3}{R^2 + \frac{(R_0-R)^2}{5} + \frac{2}{3}R(R_0 - R)} \quad (3.11)$$

Both equations 3.8 and 3.11 have the same development up to $(\frac{R_0}{R})^3$.

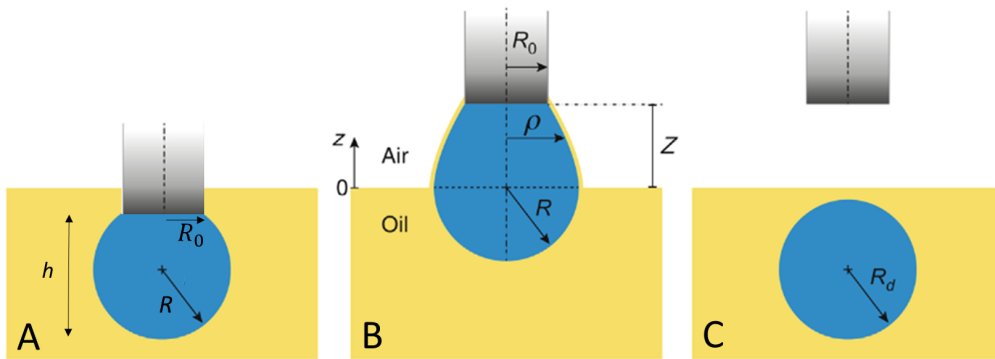
1.2 Surface free energies in the final states

We write the free energies of the two possible final states as functions of the geometrical parameters and of the three surface tensions γ_{ow} (oil/water), γ_{ao} (air/oil) and γ_{aw} (air/water). \mathcal{F}_A is the free energy of the attached state. It is the sum of the free energies corresponding to the interface between the oil and the water $\mathcal{A}_p + \mathcal{A}_c$, plus the oil part that sees the air, also of area \mathcal{A}_p since we have neglected the meniscus thickness (Fig 3.1). \mathcal{F}_D is the free energy of the detached state. It involves the following terms:

1. $4\pi R_d^2$ that corresponds to the surface of the detached droplet immersed in the oil
2. πR_1^2 that corresponds to the disk interface between oil and air, free when the neck of the droplet is cut
3. πR_0^2 that corresponds to the tip of the capillary, free from a pending water droplet.

$$\mathcal{F}_A = \gamma_{ow}(\mathcal{A}_p + \mathcal{A}_c) + \gamma_{ao}\mathcal{A}_p \quad (3.12)$$

$$\mathcal{F}_D = \pi R_0^2\gamma_{aw} + 4\pi R_d^2\gamma_{ow} + \gamma_{ao}\pi R^2 \quad (3.13)$$



In the meniscus parametrization we assume that the oil meniscus is extremely thin and that its shape matches the paraboloid line of the droplet neck. (A) The droplet is formed underneath the surface with a spherical cap shape. R is the curvature radius. The sphere is cut in R_0 the inner radius of the capillary (also called base radius). The resulting spherical cap has a height h . (B) the droplet is dragged at a distance H from the surface but is still attached to the tip of the capillary. The connection between the immersed spherical cap and the tip of the capillary is made with a paraboloid of equation $\rho(z)$. (C) the droplet is detached and fully immersed in the oil bath.

Figure 3.1: Quasistatic model of the droplet detachment.

1.3 Analytical resolution

We compute an analytical solution for the minimal radius of the detached droplet, using Eq 3.11. We use the dimensionless variables $z^* = \frac{Z}{R_0}$ and $r^* = \frac{R}{R_0}$ with R , Z and R_d^* as unknown variables. The volume conservation and the energy balance equations together are thus not sufficient to reduce the system to a single equation $R_d^* = f(\gamma_{ao}, \gamma_{ow}, \gamma_{aw})$. The approximation $R_0 \ll R$ that we exposed earlier yields also $R_d^* \simeq R$ which allows us to resolve ultimately the problem of the detached radius. We thus express the reduced surface energies as $f_A = \frac{F_A}{R_0^2}$ and $f_D = \frac{F_D}{R_0^2}$. We get the following expressions for the energy and the minimal height z^* at which the droplet is cut.

$$\begin{aligned} z^* &= \frac{\frac{1}{6}r^* \left(1 + \sqrt{1 - \frac{1}{r^*}}\right) \left(\frac{3}{r^{*2}} + \left(1 + \sqrt{1 - \frac{1}{r^*}}\right)\right) - \frac{2}{3}r^*}{1 + \frac{2\left(\frac{1}{r^*}-1\right)}{3} + \frac{\left(\frac{1}{r^*}-1\right)^2}{5}} \\ &\simeq \frac{5}{4}r^* \left(1 - \frac{1}{2r^*}\right) \\ f_D &= 4\pi\gamma_{ow}r^{*2} + \pi\gamma_{ao}r^{*2} + \pi\gamma_{aw} \\ f_A &= 2\pi(\gamma_{ow}(r^{*2} + r^*z^* + \frac{z^*}{3}(1 - r^*))) + \gamma_{ao}(r^*z^* + \frac{z^*}{3}(1 - r^*)) \end{aligned}$$

The reduced equation $f_D = f_A$ has an analytical solution in the limit $r^* \ll 1$, the same approximation that we used to derive the simplified version of Z (Eq 3.11). In this limit, we can further develop $z^* \simeq \frac{5}{4}r^*$. With this last step, we get an easy-to-read expression for r^* :

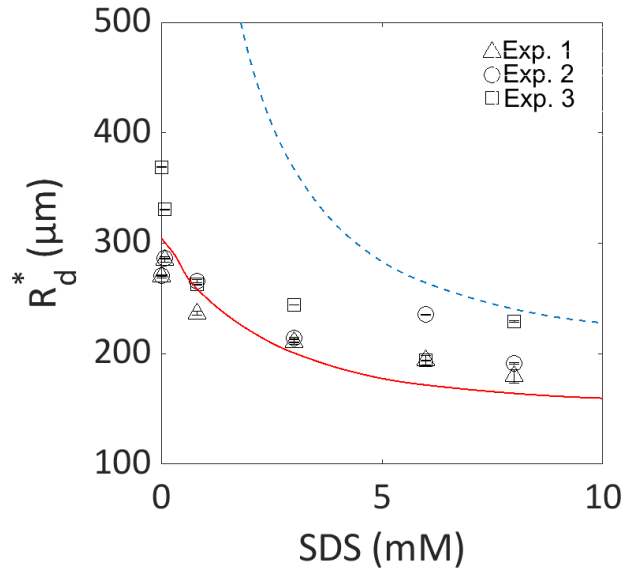
$$r^* = \frac{\sqrt{5\gamma_{ao} + 12\gamma_{aw} + 5\gamma_{ow}}}{2\sqrt{2\gamma_{ao} - \gamma_{ow}}} \quad (3.14)$$

This result is plotted Fig 3.2. We compared the model with the experimental points corresponding to the minimal detached droplet in three separate experiments Fig 3.2. We had to postulate a higher surface tension $\gamma_{oa} = 36$ mN/m than the actual surface tension $\gamma_{oa} = 18$ mN/m to capture the experimental data dependence with the introduced concentration in SDS. This is probably due to the fact that we underestimated the surface of the oil that actually sees the air, due to our hypothesis of an extremely thin film of oil instead of a meniscus. Despite this approximation, we managed to recover the dependency of the detached radius R_d on the introduced SDS concentration with a zeroth-order model. With this result, we demonstrated that the phenomenon can be understood within a minimal quasistatic theoretical frame that simply compares the energies of the two possible states.

As a further development, we present in the following section a first attempt to solve the problem without postulating the shape of the meniscus to compute the resulting surface tension energies. This resolution is still in progress and is summarized below only to present a perspective on the meniscus problem.

2 CAPILLARY FORCES RESOLUTION

In the previous section we have arbitrarily chosen the shape of the interface between the water and the oil to compute the resulting surface energies. We have also assumed that the outer radius of the capillary is comparable to the inner radius



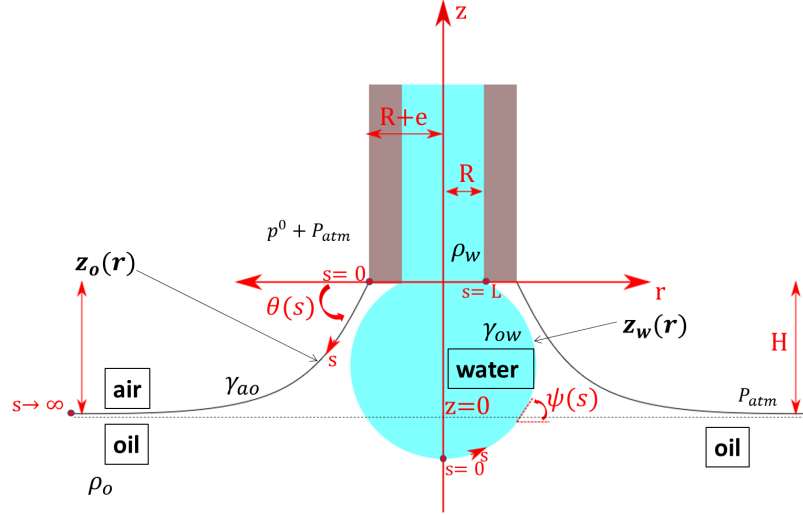
Variation of R_d^* the minimal radius of the detached droplet (geometrical model [Section 1](#)) is plotted with two values for γ_{ao} . Experimental points are best described with the red curve corresponding to $g_{oa} = 36\text{mN/m}$, which is higher than the real surface tension, $g_{oa} = 18\text{mN/m}$, plotted with the dotted blue curve.

Figure 3.2: Minimal detached droplet radius as a function of the introduced SDS concentration.

of the capillary and postulated an extremely thin shell of oil between the water and the air. We ignored in this resolution the precise mechanism leading to the detachment of the water droplet.

We propose now to derive the equations for the air/oil interface and the oil/water interface. These differential equations are driven by the surface tensions and the gravity. We show how the meniscus shape can easily be solved in one dimension. For the full cylindrical resolution, we present the beginning of a work developed in collaboration with S. Neukirch (Institut d'Alembert, Paris) and C. Josserand (LadhyX, Paris-Saclay). We then briefly explain how these equations can be solved numerically in the form of a boundary value problem. To be mentioned, this equation can also be solved analytically through asymptotic developments [98].

In this problem, the first interface is between the oil and the air, the second one is the droplet envelope which separates the oil and the water. The main idea here is that we compute the shapes of the two interfaces independently. We consider them independent as long as they do not come into contact. This is consistent with the quasistatic modeling we choose. When the tip of the capillary is moved away from the oil bath, the curvature of the oil meniscus increases. At one point there is tangency between the oil meniscus and the droplet contours. This defines a limit height and a critical volume for the droplet that is lower than what we would get with the Tate law. Indeed in the Tate problem, it is the weight of the droplet that eventually overcomes the line tension between the oil and the water to detach the droplet. In our problem, the line tension between the oil and the water ($\propto 2\pi r\gamma_{ow}$) is complemented by the line tension between the oil and the air ($\propto 2\pi r\gamma_{ao}$). Both are of the same order of magnitude when the oil meniscus contacts the water droplet. The two effects compensate and the droplet is snapped off earlier than if its apparent weight alone ($\propto (\rho_w - \rho_o)gr^3$) had to compensate the line tension $2\pi r\gamma_{ow}$.



Description of the droplet detachment with full parametrization. The shapes of the water droplet in oil and of the oil meniscus are computed separately as boundary value problems (shooting method) in Mathematica. To ease the reading of the figure, the left side presents the parametrization for the oil meniscus and the right side the parametrization for the interface between the water and the oil.

Figure 3.3: Full meniscus parametrization.

2.1 Computing the meniscus shape

The problem is considered asymmetric. The natural coordinates are thus the cylindrical coordinates $\{r, z\}$. We use $z_o(r)$ to describe the vertical position of the meniscus line between the oil and the air. We write a force balance between the hydrostatic pressure and the Laplace pressure $\gamma_{ao}(\mathcal{C}_1 + \mathcal{C}_2)$. We call \mathcal{C}_1 and \mathcal{C}_2 the two curvatures in the r, θ plane. We show Fig 3.3 the full parametrization.

We first analyze the hydrostatic pressure difference between the air and the oil at the position $z_o(r)$. We name p_o the pressure in the oil phase and P_{atm} the pressure in the air. We first establish that $p_o(z_o) - P_{atm} = \rho_o g z_o(r)$:

$$\begin{aligned} p_o(z_o = 0) &= p_o(z_o(r \rightarrow \infty)) = P_{atm} \\ p_o(z_o(r)) - p_o(z_o = 0) &= \rho_o g z_o(r) \\ p_o(z_o(r)) - P_{atm} &= \rho_o g z_o(r) \end{aligned}$$

We can then compute the two curvatures \mathcal{C}_1 and \mathcal{C}_2 :

$$\gamma_{ao}(\mathcal{C}_1 + \mathcal{C}_2) = \gamma_{ao} \left(\frac{\frac{d^2 z_o}{dr^2}}{(1 + (\frac{dz_o}{dr})^2)^{3/2}} + \frac{\frac{dz_o}{dr}}{r(1 + (\frac{dz_o}{dr})^2)^{1/2}} \right) \quad (3.15)$$

With this pressure balance, we get the following compact equation:

$$\gamma_{ao} \frac{1}{\sqrt{1 + z_o'^2}} \left(\frac{z_o''}{1 + z_o'^2} + \frac{z_o'}{r} \right) - \rho_o g z_o = 0 \quad (3.16)$$

2.1.1 One-dimensional solution

This equation can easily be solved if the capillary radius is considered infinite with respect to the capillary length. In that case, the problem is brought down to solving the ascension of the meniscus on a plane.

$$\rho_o g z_o = \gamma_{ao} \frac{\frac{d^2 z_o}{dr^2}}{\left(1 + \left(\frac{dz_o}{dr}\right)^2\right)^{3/2}} \quad (3.17)$$

Multiplying Eq 3.17 by $\frac{dz_o}{dr}$, we get an integrable form:

$$z_o \frac{dz_o}{dr} = \frac{\gamma_{ao}}{\rho_o g} \frac{\frac{d^2 z_o}{dr^2} \frac{dz_o}{dr}}{\left(1 + \left(\frac{dz_o}{dr}\right)^2\right)^{3/2}} \quad (3.18)$$

After integration:

$$z_o^2(r) = -2l_c^2 \frac{1}{\sqrt{1 + \left(\frac{dz_o}{dr}\right)^2}} + K \quad (3.19)$$

To compute boundary conditions, we consider that in the limit $r \rightarrow \infty$, the interface becomes planar and the derivative tends towards 0. We also have $z_o(r \rightarrow \infty) = 0$ and $\frac{dz_o}{dr}(r \rightarrow \infty) = 0$. That delivers the constant value $K = 2l_c^2$.

$$z_o^2(r) = 2l_c^2 \left(1 - \frac{1}{\sqrt{1 + \left(\frac{dz_o}{dr}\right)^2}}\right) \quad (3.20)$$

Eventually, far from the capillary $\frac{dz_o}{dr} \ll 1$. This leads to the following asymptotic development:

$$z_o^2(r_o) = l_c^2 \left(\frac{dz_o}{dr}\right)^2 \quad (3.21)$$

We get an exponential solution $z_o(r) \propto e^{-\frac{r}{l_c}}$.

2.1.2 Full numerical resolution

We resume now to the numerical resolution in cylindrical coordinates using a boundary value approach. Solutions can be found using a shooting method [99, 100]. We show below how to write the equations to adapt them to this numerical solving.

We introduce the curvilinear coordinate s and the angle $\theta(s)$ so that

$$\begin{cases} \frac{dz_o}{ds} = \sin \theta \\ \frac{dr}{ds} = \cos \theta \end{cases} \quad (3.22)$$

With this modification, one gets the following relations for z_o' and z_o''

$$\begin{cases} \frac{dz_o}{dr} = \tan \theta \\ \frac{d^2 z_o}{dr^2} = -\frac{d\theta/ds}{\cos^3 \theta} \end{cases} \quad (3.23)$$

Which yields the following equation

$$\frac{d\theta}{ds} = \frac{\rho_o g z_o}{\gamma_{ao}} - \frac{\sin \theta}{r} = 0 \quad (3.24)$$

The complete ODE system is given by:

$$\begin{cases} \frac{d\theta}{ds} = \frac{\rho_o g z_o}{\gamma_{ao}} - \frac{\sin \theta}{r} \\ \frac{dz_o}{ds} = \sin \theta \\ \frac{dr}{ds} = \cos \theta \end{cases} \quad (3.25)$$

This system has the following boundary conditions:

- $s = 0$: we got $r(0) = R + e$ (parameter), $z_o(0) = H$ (unknown) and $\theta(0) = \theta_0$ (unknown)
- $s \rightarrow \infty$: we got $\theta(\infty) \rightarrow 0$ (known) and $z_o(s \rightarrow \infty) = -\sqrt{\frac{\gamma_o}{\rho_o g}} \theta(r \rightarrow \infty)$ (known). The linear condition is established from the fact that $z_o \ll 1$ when $r \rightarrow \infty$. Eq 3.16 thus becomes $\gamma_o z_o'' = \rho_o g z_o$.

For a set of N coupled first-order differential equations, if we set N_1 boundary conditions for the starting point $s = 0$ then we have a remaining set of $N - N_1$ conditions for the final point $s \rightarrow \infty$ [100].

The unknown of the problem are thus H and θ_0 . In the shooting method we will define sets of initial values and solve their integration until we reach the final value corresponding to the other boundary. This final value has to match the conditions defined above. The sets that properly match boundary conditions give solutions for the H and θ_0 values.

These values correspond to the geometrical solution shown in A 1) Fig 3.2. This solution can then be adapted if we add to the problem the second interface between the water droplet and the oil meniscus, see Fig 3.2 A 2).

2.2 Computing the droplet shape

We write $z_w(r)$ the vertical coordinate describing the shape of the droplet.

We compute again the force balance at the z_w position. The pressure difference between the oil (p_o) and the water (p_w) at the height z_w can be expressed with the reference $\Delta p_{z=0}$:

$$\Delta p = (\rho_w - \rho_o) g z_w + \Delta p_{z=0} \quad (3.26)$$

From this we know that at $z = 0$, $p_o(z = 0) = p_o(r \rightarrow \infty) = P_{atm}$

We also know that $p_w(z = 0) = p^0 + P_{atm} + \rho_w g H$.

From this we conclude that:

$$\Delta p = (\rho_w - \rho_o) g z_w + \rho_w g H + p^0 \quad (3.27)$$

Injecting this in the equilibrium between surface tensions and pressures:

$$(\rho_w - \rho_o) g z_w + \rho_w g H + p^0 = \gamma_{ow} \frac{1}{\sqrt{1 + z_w'^2}} \left(\frac{z_w''}{1 + z_w'^2} + \frac{z_w'}{r} \right) \quad (3.28)$$

We can after this define an angle ψ so that $\sin \psi = \frac{dz_w}{ds}$ and $\cos \psi = \frac{dr}{ds}$ and:

$$\frac{d\psi}{ds} = -\frac{\sin \psi}{r} + \frac{p^0}{\gamma_{ow}} - \frac{\rho_w - \rho_o}{\gamma_{ow}} g z_w + \frac{\rho_w g H}{\gamma_{ow}} \quad (3.29)$$

An additional constraint exists because the water droplet volume is constant. We implement an equation for the volume conservation:

$$V(s) = -2\pi \int_{s=0}^{s=L} z_w(s) r \cos \psi ds \quad (3.30)$$

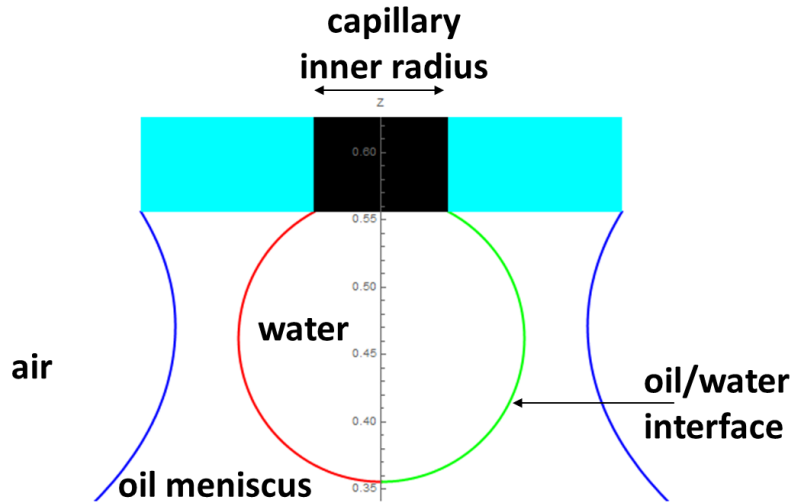
We eventually get the following system of ODEs:

$$\begin{aligned}\psi' &= -\frac{\sin \psi}{r} + \frac{p^0}{\gamma_{ow}} - \frac{\rho_w - \rho_0}{\gamma_{ow}} g z_w + \frac{\rho_w g H}{\gamma_{ow}} \\ r' &= \cos \psi \\ z_w' &= \sin \psi \\ V' &= -2\pi z_w r \cos \psi\end{aligned}$$

We define the boundaries for these variables:

- $s = 0$: we get $\psi(0) = 0$ (known), $r(0) = 0$ (known), $z_w(0) = z_0$ (unknown) and $V(0) = 0$ (known).
- $s = L$: we get $r(L) = R$ (parameter), $z_w(L) = H$ (unknown) and $V(L) = V$ (unknown).

2.3 Resolution



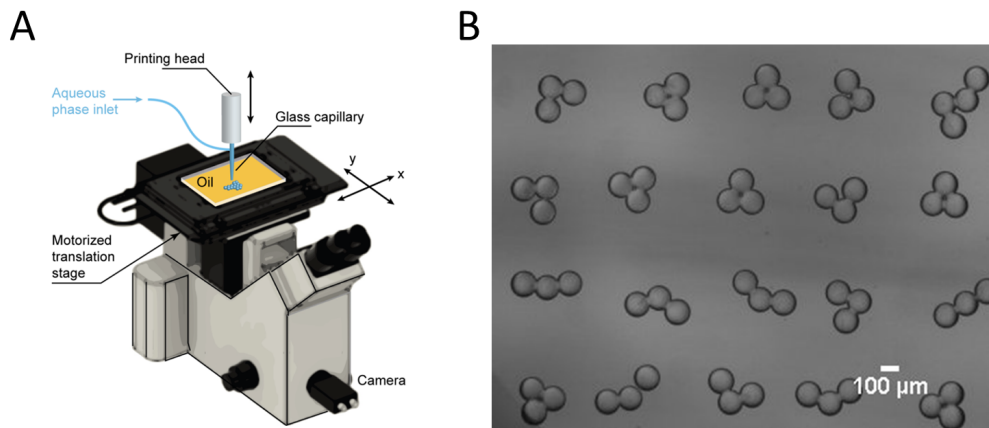
Numerical resolution of the shape of the oil meniscus (blue curve) and of the oil/water interface (red and green) with the following parameters: $R = 0.05$, $e = 0.129$, $\frac{\rho_o}{\rho_w} = 0.93$, $\frac{\gamma_o}{\gamma_{wo}}$ and $V = 0.005$. *Mathematica code provided by S. Neukirch.*

Figure 3.4: Numerical resolution of the oil meniscus and of the oil/water interface

This full system can be resolved as a boundary value problem with the following unknown: θ_0 , p^0 , z_0 , H and V . We propose the following reasoning:

- For the oil meniscus alone, there is a limit angle θ_{lim} for which the meniscus breaks. At this threshold, capillary forces alone are not sufficient to compete with the oil weight.
- For the droplet in oil, the same type of limit holds: at one point the droplet detaches for a limit angle ψ_{lim} because it cannot hold any more to the water contained in the capillary. This compares to the Tate experiment where the droplet finally detaches under its weight, except that here the droplet in the oil has an apparent weight a lot smaller than its weight value in the air.

When the two interfaces become tangent, we first assume that this corresponds to the surface detachment. We can plot the numerical resolutions of the water and oil



A) 2D Capillary Trap Printer developed on a stage microscope. Droplet layering and timelapse microscopy are done on the same stage. B) Example of small DIB groups.

Figure 3.5: Production of small DIB networks

interface together with the air and oil interface on Fig 3.4 with a Mathematica code provided by S. Neukirch. We are still investigating possible physical mechanisms leading to the droplet detachment.

3 PARTIAL CONCLUSION

In this part, we have introduced the system used in all the thesis as a biomimetic model of a cellular tissue. This system is an array of bilayers that separate water droplets in an oil bath of phospholipids. We have designed a robust and versatile technique to produce monodisperse microdroplets by using capillary forces only. This system can generate a wide range of sizes for the produced emulsions *modulo* a lower cutoff given by the inner radius of the capillary. We have also observed that the droplet formation seemed quasistatic. We have thus described the detachment mechanism of the water droplets through a minimal model that compares surface energies between two states. We have successfully recovered the dependency of the experimental mean radius of the emulsion on the surface tension between the two phases - oil and water. A more accurate modelization is under progress thanks to the collaboration with C. Josserand and S. Neukirch.

We now expose the production of compact linear arrays from the production of emulsions using a capillary trap device (Fig 3.5 A). We take advantage of the fact that if we layer the droplets next to each other, they spontaneously adhere to constitute the beginning of a network (Fig 3.5 B). In the following part, we will connect the water droplets together by using a bacterial toxin called hemolysin that assembles as a nanopore in the bilayer. We will show how the transport kinetics depend on the introduced concentration in nanopores.

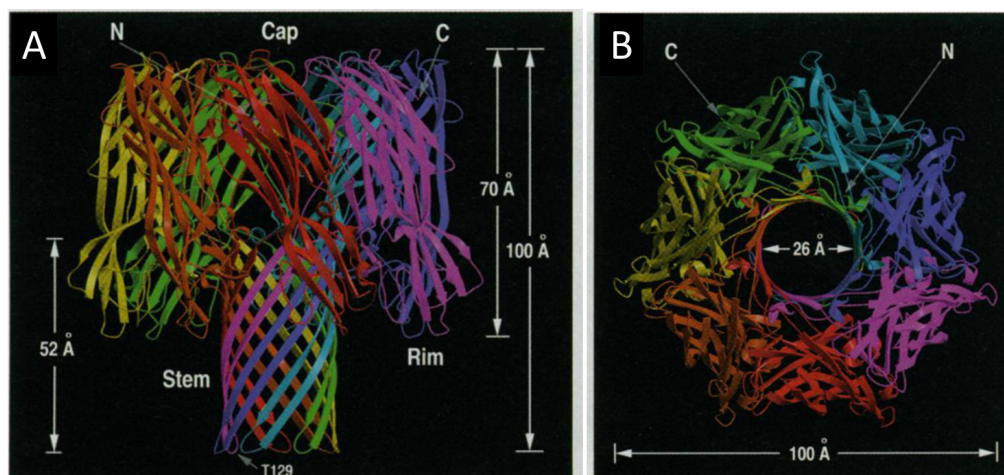
Part II

DIFFUSIVE TRANSPORT IN AN ARTIFICIAL TISSUE

In the following chapters ([Part ii](#)), we assemble the droplets produced in [Part i](#) into 1D and 2D networks. We functionalize these DIB arrays by introducing hemolysin pores in the bilayers. We put a source droplet containing a fluorophore in the network and monitor the increase in signal in the source neighbors while the probe diffuses through the connecting nanopores. [Chapter 4](#) focuses on the spontaneous insertion of the bacterial toxin in an artificial monolayer. [Chapter 5](#) details the method used to layer one dimensional networks connected by hemolysin, and how we quantify the diffusion in such networks. [Chapter 6](#) links the characteristic time of transport of the fluorophore from the source droplet to the first neighbor to the adsorbed concentration in pores. Last, we extend in [Chapter 7](#) the formalism developed in the 1D case to the 2D constitution of networks. This work was submitted [[101](#)], see [Appendix E](#).

CONNECTING DROPLETS WITH HEMOLYSIN PORES

1 INSERTING HEMOLYSIN IN BILAYERS



(A) Side view of hemolysin in its heptameric form. The stem inserts fully in the target membrane and the cap remains outside (B) Top view of the cap of the heptamer. Reprinted with permission from AAAS [17]

Figure 4.1: Hemolysin crystal structure with characteristic dimensions .

hemolysin - sometimes called α toxin - is a β -barrel¹ [102] protein produced by *Staphylococcus aureus*. The monomeric form is made of 293 amino acids. Its role is to target mammalian erythrocytes, also called red blood cells, to induce perforation of their membrane [16]. Monomers oligomerize into heptamers when introduced in membranes or in detergent solutions. The structure of the pore was characterized using X-ray diffraction in 1996 by Song and coworkers [17]. Fig 4.1 A and B show the overall dimensions of the pore. Once inserted in the bilayer, the protein exhibits a mushroom-like shape, with the cap pointing outside of the membrane of the target cell, the rim on the outer leaflet of the membrane and the stem inserted in the membrane.

This structural study confirmed that hemolysin was indeed a symmetrical heptamer. The monomer structure in water was characterized later with a combination of simulation and low resolution X-ray scattering [103]. The hemolysin monomer is highly soluble in water with a solubility of 0.3 mM or 10 g/L [17]. To form the pore, solubilized monomers have to bind to the membrane (1), then oligomerize (2), then fully insert in the membrane (3) and eventually form an open channel (4) [19]. Once the pore is formed within the bilayer, it exhibits a cylindrical funnel of maximal size 2.5 nm and minimal size 1.4 nm in the narrowest part of the stem. This funnel allows a molecular flow up to 1 – 4 kDa [18].

In this part, our aim is to insert hemolysin in membranes and monitor a molecular flow through the pore once it is equilibrated in the bilayer. We hence need a basic

¹ Proteins can have a β sheet structure with hydrogen-bonded backbones. This β sheet forms a 3-dimensional closed structure that looks like a barrel, hence the term β barrel.

understanding of the time required for the pore equilibration as well as of the fraction of pores adsorbed in the membrane in function of the number of introduced monomers.

2 CHEMICAL MODEL FOR PORE EQUILIBRATION

After discussing previous affinity measurements reported in the literature, both for *in vivo* and *in vitro* membrane insertion, we will expose a short model to describe monomers adsorption in synthetic membrane systems.

2.1 Previous studies of hemolysin insertion

Hemolysin can insert in cell membranes and in pure bilayers. It has thus been suggested that the insertion mechanism relies on hydrophobic interactions only and does not require any external agent [19]. On the other hand, it was known early that the protein had also a higher affinity in some very restrained conditions, in the presence of a protease [16]. The binding constant of hemolysin was measured by Cassidy and coworkers [104] in the case of rabbit erythrocytes (K_d of 6.10^{-9} at 20°C). The two regimes for erythrocyte membranes - low-affinity and high affinity binding - are discussed in [105]. Half-maximal binding happens at a concentration of 2 nM [106]. When the introduced concentration exceeds 200 nM, the toxin binds without specificity to the membrane. In the late 2000's, Wilke and Wardenburg eventually identified A Disintegrin And Metalloprotease (ADAM10) as the proteinous potential candidate for high affinity binding of hemolysin to the membrane [107]. This enzyme is included in the cell membrane and degrades proteins in the cell environment.

Studies *in vitro* focused on the effect of the lipid nature on the binding of hemolysin, in the low-affinity regime. Gouaux et al. evidenced binding of the beta structures between the rim and the stem to the choline heads of phospholipids [108], hence inferring that hemolysin would integrate preferably in choline-constituted bilayers. This binding can be perturbed by cholesterol depletion or choline competition from the environment [18], which again points at a low affinity binding between hemolysin monomers and phosphocholines. Hemolysin is also able to target lipid monolayers, as it was primarily evidenced by Freer et al. [109] in 1968, with micelles (*spherules*) made of a lecithin-DPC-cholesterol mixture.

Working with hemolysin in droplet interface bilayers made of DPhPC, we are in the low-affinity regime compared to the *in vivo* case. The binding of the monomer to the bilayer is permitted by the bilayer composition, made of a single type of phospholipids with choline heads. In this configuration, the protein assembly has been reported by Bayley et al. [7] to occur extremely fast, in less than 5 ms.

2.2 Model exposition

Even though there should be intermediate steps, we postulate a single-step equilibrium for the pore assembly defined by the equilibrium constant K (Eq 4.1). We use this short model to scale the adsorbed concentration of pores in the bilayer $[\alpha\text{HL}]_{7,bilayer}$ (called C_s) with respect to the introduced concentration in monomers $[\alpha\text{HL}]_{aq}$ (called C_i).



We consider a gas of monomers in equilibrium with a planar bilayer with A occupancy sites [20]. The number of adsorbed pores is called N_a^p . If \mathcal{A}_D is the area of the bilayer and \mathcal{A}_p the area of the pore (outer dimensions), then $A = \frac{\mathcal{A}_D}{\mathcal{A}_p}$. We then use the classical model of Langmuir adsorption with the approximation that $A - N_a^p \simeq A$ (see details in [20] and in Appendix B). With this model we express the chemical equilibrium constant K as a function of C_i and C_s , with C_0 and $C_{0,s}$ normalization constants.

$$K = 7 \ln C_i / C_0 - \ln C_s / C_{0,s} \quad (4.2)$$

From this adsorption model we also get the scaling between the introduced concentration in monomers C_i and the surface concentration of adsorbed pores C_s :

$$C_s = \frac{N_a^p}{\mathcal{A}_D} \propto C_i^7 \quad (4.3)$$

From now on, knowing the scaling between C_i and C_s (Eq 4.3) we will refer simply to c the introduced concentration in monomers as our control parameter. Once the pore is inserted in the bilayer, the communication between the droplets is pore-mediated: the molecular probe diffuses from a droplet to its neighbor through the pore.

3 DIFFUSION THROUGH HEMOLYSIN

Hemolysin has a lot been used in the literature to allow communication through a model bilayer, either in liposomes or in droplet interface bilayers. However, most of the studies dealing with it relied on proof of concepts rather than in a quantitative study of transport.

Bayley and coworkers used extensively hemolysin in their DIB systems, with bilayer assemblies ranging from linear arrays [110] to 3D biomimetic tissues in [13, 4]. In [13, 4], droplets are printed with an electrical nozzle into 3D architectures. The authors managed to mix several droplet populations including a connected one seeded with hemolysin pores to create conductive paths in the tissue. These paths were evidenced optically through the diffusion of a fluorescent dye known as pyranine. Despite this bioengineering achievement, no quantitative assessment of the probe diffusion was provided. In particular the link between the increase of the fluorophore concentration and the inserted hemolysin concentration is not studied. However, the same authors developed quantitative analysis through single membrane conduction studies in [82]. In this work, they studied calcium transport through hemolysin pores. They added a channel blocker called TRIMEB to discretize fluxes through the protein funnel. Calcium translocation was evidenced through a fluorescence indicator named Fluo-4, but as a way to infer the blocker binding kinetic constant to the pore. The dependence of calcium transmission on the number of pores is not studied as the work in [82] is limited to single conduction events.

We found two quantitative studies of molecular transmission through hemolysin pores that were more similar to what we intended to do. These two papers [111, 21] are based on optical measurements of the diffusion of a probe through hemolysin pores. Signal transfer of Alexa 488 through hemolysin was thoroughly characterized by Watanabe and coworkers in [111]. The authors depict the transport of the

fluorophore using a Fick's law $\frac{dC}{dt} \propto J$ with the flux vector $J = -D_{eff}\nabla C$, ∇C being the gradient of the fluorophore through the bilayer. They are able to extract the effective diffusion coefficient $D_{eff} \simeq 5.10^{-11} \text{ m}^2/\text{s}$ that is roughly 10 times smaller than the bulk diffusion coefficient of Alexa 488 in water. However this coefficient is not linked to the number of pores adsorbed in the membrane. Dupin and Simmel [21] provided a more detailed model of transport through hemolysin, using again a modified diffusion coefficient to take into account the permeability of the membrane. Their description of membrane permeability is based on inserted hemolysin channels. If they provide a link between the flux vector J and the number of pores in the bilayer N , they do not rely on a microscopic description of the spatial arrangement of the pores.

We propose to describe a probe diffusion in arrays of connected droplets through microscopic considerations. The probe has to find the pore hemolysin (the target) while randomly exploring the compartment, then escape through the pore. This problem is generally described in theoretical physics as the narrow escape problem. We benefitted from a collaboration with R. Voituriez (Laboratoire Jean Perrin, Paris - France) for these theoretical aspects.

4 MEAN FIRST-PASSAGE TIME

We consider a diffusive object that has to hit a target. The First-Passage Time (FPT) relates directly to the following questions: how long should we wait before this object hits this target ? Or more formally, what is the probability that this brownian object reaches this target at position \mathbf{r} for the first time at time t ?

In a broader context, first-passage quantities are of prime interest in the study of a diffusive motion [112]. They were derived within the random walk framework by Montroll and Weiss in 1965 [113], but were introduced as early as 1958 to study chemical interactions [114]. First-passage quantities can be directly applied to biological systems, first of all to study the motion of brownian objects such as molecules that need to reach a precise target within the cell. A canonical example for this problem is given in [22]. The authors consider the case of a receptor on a synapse that is going to propagate an electrical signal to the brain, providing that it is hit by its molecular ligand. This probabilistic approach has also shed new light on experimental results that seemed less obviously linked to the random walk framework. These include for instance rupture experiments where a single molecule is stretched until it breaks [115] as well as genomic interaction dynamics [116].

This FPT is particularly useful to describe the narrow escape problem, where a diffusive object has to find an absorbing target in a closed and confined domain with reflecting boundaries [22]. Closed means that the brownian object cannot exit the domain without hitting the target. When it hits the target, it disappears because the target is absorbing. A reflecting boundary means that when the object hits the boundary and not the target, it bounces in the reverse direction. In this theoretical description, the FPT is sometimes called the Narrow-Escape Time (NET). A brownian probe with a diffusion coefficient D will escape from a spherical cavity of radius R and escape aperture a with a typical characteristic time $\langle T \rangle$ [112]:

$$\langle T \rangle = \frac{R^3}{a.D} \quad (4.4)$$

This time can be compared with the relaxation diffusion time inside the cavity, $T_r \propto \frac{R^2}{D}$. For a cavity of size $R = 10^{-4} \text{ m}$ and aperture $a = 10^{-9} \text{ m}$ we get

$\frac{\langle T \rangle}{T_r} = \frac{R}{a} = 10^5$. The dimensions of the aperture are so small compared to the size of the domain that the typical time for the domain exploration is larger by 5 orders of magnitude than the exit time. Calculations to express the FPT in arbitrary domains were performed through asymptotic developments, firstly in [24] then through a unified approach in [25].

We now assume an environment with a pore of typical diameter size a , diffusing on the surface of a sphere with a radius R . Then the mean time $\langle T \rangle$ necessary for a probe inside the droplet to reach the pore is:

$$\langle T \rangle = \frac{V}{2Da} = \frac{2\pi R^3}{3 Da} \quad (4.5)$$

To get a sense of how $\langle T \rangle$ connects to a diffusion problem, we can consider limited diffusion in a porous medium [117]. We further consider low permittivity media: in this approximation, the typical diffusion time T_r inside a cavity is much smaller than the time $\langle T \rangle$ necessary to escape from the cavity [118, 119]. In a limited diffusion process, we can write an effective diffusion coefficient in the porous media taking into account the time needed to go from one cavity to another [117]:

$$D_{eff} = \frac{l^2}{2d\langle T \rangle} \quad (4.6)$$

l being the typical size of the cavity, d the dimension of the problem and $\langle T \rangle$ the FPT.

We choose an approach slightly different from the one developed above. We want to describe diffusion in an array of connected droplets not as a continuous spatial process with an effective diffusion coefficient D_{eff} but as a random walk on discrete spatial sites pictured by the droplets at positions $\{\mathbf{r}_0 \dots \mathbf{r}_N\}$. We thus establish a link between $\langle T \rangle$ and the random walk on sites $\{\mathbf{r}_0, \mathbf{r}_1, \dots, \mathbf{r}_N\}$ in the Continuous Time Random Walk (CTRW) framework.

We will refer later to the FPT as the microscopic timescale of our study. We will use it to characterize experimentally and theoretically diffusion in arrays of droplet interface bilayers connected by hemolysin.

5 CONTINUOUS TIME RANDOM WALKS

All the following section relies on the book of B.D. Hughes, *Random Walks* [26].

In this section we will adopt the following notations while considering the function $f(\mathbf{r}, t)$ with a double space \mathbf{r} and time t dependence.

- $\hat{f}(\mathbf{r}, s)$ stands for the Laplace transform of f in the reciprocal space of time t , using the variable s . $\hat{f}(\mathbf{r}, s) = \int_0^\infty f(\mathbf{r}, t) \exp(-s.t) dt$
- $\tilde{f}(\mathbf{k}, t)$ stands for the discrete Fourier transform in the reciprocal space of \mathbf{r} with $\tilde{f}(\mathbf{k}, t) = \sum_{\mathbf{r}} \exp(i\mathbf{k}\mathbf{r}).f(\mathbf{r}, t)$

5.1 Translationally invariant random walks

We first consider a random walk on a discrete lattice of arbitrary dimension d , with discrete time steps. We call $P_n(\mathbf{r})$ the probability to meet the walker at the position \mathbf{r} after n steps.

With this, we know that $P_0(\mathbf{r}) = \delta_{\mathbf{r},0}$ when the walker starts at site $\mathbf{0}$. For a unit time step, the probability of stepping a length $\mathbf{r} - \mathbf{r}_0$ writes $p(\mathbf{r} - \mathbf{r}_0)$.

If there is no bias in direction and all steps on the lattice are equally permitted, the walk is of Pólya Type. The probability of being at site \mathbf{r} at step $n + 1$, being at site \mathbf{r}_0 at step n is described by the recurrence relationship:

$$P_{n+1}(\mathbf{r}) = \sum_{\mathbf{r}-\mathbf{r}_0} p(\mathbf{r} - \mathbf{r}_0)P_n(\mathbf{r}_0) \quad (4.7)$$

In Fourier Space, Eq 4.7 becomes:

$$\tilde{P}_{n+1}(\mathbf{k}) = \Lambda(\mathbf{k})\tilde{P}_n(\mathbf{k}) \quad (4.8)$$

While introducing $\Lambda(\mathbf{k})$ as the function describing the nature of the lattice and the random walk:

$$\Lambda(\mathbf{k}) = \sum_{\mathbf{r}} e^{i\mathbf{k}\mathbf{r}} p(\mathbf{r}) \quad (4.9)$$

\tilde{P}_n in Fourier space simply writes:

$$\tilde{P}_n(\mathbf{k}) = \Lambda(\mathbf{k})^n \tilde{P}_0 = \Lambda(\mathbf{k})^n \quad (4.10)$$

In the continuous \mathbf{r} space of dimension d ,

$$P_n(\mathbf{r}) = \frac{1}{(2\pi)^d} \int_{\mathcal{D}^d} \exp(i\mathbf{k}\mathbf{r}) \Lambda(\mathbf{k})^n d^d \mathbf{k} \quad (4.11)$$

This integral expression can be used in the asymptotic development of the generating function² $P(\mathbf{r}, \zeta)$.

$$\begin{aligned} P(\mathbf{r}, \zeta) &= \sum_n P_n(\mathbf{r}) \zeta^n \\ &= \sum_n \left(\frac{1}{(2\pi)^d} \int_{\mathcal{D}^d} \exp(i\mathbf{k}\mathbf{r}) \Lambda(\mathbf{k})^n d^d \mathbf{k} \right) \zeta^n \\ &= \frac{1}{(2\pi)^d} \int_{\mathcal{D}^d} \exp(i\mathbf{k}\mathbf{r}) \frac{1}{1 - \zeta \Lambda(\mathbf{k})} d^d \mathbf{k} \end{aligned} \quad (4.12)$$

We will see now that the variable ζ can be conveniently replaced by the waiting-time density corresponding to the continuous time description of our work.

5.2 Waiting-Time Density

We can obtain a continuous description of a random walker by taking the continuum limit in time and space, yielding a standard diffusion equation. We propose instead to adopt the framework of CTRWs where the time is continuous and the spatial discretization of steps is preserved. In this description, a random walk occurs on a lattice with waiting times between each step. These times are distributed according to a probability density function $\psi(t)$ called the waiting time density.

In the canonical case, an exponential waiting time density $\psi(t) = \lambda \exp(-\lambda t)$ is chosen. This choice is motivated in our case by the narrow escape problem. The

² It is convenient to write the different probabilities $P_n(\mathbf{r})$ as coefficients of a power series. The resulting power series is called *generating function*.

survival probability of the probe in a domain of radius R is the probability to find at time t the probe in the domain. It decreases as time increases because the probe can escape through the hole between $t = 0$ and t . In this particular situation there is a limit called by Holcman et al. the *small hole approximation* [27], in which $\frac{a}{R} \rightarrow 0$. In this asymptotic limit the survival probability is exponentially decreasing which implies that the waiting time density is also going to be exponentially decreasing.

For the canonical waiting time density:

$$\hat{\psi}(s) = \int \lambda \exp(-(\lambda + s)t) dt = \frac{\lambda}{\lambda + s} \quad (4.13)$$

Montroll-Weiss Theorem

We will now provide a quantitative link between discrete random walks on a lattice (Section 5.1) and the continuous time description that is given by $\psi(t)$. This correspondence is given when spatial and temporal dependencies can be decoupled, i.e. the transition probability between two sites $p(\mathbf{r}|\mathbf{r}_0)$ is independent of time. We will then use the Montroll and Weiss theorem:

Theorem. *If $P(\mathbf{r}|\mathbf{r}_0, \zeta) = \sum P_n(\mathbf{r}|\mathbf{r}_0) \zeta^n$ is the generating function for the site occupancy probabilities in a discrete-time lattice walk, we can write the Laplace transform of the probability $p(\mathbf{r}|\mathbf{r}_0, t)$ that a walker starting at site \mathbf{r}_0 at time $t = 0$ will be found at a later time t at site \mathbf{r} :*

$$\hat{p}(\mathbf{r}|\mathbf{r}_0, s) = s^{-1} \{1 - \hat{\psi}(s)\} P(\mathbf{r}|\mathbf{r}_0, \hat{\psi}(s)) \quad (4.14)$$

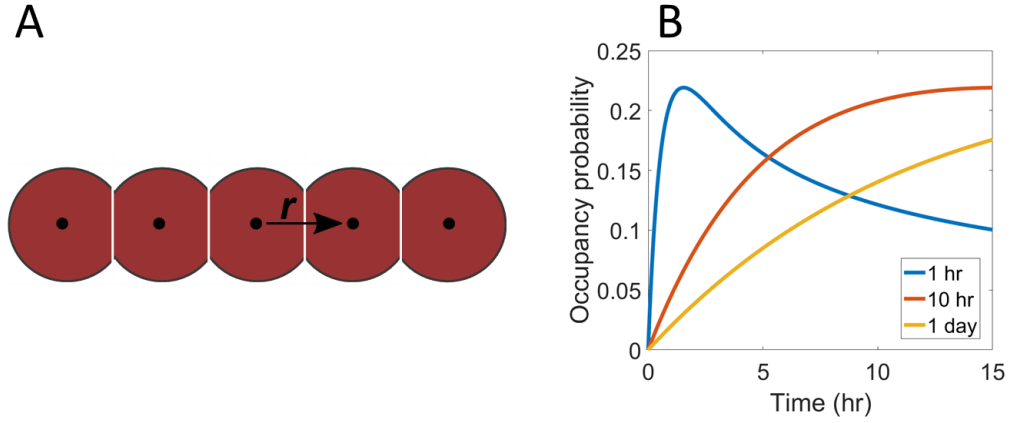
We took as initial condition a walker starting in $x = 0$ at $t = 0$. We thus replace in the previous expression $\mathbf{r}|\mathbf{r}_0$ by \mathbf{r} . We combine Eq 4.14 with Eq 4.12 while making the change $\zeta \leftrightarrow \hat{\psi}(s)$. We get the full expression of $\hat{p}(\mathbf{r}, s)$:

$$\hat{p}(\mathbf{r}, s) = s^{-1} \{1 - \hat{\psi}(s)\} \frac{1}{(2\pi)^d} \int_{\mathcal{D}^d} \frac{\exp(i\mathbf{k}\mathbf{r})}{1 - \hat{\psi}(s)\Lambda(\mathbf{k})} d^d \mathbf{k} \quad (4.15)$$

We use the waiting time distribution $\psi(t)$ to inject the timescale in the CTRW description. Practically, discrete spatial sites in Fig 5.4 are connected by small apertures that set the timescale of the diffusion process. This timescale is the FPT discussed earlier (Section 4). We set $\tau = \frac{1}{\lambda}$ to be this FPT in the expression of the waiting-time density $\psi(t) = \lambda e^{-\lambda t}$. We link CTRW and FPT in the one-dimensional case in the following subsection.

5.3 One-Dimensional Case

Using the formalism developed above in the general case of a Montroll-Weiss CTRW, we restrain to the one-dimensional lattice sketched in Fig 5.4 A. The lattice is translationally invariant and can be fully parametrized with the sole vector $\mathbf{r} = \mathbf{e}_x$. In that case,



(A) Modeling of the transport on a one-dimensional lattice described by the vector \mathbf{r} . (B) Representation of the probability of being at site $x = \pm 1$ (occupancy probability) for different timescales (cf Eq 4.17). $\frac{1}{\lambda} = 1$ hr, 10 hr and 1 day.

Figure 4.2: Modeling of a 1D Continuous Time Random Walk.

$$\begin{aligned}
 \Lambda(k) &= \sum_x \exp(ikx) p(x) \\
 &= \sum_x \exp(ikx) \frac{1}{2} (\delta_{0,-1} + \delta_{0,1}) \\
 &= \frac{1}{2} (e^{-ik} + e^{ik}) = \cos k
 \end{aligned} \tag{4.16}$$

In addition, using Eq 4.15, we get an explicit formulation for the probability of being at a site x at time t , starting at $t = 0$ at $x = 0$:

$$\begin{aligned}
 p(x, t) &= \int_0^\infty e^{-st} s^{-1} (1 - \hat{\psi}(s)) P(x, \hat{\psi}(s)) ds \\
 &= \int_0^\infty e^{-st} s^{-1} \left(1 - \frac{\lambda}{\lambda + s}\right) \frac{1}{2\pi} \int \frac{\exp(ikx)}{1 - \frac{\lambda}{\lambda + s} \Lambda(k)} dk ds \\
 &= \int_0^\infty e^{-st} \frac{1}{2\pi} \int \frac{\exp(ikx)}{\lambda(1 - \cos k) + s} dk ds \\
 &= \frac{1}{2\pi} \int \exp(ikx) \exp(\lambda(1 - \cos k)t) dk \\
 &= e^{-\lambda t} \frac{1}{2\pi} \int_{-\pi}^{\pi} (\cos(kx) + i \sin kx) \exp(\lambda \cos kt) dk \\
 &= e^{-\lambda t} \frac{2}{2\pi} \int_0^{\pi} \cos(kx) \exp(\lambda \cos kt) dk \\
 &= e^{-\lambda t} \mathcal{I}_x(\lambda t)
 \end{aligned}$$

We thus have an analytical formula that involves $\mathcal{I}_x(\lambda t)$, the modified Bessel function of the first kind which has the following representation ($x = n$ integer):

$$\mathcal{I}_n(t) = \frac{1}{\pi} \int_0^{\pi} \cos kn \exp(t \cos k) dk \tag{4.17}$$

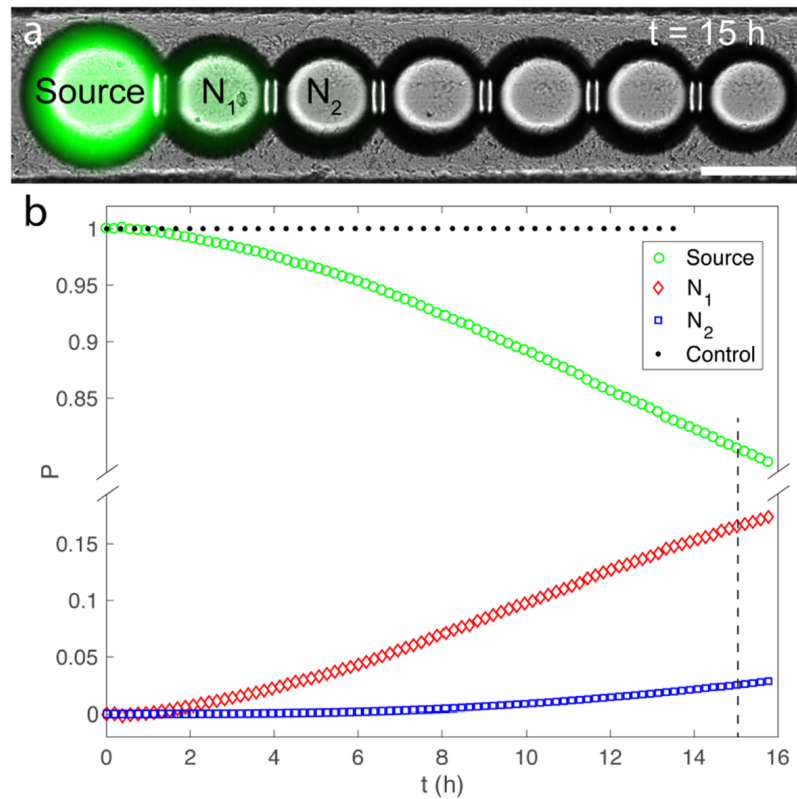
We plot in Fig 5.4 B the resulting occupancy probability for $x = 1$ for three different λ s, 1 hour, 10 hours and 1 day. The function first increases due to the fact

that many walkers starting at $x = 0$ arrive at site $x = 1$. Then the walkers continue to explore the entire line and the probability of finding a walker at site $x = 1$ tends to 0 when $t \rightarrow \infty$ because we are in a 1D spatially infinite case.

In the following part we will present how we have related transport kinetics to the number of embedded pores through average optical measurements. We have linked these kinetics to a microscopic description of the pore arrangement in the membrane through the concept of [FPT](#) in a [CTRW](#) framework.

MOLECULAR TRANSPORT IN LINES OF DROPLETS

Linear arrays of droplets connected by DIBs were obtained with a capillary trap device described earlier in Part i. We first form the water-in-oil droplets on micromilled patterns in order to assemble them in connected lines. We then add a source droplet containing a fluorophore in the line. On Fig 5.1, the source droplet connects to the other droplets and diffuses its content in the nearest neighbors on a typical timescale of $\simeq 10$ hours. Figure 5.1 shows an example of such an experiment with a source droplet connected to a line of droplets. The source droplet is filled at t_0 with a fluorophore and we monitor over time its diffusion through the network. While the source droplet is depleted in fluorophore, its neighbors are progressively filled. It is precisely this diffusion through the nanopores connecting the droplets that we now describe. We provide first the materials and methods used for these experiments.



(a) A typical linear array after 15 hours of experiment, the source droplet has transferred part of its fluorescent content to its first neighbor. The scale bar is $100 \mu\text{m}$ long. (b) Quantification of the renormalized signal P in this array. P will be defined later in Eq 5.1. P decreases in the source droplet and increases in the first neighbor (NN1). It also increases in the second neighbor (NN2), with a time delay and attenuation with respect to the NN1 signal. We also show that the source signal in a control experiment (no pores inserted) remains constant.

Figure 5.1: Typical diffusion experiment in a line of droplets connected with hemolysin nanopores.

1 LAYERING CONNECTED DROPLETS

1.1 Chemical composition of the two phases

We prepared the two phases composing the emulsion as follows. For the oil phase, we mixed hexadecane with silicone oil AR20 at a 1 : 1 v/v ratio (Sigma Aldrich). DPhPC (4ME 16:0 PC Avanti Polar Lipids) was dissolved in the oil mixture at a final concentration of 6.5 mg/mL. Aliquots of α hemolysin monomers (Sigma Aldrich) were prepared at various concentrations, from 100 to 300 μ g/mL, in a buffer (100 mM [KCl], 10 mM HEPES, pH=7.5). We dissolved the integrality of the hemolysin powder in the buffer at a stock concentration of 0.5 mg/mL. We checked the protein concentration with Nanodrop measurements. We then diluted the product in 100, 150, 200, 250, 300 and 350 μ g/mL aliquots. The fluorescent probe was carboxyfluorescein prepared in the same buffer, at a final concentration of 20 μ M.

1.2 Droplet production

We injected the aqueous buffer containing hemolysin at the working concentration to layer small droplets of dimension 150 to 200 μ m in diameter (Phase 1). These droplets were formed in the oil containing the lipids. We injected afterward a droplet of solution containing carboxyfluorescein (Phase 2) in the middle of a line. The source droplet spontaneously formed bilayers with its neighbors on one or both sides. For this reason, the source droplet could have one or two connected neighbors. Variability in bilayer formation led to a network size ranging from 3 to 10 connected droplets. Aqueous droplets were produced using a capillary trap device described [Part i](#), motorized on an (x,y) translation stage (Fig 5.2 B). The flow rate was controlled by a Cetoni NemeSys Syringe Pump. Because we used hemolysin in relatively small amounts for each experiment, we needed to inject smaller aqueous batches in the capillary than what we were typically using in [9]. We thus modified the protocol and injected $V = 10 \mu$ L of hemolysin solution in the capillary by pushing the aqueous phase with air in the tubing, using a 1 mL Gastight Hamilton Syringe. We used microfluidic IDEX connections (Fig 5.2 A) to adapt Polymicro silicate capillaries (Molex) of various sizes to Tygon tubing (Phymep). The Tygon tubing was tightened into an IDEX microfluidic connection with a microferrule of diameter 0.9 mm (1/16 inch). On the other side of the connection, the capillary was adapted using a sleeve and a microtight ferrule. For 1D arrays experiments, droplets were obtained with capillaries of dimensions 20 μ m internal diameter and 90 μ m external diameter. To produce larger droplets for 2D arrays, we used capillaries of internal diameter 100 μ m and external diameter 360 μ m.

Phase 1 is detailed step by step in the following protocol. We sucked the hemolysin solution in the Tygon tubing and then tightened the microfluidic junction. We pushed at 500 μ L/hr in the tubing until the first droplet at the tip of the capillary was seen. During this step, an air plug is compressed and starts pushing the liquid in the capillary. When the capillary was entirely filled with the aqueous phase, we decreased the flow rate to 100 μ L/hr and layered droplets with a period of 1 s.

In the steady state regime we should thus inject 28 nL at each period. This corresponds roughly to 380 μ m in diameter, which is larger than the droplets we produce (200 μ m in diameter). The most probable reason for this difference is that we were not exactly in a steady state regime. During the compressive step we had to overcome

the hydrodynamic resistance to enforce flow through the capillary. We thus adjusted visually the period of layering to have droplets adapted to the grooves in which they sit.

1.3 *Networks fabrication*

Deposition of the droplets was fully automatized through the use of motorized stages (Fig 5.2 B). The x/y motion was decoupled from the z motion. For the x and y axis we used Thorlab linear motors MTS50-Z8 with a TDC001 controller. For the z motion we used a Newport stage with a Newport Motion Controller of the SMC101 Series. These motors were controlled through Labview interfacing. Inputs of the program were the expected (x,y) locations of the droplets, a Δz step and a time period. We could tune on the fly the period of deposition. The flow rate was controlled separately through the QmixElements software (Cetoni). Droplets were layered in the grooves to create parallel lines on which to perform acquisition.

1.4 *Microfabrication of patterned substrates*

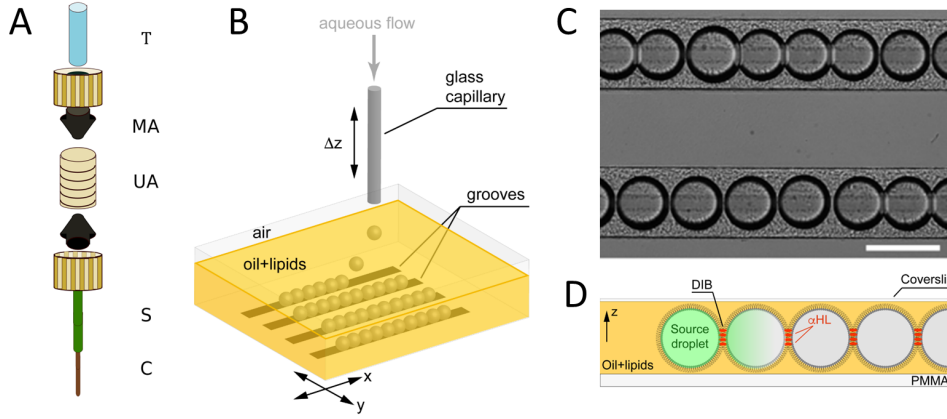
Full details on microfabrication are given in [Appendix A](#). Briefly, we constrained the droplets on patterns micromilled in Poly(methyl methacrylate) (PMMA) to ensure reproducibility of the networks from one experiment to the next.

- For linear arrays, we milled hemicylindrical grooves of 100 μm in depth using a ball-end micromill of diameter 200 μm . The linear grooves were typically 5 mm in length with a spatial periodicity of 1 mm.
- For the 2D arrays, we milled holes of 400 μm in diameter and 200 μm in depth with a ball-end mill. We arranged these holes according to the desired 2D configuration, in square or triangular lattices.

We then layered the droplets in these arrays to force them into a defined coordination. Patterned substrates were cleaned before each experiment with isopropanol.

1.5 *Timelapse Acquisition*

The chip was placed under an upright BX51WI Olympus microscope for fluorescence acquisition. A typical experiment lasts 12 to 16 hours. We took pictures with a 10X objective every 11 min on average, using 500 ms of exposure time. Fluorescence illumination was performed with a blue LED M490L4 with LEDD1B driver (Thorlabs). A Labview Routine controlled both the BX-UCB (controller unit for the bx microscope series) and an Orca Flash 4.0 Camera (Hamamatsu). With this setup we took every time step simultaneously a bright field and a fluorescence image. Evaporation occurred on the experiment timescale and droplet networks tended to contract. The droplet size shrank by 10% maximum by the end of the experiment. We corrected this effect with signal normalization ([Section 2.2](#)).



(A) Microfluidic connection between capillaries and Tygon tubing with the following abbreviations: C. Capillary, S. Sleeve, U.A. Union Assy, M.A. Microtight ferrule, T. Tygon tubing (B) Mechanical apparatus to layer aqueous droplets in a lipid bath. The capillary is motorized along the z axis, the pool containing the resulting water-in-oil emulsion is motorized along the x and y axis to layer the droplets in the corresponding grooves. (C) Connected droplets in linear arrays, scale bar=200 μm (D) Sketch of a diffusion process occurring in the droplets connected with hemolysin pores.

Figure 5.2: Droplet layering and timelapse acquisition

2 FLUORESCENCE QUANTIFICATION

2.1 Image analysis

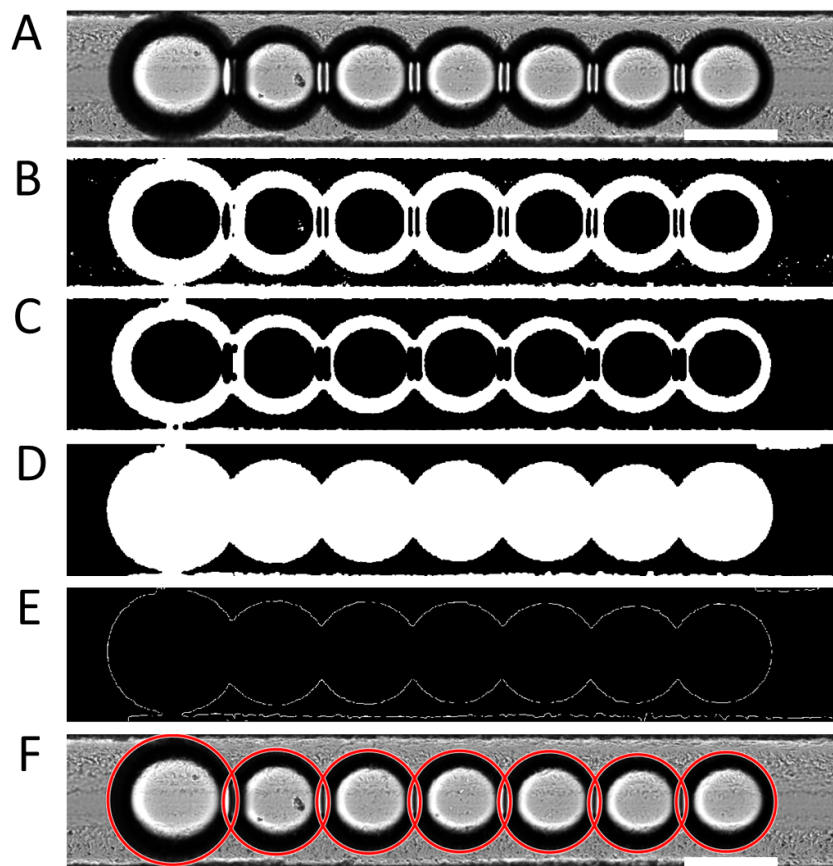
Fluorescence intensities in droplets were obtained with a custom Matlab routine. First, we performed detection of each droplet contour using morphological operations (Fig 5.3). After Gaussian filtering (Fig 5.3 A), we binarized the bright field image (Fig 5.3 B) and filled the empty zones to obtain only portions of plain white disks (Fig 5.3 D). After implementing edge detection with the function canny, we detected circular contours thanks to the Hough Transform. Hough Transform was primarily developed and patented by Paul Hough in 1962 [120] and quickly applied to the detection of curves [121]. Results of this detection are plotted in Fig 5.3 F.

With this protocol, each droplet was assigned a label, including the source droplet.

We could thus compute the intensity in each detected circle, using a circular mask with a radius half that of the detected contour. We normalized the intensities to build probabilities, such that the sum of all probabilities detected on an entire line was equal to 1. If we denote the source droplet by the index s , then the signal P_i normalized for each droplet of index i - we call it *occupancy probability* - can be expressed as:

$$P_i(t) = \frac{I_i(t) + (\delta_{i,s} - 1)I_i(0)}{\sum_k I_k(t) + (\delta_{k,s} - 1)I_k(0)} \quad (5.1)$$

P_i is equal to 0 at time $t = 0$ for all the droplets except the source. The lines that we formed had between 3 and 10 connected droplets. Because of this finite effect, we got a probability P_i that tends to $\frac{1}{n}$ when $t \rightarrow \infty$, with n the number of connected droplets on a line. In our experiments, we could measure a slow increase in signal in the first neighbor, then to the second neighbor. It was not possible to measure the signal in droplets further away from the source as the kinetics are typically too slow compared to the experiment duration, 12 hours on average. We



A) Original image B) Binarization C) Erosion to remove secondary patterns in the bilayer areas D) Fill the main remaining areas E) Perform edge detection on the treated binary image F) Perform Hough transform on detected contours and find corresponding circles, here plot in red on the original image. The resulting disks are used to define a mask centered on each droplet. The scale bar is 100 μm long.

Figure 5.3: Morphological operations to detect droplet contours.

chose to study the evolution of this occupancy probability in the first neighbor(s) of the source droplet.

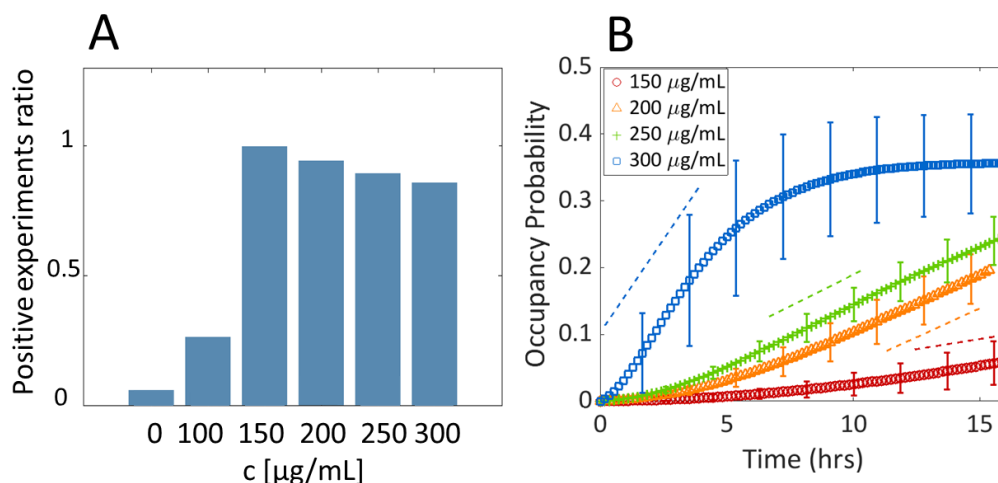
2.2 Possible Artifacts

The signal normalization removes the background at $t = 0$ and tempers photobleaching and evaporation effects. Without normalization, evaporation tends to increase fluorophore concentration within the droplet and photobleaching tends to decrease the intensity measured in the droplet. On average, we saw that the increase in fluorescence due to diffusion is stronger than the fluorophore concentration due to evaporation. It is also stronger than the intensity decrease due to photobleaching. Both effects can be quantified on the control experiments with no pores, where the signal is supposed to remain constant in the source droplet and no diffusion should occur in the neighboring droplets. We show in Fig 5.1 B a probability P_s for a control experiment without any introduced pores. This signal is constant as expected.

3 THE NUMBER OF PORES TUNES DIFFUSION

On the performed experiments, we first selected the concentration range that allows us to detect diffusion. To do so, we required that the occupancy probability computed from detected signal in the first neighbor is above 1% at the end of the experiment. We further checked that moving this arbitrary threshold did not change the frontier between positive and negative experiments. We called positive experiments those where we see effective diffusion. False positive are experiments where diffusion is seen without introduced pores. We performed no prior selection of experiments before doing this threshold analysis, meaning that osmotic shocks that may result in false positive are also included in the data (Fig 5.4 A).

From this analysis, we detected 6% of positive for the 33 experiments at $c = 0 \mu\text{g/mL}$, 27% of positive for the 30 experiments at $c = 100 \mu\text{g/mL}$, 100% of positive for the 33 experiments at $c = 150 \mu\text{g/mL}$, 94% for the 36 experiments at $c = 200 \mu\text{g/mL}$, 89% for the 38 experiments at $250 \mu\text{g/mL}$ and eventually 86% for 43 experiments at $300 \mu\text{g/mL}$. There is a clear separation between the experiments at 0 and $100 \mu\text{g/mL}$ and the interval $[150-300] \mu\text{g/mL}$. We thus decided to perform kinetics analysis on the hemolysin protein concentration range comprised between $c = 150 \mu\text{g/mL}$ and $c = 300 \mu\text{g/mL}$.



(A) Threshold concentrations to witness diffusion. We define as positive experiment an experiment where $P_1(t_f) > 0.01$ (occupancy probability for the first neighbor larger than 1%). We define the interval $150-300 \mu\text{g/mL}$ as the concentration range on which we see reproducible diffusion. (B) Average occupancy probabilities for the first neighbors plotted for each concentration, $150, 200, 250$ and $300 \mu\text{g/mL}$. Transient regimes can be fitted with a linear function. When the introduced concentration in pores increases, the slope of the transitory regime also increases.

Figure 5.4: Transport Kinetics

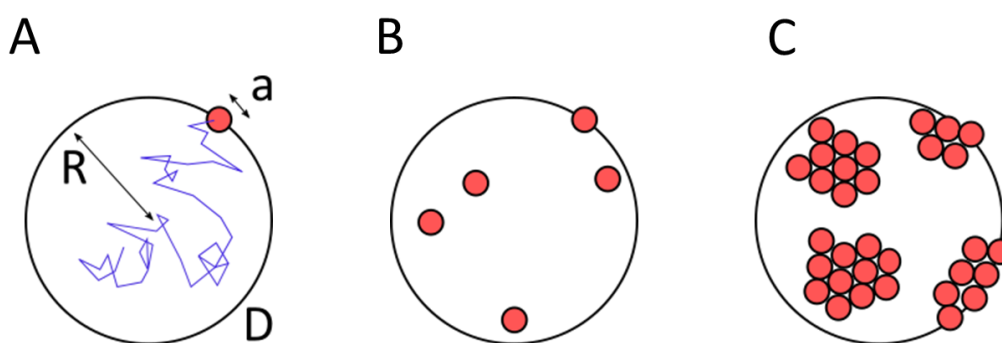
From this data set we removed the experiments where the intensity in the source droplet increased over time because of an abnormally high evaporation. We also removed experiments where we suspected osmotic imbalance. We averaged the curves for each condition on this reduced set (Fig 5.4 B). There is a clear dependence between the introduced concentration in pores and the transport kinetics from the source droplet to the first neighbor. We see a transient regime only for the concentrations $150, 200$ and $250 \mu\text{g/mL}$. For the highest concentration, $300 \mu\text{g/mL}$, there is a plateau when the concentration starts to equilibrate in the first neighbor. Droplet arrays are on average shorter at high concentrations and we see this finite size effect before the end of the experiment. Despite this finite effect, the transitory

regime does not depend on the number n of connected droplets in the array, which is not the case for the limit plateau of each probability. We will hence limit our analysis to the slope of the transitory regime only. From this data we conclude there is probably a link between the introduced concentration of pores and the duration of the transitory regime. In the next chapter we will now discuss how this scaling can be understood within the theoretical frame of first-passage times.

TUNING THE DIFFUSION PROCESS

1 MEAN-FIRST PASSAGE TIME

In our experiment, the fluorescent probe can go from the source droplet to the first neighbor droplet only through a small portion of the whole set of trajectories that sample randomly the volume of the droplet. These trajectories are the ones that end on the target, i.e. the hemolysin in the bilayer. The **FPT** appears thus as a natural way of describing this effect, in the narrow escape problem framework. In this model, the target is assumed to be an absorbing disk of diameter a . By absorbing, we mean that when the probe touches this disk, it disappears from the sphere of radius R ¹ (Fig 6.1 A).



(A) FPT sketch for one target only in a closed spherical domain. The brownian particle can explore randomly (with the associated bulk coefficient D) the inside volume delimited by the sphere of radius R . It exits from the sphere if its trajectory meets the target of size a . The mean time it takes for the probe to escape from the sphere for the first time is the **FPT**. (B) Case where several pores/exits are dispatched on the spherical domain. The distance between the pores is greater than the pore size. (C) Case where the pores start to cluster, with the assumption that it is most likely the regime where pores are highly concentrated.

Figure 6.1: Mean First Passage Times graphical representations.

We can compute an estimate of the **FPT** in the case of a single hemolysin, where the inner diameter of the pore² sizes 1 nm, embedded in a droplet of radius 100 μm and considering for the fluorescein diffusion coefficient in water $D = 4.10^{-6} \text{ cm}^2/\text{s}$ [28]. With Eq. 4.5, we obtain $\langle T \rangle \simeq 5.10^5 \text{ s}$. This time is huge compared to our experimental time. The **FPT** is however decreased because instead of having a single pore inserted in the bilayer we have N embedded pores.

There is an additional result when several exits of similar size a are distributed on the boundary of the domain [24, 25]. If the pores can be considered independent, then the **FPT** in the case of N pores scales as the **FPT** for a single pore divided by N , Fig 6.1. This result is independent of the shape of the domain as long as pores can be considered independent, i.e. $d \leq a$ with d the average distance between two pores. In this case, the **FPT** writes:

¹ N.B.: the pore is defined as an absorbing subdomain.

² We take as reference the narrowest part of the pore which sizes 1.4 nm.

$$\langle T \rangle = \frac{V}{2DNa} \quad (6.1)$$

Eventually, when N becomes very large, we assume that the pores start to cluster, forming larger exits of surface $S = Na^2$ and typical size $\sqrt{S} = \sqrt{Na}$. $\langle T \rangle$ thus becomes:

$$\langle T \rangle = \frac{V}{2D\sqrt{Na}} \quad (6.2)$$

We look for the asymptotic regime in which all the bilayer would contain densely packed pores. In this regime, we expect to find the shortest possible NET. A rough estimate of the area of contact (*i.e.* area of the DIB) can be deduced from microscopy measurements. The typical interface between two droplets has an area of $10^4 \mu\text{m}^2$. If we assume all the pores of external diameter 10 nm [122] are compacted in a plane (compacity 0,9 in 2D [123]), we get a number N of pores per DIB :

$$N \simeq \frac{10^4}{10^{-4}} = 10^8 \quad (6.3)$$

We estimate the lower boundary for the FPT in the pore-dependent regime:

$$\langle T \rangle \simeq 500\text{s} \quad (6.4)$$

This time remains larger than the time $T_r = \frac{R^2}{D} = 25 \text{ s}$ (Section 4) due to the external radius of the pore (10 nm) that is larger than the aperture of 1 nm. We can also estimate the concentration we need to introduce to saturate the DIB if all the monomers are going to the bilayer to assemble pores. Considering again the molecular weight of the hemolysin monomer (33 kDa) and a single droplet with a volume of 4 nL, the introduced concentration in monomers c is thus:

$$c = \frac{7.N}{\mathcal{N}_A V} = \frac{7.10^8}{6.02.10^{23}.4.10^{-9}} \simeq 300 \text{ nM} \quad (6.5)$$

This concentration corresponds to $10 \mu\text{g/L}$, one order of magnitude lower than the concentration range we use. This result is to be expected since an important fraction of the hemolysin we introduce does not adsorb to the bilayer. This is due to a low affinity constant between hemolysin and the bilayer as well as partial adsorption in the phospholipid monolayer surrounding all the droplet. This monolayer adsorption was indeed shown for micellar systems [109]).

We do not know the affinity constant in this problem but we can use the short model developed in Section 2 to scale the number of adsorbed pores as a function of the introduced concentration. The FPT discussion (Fig 6.1) defines two limit regimes for the timescale of the experiment.

In the independent pore regime,

$$\langle T \rangle \propto \frac{1}{N} \propto c^{-7} \quad (6.6)$$

In the clustered regime,

$$\langle T \rangle \propto \frac{1}{\sqrt{N}} \propto c^{-\frac{7}{2}} \quad (6.7)$$

The FPT gives a microscopic origin for the timescale of the diffusion process in the bilayer networks. To map completely our data to this model, we need a full description of the kinetics that link the FPT to the diffusion we observe. We will use

the [CTRW](#) framework developed earlier. The first neighbor site corresponds to the coordinate $x = 1$ and the occupancy probability writes:

$$p(1, t) = \mathcal{I}_1(\lambda t)e^{-\lambda t} \quad (6.8)$$

This expression can be developed through a Taylor expansion ($\lambda t \ll 1$) with Mathematica, yielding:

$$p(1, t) \simeq \frac{\lambda t}{2} - \frac{(\lambda t)^2}{2} + \frac{5(\lambda t)^3}{16} - \frac{7(\lambda t)^4}{48} + o(t^5) \quad (6.9)$$

It is linear in the first order with respect to t .

2 COMPARING THE MODEL TO OUR EXPERIMENTAL DATA

2.1 *Extracting the timescale of the problem*

We see Fig 5.4 B that we mainly explore the transient regime for the diffusion of the probe in the network. We used the previously derived Taylor expansion of the occupancy probability at site 1 to fit adequately the different curves and obtain a timescale $\tau = \frac{1}{\lambda}$, knowing from Eq 6.9 that the first order of the expansion is $\frac{\lambda t}{2}$. The curves are not linear during the first moments of the experiment ($t \leq 1$ h). We assumed that the system is not fully stabilized, as the linear arrays tend to "contract" during the first hour due to bilayer adhesion. The majority of these curves presents however an inflection point. We thus looked for the linear regimes by fitting the curves around the inflection point. At low c (150 $\mu\text{g}/\text{mL}$), the inflection point was sometimes not present and in that case we fitted only the last 3 hours of the data. We fitted the slope of the individual experiment curves in the linear regime with the function $a.x + b$, a being $\frac{\lambda}{2}$ if we stick formally to the Taylor expansion.

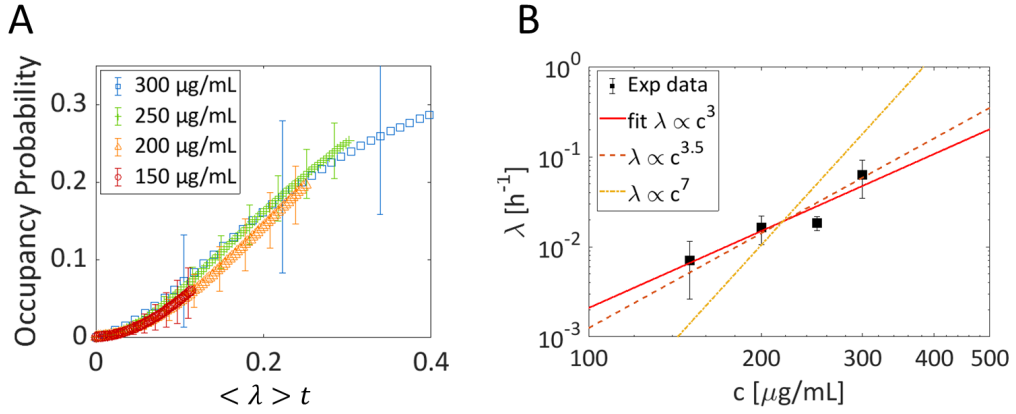
We firstly checked that λ governs the timescale of the experiment alone. To do so, we rescaled each average probability curve on a dimensionless timescale, using the average λ extracted from the single curves corresponding to each concentration. In Fig 6.2 A we see that the curves collapse within the errorbars. The shortest curve (150 $\mu\text{g}/\text{mL}$) is hence the one with the longest characteristic time τ . The resulting λ s are plotted in Fig 6.2 B. For a concentration c of 150 $\mu\text{g}/\text{mL}$, $\lambda = 7 \pm 4.10^{-3}\text{h}^{-1}$ which corresponds almost to 6 days. For $c = 200 \mu\text{g}/\text{mL}$, $\lambda = 16 \pm 5.10^{-3}\text{h}^{-1}$, with $\tau \simeq 2.5$ days. For $c = 250 \mu\text{g}/\text{mL}$, $\lambda = 18 \pm 3.10^{-3}\text{h}^{-1}$ hence roughly 2 days. And for the highest concentration $c = 300 \mu\text{g}/\text{mL}$, $\lambda = 63 \pm 3.10^{-3}\text{h}^{-1}$, hence 16 hours.

These timescales are large compared to the experiment duration. It is a confirmation that we most likely explore only the transient regime in our experiments. We performed a power law fitting on these average λ s to investigate their relationship to the introduced concentration. The fit resulted in a coefficient 3 ± 1 . We deduced that λ scales as $c^{3 \pm 1}$ for the power law dependency.

Back to the [FPT](#) discussion [Section 1](#), we sought to discriminate between two regimes:

- A regime with independent pores in which $\lambda \propto c^7$
- A regime with clustered pores in which $\lambda \propto c^{7/2}$

From the inferred value of the exponent, we see that the clustered pores regime - $\propto c^{7/2}$ - is likely to be the limit regime that describes accurately the pore spatial arrangement. We confirmed this hypothesis by plotting on the experimental data



(A) Rescaling the four different conditions using their own timescale τ deduced from the linear fit of the transient regime. All the curves collapse within the errorbars, testifying that $\tau = \frac{1}{\lambda}$ is indeed the only timescale driving the problem. (B) Power law fitting on the resulting λ s. The scaling deduced from the fit is $\lambda \propto c^{3 \pm 1}$ (red solid line). Given the errorbars, the slope $\lambda \propto c^{7/2}$ describes also accurately the data (red dotted line). On the contrary the regime $\lambda \propto c^7$ (orange solid line) is clearly to exclude. This power law favors most likely the clustered pore regime.

Figure 6.2: Analysis of the timescales

points the two expected dependencies, orange dashed line for the independent pores regime and red dashed line for the cluster regime. The cluster regime is well within the errorbars and the independent pores regime is clearly out of the confidence interval for the power law fitting.

From this analysis we concluded that the pores are most probably clustered within the bilayer. Intuitively, it increases the FPT because the particle trajectories have less chance of encountering the clusters that are not "sampling" homogeneously the bilayer.

2.2 Derivation of a cluster size

To extract a cluster size from the inferred characteristic times, we used Eq 4.5 with $\langle T \rangle = \frac{2\pi R^3}{3\sqrt{Na}}$. We deliberately chose for the exit a the geometrical inner diameter of the pore. The description could be refined through an effective size a_{eff} that would here take into account the cross section of the probe meeting the pore entrance, with possible short-range interactions. We provide the following estimations, taking again $D = 4.10^{-10} \text{ m}^2/s$, $a = 1.10^{-9} \text{ m}$ and $R = 1.10^{-4} \text{ m}$. The cluster size $\sqrt{Na} = \frac{V}{2D\langle T \rangle}$ goes from 10 nm for the smallest concentration (150 μg/mL) up to 100 nm for the highest concentration (300 μg/mL). This corresponds to 100 pores (150 μg/mL) up to about 10000 pores (300 μg/mL).

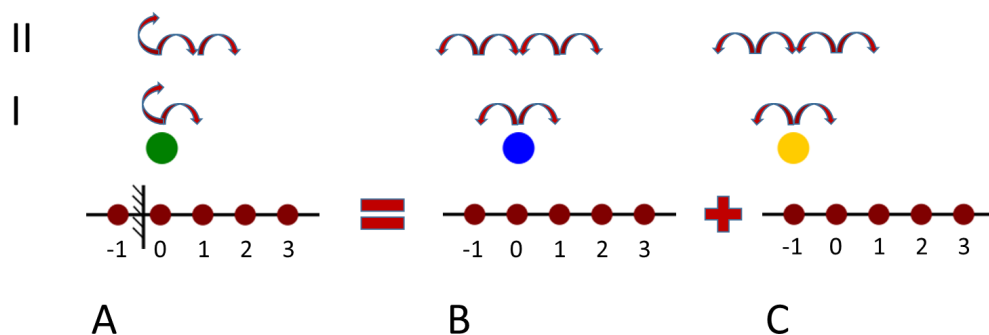
We can compare these results to a study by Belmonte et al. [124] who measured the steady state of pore insertion into supported bilayers. In their framework, the number of inserted pores is 4.10^2 for a working monomer concentration of 10 μg/mL and 4.10^4 for 100 μg/mL. They roughly got the same number of inserted pores for a concentration that is 10 times lower than ours. However, it is difficult to know the membrane size in their system as they constitute the planar bilayer on a hole of 200 μm in diameter. In this geometry, the two monolayers are assembled into a bilayer only at the center of the hole, with some variability in the bilayer area. Apart from this, we do not expect the same affinity constant since they used hemolysin prepared with another protocol (different purifications and buffer).

Belmonte et al. [124] also showed that the number of inserted pores at equilibrium scales to the introduced monomer concentration with a power law of exponent 2.3 although it should vary as c^7 in the short model exposed in Section 2. One explanation we have for this discrepancy is the existence of intermediate monomer assemblies, meaning that all the monomers in the bilayer do not assemble into a fully functional heptameric heptamer.

Membrane protein clustering has been described previously in literature. This clustering can be attributed to a specific biochemical interaction through protein-lipid anchorage, the lipids themselves being clustered in rafts in the membrane [125]. Clustering could also be due to protein-protein interactions only, as in the case of syntaxin 1 clusters that appear to be mediated by electrostatic attraction between the individual proteins [VandenBogaart2011]. Eventually, clustering can occur through modifications of the membrane landscape, these modifications being attributed to the insertion of these proteins. Bruinsma and Pincus dedicated a review [125] to these specific membrane-mediated aggregations. Proteins in this case may aggregate to minimize the resulting mismatch with the membrane thickness [126, 75] or because of the local changes they introduce in the membrane stiffness. Numerical simulations of this membrane mediated clustering have been realized with hemolysin as a model for a β barrel pore. The authors demonstrate such clustering *in silico* but the result of their study shows a linear aggregation (ribbon-like) of β barrel type proteins rather than a 2 dimensional clusterization, in certain membrane types. Altogether, we conclude that our inference of hemolysin aggregation is not in contradiction with previously published articles. We however need a direct experimental evidence for hemolysin aggregation in synthetic membranes that is still missing to the best of our knowledge.

2.3 Edge and Finite Effects

Some of our experimental measurements dealt with lines where the source droplet was at the end of the chain, meaning that the random walk occurred on a semi-finite line. This is a particular case of a network with reflective boundaries. It can be dealt with using either an image method [127] or a method based on the properties of differential equations [128]. These methods are contextualized in [112, 26].



(A) Semi-infinite random walk with a reflective barrier between the sites $x = -1$ and $x = 0$. The first and second steps I) and II) of possible choices for a random walker starting in $x = 0$ at $t = 0$ are represented. This process can be seen as the sum of two random walks on 1D infinite lattices with (B) the walker starting in $x = 0$ at $t = 0$ and (C) the walker starting in $x = -1$ at $t = 0$.

Figure 6.3: Random walk with a reflective boundary.

We developed only the image method that greatly simplifies the calculus. The image method for the reflecting barriers deals with nul current at the reflecting site. In this picture, we considered the superposition of two cases. In the first case, one particle starts at site $x = 0, t = 0$ with the associated probability $P_{\infty,re}$ whereas in the second case the image particle starts at site $x = -1, t = 0$ with the associated probability $P_{\infty,im}$.

With this definition, the reflecting boundary lies between the site 0 and the site -1 and we consider only the semi-infinite space between $x = 0$ and $x \rightarrow \infty$ with $P_R(x, t/x = 0)$ being the probability of finding a walker in x at time t in the reflecting barrier configuration.

$$\begin{aligned} P_R(x, t/x = 0) &= P_{\infty,re}(x, t/x = 0) + P_{\infty,im}(x, t/x = -1) \\ &= P_{\infty,re}(x, t/x = 0) + P_{\infty,im}(x + 1, t/x = 0) \end{aligned} \quad (6.10)$$

We used the propagator computed in the general case (Eq 4.17) and performed a translation to take into account the two possibilities (the source is in $x = -1$ and the source is in $x = 0$).

$$P_R(x = 1, t/x = 0) = e^{-\lambda t} (\mathcal{I}_1(\lambda t) + \mathcal{I}_2(\lambda t)) \quad (6.11)$$

If we perform a Taylor expansion of Eq 6.11, we see that the first term is still $\frac{\lambda t}{2}$. It equals to the first term in the serial development of the unidimensional case (Eq 6.9):

$$P_R(x = 1, t/x = 0) = \frac{1}{2}\lambda t - \frac{3}{8}\lambda^2 t^2 + \frac{3}{16}(\lambda t)^3 - \frac{7}{96}(\lambda t)^4 + o(t^5) \quad (6.12)$$

Because of this similar behavior in the $\frac{t}{\tau} \ll 1$ regime, we analyzed as part of the same batch the experiments where the source droplet is in the middle of a line and the experiments where the source droplet is at the end of the line. We also checked experimentally that we do not see significant differences between both situations. The scaling between τ and the introduced concentration is the same in both situations for the transient regime. It is only the plateau value that differs between the case *one neighbor* and *two neighbours* since its value is determined by the total number n of droplets.

2.4 Long-time behavior

We also looked at the long-time behavior of this pore-limited diffusion in the case of linear arrays of connected droplets. For a standard 1D diffusion process with a walker starting at $t = 0$ in $x = 0$ ($p_d(x, 0) = \delta(x)$), the occupancy probability p_d obeys the following equation:

$$D \frac{\partial^2 p_d}{\partial x^2} = \frac{\partial p_d}{\partial t} \quad (6.13)$$

Solving Eq 6.13 we get $p_d(x, t) = \frac{1}{\sqrt{4\pi Dt}} \exp \frac{-x^2}{4Dt}$. The diffusion coefficient D in this case can be defined from the variance $Var[X] = 2Dt$ with:

$$Var[X] = \int x^2 p_d(x, t) dx - \left(\int x p_d(x, t) dx \right)^2 \quad (6.14)$$

We derive an effective diffusion coefficient D_{CTRW} from the [CTRW](#) [26] using the same definition between D_{CTRW} and the variance:

$$D_{CTRW} = \lim_{t \rightarrow \infty} \frac{\langle X^2 \rangle - \langle X \rangle^2}{2t} \quad (6.15)$$

The [CTRW](#) is called diffusive if this coefficient D_{CTRW} is itself finite and non null. It is the case for the process chosen here because τ and the displacement per step are finite and non null.

We thus compute the first and second moment corresponding to $p(x, t)$, knowing that the moments $\widehat{M}_n(s)$ of order n are conveniently expressed in the Laplace space with the following generic formula:

$$\widehat{M}_n(s) = \int_0^\infty M_n(t) e^{-st} dt = (-i)^n \frac{d^n p(k, s)}{dk^n} \quad (6.16)$$

For an unbiased [CTRW](#), the displacement is favored equally in both directions. The average displacement per step and thus the total average displacement will be null.

Therefore the first moment is null and we only have M_2 to compute [26]. We call σ^2 the mean-squared displacement per step.

$$\widehat{M}_2(s) = \frac{\hat{\psi}(s)}{s(1 - \hat{\psi}(s))} \sigma^2 = \frac{\lambda \sigma^2}{s^2} \quad (6.17)$$

The inverse Laplace transform of $\frac{\widehat{M}_2(s)}{2t}$ gives the same result than for the traditional discrete random walk on a one-dimensional lattice:

$$D_{CTRW} = \frac{\lambda \sigma^2}{2} = \frac{\sigma^2}{2\tau} = \frac{2R^2}{\tau} \quad (6.18)$$

We expect D_{CTRW} to scale as \sqrt{N} , N being the number of pores inserted in the bilayer. This scaling is different from what to expect in a classical permeability model where the permeability is proportional to the number of pores in the membrane, similar to the membrane-transport expression proposed in [21].

The effective diffusion coefficient for a typical $\tau \simeq 10$ h yields:

$$D_{CTRW} = 5.10^{-13} \text{ m}^2/\text{s} \quad (6.19)$$

This effective diffusion coefficient is three orders of magnitude smaller than the bulk diffusion of carboxyfluorescein in water, $D \simeq 4.10^{-10} \text{ m}^2/\text{s}$.

3 IMPROVING THE TRANSPORT KINETICS

As we have seen in this part, the number and spatial arrangement of pores in the bilayers significantly change the transport kinetics. Our experiment has still a long duration compared to the shortest [FPT](#) we found. This prevents us from monitoring transport kinetics on a large range of connected droplets. Therefore another parameter that we wish to investigate later is the role of the probe size in the transport kinetics. A smaller probe would indeed have a higher bulk diffusion coefficient D . We also expect that the effective pore size a seen by this probe would be larger. We would then be diminishing the [FPT](#) $\langle T \rangle = \frac{2\pi R^3}{3Da}$ by increasing both D and a . To support this, we found in [21] that the use of arabinose - a smaller molecule than carboxyfluorescein - as probe in linear arrays of DIBs resulted in an experimental timescale $\Delta t \leq 1$ h to monitor diffusion along several droplets.

As immediate prospect, we thus have the project to use calcium imaging in larger arrays. The bulk diffusion coefficient of calcium in water is $D \simeq 10^{-9} \text{m}^2 \cdot \text{s}$ [129]. This would enable us to study the signal transport to the second neighbor and further away from the source. and would improve the comparison of experimental data to the CTRW modeling that we did.

Now that we have precisely quantified the dynamics of transport in one-dimensional bilayer arrays, we will develop some considerations on 2D networks.

ENGINEERING 2D NETWORKS

In this part, we start by showing how we can extend the 1D CTRW formalism to the 2D network case. We present our first attempts to produce experimentally compact 2D droplet networks in which we probe the 2D diffusion transport process of carboxyfluorescein from a centered source droplet. On the few available data we managed to acquire, we measured the occupancy probabilities for the first and second droplet neighbors but did not provide any direct comparison between the theory and the data.

1 THEORETICAL MODELING

We will treat here two cases of regular 2D lattices, the square lattice and the triangular lattice which are represented in Fig 7.1. Both square and triangular lattices have neighbors separated by bonds of identical lengths. In the square lattice case, a walker that starts at the source position goes to one of the first neighbors then in the second step can go towards the second neighbor or back to the source. But it cannot reach another first neighbor directly. We will see that the occupancy probability for the first neighbor easily factorizes for the square lattice and takes the same allure than in the 1D case. It is not the case for the triangular lattice where first neighbors are interconnected. In that case we did not manage to find an analytical solution for the occupancy probability.

1.1 Square lattice

In the square configuration (Fig 7.1 A), the lattice can be described by two vectors \mathbf{k}_1 and \mathbf{k}_2 and the corresponding structure function is [26]:

$$\Lambda(\mathbf{k}) = \lambda(k_1, k_2) = \frac{1}{2} \{ \cos k_1 + \cos k_2 \} \quad (7.1)$$

$$p(\mathbf{r}, t) = \frac{1}{4\pi^2} \int_0^\infty \int \int \frac{\exp(-i\mathbf{k}\mathbf{r}) d\mathbf{k}}{\lambda \{ 1 - \frac{\cos k_1 + \cos k_2}{2} \} + s} e^{-st} ds \quad (7.2)$$

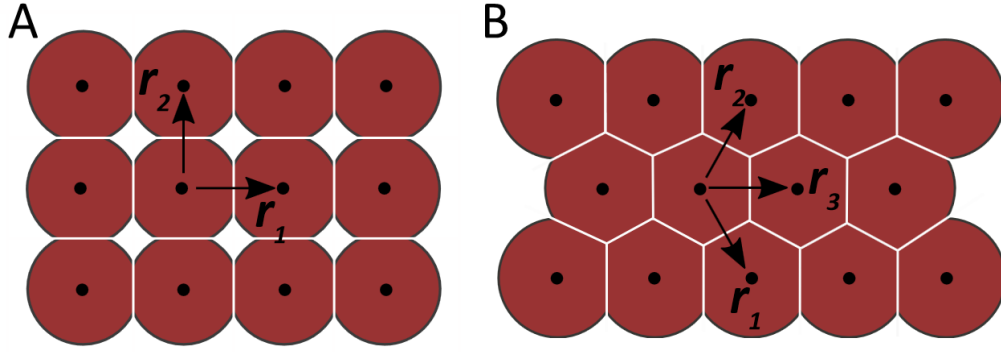
Let us choose one of the possible sites for the first neighbor, $\mathbf{r}_1 = \begin{bmatrix} 1 \\ 0 \end{bmatrix}$

$$p(\mathbf{r}_1, t) = e^{-\lambda t} \mathcal{I}_1\left(\frac{\lambda t}{2}\right) \mathcal{I}_0\left(\frac{\lambda t}{2}\right) \quad (7.3)$$

This function can be expanded using Mathematica, in a similar way than for the 1D case and yields:

$$\frac{\lambda t}{4} - \frac{(\lambda t)^2}{4} + \frac{19(\lambda t)^3}{128} - \frac{25(\lambda t)^4}{384} + o(t^5) \quad (7.4)$$

We see that the linear regime is twice slower compared to the 1D case. This is due to the fact that the 2D aspect of the network "dilutes" isotropically the random walker compared to the 1D case.



(A) Square lattice described with vectors r_1 and r_2 . (B) Triangular lattice fully described by the translation of 3 vectors r_1 , r_2 and r_3 .

Figure 7.1: Examples of lattices

1.2 Triangular lattice

For a hexagonal packing of the droplets, the centers of the droplets form a dual lattice which is triangular (Fig 7.1 B). This lattice is well represented by a set of 3 vectors that are not linearly independent, k_1 , k_2 and k_3 . The structure function for this lattice is :

$$\Lambda(\mathbf{k}) = \frac{1}{3} \{ \cos k_1 + \cos k_2 + \cos(k_1 + k_2) \} \quad (7.5)$$

With this description, the corresponding probability is:

$$p(\mathbf{r}, t) = \frac{1}{4\pi^2} \int_0^\infty \int \int \frac{\exp(-i\mathbf{k}\mathbf{r}) d\mathbf{k}}{\lambda \left\{ 1 - \frac{\cos k_1 + \cos k_2 + \cos(k_1 + k_2)}{3} \right\} + s} e^{-st} ds \quad (7.6)$$

We have not found an analytical solving of this equation but a numerical integration remains possible.

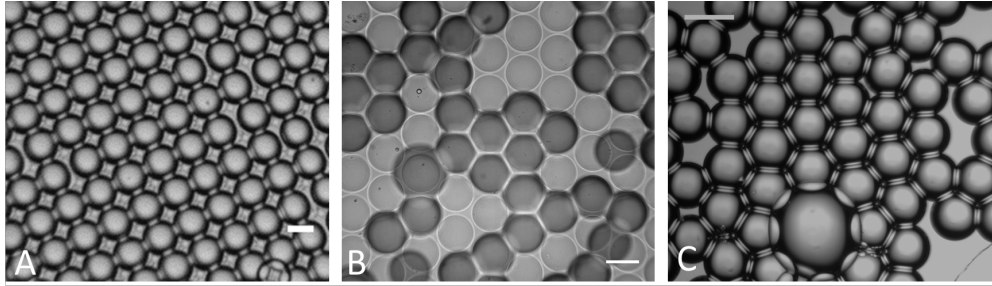
2 2D COMPACT NETWORKS

2.1 Experimental networks

We picked two ways of arranging droplets in a 2D configuration. In the first one, we forced the coordination of the droplets by milling places where to put the droplets (Fig 7.2 A and B). In the second one, we let the droplets adhere freely to constitute compact networks.

1. In the first configuration we implemented square and triangular lattices. It required to have a good control on the size of the droplet to be able to adjust it in the milled hole. When sedimenting, droplets could deviate from the initial projection of their detachment coordinates. This limited the precision of the technique and introduced holes (Fig 7.2 B) or 3D packing in the resulting networks.

The patterned substrate was easier to fill with a square lattice (Fig 7.2). The degree of compaction being less important in the square configuration, post-layering adjustments were still possible. In the hexagonal configuration,



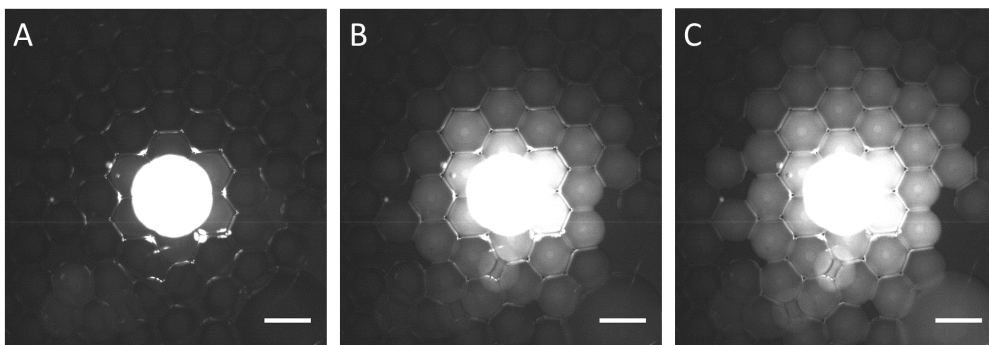
Different experimental ways of arranging Droplet Interface Bilayers in 2D arrays. A) Square lattice pre-patterned on PMMA plate. B) Hexagonal and loose packing pre-patterned on PMMA plate. C) Free hexagonal packing on the bottom of a 96 wells plate. All scale bars are 400 μm long.

Figure 7.2: Experimental 2D compaction

droplet assemblies were difficult to constrain on patterns, probably because their assemblies were a lot more cohesive.

2. In the second configuration we decided to rather let the droplets adhere freely on smooth surfaces such as the bottom of multiwell plates (Fig 7.2 C). In this configuration, we could get small portions of networks that were fully compact (hexagonal packing) but with some 3D packing. For this reason we could not straightforwardly apply the theoretical modeling to the performed experiments. However, we will show quickly how we can extract diffusion data in this geometry.

We chose this second option - free hexagonal packing without a patterned substrate. In this configuration, we layered aqueous droplets containing hemolysin at a concentration of 100 $\mu\text{g}/\text{mL}$ in the usual buffer. In Fig 7.3, we show several timepoints of a 2D experiment. The source droplet is at the center and diffuses on a large scale - compared to the 1D data - over 24 hours of experiment. We performed segmentation on this network in order to compute the same occupancy probabilities than in the one-dimensional case.



Carboxyfluorescein diffusion over 24 hours of experiments in a 2D network of DIBs. Rearrangements of the droplets during the first hours set the initial time for acquisition. This instant corresponds to the disappearance of any spontaneous motion due to these rearrangements. In the case of this particular experiment it corresponds to $t = 5$ hours after the network is layered. (A) $t = 5$ h the source droplet has already started to empty its content in its neighbors (B) $t = 15$ h the signal has already reached the second and the third neighbors (C) $t = 24$ hrs, we see that the signal continues to propagate in the network. Scale bars are 400 μm long.

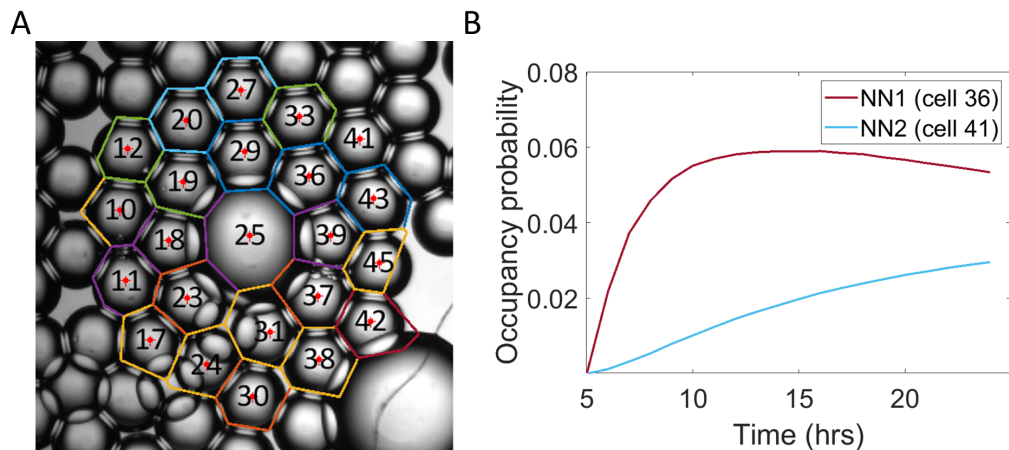
Figure 7.3: Diffusion in 2D networks of DIBs.

2.2 Voronoi segmentation

Segmentation is traditionally used to detect bounded objects in images. In the case of cellular tissues, a particular type of segmentation called Voronoi tessellation can be implemented and we inspired from this approach. Voronoi tessellation performs a paving of the space using polygonal jointed shapes. It can be used in image analysis but also in quantitative modeling and belongs to the vertex model class [130, 131, 132]. We used this tessellation because binarization alone gave poor results in area distributions due to thick boundaries between the droplets.

After filtering and binarization of the images we detected the inside of the droplets using the function `regionprops`. We applied the function `powerDiagramWrapper` on the droplet centers returned by `regionprops`. This function performs a weighted Voronoi tessellation, also known as Generalized Voronoi Tessellation, k-Order Voronoi or Power Diagram. In our case the weights we provided were the droplet radii.

We could build the polygon corresponding to each cell from the result of the algorithm. In Fig 7.4 A we show an example of a Power Diagram tessellation performed on a DIB array. This particular type of tessellation takes into account the size differences between some droplets to increase the robustness of the segmentation to the presence of holes. We displayed on purpose the indices of each cell on the tessellation. We compared the size distribution from the rough binary detection `regionprops` to the size distribution of the Power Diagram tessellation. From the binarization we got a mean radius of the detected areas $\bar{r} = 103 \pm 18 \mu\text{m}$. This is due to the black thickness of the droplet contours that results in an average area smaller than the real one. By contrast, when we computed the radius of each Voronoi polygon through the approached formula $\bar{r} = \sqrt{A_{poly}/3.14}$, the mean radius was $213 \pm 57 \mu\text{m}$.



(A) Voronoi tessellation for the first and second neighbors, the source droplet is at the center (label 25). (B) Occupancy probabilities for two droplets, a first neighbor (label 36) and a second neighbor (label 21). Fitting of the linear transient regimes yield a slope of $15 \cdot 10^{-3} \text{ h}^{-1}$ for the first neighbor and a slope of $1,6 \cdot 10^{-3} \text{ h}^{-1}$ for the second neighbor.

Figure 7.4: Power Diagram results.

To compute the intensity in each cell, we defined a shrunked polygon to exclude the borders of the voronoi cell. This polygon is $1/3$ smaller than the original Voronoi cell.

3 2D DIFFUSION AT A GLANCE

Figure 7.4 B shows the occupancy probabilities computed with the formula Equation 5.1, for two examples taken from the first and second neighbors. We indicate the corresponding labels in order to refer to Fig 7.4 A for the particular position of the corresponding droplets. We observed heterogeneity in the slopes of the transient regime of the first neighbor pool.

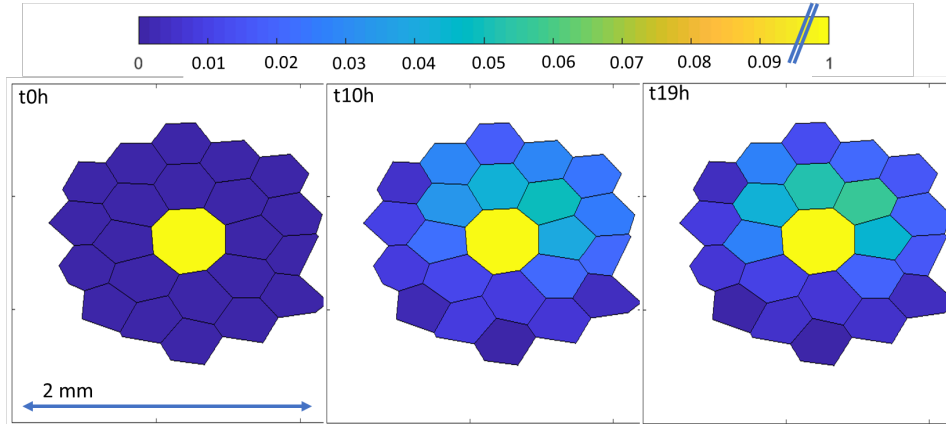


Figure 7.5: Occupancy probability map on Power Diagram Cells

To ease the representation and display the anisotropy of the system, we report the occupancy probability color-coded on the detected Voronoi polygons Fig 7.5. The presence of 3D packing is likely one of the main reasons for the heterogeneity in signal.

We noticed that transport seemed to happen faster than in the 1D configuration with a similar concentration of introduced monomers. Indeed, if we refer to Fig 6.2 B we expect at $c = 100 \mu\text{g}/\text{mL}$ to have $\lambda \simeq 10^{-3} \text{ h}^{-1}$. From the plot Fig 7.4 we have instead $\lambda \simeq 10^{-2} \text{ h}^{-1}$. This gap between the values in the 1D case versus 2D is most likely due to the difference in adhesive areas. In the former one-dimensional case, by constraining the droplets in 1D in their grooves, we had smaller contact areas than what we got in the 2D configuration, where adhesive area is probably as its maximum since position is not constrained.

4 PARTIAL CONCLUSION

Through this second part, we have shown how droplets can be assembled in functional networks. Arrays of droplet interface bilayers are not new in the literature, but until now they seemed to be used only as engineering proofs of compartmentalization at the micrometer scale.

We wanted to prove that a quantitative assessment of communication in these networks is possible. Instead of directly measuring an effective diffusion coefficient at the porous network scale, we focused on the timescale driving the passage of the probe from one droplet to another one. This timescale is linked to the spatial arrangement of the pores in the bilayer in the FPT formalism. We hence linked the diffusion kinetics to the introduced pore concentration and further inferred that the pores are likely to be clustered in the membrane.

In these systems, the inserted pores are inert. Diffusion is thus analog to what we would expect in a conventional porous medium. In biological systems molecular

transport can be affected by mechanical constraints. In particular, mechanotransduction in morphogenesis motivated us to implement a mechanically tunable diffusion in our 2D arrays of bilayers. To do this, we aimed at changing the nature of the incorporated membrane protein by replacing the hemolysin pore with a mechanosensitive one, that we chose to be MscL. This hydrophobic protein can not be incorporated directly in the aqueous buffer and has to be produced in the immediate bilayer vicinity.

In the following part, I will thus discuss how we implemented a cell-free reaction in bilayer arrays to fulfill this purpose.

Part III

IN SITU SYNTHESIS OF A TRANSMEMBRANE PROTEIN THROUGH DNA PROGRAMMING

In this last part we aim at producing mechanosensitive transmembrane pores with cell-free reactions directly in the connected droplets so as to insert them in the bilayers. [Chapter 8](#) presents the development of these systems in the synthetic biology community. We then describe in [Chapter 9](#) how to assemble a cell-free reaction to produce proteins. As cell-free reactions can quickly destabilize DIBs, we show in [Chapter 10](#) how we managed to adapt this new system to the DIB environment by playing on the solvent composition, reaction dilution and size of the produced droplets. We furthermore demonstrate the insertion and functionality of cell-free synthesized hemolysin in this way in [Chapter 11](#).

CELL-FREE EXPRESSION SYSTEMS TO PRODUCE PROTEINS IN SITU

1 CELL-FREE SYSTEMS - STATE OF THE ART

In 1961, Nirenberg and Matthaei produced the first account of cell-free protein production [133]. Cell-free protein synthesis hijacks the transcription/translation machinery of a host organism to synthesize directly in a test tube the protein of interest [29]. Compared to the traditional recombinant synthesis in bacteria (Fig 8.1), cell-free synthesis decouples the bacterial life cycle from the protein synthesis itself by storing purified bacterial extract prior to protein expression. This biotechnological tool enables parallel and reproducible screening experiments on a relatively short amount of time to investigate protein function and genetic regulation. It also conveys more reproducible results. It has even been used recently to prototype CRISPR reactions in a test tube [134].

In the early versions of cell-free production, ribosomes were extracted and purified from cultured bacteria, then supplemented with a solution of RNA templates and amino acids to assemble short polypeptide sequences. Shortly after, researchers started to couple transcription¹ and translation systems² [135] to avoid the introduction of synthetic mRNA, while improving the recycling of reagents to fuel the reaction for longer times [136]. These pioneers paved the way for two distinct approaches co-existing today in cell-free modern production:

- A bottom-up approach symbolized by the PURE system in which all constituents are separately extracted, purified and reassembled to form the reaction [30]
- A top-down approach where crude bacterial extracts are partially purified and combined with exogenous DNA, amino acids, nucleotides and regeneration systems [31, 32]. Cellular extracts of an increasing number of hosts organisms - including vertebrates - are now commonly available.

Cell-free systems are used today to produce several types of proteins. They revealed to be particularly useful in the synthesis of transmembrane proteins, in micellar systems and in model bilayer environments [33].

2 MEMBRANE PROTEIN INSERTION

Membrane proteins are low-solubility giant molecules that need to fold properly in mixed environments to be functional. They have typically hydrophilic domains spanning aqueous compartments on both parts of the membrane, and hydrophobic domains inside the bilayer. Membrane proteins are often multimeric and a

¹ Transcription is the first step of the central dogma where DNA is translated into messenger RNA (mRNA) by the RNA polymerases. This stage requires ribonucleotides as building blocks for RNAs.

² Translation is the second step of the central dogma where ribosomes decipher the genetic code and assemble amino acids into a primary protein structure, which sequence is encoded by mRNA which is itself a footprint of DNA.

requirement for pore functionality is the assembly of monomers. If α HL presents the advantage of being water-soluble in its monomeric form, it is not the case for a lot of transmembrane proteins. Instead of being added straightly to the aqueous buffer, hydrophobic channels have to be first reconstituted in mixed environments. Solubilization and reconstitution of membrane proteins have been obtained using detergent micelles, small and large unilamellar vesicles as well as, more recently, nanodiscs [137, 76, 138]. These last structures were developed to solubilize individual membrane proteins. They consist in a nanometric bilayer inserted on a scaffold. Cell-free systems offer a convenient platform for direct *in situ* synthesis of these proteins that can otherwise be hard to purify and reconstitute prior to their use.

Our long-term goal - clearly beyond the scope of this thesis work - is to study mechanically tuned molecular transport in a biomimetic model of a morphogenetic process. For this, we need to insert mechanosensitive pores in the bilayer networks. A good candidate for the mechanosensitive model pore is Mechanosensitive Channel of Large Conductance (MscL), a hydrophobic transmembrane pentamer channel used by the bacterium *E. coli* to regulate its osmotic pressure [139, 140]. Communication between connected droplets in DIBs array would then occur through MscL channels upon precise delivery of a mechanical stimulus. Since the five identical monomers of MscL are not soluble in water, we seek to implement monomer synthesis directly in the DIB networks previously developed. *In situ* synthesis of MscL in the immediate vicinity of the membrane would provide the proper environment for protein folding [34]. This solution brings cell-free synthesis into the game and has been demonstrated for MscL in the liposome model membrane case [35]. Liposomes thus provide the bilayer environment necessary for the insertion of these transmembrane proteins. Giant Unilamellar Vesicles (GUVs) in particular can be prepared with an emulsion transfer technique, published by Pautot et al. [37], then adapted to cell-free systems encapsulation by Noireaux and Libchaber [38]. GUVs are giant liposomes with a diameter larger than the micron and comparable in dimensions to living cells [36]. In the liposome configuration, the insertion of membrane proteins inside the bilayer is supposed to happen simultaneously with the cell-free production [141, 142, 143]. Interestingly enough, the first time hemolysin was expressed in cell-free encapsulated liposomes, it was for the purpose of allowing fluxes through the membrane. The energetic supplies in the external medium continuously fuel the inside compartment of the liposome while byproducts of the reaction can be evacuated in the surrounding. This compartment-mediated effect provisions the reaction and was witnessed even when hemolysin was not supplied. Indeed, in liposomes where the protein eGFP was expressed without added hemolysin, the yield was higher than in bulk reactions expressing eGFP, presumably because of small osmotic imbalances that permeated the bilayer [38]. It means that the liposome is not only a good proxy for the cell membrane. It is also a compartmentalization tool that increases the efficiency of cell-free reactions. This type of chemical reaction can be sustained longer if dissipation of byproducts in the external medium is allowed [59].

Droplet interface bilayers typically delimit larger compartments than in the liposome case. Originally, membrane proteins were expressed through IVTT systems and then partially purified and reconstituted in proteoliposomes before being inserted in droplet interface bilayers [39]. A similar approach followed later by Findlay et al. [42] was to pre-incubate the cell-free reaction (PURE system) with liposomes at optimal expressing temperature, 37 °C, then lower the temperature around 25 °C to produce the emulsion. The membrane proteins in this configuration

were pre-solubilized inside liposomes. Researchers then developed *in situ* expression by encapsulating the cell-free systems in emulsions and allowing the expression to occur *after* the bilayer constitution. Bayley and Holden published in 2008 a study where they produced hemolysin with two cell-free systems (either PURE or Promega IVTT systems), and immediately formed the droplets containing a mixture of liposomes, DNA template and cell-free reaction [45]. Liposome addition was presented as both a way to solubilize membrane proteins prior to DIB insertion, as well as a way to stabilize DIBs by introducing phospholipids in the aqueous buffer. IVTT production after emulsification is reported in [43], where the solvent has been optimized to increase the bilayer stability. The authors studied protein expression until 5 hours, for α HL monomers and a highly hydrophobic transporter, EmrE. Other recent direct *in situ* synthesis of hemolysin using IVTT has been reported in [40, 41, 42], as well as in [21], involving PURE-derived systems or cell extracts. Several achievements regarding cell-free expression in droplet interface bilayers are summarized by Ces in [34].

A considerable part of these cell-free expression studies deal with ion channel production and insertion. Following the channel insertion, characterization of the transmembrane protein activity is traditionally achieved through optical and electrophysiological measurements.

3 CHARACTERIZATION OF THE PRODUCTION DYNAMICS

Recent years have witnessed the development of fast-imaging optical probes to investigate the dynamics of neuronal networks, with high spatial resolution as their prime feature. On the other side, electrophysiology remains a powerful tool to investigate single pore insertion and functionality because of its temporal resolution (up to the megahertz) and sensitivity. Electrophysiological measurements can indeed detect membrane potential variations from 10^{-6} to 10^{-1} V [46].

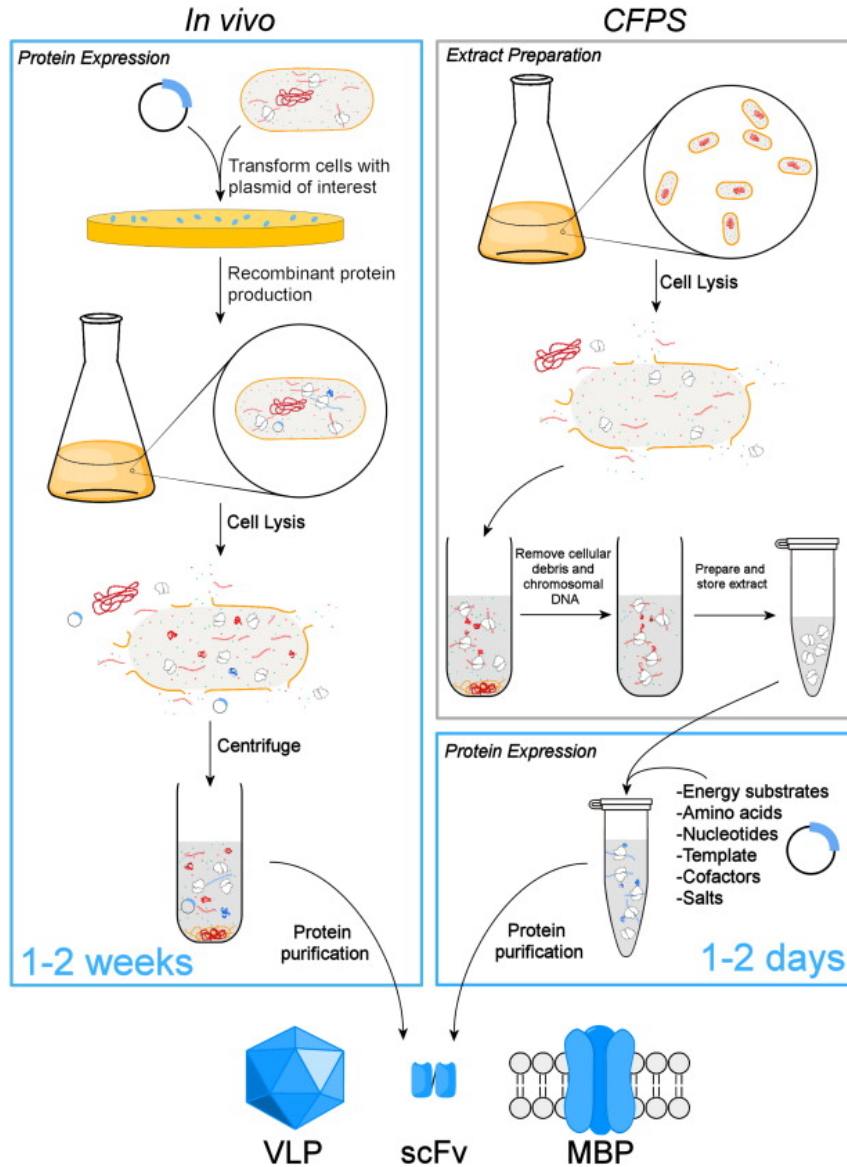
Planar lipid bilayers were developed as a prime tool to measure currents through single ion channels [47]. In a bottom-up approach, they provide a simplified environment devoid of other proteic interferences in which to add purified transmembrane proteins. In this environment, it is possible to lead single channel mechanistic studies where the response of the protein can directly be attributed to a precisely delivered stimulus. In this framework, biological membranes are usually represented by an equivalent electronic circuit with a resistance R and a capacitance C in parallel [48]. Some electrical considerations on pure bilayer electrical properties can be understood from *Membranes by the Numbers* [144]. A biological membrane should show a behavior similar to the planar capacitance model where an insulator medium between two conductive plates can maintain electrical charges separated. Charges from the polar heads of the lipids are maintained on both sides of the bilayer (spatial segregation) as long as the bilayer remains intact. In the planar capacitance model, the capacitance C is simply defined as:

$$C = \epsilon_r \epsilon_0 \frac{A}{d} \quad (8.1)$$

Where ϵ_r is the relative dielectric constant of the insulator medium, ϵ_0 the absolute permittivity, A the area of the facing plates and d the distance between these two plates. Taking $\epsilon_r = 2$ for the hydrophobic bilayer and 5 nm for the bilayer thickness [144], we can estimate the surface capacitance of the pure bilayer as

$C = 0.4 \mu\text{F}/\text{cm}^2$. This value can be compared with experimental measurements on cell membranes, $C_{exp} \simeq 1 \mu\text{F}/\text{cm}^2$. In the general case, membranes are simply described as the association of a capacitance and a resistance in parallel, to account for the membrane permeability to certain solutes. Some non-linearities in the electrical response of biological membranes can appear and call for more elaborated electrical models [145] but we will stick to the simpler model of a capacitance/resistance association. The resistance of the pure bilayer has been estimated by Montal and Mueller [49] between 10^6 and $10^8 \Omega/\text{cm}^2$. These membranes were originally made from a mix of glyceroldioleate/cholesterol/oleoyl. The authors noticed that introduction of Gramicidin at a concentration of $0.1 \mu\text{M}$ lowered the resistance to $10^3 \Omega/\text{cm}^2$. Gramicidin is indeed a transmembrane pore which increases the permeability of the bilayer to ion currents.

We will use single channel insertion events to characterize the insertion of the cell-free synthesized hemolysin. Electrophysiological characterization of spontaneous insertion of hemolysin in a Droplet Interface Bilayer has already been demonstrated by Wallace, Bayley and coworkers, for instance in [5]. Hemolysin conductance is asymmetric. Gu and Bayley measured its effective conductance with an applied transmembrane voltage 40 mV to be $720 \pm 6 \text{ pS}$ ($\text{pH } 7.5$ and $[\text{KCl}] = 1 \text{ M}$). At -40 mV , this conductance is $651 \pm 4 \text{ pS}$, hence approximately 90% of the opposite conductance [50]. Auvray et al. [51] gave new conductance measurements for hemolysin. Under an applied voltage of $\pm 100 \text{ mV}$ and a salt concentration $[\text{KCl}] = 1 \text{ M}$, they measured a conductance $G = 1,09 \pm 0,04 \cdot 10^{-9} \text{ S} = 1090 \pm 40 \text{ pS}$ and in the reversed state $G = 720 \pm 61 \text{ pS}$. The detergent used to solubilize the protein induces some noise on the baseline of the recorded signal. If it is highly concentrated, it can also induce channel-like events. We assume that differences between 1) signal-to-noise ratio in separate experiments 2) the detergents used to extract and purify hemolysin 3) external composition of the aqueous buffer (salts) can induce discrepancies between the conductances measured between different experiments. We will use the values published in [51] as references to compare the conductance we measure in the case of the cell-free synthesized hemolysin. Prior to presenting the results of our actual experiments performed with cell-free reactions in DIBs, we start by explaining in the following chapter how to compose a reaction that synthesizes hemolysin.



(Left) Traditional recombinant synthesis of proteins in bacteria. The genetic construct encoding for the protein of interest is transfected into the host bacteria. After their selection, successfully transfected bacteria are cultivated to amplify the number of produced proteins. Bacteria are lysed and the protein is extracted after several cycles of concentration and purification. This technique takes usually between 1 and 2 weeks. (Right) Cell-Free Protein Synthesis (CFPS) takes on the contrary between 1 and 2 days. Extract from bacteria is separately prepared and stored after removal of cellular debris and chromosomal DNA. This preparation can then be readily supplemented by the DNA template for the protein of interest and a mixture of necessary constituents (energy substrate, amino acids, nucleotides, cofactors and salts). The protein is synthesized by the mixture in less than a day and has to be purified. In vivo synthesis and CFPS have been used to successfully prepare viral proteins (VLP), antibody fragments (scFv) and membrane bound proteins (MBP). Reprinted from [29] with permission from Elsevier

Figure 8.1: Comparison between cell-free protein synthesis and traditional recombinant synthesis.

TXTL COMPOSITION AND FABRICATION

1 CELL-FREE REACTION

We use a TXTL¹ protein expression system developed by the Noireaux Lab (University of Minnesota, Minneapolis, USA). What we call TXTL in the remaining chapters of this thesis therefore means the particular *cell-free* protein expression system developed by Noireaux and collaborators. This *E. coli* based system underwent several steps of optimization [52, 53, 32]. The reaction mix can be decomposed into three main components: the cellular extract itself, the amino acid mix and the energy mix. All three ingredients have been provided to us by the Noireaux lab².

1. The extract is the part of the TXTL reaction that provides all the necessary machinery for the protein production, including the RNA polymerase assembling mRNAs from the DNA template and the ribosomes knotting amino acids into proteins according to the mRNA sequence. The lysate from bacterial cultures is dialysed to remove undesired components such as endogenous DNA, ions from cell medium and degradation products. It is flash frozen and kept at -80 °C. This extract constitutes roughly one third of the total reaction volume. The average protein concentration in it is 10 times smaller than the average protein concentration in bacteria - 200 mg/mL [146]. It makes the speed of translation in TXTL slightly under 4 amino acids per second [147], whereas the *in vivo* rate is approximately 10 aminoacids per second [148]. As a comparison, the rate of elongation in the PURE system has been quantified around 0.5 amino acids per second.
2. The amino acid mix contains the 20 canonical amino acids at 17 mM to give a final concentration of 3 mM for each amino acid in the total cell-free reaction.
3. The last part of the reaction is the energy buffer 3-phosphoglycerate (3PGA). Its exact composition can be found in [Table C.1](#). Apart from containing the ribonucleotides necessary to fuel the reaction, the energy mix includes several metabolites and enzymes important in ATP regeneration, the main one being 3PGA, 3-phosphoglycerate [54].

To these three essential reaction parts (cellular extract/amino acid mix/energy buffer), we add ourselves modular components that allow us to tune the reaction yield to the amount of proteins we desire. These additional components are salts: Magnesium Glutamate (MgGlu) and Potassium Glutamate (KGlu) to the final concentration of respectively 5 mM and 90 mM. Magnesium is essential for ribosome optimal physiology [149, 150] and Potassium tunes the ionic strength of the solution. We also add Maltodextrin (a carbon source) to a final concentration of 30 mM and eventually the plasmid template encoding the protein sequence. We add as well some Polyethylene Glycol (PEG 8000 - final concentration 4,5% w/v) to increase the molecular crowding in the reaction.

¹ abbreviation for Transcription-Translation.

² I spent a total of 5 weeks in the Noireaux lab to learn the basis of TXTL assembly and characterization.

To sum up the assembly, we show in Table 9.1 the relative volumetric proportions of the different compounds. We prepare stocks solutions of KGlu, MgGlu, Maltodextrin and PEG as well as of plasmid templates. We complement with these the cellular extract, the energy buffer and the amino acid mix that are provided to prepare a reaction of 90 μ L.

NAME	v (μ L)	C_f (mM)
Cellular extract	28	
KGlu	2,7	0,09
MgGlu	2,5	0,005
Maltodextrine	5,4	0,03
3PGA	5	0,005
AA	15,9	0,003
PEG	5,6	2,5
P7oas28	1,8	0,2
P28adeGFP	9	5
Water	14,1	

Table 9.1: Reaction assembly, 90 μ L final volume, no dilution

2 PLASMID TEMPLATES

Plasmid DNA is a circular double-stranded construct of DNA. This relatively small piece of genetic information (10^3 to 10^6 base pairs) is physically separated from the bacterial genome and independently replicated by the host. Plasmids have been optimized to be easily inserted in bacteria, replicated and extracted. They are made of several functional blocks besides the protein encoding sequence itself. There is an origin of replication (ORI), essential to maintain and replicate the plasmid within the host. The promoter region defines the strength of the transcription. An antibiotic resistance gene is added to select bacteria that have successfully integrated the plasmid. There are also several Untranslated Regions (UTR). We show a schematic map of a plasmid construct with these different areas in Fig 9.1 A. To use DNA templates in a cell-free reaction, we need to prepare these plasmids according to a cycle of transformation/amplification/extraction. The purified plasmids can then be added to the remaining TXTL reaction to produce the desired protein.

1. Plasmids are inserted into bacterial hosts according to a process called *transformation*. Every transformed bacterium can contain from a few plasmid copies (low-copy number plasmid) up to several hundred plasmid copies (high-copy number)³. We use calcium chloride transformation to permeate bacteria to the plasmids.

³ In the plasmids that we use for TXTL expression, ColE1 is a high copy plasmid and p15A a low copy plasmid.

2. Once the host has integrated the plasmid, the second step - amplification - can be performed. ⁴ In this process, host bacteria replicate many times in a culture volume and increase *de facto* the plasmid concentration in the culture volume.
3. The plasmid is eventually extracted and purified from the bacterial culture with a miniprep culture or a midiprep culture ⁵.

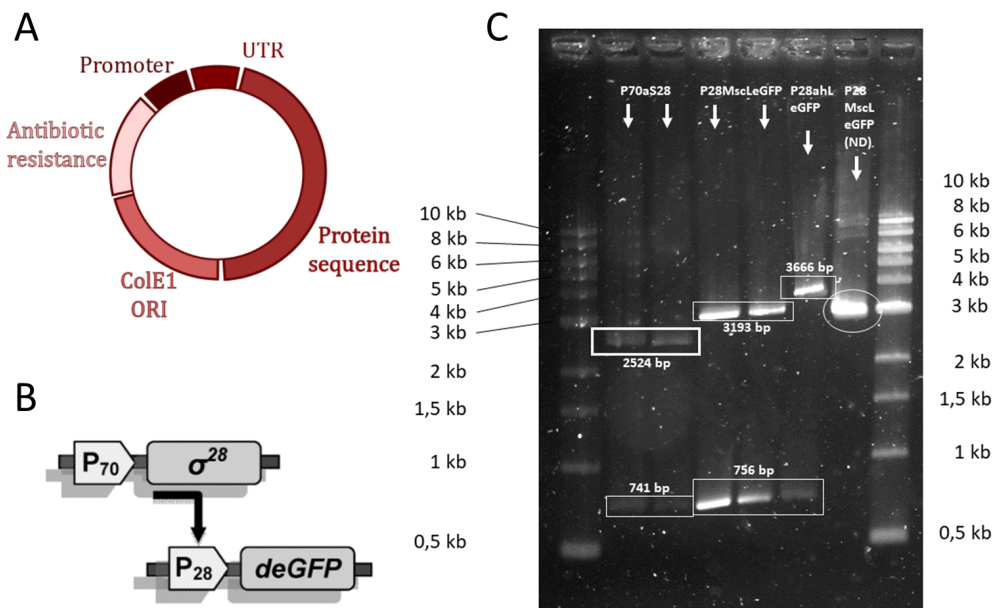
The different plasmids we have used are listed in [Table C.2](#). Plasmid constructions are generally designed to ensure that standard transformation and amplification techniques can be used [151]. Furthermore, the particular constructs that we use have been optimized for specific TXTL expression and are provided by the Noireaux Lab. I explain below the overall strategy used to design the right plasmid for the proper reporter protein. In *E. coli*, the core RNA polymerase binds to specific promoters via a set of transcription factors known as *sigma factors*. Sigma factors together with the core RNA polymerase constitute a holoenzyme, the fully efficient RNA polymerase. To design the plasmid construct, several choices of promoter can be made. These choices change the nature of the binding sigma factor. A standard procedure in molecular biology consists in placing the coding sequence under the control of P70, a native promoter that will be recognized by σ_{70} , the "housekeeping sigma factor" [152]. Most of the genes that need basal transcription in usual metabolic conditions are placed under the control of this promoter P70. With a genetic construct involving P70, the transcription machinery present in the cell extract synthesizes the messenger RNA of the gene of interest in normal growth conditions. Problems can occur when considering that the plasmid has to be amplified *in vivo* before being put in cell-free reactions. During amplification, *E. coli* bacteria not only replicate the plasmid, they also transcribe it. If the transcription of the gene of interest is not repressed or inactive, copies of the protein of interest with associated toxicity issues are found in these bacterial colonies. It is a minor problem if the protein expressed is small enough and non toxic for the host organism. This is the case for fluorescent reporters such as eGFP or mRuby. On the contrary, transmembrane pores can easily be toxic for their hosts when produced in high quantities. Hemolysin and MscL typically fall into these categories. It is therefore necessary to clone the plasmids coding for transmembrane pores under a promoter which is usually inactive in ideal growth conditions, such as P28, the promoter for σ_{28} , or a viral promoter such as the one recognized by the T7RNA polymerase. The expression of α HL or MscL in cell-free reactions then requires two steps: a first step in which the exogenous transcription factor, σ_{28} or T7RNAP, is produced through a P70 promoter, and a second step where the transmembrane protein itself is expressed under the control of the promoter P28 or T7RNAP (Fig 9.1 B). In some cases, it is not possible to use this approach to clone toxic proteins, such as MscL mutants that are open all the time and therefore deadly for the bacteria. In these particular cases, linear DNA can be used as a template. It is amplified through the Polymerase Chain Reactions (PCR) and not in bacteria as we did with plasmids. The use of two or more sequential constructs - P70S28 followed by the plasmid

⁴ At this stage, it is possible to keep transformed colonies (several weeks on a plate at -4°C or several months in a glycerol stock) to avoid performing transformation every time more plasmid stock solution is needed.

⁵ Miniprep cultures are adapted to high copy number plasmids and deliver from 10mL of culture typically 50 μL of DNA plasmid concentrated around 100 $\mu\text{g}/\text{mL}$. Midiprep yield from 50mL culture DNA from 100 to 300 $\mu\text{g}/\text{mL}$.

encoding the protein under the control of P28 - is called a transcriptional activation cascade. Fig 9.1 B we show the sketch of a typical cascade for eGFP production.

After amplification, plasmids are characterized using a double digestion and a migration on agarose gel (Fig 9.1 C). We used ApE software⁶ to determine double digestion sites in the plasmid construct. In the example we show Fig 9.1 C, we identify the plasmid P70S28 which shows a stripe at 2524 bp and another one at 741 bp. This is the result of a double digestion by the restriction enzymes BamH1 and Xho1 (two restriction sites). P28MscLeGFP shows two stripes at 3193 bp and 756 bp after a digestion by Xho1. P28aHLeGFP shows a similar pattern after a Xho1-digestion, except that the fragment at 3193 is now at 3666 bp.



(A) A generic plasmid map figuring the different functional units: the promoter, the Untranslated Region (UTR), the protein encoding sequence itself, the origin of replication specific to the plasmid backbone and the gene encoding antibiotic resistance. (B) A genetic cascade involving two promoters, P70 and P28, to produce eGFP [53]. (C) DNA gel with the following plasmids: P70S28, P28MscLeGFP and P28aHLeGFP. Ladder from Sigma, digestion using Xho1 and Bamh1, staining with SYBRGold. Double-digested plasmids show distinctive double bands at sizes predicted with ApE. (ND) stands for not digested, with a smear for migrating circular P28MscLeGFP plasmid

Figure 9.1: Example of genetic constructs and characterization on agarose gel.

The plasmid concentration after the miniprep or the midiprep is measured using DNA absorption at 260 and 280 nm (Nanodrop Thermofisher). Stock solutions of a few hundred of ng/ μ L are kept at -20°C .

3 REPORTER PROTEINS

It is common to use fluorescent proteins as readouts of the final reaction outputs. The reference we used is eGFP (enhanced GFP), natively produced as GFP in the jellyfish *Aequa victoria* and engineered to strengthen its fluorescent properties. This protein absorbs at 488 nm and emits at 509 nm⁷. To be able to similarly quantify

⁶ <http://jorgensen.biology.utah.edu/wayned/ap/>

⁷ <https://www.biotek.com/resources/technical-notes/excitation-and-emission-of-green-fluorescent-proteins/>

the amount of transmembrane proteins we produced, we used fusion proteins that couple eGFP to the transmembrane protein of interest, in our case hemolysin or MscL. For hemolysin we used a plasmid construct P28 α HL coupling the promoter specific to the transcription factor σ 28 to the sequence coding for hemolysin. We used a similar construct for the associated fusion protein P28 α HLeGFP. For the mechanosensitive pore MscL we used P28MscL and P28MscLeGFP. The fluorescent readouts can be quantified in conventional fluorimetry methods or using fluorescence microscopy. The yield of the reaction depends on the initial concentration of the different compounds but also on the environment of the reaction, in particular on the volume-to-surface ratio. Oxygen is needed both to ensure enzyme optimal efficiency and also to allow for eGFP maturation [153]. The chromophore maturation of this protein requires the following steps for the backbone maturation: folding, cyclisation, oxidation and dehydration. Oxidation is oxygen dependent. The oxygenation environment can change the output in protein of the cell-free reaction in dramatic ways. For example, we had a maximal output of eGFP for the 90 μ L initial reaction volume when this volume was aliquoted per 12 μ L in 1.5 mL Eppendorf tubes, hence providing a higher surface-to-volume ratio. In the Noireaux lab, fluorescence kinetics were obtained in a 96 well plate, 2 μ L per well, Biotek Synergy 2 Plate Reader. In Paris, we used a Quiagen RotorQ, 10 μ L per reaction. In both cases, the reaction was maintained at 29 ° C, the optimal temperature for TXTL expression. The different fluorescent characterizations that I made, both in Minneapolis and in Laboratoire Jean Perrin (Paris), are thus not directly comparable.

4 BULK EXPRESSION

We investigated the kinetics and outputs of bulk TXTL expression. The question we asked is the following: should we allow TXTL reactions to express proteins before making the droplets and constituting the network ? Or should we make the droplets and assemble them immediately after TXTL preparation to allow for protein production in a bilayer environment ?

There are several advantages to the first approach:

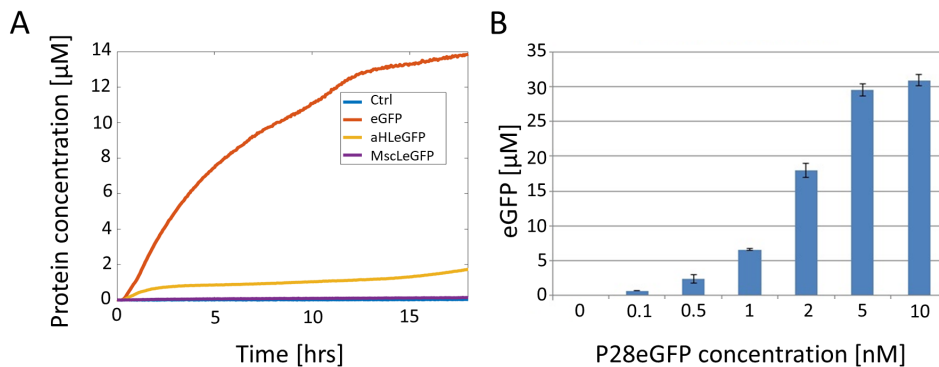
1. The TXTL reaction can last 10 hours in bulk but the lifetime of a droplet interface bilayer is rather of the order of 1 hour⁸. If we make the droplets after the TXTL mediated protein synthesis, a wider range of protein concentration can be accessible. We can for instance make the droplets with the TXTL reaction after 1, 2 or 8 hours of protein expression depending on the amount of protein we want in the droplet.
2. Another interesting point is that the optimal expression temperature for TXTL systems is 29 °C. This temperature is significantly lower than the PURE optimal temperature (37 °C) but it is still slightly above the DIB working temperature (25 °C or room temperature). If we separate the protein expression stage from the bilayer constitution, we can optimize the temperatures for both processes - cell-free expression and bilayer formation.
3. This temperature shift can be further exploited. We eventually want to perform a measurement to screen mechanical properties of a transmembrane pore. We require the protein concentration to be rather stable on the timescale of the

⁸ DIB lifetime significantly decreases with TXTL, compared to α HL diffusion experiments

measurement. Working at a temperature that significantly lowers the rate of protein production is an advantage in this configuration.

These different points weight in favor of expressing the proteins before making the droplets from the TXTL reaction and assembling them into bilayer arrays.

Bulk kinetics of TXTL expression at 29 ° C are characterized Fig 9.2. Production of eGFP steadily increases over 18 hours and eventually reaches 14 μM . αHLeGFP production rate is significantly lower and MscLeGFP production does not overcome the baseline of the control, a TXTL reaction without plasmid. The kinetics can be described using a Michaelis-Menten model [147] if exhaustion effects are neglected in the transient regime of expression. The experimental decay of the production rate after $\simeq 1$ hour of expression is due to the accumulation of byproducts and the depletion of reagents. Less than 4 amino acids are synthesized per second in the first hour of expression. αHLeGFP weighs 60 kDa whereas eGFP weighs only 27 kDa, which means that in the linear regime, eGFP production is twice as fast as αHLeGFP production. MscLeGFP fluorescence can not be measured in bulk fluorimetry (Fig 9.2 A), which points towards several explanations. The protein may precipitate due to its high hydrophobicity and no bulk fluorescence can be observed. It is also possible that this absence of bulk fluorescence is due to the eGFP part which would not be properly folded because the fusion protein is not in its native environment.



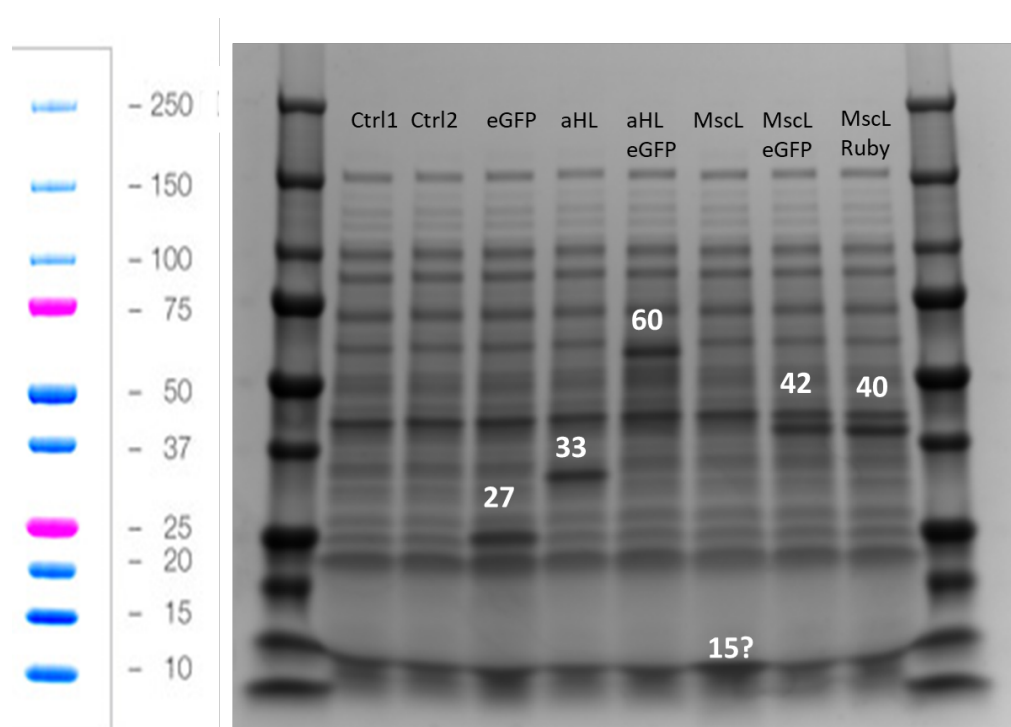
(A) Characterization of the bulk production, 2 μL reactions on plate reader, Minneapolis. We plot the protein concentration with respect to time for the three genetic cascades involving the promoter P28 and the protein sequences eGFP, αHLeGFP and MscLeGFP. MscLeGFP (violet solid line) is not separable from the control experiment (no plasmids, blue solid line) on the figure. (B) Final output of the reaction after 24 hrs expression for different initial plasmid concentrations. For concentrations larger than 5 nM, the protein output saturates around 30 μM . The final protein concentration can be tuned on more than one order of magnitude.

Figure 9.2: Quantifying kinetics and yielding of TXTL production in bulk.

Also, it should be noted that in the case of αHLeGFP synthesis, the expression considerably slows down after a couple of hours, which means that post-expression encapsulation could work in a quasi-steady regime. To adapt the protein output to our requirements, it is possible to change the amount of introduced plasmid and span one order of magnitude in the final output concentration - see Fig 9.2 B. This is particularly useful depending on the nature of the measurement we want to perform. With electrophysiological measurements, we need a tiny amount of pores to be able to record single pore events. On the other hand, fluorescence quantification of

membrane protein concentration in the bilayer requires larger amounts of protein production.

Because MscL-based constructs and non-fluorescent membrane proteins cannot be properly characterized through bulk fluorimetry, we checked that the desired proteins were indeed present in the bulk reaction by performing a SDS Page Protein gel (Fig 9.3). After 8 hours of expression, the reaction is diluted 15 times to avoid overloading of the gel, and the several proteins are analyzed on a gradient gel (BioRad Protein Cast 4 – 15%, Coomassie Staining). The gradient makes it possible to resolve different protein sizes on the same gel. Compared to the two control reactions, P28deGFP 5 nM reaction shows a stripe at 27 kDa for the protein eGFP. P28 α HL reaction product appears at 33 kDa, P28 α HL-eGFP at 60 kDa, P28MscL is barely seen at 15 kDa, P28MscL-eGFP shows a stripe at 42 kDa and P28MscL-Ruby at 40 kDa. Protein sizes in kDa are given for each reaction just above the corresponding band.



SDS Page gradient gel of TXTL reaction products after 8 hours of incubation. The lanes corresponding to the different proteins have been identified with the expected size in kDa at the correct location. MscL is the smallest protein and is barely noticeable at 15 kDa. The gel is a 4 – 15% Protein Gel Cast (BioRad), stained with Coomassie dye to identify the different protein stripes. Multiple secondary stripes are present as TXTL reactions are composed of a lot of different proteins. They are identified as non specific with the control lane (no plasmid added to the reaction).

Figure 9.3: SDS Page of TXTL reaction products.

The main issue with allowing TXTL reactions to express the proteins before making the droplets is that hydrophobic membrane proteins have to be somehow solubilized in the reaction prior to droplet formation. We have thus tried to add liposomes to the reaction to be able to partially solubilize MscL-eGFP. These experiments were not conclusive and are summarized in [Appendix D](#). We deduced from these results that it is necessary to have protein expression directly in the DIB systems. It means that immediately after TXTL preparation, we have to form and

assemble the droplets. In that way, we can insert MscL - which is hydrophobic - directly in the membrane.

In the following section, I discuss how we adapted the cell-free reaction to the particular requirements of the droplet interface bilayer configuration.

LOCALIZATION OF CELL-FREE SYNTHESIZED PROTEINS

The goal of this chapter is to show how we adapted a demonstrated result - proper insertion and functionality of cell-free synthesized proteins in liposomes - to the Droplet Interface Bilayer configuration.

MscLeGFP does not exhibit any fluorescence signal when it is expressed in bulk reactions. We first demonstrate that if we encapsulate in a liposome a TXTL reaction producing MscLeGFP, it is possible to recover fluorescence localized at the membrane. It means we can directly insert a membrane protein in a model bilayer when we allow TXTL to express the protein of interest *in situ*.

To adapt TXTL reactions to a DIB system, we show that cell-free production is possible in a water-in-oil emulsion by monitoring eGFP production over 2 hours.

Thirdly, we show how we can stabilize the membrane while expressing MscLeGFP in a DIB configuration.

Last, we demonstrate the insertion of the fusion membrane proteins α HLeGFP and MscLeGFP in DIBs.

1 MATERIALS AND METHODS

1.1 *TXTL and lipid composition*

Apart from the dilutions, all the experiments described in [Chapter 10](#) were done with the standard TXTL configuration, which composition is specified [Table 9.1](#). For the dilution experiments, two dilution protocols were followed:

1. The 90 μ L reaction with the standard composition is diluted 2 or 4 times ([Fig 10.5](#)).
2. The cellular extract only is diluted in the 90 μ L reaction, the other compounds are adjusted around their usual concentration to maximize the yield ([Fig 10.6 A](#) and [Table D.2](#)).

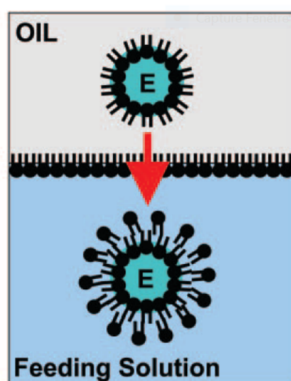
Dilutions were made using *S30B* buffer with 2 mg/mL DPhPC SUVs. The protocol to extrude SUVs can be found in [Appendix D](#).

For the stability screenings we did not change the nature of the produced protein. We always expressed MscLeGFP.

For the lipid composition of the DIB configuration, we used DPhPC at 5 mg/mL in hexadecane/silicone AR20 1:1 v/v except for [Section 3.3](#) and [Section 4](#) where we used the optimized lipid composition published by Dupin and Simmel [21]: 0.25 mM cholesterol, 0.25 mM DOPG, 4 mM DOPC and 0.5 mM DPhPC in 1:1 hexadecane:AR20.

1.2 *Liposome encapsulation*

Encapsulation was done with an emulsion transfer protocol adapted to TXTL requirements, published for the first time in [38].



Sketch of the emulsion transfer technique. The aqueous reaction that eventually constitutes the inside of the liposome is emulsified in the oil containing the lipids. The sketch shows phospholipid monolayers equilibrated around the resulting water-in-oil droplets. These droplets are then gently centrifuged through a second monolayer separating the oil from the outer solution (feeding solution). When crossing the interface, the two monolayers assemble into a bilayer. - reproduced from [38] ©2004 National Academy of Sciences

Figure 10.1: Emulsion Transfer Technique.

Emulsion transfer relies on the spontaneous assembly of phospholipid monolayers due to hydrophobic interactions. EggPC¹ lipids dissolved in chloroform were added at a concentration of 2 mg/mL to paraffin oil (Wako, Fujifilm chemicals). The oil containing the lipids was dutifully mixed then heated at 50 °C for 2 hours to evaporate the chloroform and dissolve the lipids in the organic mixture. 2 μ L of the TXTL reaction were then emulsified in this oil by vortexing for 5 s. The emulsion was then put on top of 20 μ L of feeding reaction, a solution similar to the 90 μ L TXTL reaction (Table 9.1) but that did not contain plasmid DNA nor bacterial extract. This feeding solution was osmotically balanced with the TXTL reaction encapsulated inside. The superposition of aqueous and lipid phases was gently centrifuged at 1.5 G for 10 min.

During this process, the aqueous droplets surrounded by a monolayer of phospholipids cross the second monolayer at the interface between oil and water (Fig 10.1). Both monolayers can thus assemble into a bilayer. The oil on the top was then removed so as to keep only the feeding solution containing the liposomes.

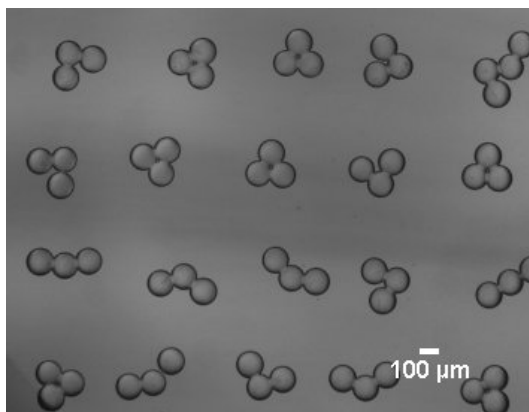
Liposomes were incubated at the optimal temperature of expression, $T = 29$ ° C, for up to 24 hours. Samples for optical characterization were prepared on microscope slides. We used Gene Frames (Thermofisher) as spacers to prevent GUVs from bursting. We used phase contrast for bright field imaging and eGFP filters for fluorescence acquisition.

1.3 Stability Analysis

After using liposomes to demonstrate membrane insertion of TXTL synthesized proteins, we focused on encapsulating TXTL reactions in the droplets constituent of the DIB. To test the stability of bilayers, we developed a protocol where multiple groups of up to three bilayers were produced for each experiment. Their lifetime was acquired through timelapse microscopy (Fig 10.2). Stability was quantified by moni-

¹ Lipids extracted from the lysozyme of the hen egg.

toring the number of remaining DIBs over time. We grouped these results according to the droplet size using 10 μm wide bins for the droplet diameters.



Example of TXTL droplet layering with 25% extract in the total reaction (Table D.1) to screen for DIB stability. The protein expressed is MscLeGFP. Small groups of droplets are formed to isolate individual bilayers.

Figure 10.2: Formation of small droplet networks for stability assays.

1.4 Fluorescence Measurements on DIBs

Expression in water-in-oil emulsions was quantified using epifluorescence microscopy (Fig 10.4). Droplets were formed in 96 well plates under the microscope (Fig 3.5 A). Their fluorescence was acquired with a 5 min step timelapse and a 20X objective (100 ms exposure time/ FITC filters).

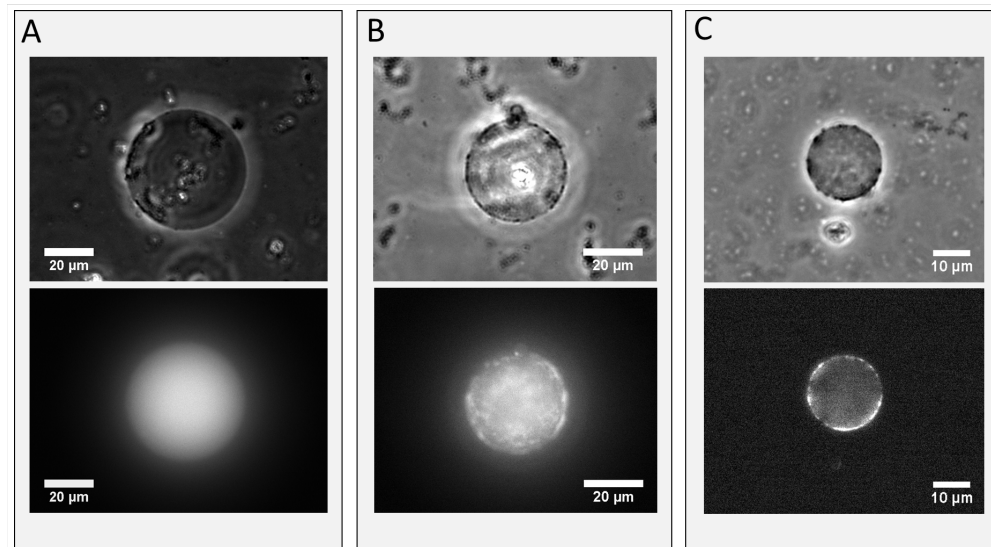
We used confocal microscopy to quantify membrane protein expression. For these experiments 10 μL TXTL reactions were incubated at 29 ° C for 5 hours. After the incubation period, reactions were spun at maximal speed for 1 min on a table top microcentrifuge to pellet the aggregates. Droplets of roughly 40 to 50 μm in radius were formed with an automated capillary trap in cavity microscope slides containing the optimized lipid composition published by Dupin and Simmel [21].

The resulting DIBs were imaged under a Nikon microscope with a confocal spinning disk module (Xlight V2 system, Gataca systems). Stacks with a z-axis resolution of 0.5 μm were performed with a 20X Nikon Apo Plan objective. We set an exposure time of 50 ms and the laser excitation wavelength at 470 nm. In the case of eGFP, we reduced the exposure time to 10 ms to avoid light saturation of the camera pixels.

2 IN SITU EXPRESSION

2.1 Liposome encapsulation

We encapsulated TXTL reactions expressing eGFP, αHLeGFP and MscLeGFP in liposomes. We monitored the intensity signal increase during the reaction expression. The fluorescent proteins eGFP, αHLeGFP and MscLeGFP were produced in the liposomes and their presence characterized by epifluorescence microscopy (Fig 10.3 A, B and C). The integrity of the liposome posterior to encapsulation was checked by using an additional fluorophore, Dextran-TRITC, in the internal buffer.



(Top) Bright Field Phase Contrast Imaging of GUVs encapsulating TXTL reactions (Down) eGFP fluorescence imaging of GUVs encapsulating TXTL Reactions. TXTL expression in EggPC GUVs, 7 hours of incubation (A) eGFP expression. The fluorescence is homogeneous in all the liposome (B) α HLeGFP expression. There is fluorescence in bulk with a signal increase at the membrane, consistent with the transmembrane localization of α HLeGFP heptamers. (C) MscLeGFP expression. There is fluorescence at the membrane only, which is likely due to the hydrophobicity of MscLeGFP monomers and pentamers.

Figure 10.3: TXTL reactions encapsulated in GUVs.

The liposome phenotype revealed the nature of the expressed fluorescent protein. If the protein did not have a membrane-inserted domain, which is the case of eGFP, liposome exhibited bulk fluorescence (Fig 10.3 A). If the membrane protein that was expressed was soluble in water, liposome were fluorescent inside but the bilayer showed also increased intensity patches. This was a clear evidence of preferential membrane insertion of the protein (Fig 10.3 B). Last, in the MscLeGFP case, liposomes showed mostly rough patches on the membrane (Fig 10.3 C), which is a probable consequence of MscLeGFP hydrophobicity.

With this experiment we showed that although no bulk fluorescence was observed for MscLeGFP production, there was production of a fluorescent membrane protein when the same reaction was encapsulated in a liposome. This confirmed that insertion of a highly hydrophobic protein in a membrane is possible if we implement the TXTL reaction directly *in situ*.

2.2 Encapsulation in DIBs

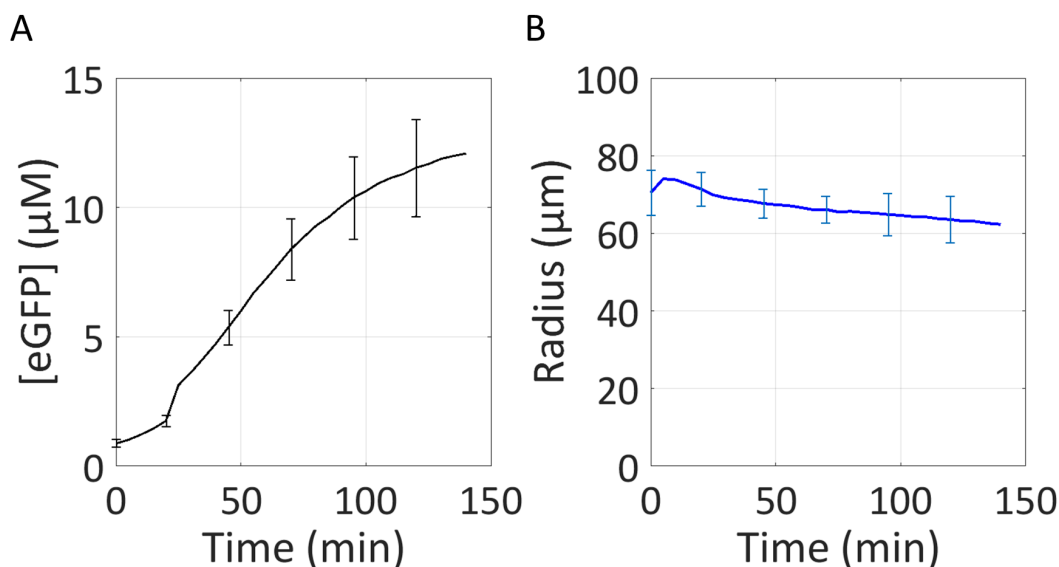
Prior to any encapsulation in DIBs we first checked that TXTL reactions could express a protein with a reasonable yield in the microdroplets of a water-in-oil emulsion. To do so we quantified the kinetics of eGFP production in a water-in-oil emulsion. We eventually compared the dynamics of the reaction to the previous in bulk characterization (Section 4). We found that reaction in a microdroplet occurred on a timescale much shorter than in bulk production - typically 2 to 3 hours before plateauing, compared to the 24 hours of the bulk production. These limitations can be understood as resulting from:

1. a lower reservoir of reagents,

2. a limited dissipation of byproducts,
3. a limited oxygen fueling,
4. surface and volume effects,
5. and lifetime of the droplet/protein precipitation effect.

The first two points are a direct consequence of the lower volume of the droplets as we form droplets of typically 50 μm in size, which gives a final volume of 500 pL, to be compared to the 10 μL of bulk reaction volumes. The third point is linked to the emulsion environment: droplets are surrounded by a thick layer of oil in which oxygen diffusion is impaired. The fourth point, discussed in [154], is due to non-specific adsorption at the water-and-oil interface. Last, evaporation and protein precipitation at the interface [4] might impair the reaction by altering the concentrations.

Fig 10.4 A, we see a strong increase of the fluorescence intensity due to eGFP expression, with a final protein concentration above 10 μM . This expression is faster than the bulk kinetics (Fig 9.2), maybe because of the droplet confinement effect. We stopped the acquisition when heterogeneity in fluorescence within the droplet started to appear ($\simeq 2$ hours after encapsulation). In bright field, this observation is consistent with the deformation and deterioration of the droplet surface. On average, water-in-oil droplets show a shortened lifetime when crowded and complex reactions are encapsulated. This deterioration is reported in the literature as resulting from the precipitation of proteins [21]. We also plotted in Fig 10.4 B the evolution of the droplet radii. Droplet size decreases over the timecourse of the experiment as the water content tends to evaporate. We further checked that the increase in intensity was due to eGFP production and not to an overconcentration due to evaporation.



Expression of eGFP from TXTL reactions in water-in-oil emulsions. Fluorescence measurements are averaged over $N=92$ droplets. (A) Evolution of averaged eGFP concentration in the droplets over $\simeq 2$ hours of acquisition. The rate of production decreases slowly over time. (B) Shrinkage of the droplets radii over time.

Figure 10.4: In situ TXTL expression of eGFP.

When assembling the droplets together, we found out that bilayers were not stable in the initial configuration (DPhPC 5 mg/mL in hexadecane:silicone oil

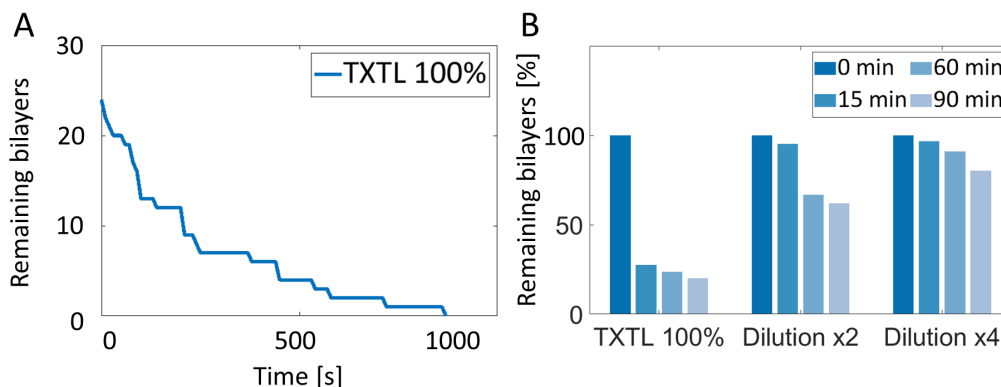
AR20 1:1 v/v, TXTL 100%). We thus decided to focus on the stability of the bilayer by investigating different strategies: diluting the TXTL reaction, diminishing the droplet size and changing the lipid composition of the oil phase.

3 MEMBRANE STABILIZATION

We sought to stabilize the bilayers while the reaction is occurring in the droplets. We started by using the working protocol performed in [Part ii](#) to produce DIBs with a standard TXTL composition expressing MscLeGFP. We got immediate droplet fusion (Fig 10.5 A). From previous articles dealing with stability of droplet interface bilayers, we consider three parameters that could participate in the stabilization of the membranes:

1. Dilution of the aqueous buffer with a solution of liposomes,
2. Producing smaller droplets to get smaller membranes,
3. Optimizing the lipid composition of the organic phase.

3.1 Dilution



(A) Study of DPhPC bilayers stability over time for a standard TXTL reaction expressing MscLeGFP. All the droplets fuse within 15 min (single experiment). (B) Impact of the TXTL reaction dilution on DIB stability for a 2X and a 4X dilution, averaged on several experiments (N=80, N=145, N=122). There is a significant improvement in DIB stability when diluting the reaction.

Figure 10.5: Stability analysis of DIBs in the context of TXTL production.

We first investigated the dilution of the reaction with a solution of liposomes (see Materials and Methods [Section 1.1](#)). Adding liposomes to the dilution buffer should improve membrane stability if we refer to the *lipid in* method [4]. Besides, dilution decreases drastically the average protein concentration and hence the number of potentially lipophile molecules that would compete with lipid adsorption at the interfaces. We thus decided to perform experiments where we diluted a reaction prepared at t_0 with a solution containing small unilamellar liposomes. We diluted the TXTL reaction 2 and 4 times. We found that dilution significantly improved the lifetime of the bilayers as shown Fig 10.5 B. This global dilution that we performed did not preserve TXTL expression and we obtained in that case a poor yield in protein. We thus decided to work with an extract diluted 4 times with the liposome solution. We call this condition "extract 25%". We adjusted in consequence the

different salt and PEG concentrations to get the maximum yield of the TXTL reaction, using data provided by Noireaux and coworkers (Figure C.1). The new chemical composition can be found in Table D.2. However, we still observed some fusions in that case. We thus worked on diminishing the size of the produced droplets to increase the lifetime of the DIBs.

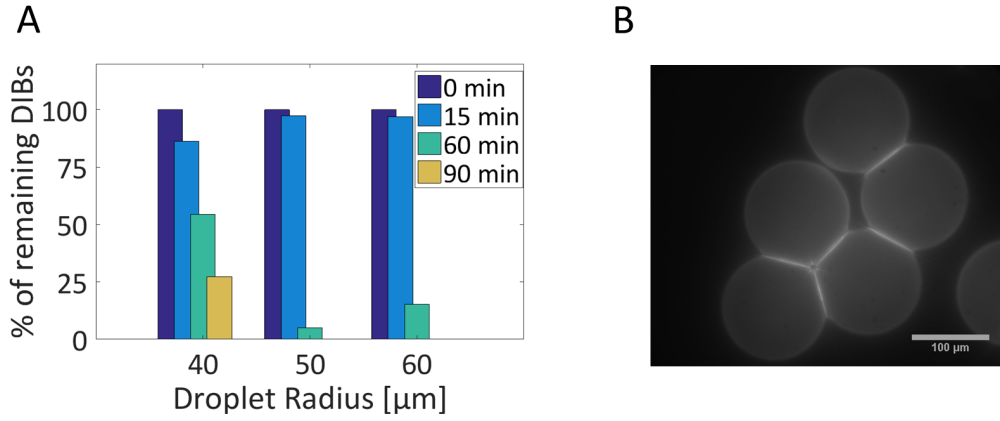
3.2 *Size*

We have then looked at size effects with stability assays where we simply timelapsed the number of remaining bilayers. In Fig 10.6 A, we show the influence of the size on the droplet stability. We found that droplets that are 40 μm in radius live longer by at least 30 minutes than droplets that have a radius larger than 50 μm .

3.3 *Lipid Mix*

We found that a dilution up to 25% of the extract within the TXTL reaction combined with the production of smaller droplets improved the DIBs stability. DPhPC has been used first for supported lipid bilayers and then for droplet interface bilayers for decades. However, a more stable lipid mix was proposed recently by Dupin and Simmel [21]. The composition proposed by the authors is the following: 0.25 mM cholesterol, 0.25 mM DOPG, 4 mM DOPC and 0.5 mM DPhPC in 1:1 hexadecane:AR20. The strategy followed for the optimization was to look for faster assembly of lipids at the interface to avoid presupposed denaturation of proteins from the cell-free extract at the interface. We abbreviate this lipid mix as "Dupin mix" for the remaining part of this thesis. In these conditions, we found out that it was possible to encapsulate droplets of TXTL at 100%, with a diameter up to 200 μm , without encountering stability issues. The fabrication of DIBs networks was considerably eased by these modifications. We managed with this new configuration to encapsulate TXTL reactions expressing αHLeGFP in DIBs. Figure 10.6 B shows the first DIB networks made with this configuration using epifluorescence microscopy. We clearly see that αHLeGFP is localized at the DIB interface between the droplets.

We have shown that for the purpose of inserting membrane proteins in DIBs, in situ expression was required. We managed to isolate 3 factors that stabilize the DIBs while the TXTL reaction is running: extract dilution, droplet size and the lipid mix composition. It is the lipid mix composition that ensures the stability of the system. We have now a reaction that is working well when included in water-in-oil emulsions. We are able to stabilize the membranes between the aqueous compartments containing the reaction. To go further away, we need to prove that membrane proteins produced in this configuration can insert in the membrane as it was the case for liposome encapsulation. We already see that it is the case from epifluorescence measurements (Fig 10.6 B). We now quantify this membrane insertion by comparing fluorescence contrasts between bulk and bilayer using confocal measurements.



(A) Size effect on bilayer stability, extract dilution 25% (Table D.2). The protein expressed is MscLeGFP and the lipid composition in the oil is pure DPhPC. Initial number of droplets for the three different conditions is the following (in order): $N = 44, 40$ and 66 . Smaller droplets are significantly more stable up to 90 min. (B) Epifluorescence microscopy of α HLeGFP expressed in DIBs, TXTL 100%, $\times 40$ Olympus LUCPlanFLN. The lipid composition in the oil is the Dupin mix. There is a strong signal increase at the membrane which evidences the preferential insertion of the fluorescent monomer in the bilayer.

Figure 10.6: Increasing DIB stability with extract dilution and lipid mix optimization.

4 LOCALIZATION OF MEMBRANE PROTEINS IN DROPLET INTERFACE BILAYERS

To optically demonstrate and quantify the insertion of *in situ* synthesized proteins in the membrane, we performed confocal measurements (see Materials and Methods Section 1.4). We compared fluorescence contrasts between membrane proteins and their fluorescent counterparts, α HL versus α HLeGFP and MscL versus MscLeGFP, to distinguish between autofluorescence and fusion GFP fluorescence. We also compared our results with fluorescence emitted by eGFP. With this we could differentiate increased fluorescence at the membrane due to preferential insertion of a membrane protein in the bilayer from bulk fluorescence with no preferred localization in the eGFP case.

4.1 Bilayer intensity contrast analysis

Fluorescence images were analyzed with the following Matlab routine:

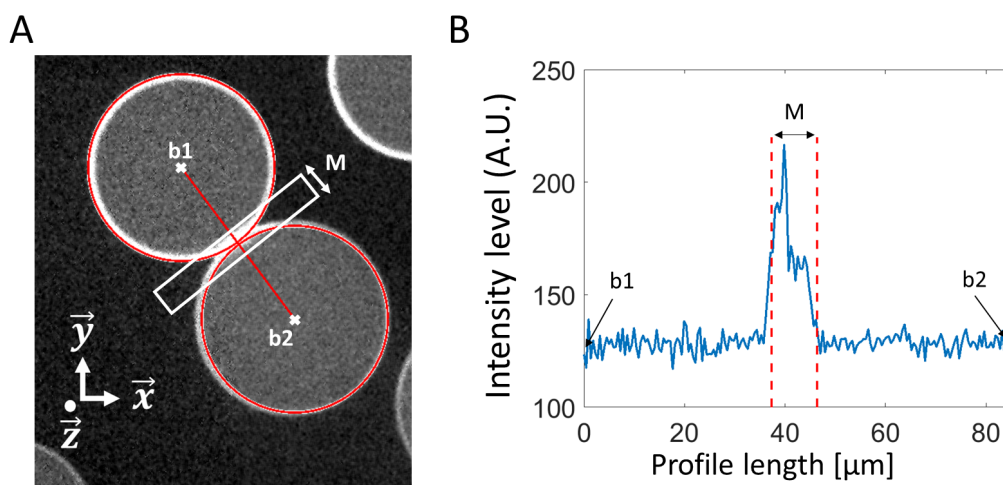
1. Detection of the droplet contours and centers in the median plane of the stack, using a Hough Transform - see Fig 10.7 A - performed on a denoised image. The centers of the two droplets forming the DIB are used to define the cut performed on the image. The cut is in the xy plane and perpendicular to the bilayer. The intensity profile is then computed using this cut, for all the confocal stacks recorded along the z-axis.
2. Intensity profiles are averaged around the median vertical position z_m in the stack, on a short height $\Delta z = 10 \mu\text{m}$. On Fig 10.7 B, we plot $\bar{I}(s) = \frac{1}{\Delta z} \int_{z_m - \Delta z/2}^{z_m + \Delta z/2} I(z, s) dz$.
3. We use this "stack-averaged" curve to compute a contrast. To do so, we compare an average of the signal in the bilayer vicinity (M region of size 20

pixels or $4.5 \mu\text{m}$) to the bulk signal in the center of each droplet (baseline assessed at b_1 and b_2 locations). On Fig 10.7 we show how we geometrically determine these locations from the circle detection. b_1 and b_2 are the detected centers of the droplets. The center of the M region is the barycenter of b_1 and b_2 weighted by R_1 and R_2 the droplets radii.

4. The difference between the bilayer signal and the bulk signal is normalized with the background value I_{bg} , outside of the droplets.

We define the contrast as:

$$C = \frac{\langle \bar{I}(s) \rangle_M - \frac{1}{2}(\bar{I}(b_1) + \bar{I}(b_2))}{I_{bg}} \quad (10.1)$$



(A) Example of cut on droplets expressing αHLeGFP . The cut is $84 \mu\text{m}$ long. (B) The intensity profile resulting from the cut annotated at the centers b_1 and b_2 of the two droplets. The maximum of the signal is averaged in the M region including the bilayer.

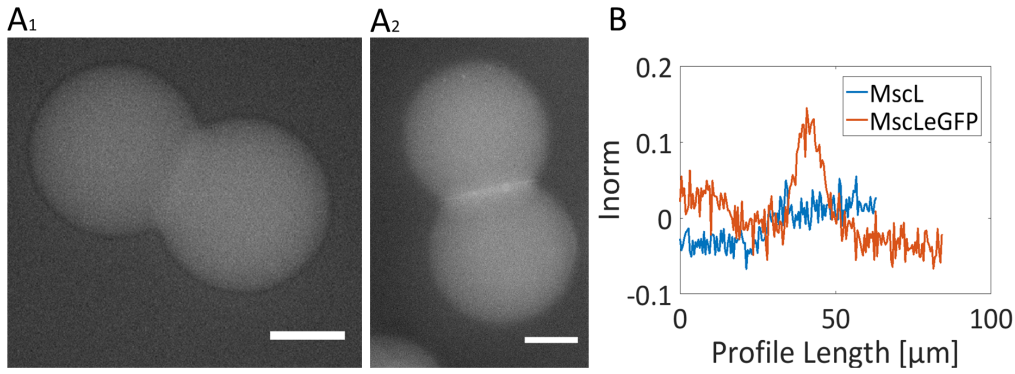
Figure 10.7: Measure of protein insertion.

4.2 Results

Averages and standard deviations of the measured contrasts for MscL, MscLeGFP, αHL , αHLeGFP and eGFP are summarized Fig 10.10 A and B.

We show examples of measurements performed on MscL and MscLeGFP Fig 10.8. There is a weak autofluorescence background (Fig 10.8 A1) and MscLeGFP does not show a strong signal in the bulk, presumably due to its high hydrophobicity (Fig 10.8 A2). However, we clearly see the formation of a "ring" at the bilayer location between the two droplets. There is indeed a timelapse of roughly 30 minutes between the bilayer constitution and the stack imaging during which MscLeGFP monomers are synthesized, similar to the case of eGFP expression directly in the droplets (shown earlier Fig 10.4). Qualitative assessment of MscLeGFP insertion in the bilayer is confirmed by the quantitative comparison of transbilayer profiles in both cases, an example of it is plotted Fig 10.8 B.

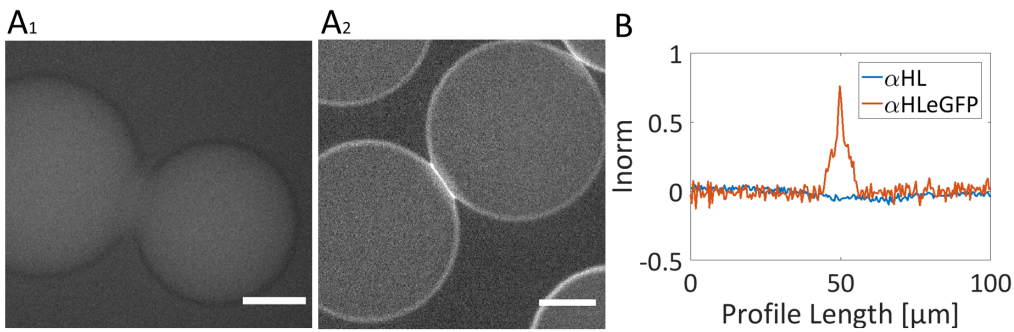
In the case of αHLeGFP and αHL Fig 10.9, the contrast is much more increased compared to the MscL case. The presence of soluble monomers inside the bulk increases the amount of adsorbed proteins. Not only the bilayer is fluorescent but



(A₁) Confocal image of MscL expressed in a DIB (scale bar = 40 μm). (A₂) Confocal image of MscLeGFP expressed in a DIB (scale bar = 40 μm). (B) Transbilayer intensity profiles in both cases - MscL and MscLeGFP - for these two example pictures. Intensity is normalized by the background of the image. We plot $I_{norm}(s) = \frac{\bar{I} - \frac{1}{2}(\bar{I}(b_1) + \bar{I}(b_2))}{I_{bg}}$ to read the contrast without further analysis right on the figure.

Figure 10.8: Insertion of MscL and MscLeGFP in the bilayer.

we also see adsorption of the fluorescent monomers in the monolayers surrounding the droplet.



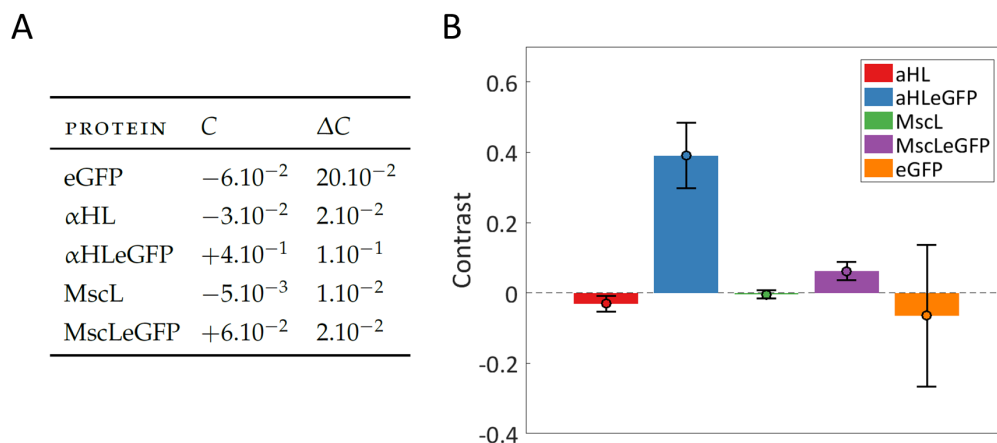
(A₁) Confocal image of αHL expressed in a DIB (scale bar = 40 μm). (A₂) Confocal image of αHLeGFP expressed in a DIB (scale bar = 40 μm). (B) Transbilayer intensity profiles in both cases - αHL and αHLeGFP - for these two example pictures. We plot $I_{norm}(s) = \frac{\bar{I} - \frac{1}{2}(\bar{I}(b_1) + \bar{I}(b_2))}{I_{bg}}$ to read the contrast without further analysis right on the figure.

Figure 10.9: Insertion of αHL and αHLeGFP in the bilayer.

To eventually demonstrate that the fluorescence increase we see in the MscLeGFP vs MscL case (αHLeGFP vs αHL case) is indeed due to a specific insertion of the fluorescent membrane protein in the bilayer, we performed the same measurements on DIBs containing expressed eGFP. These images show a behavior qualitatively close to the one observed with αHL or MscL: a "bulk fluorescence" that decreases when crossing the DIB because less fluorescence signal is integrated in this region.

The contrast definition (Eq 10.1) gives a representative measurement for the presence of membrane proteins in the bilayer between two droplets. Contrast measurements yield positive values for αHLeGFP and MscLeGFP. It is negative for non-fluorescent proteins - αHL and MscL - presumably because the bulk autofluorescence dominates over the membrane contribution. This contrast is also negative for eGFP - a fluorescent protein which does not insert into the membrane. In this case again bulk fluorescence dominates over the membrane contribution. We can summarize these results as follow: there is a specific shift in fluorescence when

crossing the bilayer for the eGFP-fusionned membrane proteins. That shift gives in return a positive contrast.



Confocal quantification with the following populations: $N(\alpha\text{HL})=12$, $N(\alpha\text{HLeGFP})=13$, $N(\text{MscL})=11$, $N(\text{MscLeGFP})=14$ and $N(\text{eGFP})=16$ ((A) Contrasts table with the 5 different proteins (B) Graphical representation of the same values. Contrasts are positive on average for the membrane proteins that are fluorescent.

Figure 10.10: Graphical representation and scoring of protein localization at the membrane.

FUNCTIONALITY OF TXTL PRODUCED PROTEINS

We have shown in [Part ii](#) that some microscopic features about pore insertion and functionality could be inferred from averaged optical measurements. In [Chapter 10](#), we have used confocal measurements to demonstrate the successful localization in the lipid bilayer of TXTL synthesized membrane proteins. To prove their functionality, we used electrophysiological recordings. We handled the case of TX-TL synthesized hemolysin as its insertion could be readily shown. MscL is closed in its resting state, and its activity requires stretching the bilayer membrane, which itself requires designing a setup for bilayer mechanical excitation. This prospect is beyond the scope of this thesis and will be the long-term goal of the activities of our group at Jean Perrin Lab. We have a collaboration with J. Mathé (LAMBE, Evry - France) for the design of electrophysiological measurements.

1 AN ELECTROKINETIC MODEL FOR THE MEMBRANE

1.1 *Pure bilayers*

Generally, electrophysiological measurements performed on a bilayer, including a pore or not, rest on the following principle: impose a voltage across the membrane, measure the resulting ionic currents. In the V-clamp mode, a voltage is applied and the current response is measured. In the I-clamp mode, a feedback loop allows the operator to tune the applied voltage, thus maintaining I at the prescribed value. Bilayer capacitance can be deduced from the measurement of I as a response to a periodic voltage input. This input may consist in the sum of two waves or a triangular input. The resulting intensity is the sum of i_1 through the resistance and i_2 through the capacitance:

$$I = i_1 + i_2 = \frac{U}{R} + C \frac{dU}{dt} \quad (11.1)$$

In the case of a triangular input of peak to peak value $\Delta U = 50$ mV and of period $T = 50$ ms (no offset), the slope of the triangular wave is

$$a = \pm \frac{2\Delta U}{T} = \pm 2 \text{ mV/s} \quad (11.2)$$

If the resistance of the bilayer can be considered "infinite", it is easy to simplify [Eq 11.1](#) and get the shape of the bilayer response, a squared wave of value $\pm C.a$ (peak-to-peak $2Ca$). In the ideal case, the intensity recorded on the membrane should give a constant capacitance value over the timecourse of the measurement. However, membranes can fluctuate in shape and area while the electrophysiological measurement is performed. In the Droplet Interface Bilayer configuration, these changes are mainly due to continuous evaporation of the droplet content. The main consequence of this effect is a decrease in the measured capacitance. Another common aspect of capacitance alteration is known as electrostriction and was evidenced for pure bilayers in 1973 [[155](#)]. The bilayer shape changes in response to the electrical field applied [[156](#)]. We assumed there is no such effect in our system.

Eventually, membranes can also be spontaneously polarized [157], either because of an asymmetry in the two lipid leaflets composition or because of the curvature of the membrane, a phenomenon known as flexoelectricity. Again, we did not consider this issue to be relevant. Indeed, in our case the lipids on the two leaflets do not exhibit charge difference and the local curvature radius can be considered infinite due to the dimensions of the interface. After discussing the case of the pure lipid bilayer, I will show how to characterize single pore insertion.

1.2 Channel insertion in pure bilayers

If the hemolysin pore is filled with water, its conductance¹ $\sigma_{\alpha HL}$ is proportional to the solution conductance [55], which itself is a function of the introduced salt concentration. In the dilute solution regime, the conductance can be considered as proportional to the ion concentration. If one can extract from the recorded current trace a jump attributable to a single pore only, then the relationship gives readily (A is the proportionality coefficient that depends on the salt concentration in the solution):

$$\sigma_{\alpha HL} = A \frac{\Delta I}{\Delta U} \quad (11.3)$$

Because of this fixed conductance $\sigma_{\alpha HL}$, an experiment where a pure bilayer is subjected to spontaneous insertion of multiples pores is expected to show discrete current jumps. These current jumps result from an increase in the conductance G by integer multiples $\Delta G = n \cdot \sigma_{\alpha HL}$.

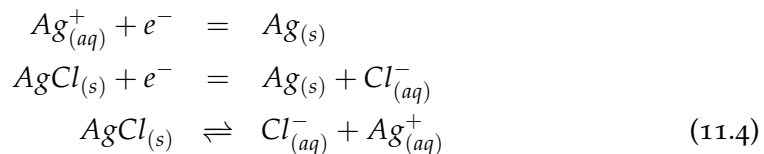
2 MATERIALS AND METHODS

2.1 Droplet formation

We developed a protocol based on [5] to characterize with electrophysiological measurements the insertion of hemolysin in a droplet interface bilayer. Droplets were layered using an automated capillary trap device in the organic solvent to get reproducible sizes and similar bilayer areas from one experiment to the next. We obtained droplets with typical diameters between 200 μm and 300 μm .

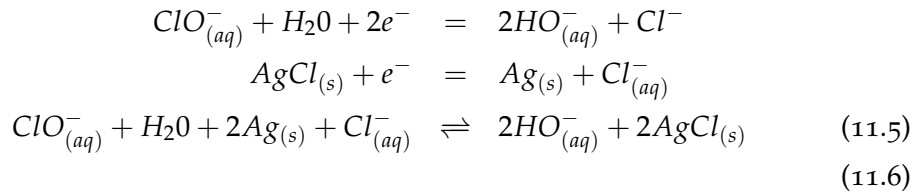
2.2 Electrode recording

In these setups, currents were recorded through a pair of Ag/AgCl electrodes according to the following scheme. As a voltage is applied, the positive electrode receives negative charges from Cl^- ions. These ions are oxidized into AgCl. At the cathode the reduction operates and the whole redox equation writes:

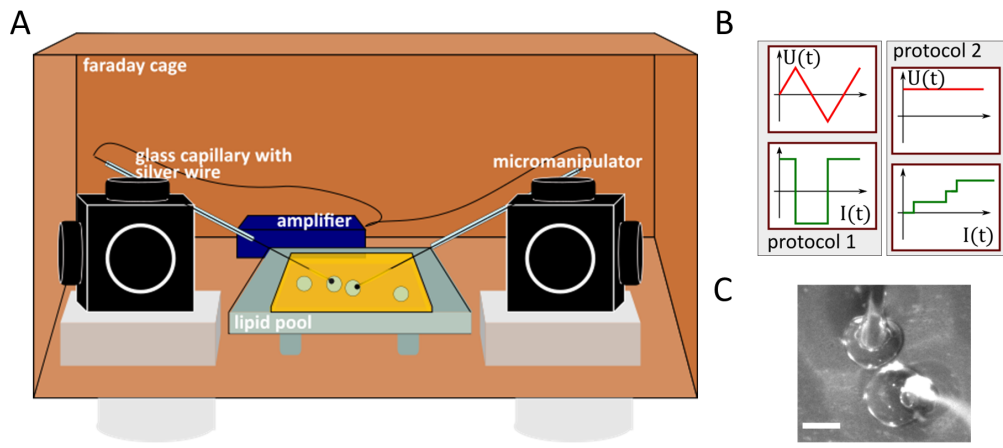


¹ The conductance itself is the ratio between the measured intensity and the applied voltage.

The use of Ag/AgCl electrodes requires A) a silver wire coated with silver chloride and B) chloride ions in solution. The first point requires either the use of bleach (Eq 11.5) or electrodeposition of the oxyde.



AgCl has a low solubility in water, meaning that after several measures, electrodes need to be chlorided again to lower the noise in the measurements.



(A) Electrophysiological setup for bilayer measurements. The electrodes and electrical amplifier are together isolated in a Faraday Cage with the pool containing the aqueous droplets surrounded by lipids. (B) Protocols for 1) Capacitance measurement 2) Visualization of single pore insertion. (C) Two droplets brought into contact, scale bar = 200 μm

Figure 11.1: Experimental setup for bilayer electrophysiology recording.

Silver wires (75 μm in diameter) were bought from Warner Instruments. Their tip was heated to the flame to allow the formation of a small silver ball on which the target water droplet easily wets. These electrodes were also coated with melt agar (ultra-low gelling, 3,5%w/v in KCl 500 mM) before each measurement to improve the droplet wetting around the electrode. After the bilayer measurement, this coating was immediately removed through gentle rubbing with a Chemwipe soaked in distilled water. Electrodes were coated again to repeat the measurement.

2.3 Electrophysiology setup

Electrodes were mounted on glass capillaries (inner diameter 1 mm) to provide a scaffold to the extremely thin silver wires. These capillaries were themselves mounted on Narishige Micromanipulators (three-axis water hydraulic micromanipulators) to provide a good spatial resolution when bringing the droplets into contact (Fig 11.1 A and C). Currents through the membrane were recorded with a current amplifier (eONE Element). We isolated the whole setup from ambient electrical noise by enclosing the apparatus in a Faraday Cage. In this environment, we could measure currents with an electrical noise close to 1 pA. The company Elements delivers a software for acquisition (Elements Data Reader) and one to analyze a posteriori the recorded

trace (Elements Data Analyzer). We chose to analyse the traces afterwards using a custom Matlab routine. Eventually, signals were acquired at a sampling frequency of 1.25 kHz which provided a natural high pass filtering on the high frequency noise. We used additionally a binocular to manually bring droplets together (Fig 11.1 C). Once the bilayer was formed, there was no more visual information recorded. We relied only on electrical measurements of the capacitance to check during the recording the integrity of the bilayer.

The setup was calibrated using a standard electronic capacitor of 100 pF. The conversion intensity to capacitance was made using a custom Matlab routine that averages the UP states of the squared wave and the DOWN states to compute the spacing between plateaux (refer to Eq. 11.1 for details and see Protocol 1 in Fig 11.1 B).

2.4 *Organic solvent composition*

We used DPhPC dissolved at 5 mg/mL in a mixture of hexadecane:silicone AR20 1:1 v/v. For these experiments, we resumed to using DPhPC lipids instead of the Dupin lipid mix to diminish the electrical noise in the bilayer capacitance recording. We compared both lipid compositions in Section 3.1.

2.5 *TXTL composition*

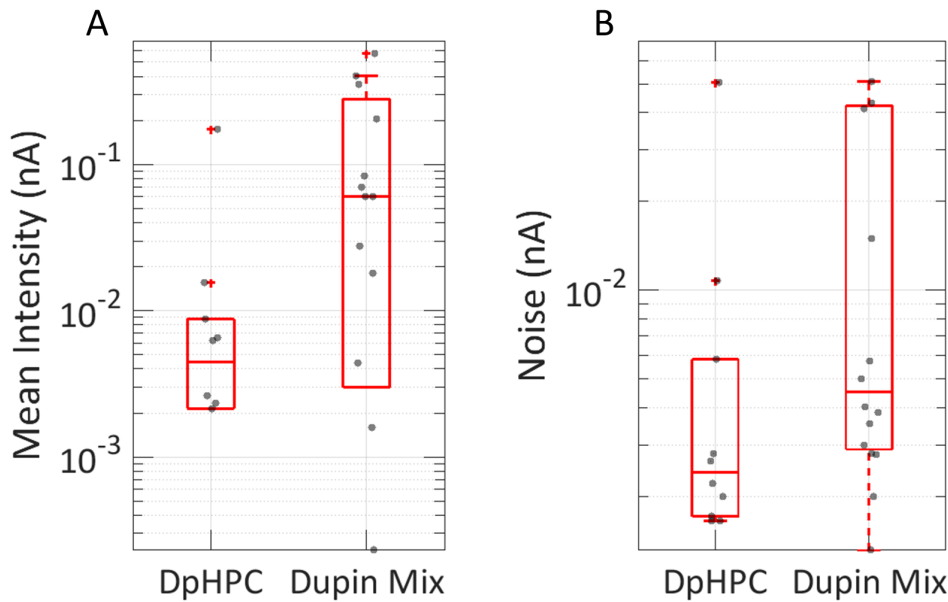
We expressed α HL in a TXTL reaction at 100% for 5 hours, then diluted 500 times the product in a [KCl]= 500 mM buffer. This protocol was elected due to the study in Section 3.2, in which we show that TXTL reactions are not compatible with high salt concentrations. Adding chloride ions increased the signal-to-noise ratio of the electrophysiological recording. The final concentration of chloride ions in the solution was 500mM. With this salt concentration, individual current jumps should measure 25 pA.

3 HEMOLYSIN CONDUCTANCE

3.1 *Lipid noise study*

Two choices can be made for the lipids-in-oil configuration. DPhPC has traditionally been used for electrical recordings in bilayers but the Dupin mix is extremely convincing in terms of stability. We decided first to compare both bilayer electrical characteristics with a KCl 500 mM buffer. In every measurement, the bilayer capacitance was recorded before performing a voltage step protocol. We checked that the capacitance was of the order of 10^2 pF. This is consistent with proper electrical contact of the electrode with the droplet, combined to the presence of a single bilayer between the two droplet-coated electrodes. We then applied a 50 mV constant voltage and measured the resulting electrical noise. We recorded the current trace for 10 min then we checked the bilayer integrity to decide whether or not to keep the recorded trace. The results are shown in Fig 11.2, $N = 9$ experiments for DPhPC bilayers and $N = 14$ experiments for Dupin Mix Bilayers. Boxplots show the median of the distribution and the two quartiles around this median (25% and 75%). The distribution being highly skewed, we have chosen this statistical representation in which the median of DPhPC related intensities is 4 pA (mean 21 pA) and the

median of Dupin mix related intensities is 60 pA (mean 230 pA). The noise median is also significantly lower in the DPhPC case (2 pA) than in the Dupin case (4 pA).



Recordings with DIBs made of either pure DPhPC or Dupin mix lipids at an applied voltage of 50 mV, KCl=500 mM. (A) Comparison between the mean intensities. The distribution corresponding to the Dupin mix is shifted towards higher intensities compared to the DPhPC distribution, indicating higher leaking currents. Points indicate experimental single recordings. The boxplot is composed of a central red line indicating the median while its bottom and edge indicate respectively the first and last quartiles. (B) Comparison between the mean noises of current recordings. The DPhPC bilayers exhibit lower noise than the DIBs made with the Dupin mix.

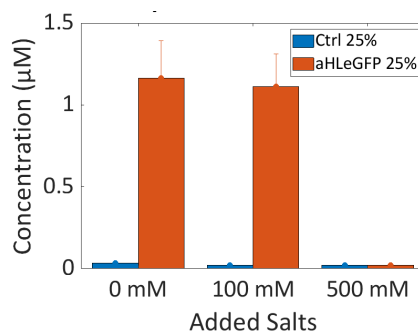
Figure 11.2: Comparison between the DPhPC and the Dupin mix.

Figure 11.2 shows that Dupin mix bilayers seem to withstand higher current leakages (average and standard deviation), maybe because of their persistent stability. DPhPC bilayers are less stable, and cases where bilayers can withstand lipid pores are rare. The use of DPhPC seems to provide a natural stability cutoff that removes from the measurement sets highly corrupted bilayers. Because on average the measured noise is lower in this configuration, we thus chose the DPhPC lipid mix to characterize individual current jumps. Capacitances for pure DPhPC bilayers range from 76 to 199 pF. Using the average value of $4 \cdot 10^{-3}$ pF/cm² this gives bilayer areas between $19 \cdot 10^3$ μ /m² and $50 \cdot 10^3$ μ /m², hence average radii of 77 μ m to 126 μ m which is consistent with the actual size of produced droplets². For the Dupin mix, capacitances range from 64 to 611 pF, giving a wider range of bilayer dimensions. Inferred radii are comprised between 71 and 220 μ m. In the case of the Dupin mix, the outstanding stability of the formed bilayer allows to "unzip" the bilayer by pulling apart the electrodes. This action decreased the bilayer area. We deduced that in this case the value of the capacitance can be decreased *on demand*, proportionally to the available area.

² We used the theoretical value of Phillips [144], 0.4μ F/cm².

3.2 Compatibility of TXTL reactions with chloride ions

TXTL reactions do not contain any chloride ions initially. We first tried to see what amount could be introduced without lowering too much the reaction yield. The system could handle 100 mM in introduced salts, but not much more. On Fig 11.3a is shown that 500 mM KCl brings the level of expressed α HL-eGFP down to the control level, whereas when the solution is not salted, or salted up to 100 mM, we get more than 1 μ M of fluorescent protein. Two approaches can be followed. If the hemolysin has to be expressed directly in the water-in-oil emulsion, we can add salts up to 100 mM. Compared to the conductance value given in [51], this means that we would have a conductance ten times smaller, hence typically 100 pS. At 50 mV the current step due to the insertion of a single pore is supposed to be $\Delta I = G \cdot \Delta U = 5$ pA which is barely above the current noise we measure (typically 1 – 5 pA). Bilayers exhibit different breakdown voltages but it is typically difficult to go a lot higher than 50 mV. To be able to characterize single jumps, we chose to both increase the salt concentration and decrease the amount of introduced pores by diluting the TXTL after expression.



Effects of introduced KCl on protein expression. The TXTL reactions are made in 1.5mL Eppendorf tubes, incubated 5 hours at 29 ° C. We measure the resulting intensity on three samples of 10 μ L for each condition using the RotorQ.

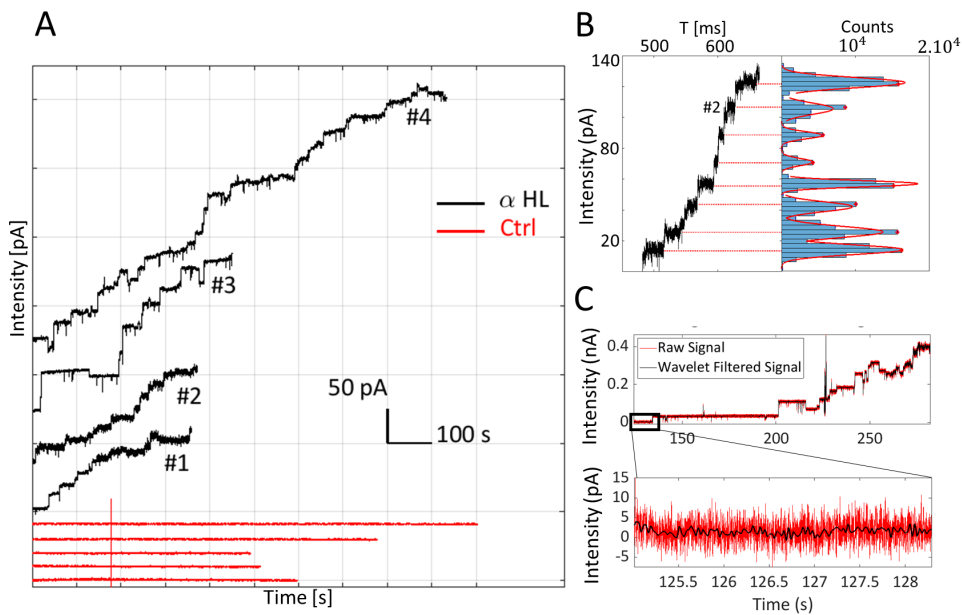
Figure 11.3: TXTL expression in presence of increasing [KCl] concentration.

3.3 Average conductance measurement

Trace currents were first denoised using a wavelet analysis as shown on Fig 11.4 C. Daubechies introduced wavelets to decompose linearly a function f on a set of vectors ψ_{mn} [56] (Discrete Wavelet Transform Denoising or DWT). Multiresolution analysis is performed to analyze the signal over several timescales. Wavelet denoising performs very well at separating sharp transitions from background noise. The Matlab routine included in the Wavelet toolbox uses the function `cmddenoise` with wavelets of `Symlet` type and a level 5 (Range of timescales explored by the wavelet function). After this analysis, the noise was reduced by a factor 5 (Fig 11.4 C). We show on Fig. 11.4 A individual traces for experiments where TXTL (extract 100%) was allowed to express α HL at the optimal temperature of 29 ° C for 5 hours. Current traces show neat jumps well above the average noise and demonstrate the insertion of more and more pores after the bilayer is formed. We repeated the same measurements on two types of controls. The first type of controls is done with a

similar reaction but diluted in KCl 500 mM at $t = 0$ hours. The 500X dilution stops the reaction and prevents any pore chemical synthesis. The resulting traces (red solid lines) are shown in Fig 11.4 A. We also checked on a control where no plasmid was added to the TXTL reaction that no jumps were observed.

The plot displays in total 4 traces for α HL expressed during 5 hours and 5 traces for the control. These traces are shifted vertically to ease the reading. Some traces display higher noise or a qualitatively different behavior with the current intensity decreasing over time. We did not analyse these traces, on the basis that if noise was higher the bilayer integrity could be suspected. Cases where intensity decreases show at best desorption of the pores but more likely loss of bilayer area in which some pores were embedded. We see that when the number of inserted pores increases, the resulting average current also increases and the signal becomes more noisy. We analyzed only the beginning of the traces when a few pores are inserted.



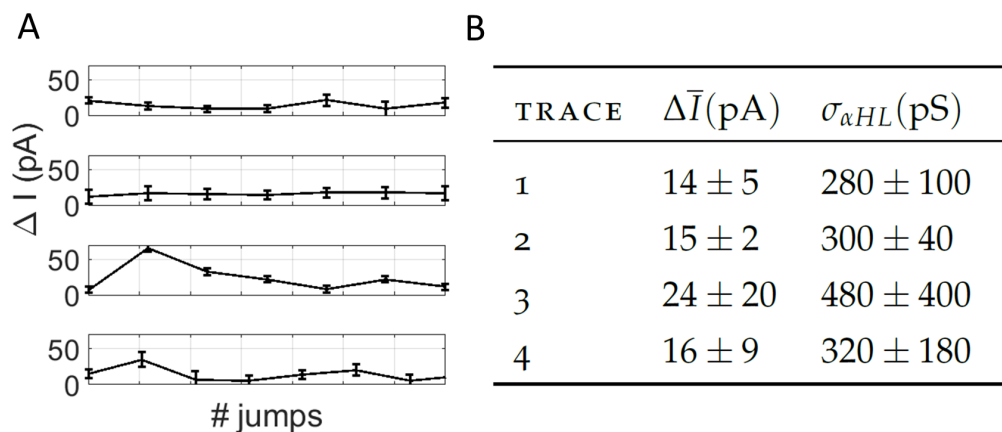
(A) Electrical traces for bilayers containing hemolysin (black solid line) and controls (red line). For the hemolysin population, the protein was expressed 5 hours before diluting the reaction in the KCl buffer. For the control population, the reaction was diluted at $t = 0$ and no protein was thus produced. (B) Detection of discrete current jumps through histogram binning. (C) Denoising electrical traces with wavelet transforms.

Figure 11.4: Description of electrophysiological recordings.

In Fig 11.4 B, we show how we computed discrete current jumps from individual traces. Bin edges are limited to 3 pA, in reasonable agreement with the average noise recorded during on-the-fly acquisition, and to limit the detection of local maxima on the histogram. Every local maximum of the histogram Fig 11.4 B is detected through the Matlab function `findpeaks`. We performed Gaussian Fits on peaks that are "prominent", i.e. at least 10% as frequent as the maximum of the histogram. We used all the bin edges distributed around the detected peak to fit the gaussian distribution. We used as lower boundary the mid-distance between the peak and the previous detected one. We used as upper boundary the mid-distance between the peak and the next one detected. The standard deviation inferred from the Gaussian distribution gives an error estimate around the peak value. For instance, on Fig 11.4 B, we detected the following maxima with the error associated: 14 ± 4 pA, 25 ± 5

pA, 41 ± 4 pA, 56 ± 2 pA, 70 ± 3 pA, 88 ± 3 pA, 105 ± 5 pA and 122 ± 4 pA. From these discrete events, we could compute the average intensity gap between each discrete jump - Fig 11.5.

We detected 8 jumps for the first three traces and 22 for the last one that was recorded for a longer time. We only probed the statistics of the first 8 jumps for each trace.



(A) Differences between each current jump (B) Mean Values of ΔI

Figure 11.5: Expected Current Jumps.

From the jumps associated to each trace, we computed the mean intensity (Fig 11.5 B) and derived the associated conductance. We used the expected theoretical value, 500 pS associated to a current jump of 25 pA at [KCl]= 500 mM to determine the proportionality A to the salts concentration in the formula $G = A \frac{\Delta I}{\Delta U}$.

From these results, we see that the individual current jumps fluctuate a lot even if they seem well discretized. We also found experimental values for conductances that are under what is predicted. We now discuss how this discrepancy can be understood knowing the details of hemolysin insertion.

3.4 Combinatorial insertion

To interpret the values of the current jumps, it is necessary to recall that pores can insert from both sides of the bilayer, according to previous experiments on supported membranes. We should see current jumps due to hemolysin inserted in one direction and in the other direction. One pore inserted gives two possibilities, one right-side or one left-side insertion (*config 1/0 or 0/1*). Two pores inserted give three possibilities, two right-side, one right-side and one left-side and two left-side (*config 2/0, 1/1 or 0/2*). The different available configurations for one or two pores inserted are represented in Fig 11.6. Auvray and coworkers showed that this asymmetry was due to the presence of the cap at one tip of the heptameric channel [51] and that symmetry could be recovered after urea denaturation of the protein.

In our configuration, it means that for N pores inserted, you can pick from 0 up to N pores on the left side, and the remaining pores come from the right side. This scheme is represented in Table 11.1. We indicate the expected current in the experimental working conditions - 50 mM [KCl], 50 mV - for different configurations. The table can be read as follow: for 1 pore in droplet 1 and 2 pores

in droplet 2, we should see an increase in current of 59 pA, which is proportional to $1 + 2 * 0.7 = 2.4\sigma_{\alpha HL}$.

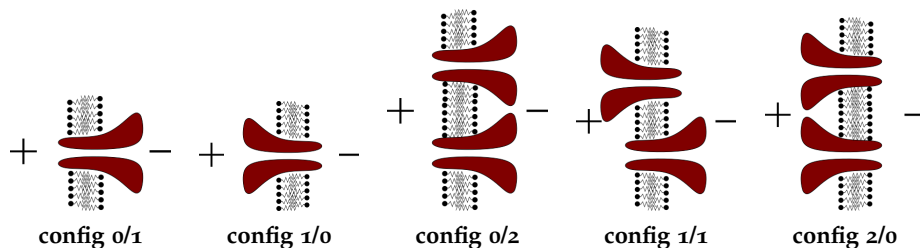


Figure 11.6: First available configurations for hemolysin insertion

CONFIG	I_{Th} (PA)	$\propto \sigma_{\alpha HL}$
0/1	17	0.7
1/0	25	1
0/2	34	1.4
1/1	42	1.7
2/0	50	2
0/3	51	2.1
1/2	59	2.4
2/1	67	2.7
3/0	75	3

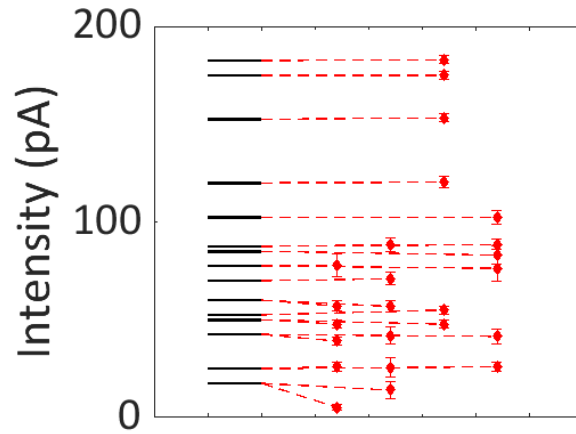
Table 11.1: Expected Current Jumps.

These expected current jumps can be represented as *intensity levels* in a loose analogy to discrete energy levels in atomic systems (Fig 11.7a). We tried to associate each experimental current jump $I_{exp,k}$ to the theoretical closest level $I_{th,i}$ by finding the minimum value $\frac{|I_{th,i} - I_{exp,k}|}{I_{th,i}}$, for the first 6 levels in each trace. Experimental points with their error bars (red) are aligned vertically according to the trace from which they are derived, which gives in total 4 vertical alignments. They are linked to their closest theoretical neighbor by a dashed red line. This alignment allows to assign to each experimental point the expected proportionality to the conductance (Table 11.1).

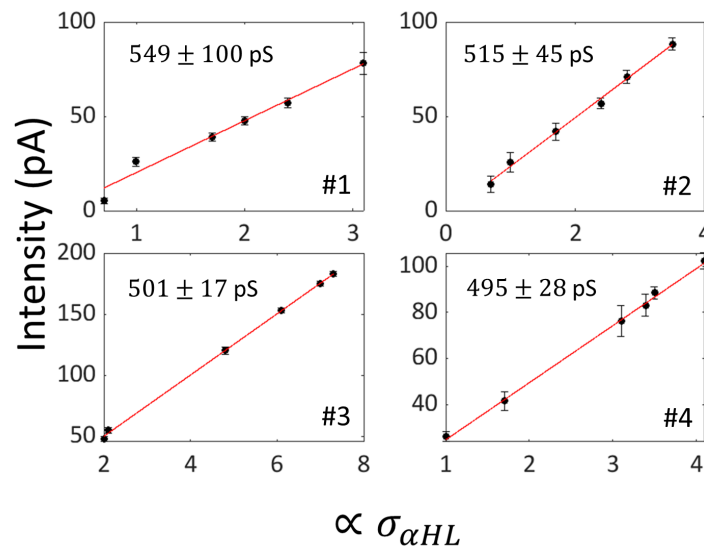
Then we can plot these current jumps with respect to their proportionality to the conductance and perform a linear fit to infer the experimental conductance. This is done Fig 11.7b for the 4 individual traces and the inferred conductance is given in pS in each frame. We find the following values: 549 ± 100 pS, 515 ± 45 pS, 501 ± 17 pS and 495 ± 28 pS. The first trace gives a significant error on $\sigma_{\alpha HL}$ (20% of the expected conductance) because of the origin offset. The remaining three give a reasonable estimate on the conductance value compared to what has been previously published.

It is however necessary to remain cautious as pure bilayers can sometimes display a behavior very similar to pore insertion events. Indeed, lipid bilayers show phase transitions between gel-like and fluid-like states, transitions known as chain melting. It has been reported that this diversity in phase behavior can lead to protein

channel-like electrical behavior [158], with no actual protein channels in the system. Membranes can even exhibit discrete conduction events, similar to the current jumps one would expect from the insertion of a transmembrane pore inside a bilayer. These changes are attributed to spontaneous lipid pores, whose opening can depend on pH, calcium concentration, temperature, pressure or voltage. Laub and coworkers [158] showed typical activities such as single channel events, conduction bursts, flickering, conduction spikes, multistep conductance and staircase behaviour in pure lipid bilayers. If we consider DPhPC alone, no gel to liquid crystalline phase transition was observed between -120 and 120 °C³. Fortunately, the lipid pore size is expected to change from one experiment to another. It is not the case for the protein pore [159], whose size is fixed in standard experimental conditions. We thus assume that because the individual conductance computed from current jumps is constant from one experiment to the next, we can reasonably link the current jumps to single hemolysin insertions. We would however need more experiments to confirm this trend. The experiments presented in this last chapter were done at the really end of my thesis. I thus did not have enough time to multiply the experiments and confirm statistically that the measured conductance was indeed fixed and imputable to hemolysin alone.



Theoretical levels of the expected current jumps are plotted in black. We represent next to them the red dots corresponding to the experimental current jumps detected on the 4 current traces, column 1 to 4. They are linked (red dashed line) to the corresponding theoretical level by finding the minimum of $\frac{|I_{th,i} - I_{exp,k}|}{I_{th,i}}$.



Individual conductance fits for the 4 different traces. We use the proportionality to the expected conductance to align the individual current jumps and fit accordingly the conductance.

Figure 11.7: Determining the experimental conductance of hemolysin.

CONCLUSION

In this last part, we have summarized how we managed to incorporate a cell-free reaction in a droplet interface bilayer environment. We demonstrated the successful localization of cell-free synthesized membrane proteins at the bilayer through confocal quantification of fluorescence. We also managed to prove native channel activity in the case of hemolysin by performing single channel electrophysiological measurements. We measured the individual conductance of the pore using a combinatorial approach to multiple pore insertions in the bilayer and found a value in reasonable agreement with the previously published data on hemolysin conductance.

The whole manuscript presents the minimalist design of an experimental model to quantitatively study passive molecular transport in biomimetic tissues. We built a rudimentary soft matter version of a biological tissue using a novel technique for assembling synthetic membranes of the *Droplet Interface Bilayer* type. We demonstrated with an original method that it was possible to produce easily compact water-in-oil emulsions by taking advantage of the differences in surface energies of the three phases in presence, water, oil and air. This capillary trap is able to build versatile geometries of 1D and 2D networks in an easy and cost-effective way, while keeping a controlled polydispersity under 1%. We chose to functionalize lipid bilayers by inserting hemolysin in the DIB networks. This pore addition implements communication in our artificial tissue model. We connected the average time taken by a fluorescent probe to go from one droplet to another to the number and spatial arrangement of the pores with a microscopic description based of the first passage times. The theoretical framework of continuous time random walks bridges the gap between the continuous experimental time description of the diffusion and the discrete spatial positions of our network. From the scaling between the number of introduced monomers and the inferred number of adsorbed heptamers in the membrane we were able to deduce a typical cluster size of pores. This indirect measurement of pore clustering can be put in perspective with previous experimental and numerical findings on the aggregation of membrane proteins in bilayers. Last, we tried to upgrade our DIB networks towards mechanosensitive arrays by inserting MscL in place of hemolysin. This mechanosensitive pore is hydrophobic and thus challenging to insert in its native configuration in artificial membranes. We thus implemented a cell-free reaction in the droplet networks in order to be able to produce MscL *in situ* and insert it in the membrane. We demonstrated in the case of hemolysin that our protocol successfully leads to the production and spontaneous insertion of this pore. We showed the localization of the pore in the bilayer with confocal microscopy fluorescence measurements. To evidence individual insertion of the fully functional pore, we recorded the intensity across the bilayer in a voltage-clamp mode. Given pores can insert from both parts of the bilayer, we inferred the expected hemolysin conductance from combinatorial analysis of the current jumps. One of the long term perspective of this work is to create mechanosensitive networks containing MscL, where the diffusion properties could be modified via a mechanical stimulus. It implies fulfillment of the following experimental procedures in the immediate continuity of the work presented here in the case of TXTL produced hemolysin:

- We need to produce MscL directly in the bilayer arrays whereas the previous work on individual jumps characterization is based on hemolysin expression *prior* to dilution and droplet formation. We would have to adapt the electrophysiological protocol to the low salt concentration regime ([KCl]=100mM) to enable TXTL expression directly in the droplets. We would first measure voltage-current curves with *in situ* expression of hemolysin. The yield of the reaction could be changed by introducing variable amounts of plasmids to ensure bilayer integrity.
- The protocol with hemolysin expression could be readily adapted to the expression of MscL mutants using linear DNA. Over-sensitive mutants encoded by the plasmid P28a-MscL-G22E are opened all the time and could be considered in a first approximation as "inert pores".

On longer timescales, prospects concerning MscL activity screening through electrophysiological measurements will require the design of a platform to mechanically stretch the bilayer. Current protocols on bilayer embedding in a gel are being developed at Laboratoire Jean Perrin in the group.

If controlled mechanical deformations can be implemented on DIB networks, our artificial tissue model could be used to transpose some aspects of the developmental mechanics involved in morphogenesis. In these simplified approaches, couplings such as force transmission through cytoskeleton are eliminated. DIB networks should thus provide a platform to investigate the force-from-lipid mechanistic scheme in multicellular assemblies, meaning the ability of bilayers alone to transmit forces to embedded proteins.

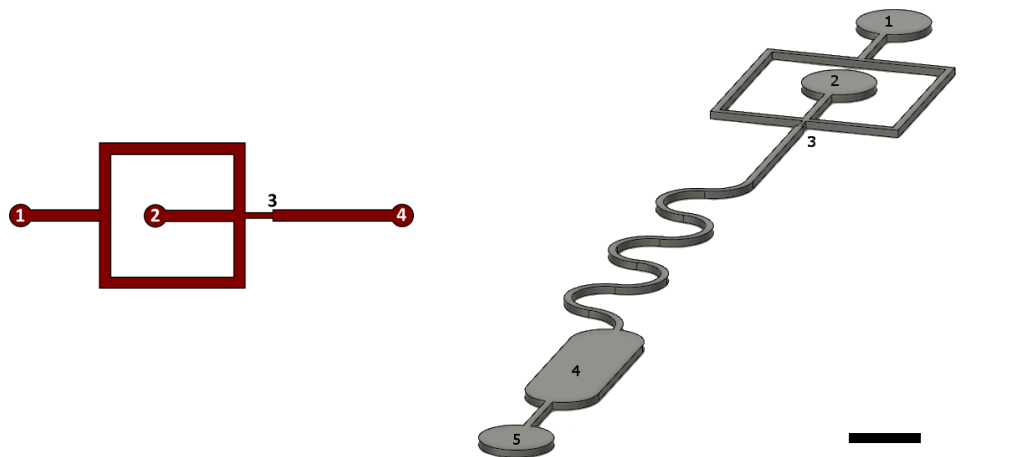
MICROFABRICATION TECHNIQUES

All the microfluidic chips we use in [Part i](#) as well as the patterns for DIB arrays ([Part i](#)) are custom made in our laboratory. We use microfabrication techniques that are detailed below.

1 MICROMILLING

We use a 4-axes Minitech micromilling machine supplemented with tools from NS tools and PMT tools. We use PMMA plates as raw material. These plates are surfaced with a 3 mm regular mill prior to the design of smaller details at the submillimetric scale. We ensure this way to work in a plane perfectly parallel to the x and y axis of the machine.

2 DESIGN OF MICROFLUIDIC CHIPS



Flow focusing geometry 1) Inlet for Oil
2) Inlet for Water 3) Exit canal 4) Outlet

CAO of counter mold engineering - scalebar 1 mm

Figure A.1: Microfluidic chip conception for emulsion production

3 DROPLET COMPACTION OUT OF THE CHIP

In this configuration, we use a microfluidic chip with a simple cross as a flow-focusing geometry - Fig [A.1a](#). All the channels are squared with $0.1 \times 0.1 \text{ mm}^2$ dimensions except for the constriction that pinches off and produces the emulsion ($0.05 \times 0.05 \text{ mm}^2$). The channels are milled with flat end micromills. We seal the chip by using a slab of PDMS (20% w/w curing agent) as a gasket between the micromilled PMMA circuit and a smooth PMMA cover. Etancheity is maintained with a pair of clamps.

Our aim was to collect the emulsion at the end of the chip and synchronize this outlet with a printing head that would simply deposit the droplets in the desired pattern. This printing head would thus have to work at the same frequency than the production rate of the microfluidic chip. We thus investigated the range of microfluidic frequencies at which the system reproducibly produces droplets and found out that the lower frequency boundary was around 100 Hz. This is hardly compatible with mechanical printing downstream of the on-chip production.

In a second step, we thus sought to pack the droplets directly on the microfluidic chip.

4 DROPLET COMPACTION IN THE CHIP

We tried to create a large reservoir to directly pack the droplets on the chip - Fig A.1b. To succeed in this design, we had to change the way the chip is fabricated. We shaped the PDMS on a PMMA cast, milled using CAO design with Autodesk. We sealed the PDMS channels with a glass slide using plasma activation. This technique was closer to conventional soft lithography techniques than the method described in Section 3. We added to the flow focusing geometry a long mixing outlet upstream of the reservoir to equilibrate faster the monolayers around the droplets. In this geometry we managed to produce DIBs. We were developing simultaneously the capillary trap and found out that this last emulsification process would ease the introduction of a source droplet as well as the reproducible arrangement of droplets in 2D arrays. We thus abandoned microfluidics on-a-chip production and resumed to inkjet like printing.

B

CHEMICAL POTENTIAL CALCULUS

The development we present here is adapted from [20]. We use a grand-canonical ensemble to describe the average number of adsorbed pores $\langle N_a^p \rangle$. N_a^p fluctuates because of a continuous exchange of monomers between the bilayer and the solution. In this model, each adsorption site has a partition function ζ (Eq B.1) associated to the absorption state described with an energy $\epsilon_0 < 0$ and an occupancy state 0 or 1.

$$\zeta = 1 + e^{-\beta(\epsilon_0 - \mu)} \quad (\text{B.1})$$

The great partition function Ξ can be easily computed if the sites are considered independant and distinguishable. We call the total number of available sites $N_s = \frac{\mathcal{A}_D}{\mathcal{A}_p}$.

$$\Xi = \zeta^{N_s} \quad (\text{B.2})$$

We develop the expression of the grand potential J to compute the average number of occupied sites $\langle N_a^p \rangle$ Eq B.4:

$$J = -kT \ln \Xi = E - \mu N_a^p - T.S \quad (\text{B.3})$$

$$\langle N_a^p \rangle = -\frac{\partial J}{\partial \mu} = kTN_s \frac{\partial \ln(1 + e^{-\beta(\epsilon_0 - \mu)})}{\partial \mu} = N_s \frac{e^{-\beta(\epsilon_0 - \mu)}}{1 + e^{-\beta(\epsilon_0 - \mu)}} \quad (\text{B.4})$$

We then retrieve the chemical potential:

$$\beta(\mu - \epsilon_0) = \ln \frac{N_a^p}{N_s - N_a^p} \quad (\text{B.5})$$

With the assumption that the membrane is not saturated, we can assume that $N_s - N_a^p \simeq N_s$ which brings us to the following simplified version of the chemical potential for adsorbed monomers:

$$\mu = \mu_0 + kT \ln \frac{N_a^p}{N_s} \quad (\text{B.6})$$

Because $N_a^p = C_s \cdot \mathcal{A}_D$ we get:

$$\mu = \mu_0 + kT \ln C_s \mathcal{A}_p \quad (\text{B.7})$$

The relation between the chemical potential of the monomer in solution and the adsorbed pore concentration is given by the extensivity of the free energy F :

$$F_{tot} = F_m + F_p \quad (\text{B.8})$$

$$\frac{\partial F_{tot}}{\partial N_{aq}^m} = \frac{\partial F_m}{\partial N_{aq}^m} + \frac{\partial F_p}{\partial N_a^p} \frac{dN_a^p}{dN_{aq}^m} \quad (\text{B.9})$$

At equilibrium the total free energy is minimum with respect to its variables (T, N_{aq}^m, N_a^p) and :

$$N = C_i \cdot V = N_{aq}^m + 7 \cdot N_a^p \quad (\text{B.10})$$

Hence

$$0 = \mu_{aq}^m + \mu_a^p \cdot \left(\frac{-1}{7}\right) \quad (\text{B.11})$$

$$\mu_a^p = 7\mu_{aq}^m = 7kT \left(\mu_{aq,0}^m + \ln \frac{[\alpha HL]_{aq}}{C^0} \right) \quad (\text{B.12})$$

Because $C_i \cdot V = [\alpha HL]_{aq} V + 7C_s \mathcal{A}_D$ and $[\alpha HL]_{aq} V \gg 7C_s \mathcal{A}_D$,

$$kT \left(\mu_{a,0}^p + \ln C_s \mathcal{A}_p \right) = 7kT \left(\mu_{aq,0}^m + \ln \frac{C_i}{C^0} \right) \quad (\text{B.13})$$

$$K = 7 \ln C_i / C_0 - \ln C_s / C_{0,s} \quad (\text{B.14})$$

With Eq B.14 we extract the scaling between the introduced concentration in monomers C_i and the surface concentration of adsorbed pores C_s :

$$C_s = \frac{N_a^p}{\mathcal{A}_D} \propto C_i^7 \quad (\text{B.15})$$

CELL-FREE PROTOCOLS

We give here technical details on the composition and yield of TXTL reactions.

1 ENERGY BUFFER COMPOSITION

ENERGY BUFFER
50 mM Hepes pH 8
1.5 mM ATP and GTP, energy sources and mRNA units
0.9 mM CTP and UTP, mRNA units
0.2 mg/mL tRNA
0.26 mM coenzyme A that is involved in the regeneration pathway (oxidator)
0.33 mM NAD, redox electron carrier
0.75 mM cAMP
0.068 mM folinic acid
1 mM spermidine
30 mM 3-PGA

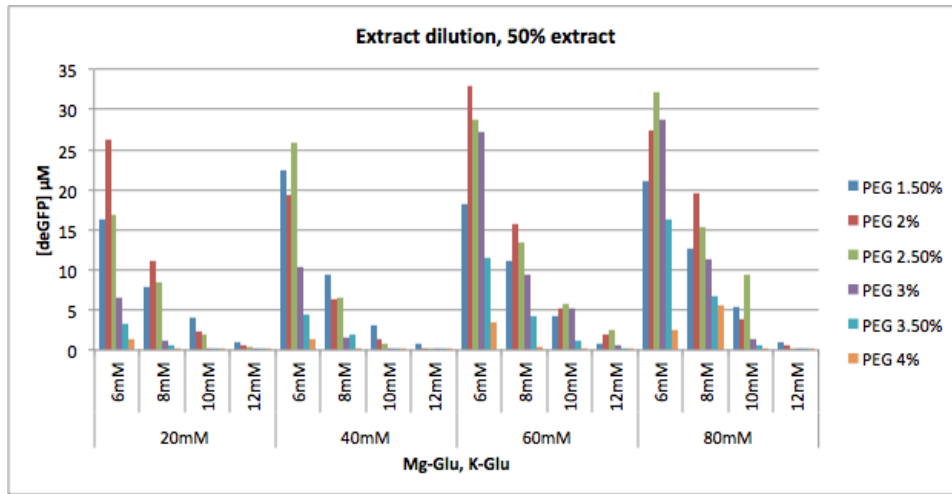
Table C.1: Energy Buffer Composition

2 PLASMID CONSTRUCTS

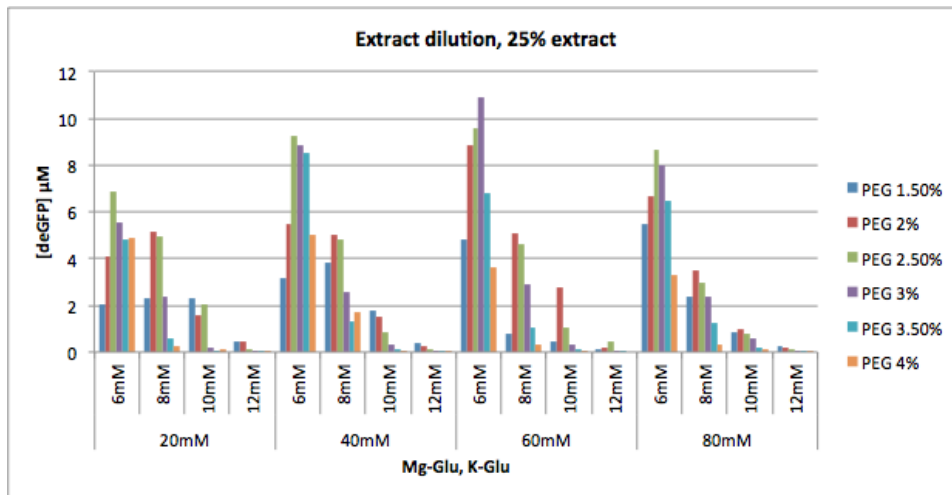
NAME	HOST BACTERIA	PLASMID TYPE	PROTEIN OUTPUT
P70 σ 28	KL740	p15A	σ 28
P70t7RNAP	KL740	p15a	T7RNAP
P70deGFP	KL740	colE1	eGFP
P70mRuby	DH5 α /KL140	colE1	mRuby
P28deGFP	DH5 α /JM109	colE1	eGFP
P28aHL	JM109	colE1	aHL
P28aHLeGFP	JM109	colE1	aHLeGFP
P28MscL	JM109	colE1	MscL
P28MscLeGFP	JM109	colE1	MscLeGFP
P28MscLmRuby	JM109	colE1	MscLmRuby

Table C.2: Construct details

3 EXTRACT DILUTION DATA



(a) Dilution 50 pc



(b) Dilution 25 pc

Figure C.1: Extract Dilution Data, Source V. Noireaux Lab, Jon Garamella

D

ADDITIONAL RESULTS REGARDING CELL-FREE REACTIONS

1 PRODUCTION IN SUVs

SUVs FABRICATION Small Unilamellar Vesicles (SUVs) can be formed by extrusion at a 2 mg/mL concentration in an aqueous buffer and supplemented to the reaction mix. They are formed in an Avanti Polar Lipid Extruder, according to the following protocol. DPhPC lipids are dried under nitrogen in 2 mg aliquots. The coating is then hydrated with S30B Buffer (14 mM MgGlu, 150 mM KGlu, 5 mM Tris pH 8) to reach a final concentration of 2mg/mL. The solution becomes blurry. After 5 cycles of freeze and thaw, the solution is extruded 20 times through a 0.2 μ m polycarbonate membrane (Whatman) then again 20 times through a 0.1 μ m membrane.

We dilute the cell-free reaction to 50% (resp. 25%) to have a final lipid concentration of 300 μ g/mL (resp. 500 μ g/mL). Dilution is performed on the cellular extract only, not on the full TXTL reaction. Instead of adding 28 μ L of extract in the normal regime, we add 14 μ L (resp. 7 μ L) of extract and complement it with 14 μ L (resp 21 μ L) of S30B buffer containing the liposomes. We adjusted salt and PEG concentrations to the new extract dilution using supplementary data about extract dilution (Fig C.1). We give the compositions of the two types of dilution when using SUVs in S30B in the following tables: [Table D.1](#) and [Table D.2](#)

NAME	v(μ L)	C _f (mM)
Cellular extract	14	
S30B	14	
(\pm SUVs 2 mg/mL)		
KGlu	1,8	0,06
MgGlu	3	0,006
Maltodextrine	5,4	0,03
3PGA	5	0,005
AA	15,9	0,003
PEG	4,5	2
P70as28	1,8	0,2
P28aMscLeGFP	9	5
Water	15,6	

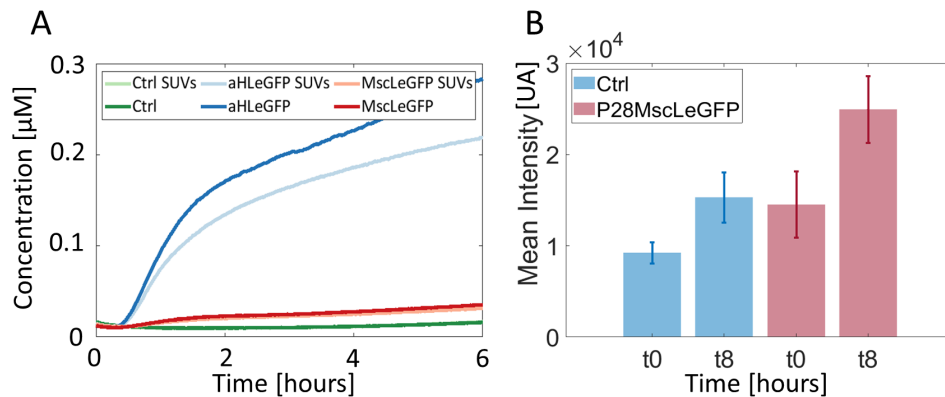
Table D.1: Reaction assembly, 50% extract

PRODUCTION OF MSCLEGF AND MSCLRUBY We tried to produce the protein in bulk and solubilize it using the added SUVs. These liposomes are a way of introducing membrane support in aqueous reactions. We get mixed results for protein solubilization - Fig D.1. In bulk fluorimetry kinetics, the presence of liposomes seems to diminish the reaction yield in the case of a soluble membrane protein

NAME	v(μ L)	C _f (mM)
Cellular extract	7	
S30B	21	
(\pm SUVs 2 mg/mL)		
KGlu	1,8	0,06
MgGlu	3	0,006
Maltodextrine	5,4	0,03
3PGA	5	0,005
AA	15,9	0,003
PEG	6,75	3
P70as28	1,8	0,2
P28aMscLeGFP	9	5
Water	13,4	

Table D.2: Reaction assembly, 25% extract

such as α HLeGFP (Fig D.1 A). In the case of MscLeGFP, no extra solubilization seems to be brought by the presence of liposomes. The interpretation we carry out is the following: bringing new components to the TXTL reaction hinders slightly the efficiency of the process, maybe because of non-specific competition. In the case of MscLeGFP production, the precipitation of the protein itself is the major issue regarding TXTL integrity and a small intake of SUVs does not change the outcome.



(a) A) Production in added liposomes configuration B) Monitoring of MscLeGFP expression in water in oil emulsions (extract dilution 25%, supplemented with SUVs)

Figure D.1: Protein solubilization, dilution TXTL 25%

The control experiment itself - a TXTL assembly without plasmid - shows a little increase in fluorescence in the GFP excitation-emission spectrum. We validated these observations under the microscope (Fig D.1 B), where droplets of radius ranging between 40 and 50 μ m were generated after expression, $\Delta t = 0$ hour and $\Delta t = 8$ hours. We see an increase in fluorescence signal for the MscLeGFP case with respect to the control.

Given that we do not manage to solubilize hydrophobic membrane proteins before encapsulation, we have chosen to focus on expression after emulsification. This process implemented in DIBs [Section 2.2](#) is similar to the case study of liposomes presented [Section 2.1](#).

PUBLICATIONS

Quasistatic Microdroplet Production in a Capillary Trap

M. Valet,¹ L.-L. Pontani,^{1,2} A. M. Prevost,¹ and E. Wandersman^{1,*}

¹*Sorbonne Universités, UPMC Université Paris 06, UMR 8237, Laboratoire Jean Perrin, F-75005 Paris, France*

²*Sorbonne Universités, UPMC Université Paris 06, UMR 7588, Institut des Nanosciences de Paris, F-75005 Paris, France*

 (Received 26 July 2017; revised manuscript received 8 September 2017; published 8 January 2018)

We develop a method to produce aqueous microdroplets in an oil phase, based on the periodic extraction of a pending droplet across the oil-air interface. This interface forms a capillary trap inside which a droplet can be captured and detached. This process is found to be capillary based and quasistatic. The droplet size and emission rate are independently governed by the injected volume per cycle and the extraction frequency. We find that the minimum droplet diameter is close to the injection glass-capillary diameter and that variations in surface tension moderately perturb the droplet size. A theoretical model based on surface energy minimization in the oil-water-air phases is derived and captures the experimental results. This method enables robust, versatile, and tunable production of microdroplets at low production rates.

DOI: [10.1103/PhysRevApplied.9.014002](https://doi.org/10.1103/PhysRevApplied.9.014002)

I. INTRODUCTION

The development of microfluidics over the last three decades has enabled monodisperse droplet production [1] at rapid emission rates (approximately 100 Hz to 10 kHz). In a typical—now popular—flow-focusing [2] or *T*-junction [3] microfluidic chip, the accessible droplet size covers one to a few hundred micrometers and is tuned by the channel size and flow rates of the dispersed and continuous phases. These techniques allow fast encapsulation of chemicals and can produce microreactors for the high throughput screening of drug efficiency [4] or directed evolution [5]. They have also been successfully used to produce colloids [6] and microcapsules [7]. However, they are not well suited when low production rates are required to allow surfactants with slower dynamics to stabilize the droplets. This is the case, for instance, with protein-stabilized emulsions [8], phospholipids, that are used to create droplet-interface bilayers [9], or particles, that can lead to microstructured droplets and colloidosomes [10]. For these reasons, various *on-demand* microfluidic systems have been developed to produce individual microdroplets with tunable rates. They rely on the introduction of additional external forces (via an electric field [11], a mechanical excitation [12,13], a laser beam [14]) that destabilize the oil-water interface and trigger the droplet formation. Such microfluidic systems with tunable production rates make it easy to implement droplet-based 3D printers [15] that pave the way to the engineering of artificial tissues [16].

We present in this work an additional and simple way to produce aqueous droplets by destabilizing the oil-water

interface. This method, surprisingly undocumented, is on demand and consists of pulling out a capillary (filled with the aqueous solution) from the oil-air interface (Fig. 1). We show that the process of droplet formation is quasistatic and yields aqueous droplets in oil of typical size the inner capillary diameter d , ranging from 20 to 700 μm , in the low-frequency limit (< 1 Hz). Using either a *single* syringe pump or only the hydrostatic pressure, we can easily produce droplets with a polydispersity (standard deviation of the radius distribution over the average radius) of about 1%, i.e., comparable to standard microfluidic techniques. Qualitatively, since the oil (*o*)–water (*w*) surface tension is lower than the air (*a*)–water one ($\gamma_{ow} < \gamma_{aw}$), it is energetically more favorable for an aqueous droplet to remain in oil than to form an air-water interface. The droplet can thus be trapped and detached in oil [Figs. 1(b)–1(d)]. Quantitatively, these findings are confronted with a model that compares interfacial energies of attached and detached droplets. Compared to the abovementioned methods [11,12,14], this technique relies on a softer forcing of the oil-water interface, which makes it compatible with the use of any material, such as charged components or fragile biological material and amenable for a wide range of applications.

The paper is organized as follows. First, we detail in Sec. II the experimental setup and protocols. We then present in Sec. III our findings related to the droplet detachment at short time scales and the droplet size distribution. We also show that the origin of the detachment process is purely governed by capillarity. We then derive a theoretical model and compare it to our experimental data. Finally, we conclude the paper in Sec. IV with potential applications of the implemented technique.

*elie.wandersman@upmc.fr

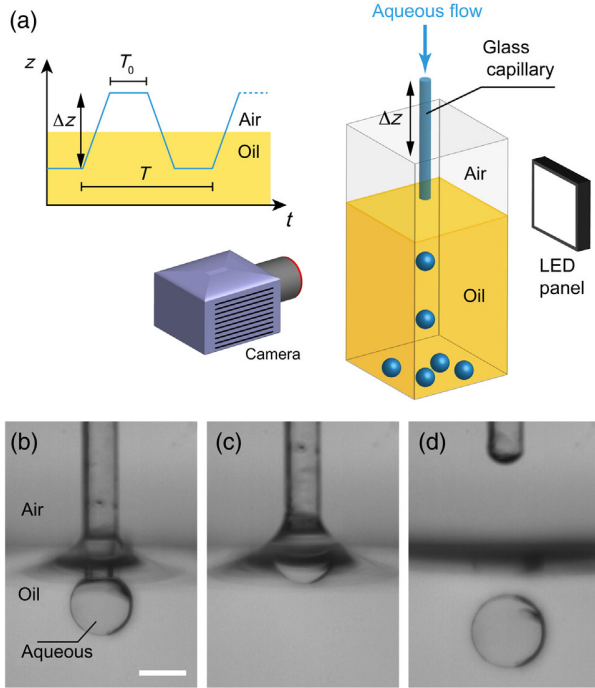


FIG. 1. (a) Sketch of the setup. A syringe pump imposes a flow of water through a glass capillary fixed to a translation stage. This one imposes a displacement of capillary tip $z(t)$, which is shown in the graphical inset. Imaging is performed with a LED panel and a camera. (b)–(d) Snapshots obtained with a fast camera. (b) The attached aqueous droplet ($[\text{SDS}] = 8 \text{ mM}$) is immersed in silicon oil at $t = t_0$. (c) The capillary moves up at $t = t_0 + 123 \text{ ms}$ and (d) the droplet finally detaches at $t = t_0 + 1.213 \text{ s}$. In (b), the white bar is $400 \mu\text{m}$ long.

II. MATERIALS AND METHODS

A. Experimental setup

The experimental setup [Fig. 1(a)] consists of a syringe pump (KDS Scientific Legato 270) that imposes the flow of an aqueous solution at a flow rate Q in a glass capillary (inner diameters $d = 2R_0$ ranging from 20 to $700 \mu\text{m}$; details below). The capillary is mounted on a motorized translation stage (M-ILS250 CCL, Newport) to impose a vertical and cyclic up-down motion across the oil-air interface [Fig. 1(a), the graphical sketch] with an amplitude $\Delta z = 2 \text{ mm}$ and a constant velocity v , ranging from $100 \mu\text{m/s}$ to 5 mm/s . A latency time $T_0 = 0.45 \text{ s}$ is required to reverse the direction of the translation stage, during which the capillary stays immobile. The total period of the displacement $T = 2(T_0 + \Delta z/v)$ is measured and is about 1.7 (40) s for $v = 5$ (0.1) mm/s. In the first phase of the experiment, the capillary is immersed in the oil container, and an aqueous droplet grows [Fig. 1(b)]. In the second phase, the capillary moves back up [Fig. 1(c)] and, as discussed below, the droplet may (depending on its size) detach [Fig. 1(d)] and sediment in the oil phase. Note that, to test the versatility of the technique, we also impose the

flow through hydrostatic pressure, which makes the whole setup quite inexpensive (see the Appendix for instruction on how to build such a setup at low cost).

B. Imaging the droplets

We characterize the droplet detachment process by optical imaging. Two different types of experiments are performed independently.

- (a) On the one hand, we use fast imaging with a Photron Fastcam APRX RS camera ($1024 \times 1024 \text{ pixels}^2$, 8 bits, 3000 frames/s), combined with a high-magnification Schneider Optics objective, to follow the detachment process at short time scales. Two types of imaging are implemented: first, using white light in transmission with a light-emitting-diode (LED) panel (Moritex MDBC CW 150) and, second, using fluorescence imaging to visualize the oil meniscus. For the latter, the oil is dyed with Nile red (Sigma Aldrich) at saturation, and it is imaged with a laser sheet to selectively illuminate the meniscus and not the surrounding oil [Fig. 2(a)]. The light source is provided by a green solid-state laser (Coherent Compass 315 M of wavelength $\lambda = 532 \text{ nm}$). The emitted light is collected through a tetramethylrhodamine-isothiocyanate emission filter. The laser sheet is obtained by first enlarging the laser beam to a final diameter of $950 \mu\text{m}$ (using a homemade beam expander with a magnification of about $8\times$ and consisting of two plano-convex spherical lenses (Thorlabs), and subsequently focusing it using a cylindrical lens of focal length 30 mm [Fig. 1(b)]. The beam thickness at its waist is measured at $30 \mu\text{m}$.
- (b) On the other hand, we record images of hundreds (typically $N = 100\text{--}500$) of detached droplets for each experimental condition, using a Chameleon3 (Point Grey, $1280 \times 1024 \text{ pixels}^2$, 8 bits) camera equipped with a high-magnification Navitar objective (with a maximum spatial resolution of $2.1 \mu\text{m}/\text{pixel}$). The imaging is performed in a transmission geometry, using a LED panel. To measure the size distribution of the droplet, we synchronize the motor displacement and the camera acquisition using LABVIEW (National Instruments). This allows us to record recursively a single image of the droplet produced at each cycle. Measures of the droplet radii are obtained by detecting their edges using a custom made MATLAB (MathWorks) routine.

C. Chemical solutions

To probe the ubiquity of the technique, experiments are performed using both ionic and nonionic surfactants. As a standard ionic surfactant, we use sodium dodecyl sulfate (SDS) aqueous solutions at various concentrations (from 0.08 mM to the critical micellar concentration [17] of

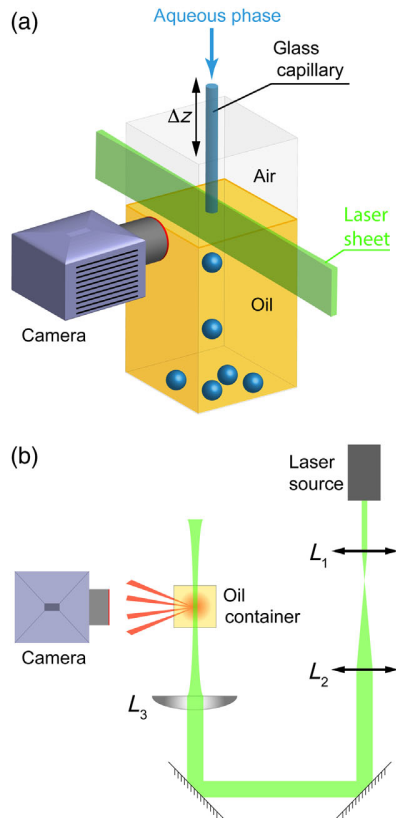


FIG. 2. (a) Sketch of the laser-sheet-based fluorescence-imaging setup. (b) Construction of the laser sheet. The light source is a green solid-state laser of wavelength $\lambda = 532$ nm. The beam expander consists of two plano-convex spherical lenses (L_1 and L_2) of focal lengths 18 and 150 mm, respectively. The laser sheet is obtained using a plano-convex cylindrical lens (L_3) of focal length 30 mm and is focused on a homemade oil container. The fluorescence emitted light is collected with a fast camera.

8 mM). In this case, the corresponding oil phase is silicon oil (viscosity 5 mPa s, Sigma Aldrich). As a nonionic surfactant, we use Span 80 (Sigma Aldrich) dispersed in pure hexadecane at a mass concentration of 2 wt %. In that case, the aqueous phase is pure water.

D. Glass capillaries

Capillaries with inner diameters d ranging from 20 to 100 μm are prepared with pipette pulling techniques, using glass capillaries from Drummond (calibrated capillary micropipettes, 25 μl). Each capillary is pulled in a laser-based micropipette puller (P-2000, Sutter Instrument). The tip of the capillary is then cut and adjusted to the desired inner diameter with a microforge (Narishige). Capillaries with inner diameters of 197 μm were purchased from Molex (Polymicro Technologies capillary tubing). The polymer coating around the glass is removed by burning it gently before rubbing it out. The capillary is then cut with a ceramic cutter to obtain a flat tip. Capillaries with inner

diameters of 700 μm were purchased from Drummond (calibrated capillary micropipettes, 30 μl). In order to make the capillaries hydrophobic, we expose them for 2 h to a vapor of 1H,1H,2H,2H-perfluorodecyltrichlorosilane, 96% (Alpha Aesar, Thermo Fisher Scientific), under a medium vacuum.

III. RESULTS AND DISCUSSION

A. Droplet detachment at short time scales

As the glass capillary is pulled out from the oil bath, the oil meniscus is deformed and the aqueous droplet is potentially (depending on its size) detached [Figs. 2(b)–2(d)]. Because of the oil meniscus surrounding the droplet, the exact shape of the droplet cannot be extracted. We can, however, use the laser-sheet technique to image the oil meniscus and test whether it is still present up to the droplet detachment (Fig. 3). To ease the visualization of the oil meniscus on the capillary, the container is filled with oil to the top. Figure 3(a) shows a typical image milliseconds before detachment. Semiquantitative analysis of intensity profiles normal to the direction of the glass capillary clearly shows a

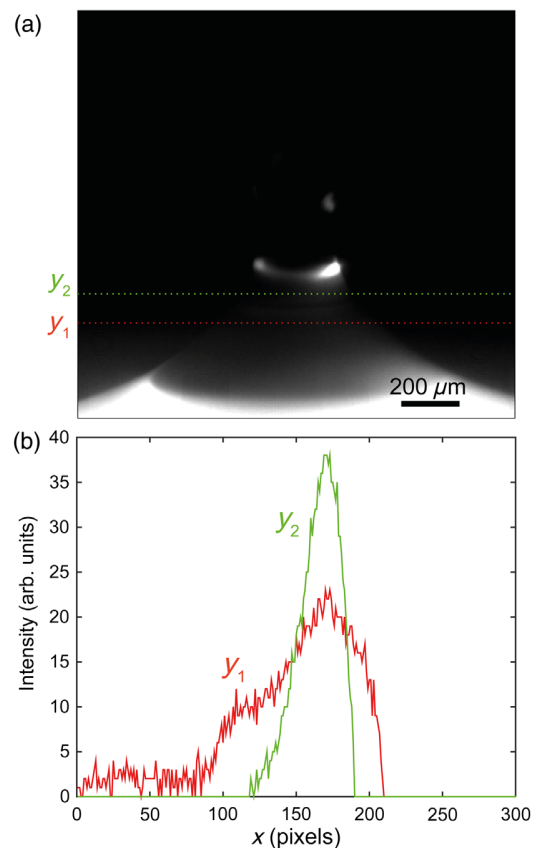


FIG. 3. (a) Laser-sheet-based fluorescence imaging of a Nile-red dyed hexadecane meniscus around a pure water microdroplet (not visible) formed at the tip of a glass capillary of inner diameter $d = 197$ μm . (b) Intensity profiles along two directions, y_1 and y_2 , normal to the capillary axis.

fluorescent signal from the oil at the location of the meniscus [Fig. 3(b)]. It suggests that a thin film of oil is still present close to detachment.

B. Tuning the droplet size

We investigate the minimal droplet size one can obtain for a given surface tension. We perform experiments with a capillary ($d = 197 \mu\text{m}$) filled with a SDS solution at 8-mM concentration. We keep the time period of the displacement T constant and gradually decrease the flow rate Q . For each Q , we measure the average radius [Fig. 4(a)]. For $Q < Q^*$, we do not produce a droplet per cycle. The corresponding minimal droplet radius R_d^* is about $2R_0$. At a given Q , the total volume of injected aqueous phase per cycle is QT . One thus trivially expects that $R_d = [3/(4\pi)QT]^{1/3}$. The data are well fitted by this equation [Fig. 4(a) and the inset of Fig. 4(b)]. Despite its apparent simplicity, this dependence on Q provides a convenient control parameter for tuning the size of the droplet above R_d^* . For droplets larger than R_d^* (by about a factor of 1.5), the polydispersity is around 1% or less [inset of Fig. 4(a)]. We find that approaching the detachment instability limit at R_d^* , the polydispersity increases but never exceeds 5%. Last, note that the droplets produced in the capillary trap have sizes much smaller than what would be obtained by a gravity-based destabilization, i.e., with an immobile aqueous droplet growing in oil. Using Tate's law [18], one expects $R_d^{\text{max}} \approx \{[3\gamma_{ow}R_0]/2(\rho_w - \rho_o)g\}^{1/3} = 1.3 \text{ mm}$, with ρ_w (ρ_o) representing the mass density of water (oil). This compares well to our measured value of $1.3 \pm 0.01 \text{ mm}$. The capillary-trap method presented in this work is therefore efficient in producing small droplets since $R_d^{\text{max}} \approx 7R_d^*$.

We also investigate whether the size of the droplet depends on the extraction velocity by forming droplets at different v values, in the range 0.1–5 mm/s but with a constant QT value. In practice, we keep Δz and T_0 constant and adapt the value of Q accordingly. The corresponding radii R_d are plotted as a function of v in Fig. 4(b) and show that R_d does not depend on v . As a consequence, the frequency of the droplet production can be tuned by orders of magnitude, from about 10 mHz to 1 Hz in our case. In a second set of experiments, we have investigated how the size of the droplets depends on R_0 . On the one hand, we perform these experiments with the [SDS] = 8 mM solution in silicon oil and, on the other hand, with the pure water in a Span 80–hexadecane mixture. The two systems have similar oil-water surface tension ($\gamma_{ow} \approx 10 \text{ mN/m}$ [17,19]). These experiments are performed by either controlling Q or using the hydrostatic pressure to impose the flow. We make sure that the droplet production is stable and only consider experiments for which at least 100 droplets can be produced, with one per cycle. We plot on Fig. 5(a) the average droplet radii as a function of R_0 . In this representation, R_d^* is given at a constant R_0 by the lowest value in the set of points. Over the whole range of R_0

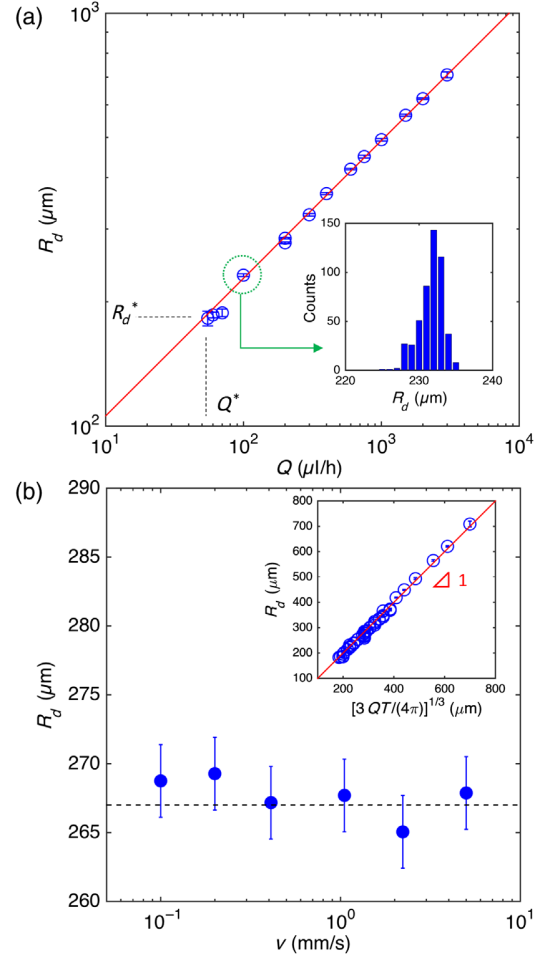


FIG. 4. (a) R_d versus Q ($d = 197 \mu\text{m}$, [SDS] = 8 mM, $v = 5 \text{ mm/s}$). The solid line is the fit $R_d = KQ^{1/3}$, with $K = 49.1 \pm 0.3 \mu\text{m h}^{1/3} \mu\text{l}^{-1/3}$, in good agreement with the expected value, $K = [3T/(4\pi)]^{1/3} = 48.5$. Q^* and the corresponding R_d^* value are shown on the graph. (Inset) Histogram of R_d ($N = 500$ droplets), for $Q = 100 \mu\text{l/h}$ (average radius of $232.1 \mu\text{m}$ and standard deviation of $1.8 \mu\text{m}$, yielding a polydispersity of 0.8%). (b) R_d as a function of v , keeping QT constant. From left to right, $Q = 8.45, 16.6, 32.6, 75.1, 137.6$, and $200 \mu\text{l/h}$, respectively. The dashed line is a guide for the eye. (Inset) R_d as a function of $[3QT/(4\pi)]^{1/3}$, for all experiments combined, with $d = 197 \mu\text{m}$ (including all v and [SDS] values). The solid line has a slope of 1.

values, we obtain $R_d^* \in [R_0 - 3R_0]$. For the largest value, $R_0 = 350 \mu\text{m}$, we observe that $R_d^* \approx R_0$. This result is likely due to the fact that the size of the droplet approaches $R_d^{\text{max}} \sim 1.9 \text{ mm}$, for which gravity effects participate in destabilizing the droplet.

C. Discussion

In this paper, we identify a simple quasistatic mechanism to produce aqueous microdroplets in oil. The polydispersity in size is about 1%, which is similar to the one achieved for

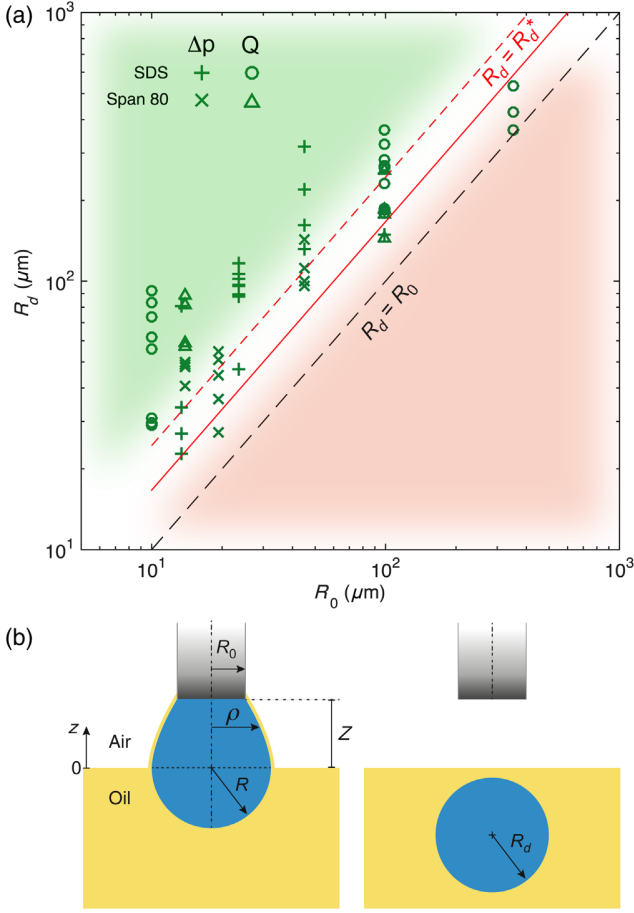


FIG. 5. (a) Phase diagram of the averaged droplet radius R_d as a function of the capillary radius R_0 . Open (crossed) symbols correspond to experiments performed by imposing the flow rate Q (the hydrostatic pressure Δp). The plus and circle (cross and triangle) symbols correspond to experiments performed at $[\text{SDS}] = 8 \text{ mM}$ concentration (Span 80 = 2 wt %). The solid (dashed) red line is the prediction of the model using $\gamma_{ao} = 36$ (18) mN/m. The green (red) shaded area corresponds to stable (unaccessible) droplet production. (b) The two states of a droplet in the capillary trap. The pending droplet is composed of a spherical cap of radius R and a paraboloid of revolution, spanning from the oil-air free surface at $z = 0$ to the capillary tip at $z = Z$.

commonly used microfluidic setups at frequencies of about 100 Hz up to tens of kilohertz [1,20,21]. It is of experimental knowledge that producing droplets at steady emission rates of a few hertz in such microfluidic setups is difficult to achieve and leads to larger size dispersions. Our method offers a robust alternative for producing monodisperse droplets at low frequencies.

Considering the typical droplet size, our method leads to a minimum droplet diameter that is about twice the capillary inner diameter. In classical microfluidic chips such as flow focusing or coflow devices, droplets can be produced through two different main modes (dripping and jetting) that depend on the competition between capillary,

viscous, and inertial forces [1]. In the dripping regime, the typical droplet size is governed by the channel dimensions and can be moderately tuned by the flow rates of the continuous and dispersed phases. This mode of production yields monodisperse emulsions. In the jetting regime involving higher flow rates, sizes significantly smaller than the channel width can be obtained, but they are, in turn, associated with an increased polydispersity [22,23]. The minimum droplet size for monodisperse emulsion production in those setups is thus limited by channel dimensions. Our capillary-trap device thus produces comparable sizes, equally limited by the capillary inner diameter. Commercial capillaries can be found down to submicron inner diameters, and the capillary-trap method we implement can thus, in principle, be used to produce droplets with radii ranging from a few micrometers up to hundreds of micrometers—and even of submicronic size. Furthermore, our method is easy to implement and requires only a single flow.

In contrast to coflow and flow-focusing production methods [1], we also establish in this paper that the detachment process is purely capillary based, with no velocity-dependent viscous effects. This result is expected since the capillary numbers of the problem $(\eta v)/\gamma$ and $[\eta Q/(\pi R_0^2 \gamma)]$ are very small in the explored v and Q ranges. Since the only length scale of the problem is R_0 , one expects $R_d^* \sim R_0$. To go beyond this scaling argument, we model the capillary trap as follows. When fully immersed in oil, the pending drop is a spherical cap of radius R attached at the capillary tip. When the capillary tip overpasses the oil-air interface (that defines $z = 0$), the aqueous droplet is deformed [Fig. 5(b)]. To make the problem analytically solvable, we postulate that the droplet shape is the union of a spherical cap of radius R and a paraboloid of revolution [radius $\rho(z) \in [R_0 - R]$, with $\rho(Z) = R_0$ at the capillary tip]. We impose the continuity of the curvature at the cap-paraboloid junction. Considering the smallest unstable droplet, the cap-paraboloid junction has to be located at the sphere equator since it maximizes the droplet surface, which yields $\rho(z) = R + (R_0 - R)z^2/Z^2$. For a given droplet of size R , volume conservation imposes that $Z/R_0 = 10r^3/(3 + 4r + 8r^2)$, with $r = R/R_0$. Since $r > 1$, $Z/R_0 \approx 5r/4 - 5/8$ [24]. We then deduce the total area of the deformed droplet A_{tot} . Close to detachment, fast imaging of the process using laser-sheet fluorescence imaging (see Fig. 3) suggests that a thin film of oil persists and surrounds the droplet. We therefore hypothesize that the oil-air interface follows the paraboloid shape of the aqueous droplet [Fig. 5(b), left panel]. The model thus neglects the oil meniscus due to the wetting of the glass capillary by the oil phase. Within this geometrical description, we can compute the surface free energy in the pending attached state,

$$F_a = A_{\text{tot}}\gamma_{ow} + A_p\gamma_{ao}, \quad (1)$$

where A_p is the paraboloidal part of the droplet area. This energy, F_a , has to be compared to the detached configuration. If the pending droplet is cut at the capillary-tip extremity, we produce a detached droplet whose radius, $R_d \approx R$ [24], is simply set by volume conservation. By doing so, we restore an oil-air interface of typical area πR^2 and also create an air-water interface at the capillary tip. We therefore write the free energy in the detached state as

$$F_d = 4\pi R_d^2 \gamma_{ow} + \pi R_0^2 \gamma_{aw} + \pi R^2 \gamma_{ao} \quad (2)$$

Equating Eqs. (1) and (2) yields

$$R_d^* = \frac{R_0}{2} \left(\frac{5\gamma_{ao} + 12\gamma_{aw} + 5\gamma_{ow}}{2\gamma_{ao} - \gamma_{ow}} \right)^{1/2}. \quad (3)$$

We plot in Fig. 5(a) the predicted values of R_d^* as a function of R_0 , using $\gamma_{ow} = 11.7$ mN/m [17] and $\gamma_{aw} = 35.9$ mN/m [25]. We compute R_d^* for γ_{ao} in the range 18–36 mN/m, yielding R_d^*/R_0 between 2.44 and 1.67, which is in reasonable agreement with the experimental data.

To further check the validity of our model, we explore the dependence of R_d^* on γ_{ow} and γ_{aw} by varying the SDS concentration. The results of the experiments ($d = 197$ μm) are presented in Fig. 6, where we plot R_d^* as a function of the SDS concentration. The variation of R_d^* is moderate, increasing by about a factor of 1.6 from [SDS] = 8 mM to [SDS] = 0. As mentioned above, the size measurements close to the instability threshold at R_d^* exhibit stronger fluctuations, which may explain the scattering of the data. The model is derived at each

[SDS] concentration using γ_{ow} and γ_{aw} values deduced from Refs. [17,25]. The model captures the slow decrease of R_d^* when the surface tensions γ_{ow} and γ_{aw} are decreased as [SDS] increases. At higher values of γ_{ow} , Eq. (3) predicts a divergence of R_d^* at $\gamma_{ow} = 2\gamma_{ao}$. We indeed observe a sharper increase of R_d^* at low [SDS] values. The best comparison to our data (Fig. 6) is, however, obtained with $\gamma_{ao} = 36$ mN/m instead of 18 mN/m, as measured independently (not shown). Since we neglect in our model the oil meniscus wetting the glass capillary, the oil-air interface area is clearly underestimated. Moreover, the exact shape of the interfaces at play remain to be computed, to go beyond the basic paraboloid-shape assumption. Taking both points into account should modify the predicted value of R_d^* and may explain this discrepancy with the data. Establishing more precise scaling laws of R_d^* requires additional experimental and theoretical investigations and is beyond the scope of the present work.

IV. CONCLUSION

In total, our method offers an easy-to-implement system to produce microdroplets when low frequencies (< 1 Hz) are required. It offers independent control of the size (through the injected volume QT) and the emission frequency. Since the process is quasistatic, the production rate can be rendered as low as required by simply reducing the flow rate Q or stopping the flow and adjusting the value of the period T . The method is versatile and is found to work with ionic and nonionic surfactants and phospholipids (not shown), and even without a surfactant. To increase the emission frequency, parallel droplet production can be easily implemented using a matrix of capillaries. We think this method could be particularly interesting in the field of chemical or biological encapsulation, for which precise volume and content control as well as kinetics may be crucial. This could be the case, for instance, for protein-stabilized emulsion [8] or droplet-interface bilayers [9] that require long times (several minutes) to allow for surfactant migration at the oil-water interface. Moreover, our technique does not involve high electrical fields, heat, or ultrasound to trigger droplet formation that may damage fragile materials such as proteins or cells. Our method should, therefore, be especially relevant for applications in biotechnology. In principle, this method should function at smaller length scales and could be used to produce droplet sizes of about 1 μm . It could, therefore, be used to produce colloids and microcapsules.

In addition, the capillary trap is also very simple to set up and does not require any particular high-tech facilities, such as a clean room, photolithography, or micromilling techniques usually used to produce microfluidic chips. The method can function by using hydrostatic pressure to impose the aqueous flow and a simple translation stage. As a consequence, our technique can be implemented at low cost

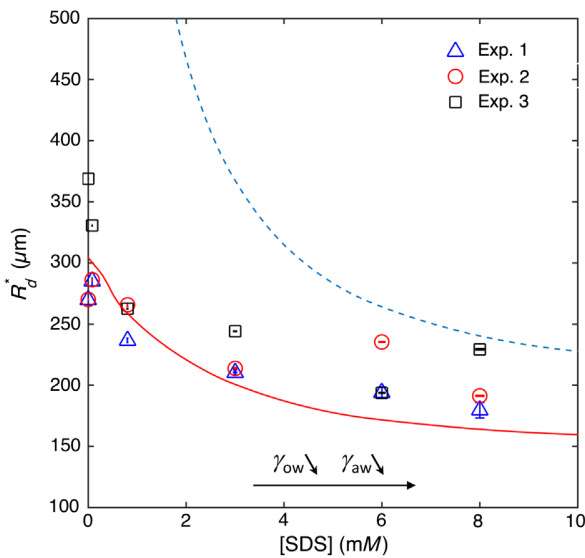


FIG. 6. Minimum radius R_d^* (each point is averaged over 200 droplets), as a function of the SDS concentration, for a 197- μm -diameter capillary. For each concentration, the experiment is repeated three times (indicated by different symbols) using freshly prepared SDS solutions. The solid (dashed) line is the model prediction with $\gamma_{ao} = 36$ mN/m ($\gamma_{ao} = 18$ mN/m).

(see the Appendix) and could be used for biomedical or materials-science applications in developing countries.

ACKNOWLEDGMENTS

We thank Yannick Rondelez, Olivier Dauchot, and Raphaël Voituriez for the fruitful discussions, Laurence Talini for the surface-tension measurements, and Gaele el Asmar and Ibra Ndiaye for their help during the experiments.

APPENDIX: LOW-COST CAPILLARY-TRAP SETUP

In parallel to the experiments described in the main text, we also develop a low-cost and easy-to-implement

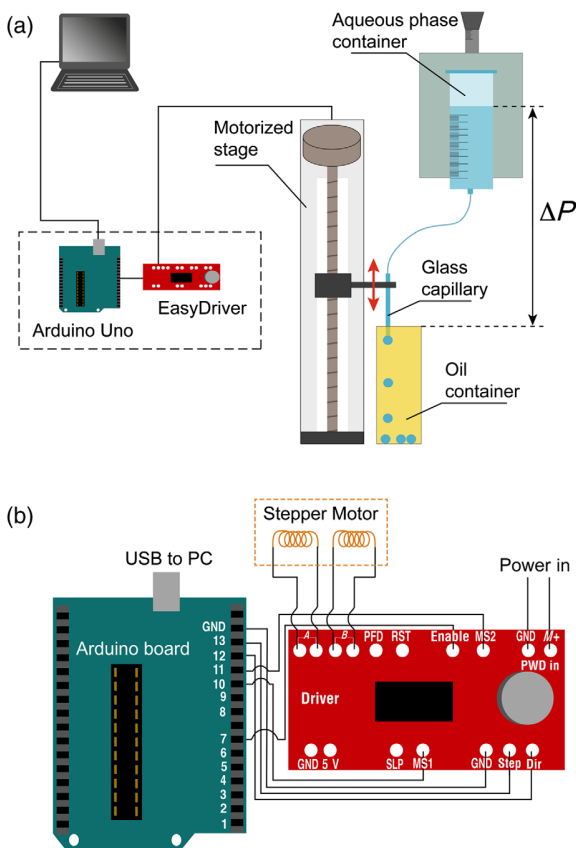


FIG. 7. (a) Sketch of the low-cost capillary-trap setup. (b) Wiring of the Arduino Uno board pins to the EasyDriver motor driver. Pin 7 is wired to the socket Enable (this function enables and disables the motor), pin 10 to the socket MS1 (microstepping 1), pin 11 to the socket MS2 (microstepping 2), pin 12 to the socket Step, pin 13 to the socket Dir. (to impose the direction of the motor), and, finally, the ground (GND) pin is connected to the GND socket of the EasyDriver board. The Arduino board is connected to the computer (PC) by a Universal Serial Bus (USB) port. Use the additional pins PFD (Percent Fast Decay) to select output decay mode, RST (Reset) to ignore all Step commands, SLP (Sleep) to disable outputs and minimize power consumption, and PWD (Power In) to power the board.

setup to test the robustness of the technique. We evaluate the maximum cost of this setup to be about a few hundred euros.

We use a small translation stage coupled to a stepper motor (B04F 5V DC, SeedStudio) to move up and down the glass capillary [Fig. 7(a)]. The motor is powered and controlled with a small driver (EasyDriver Stepper Motor, Sparkfun Electronics) controlled by an Arduino Uno board connected to a personal computer (PC) [Figs. 7(a) and 7(b)]. The driver is powered by an RS 148-957 power supply, which can be tuned easily to deliver the voltage required by the motor (4 to 5 V, with a maximum current of 500 mA). This driver allows us to perform microstepping in order to operate the motor at different velocities. Figure 7(b) shows the wiring that we implement between the Arduino Uno board and the motor driver [26]. The glass capillary ($R_0 = 98.5 \mu\text{m}$) is mounted on the motor using a homemade Plexiglas adaptor. With this setup, we verify that the capillary can be easily moved at velocities up to a few mm/s.

The droplets are obtained by imposing a hydrostatic pressure ΔP , which is set by a lid-free container (such as a syringe without its piston) mounted on a vertical manual translation stage [Fig. 7(a)]. To produce droplets with a radius $R_d = 100 \mu\text{m}$ at a rate of 1 Hz, one has to impose the flow rate $Q \approx 15 \mu\text{l/h}$. Assuming a Poiseuille cylindrical flow in the capillary, this flow rate corresponds to a water-column height of 1 cm with a $d = 200 \mu\text{m}$ capillary, and 10 cm for a $d = 100 \mu\text{m}$ capillary. With this low-cost setup, we quantify the polydispersity of microdroplet production for a given ΔP value. Figure 8 shows an

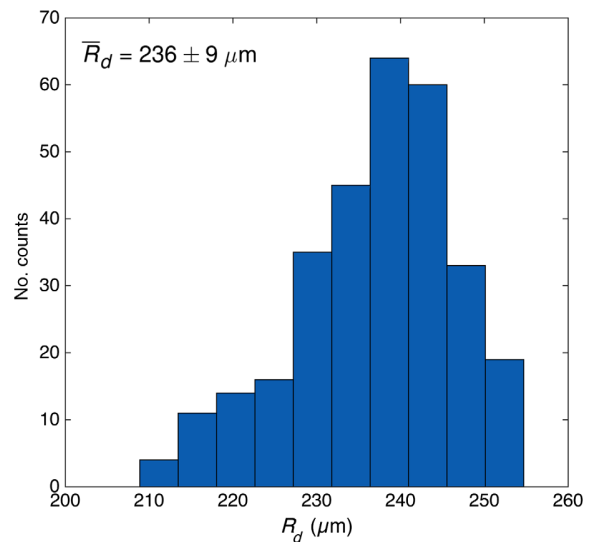


FIG. 8. Distribution of radii R_d of pure water microdroplets detached in hexadecane containing Span 80 of 2 wt %. The total number of droplets is 300. The average radius is measured to be $\bar{R}_d = 236 \mu\text{m}$, with a standard deviation of $9 \mu\text{m}$.

example of a size distribution over a sample of 300 microdroplets. The polydispersity is found to be 4%, which compares very well with what one usually obtains using standard microfluidic techniques at low production rates.

-
- [1] P. Zhu and L. Wang, Passive and active droplet generation with microfluidics: A review, *Lab Chip* **17**, 34 (2017).
- [2] S.L. Anna, N. Bontoux, and H.A. Stone, Formation of dispersions using flow focusing in microchannels, *Appl. Phys. Lett.* **82**, 364 (2003).
- [3] T. Thorsen, R.W. Roberts, F.H. Arnold, and S.R. Quake, Dynamic Pattern Formation in a Vesicle-Generating Microfluidic Device, *Phys. Rev. Lett.* **86**, 4163 (2001).
- [4] O. J. Miller, A. El Harrak, T. Mangeat, J.-C. Baret, L. Frenz, B. El Debs, E. Mayot, Mi. L. Samuels, E. K. Rooney, P. Dieu, M. Galvan, D. R. Link, and A. D. Griffiths, High-resolution dose response screening using droplet-based microfluidics, *Proc. Natl. Acad. Sci. U.S.A.* **109**, 378 (2012).
- [5] J. J. Agresti, E. Antipov, A. R. Abate, K. Ahn, A. C. Rowat, J.-C. Baret, M. Marquez, A. M. Klibanov, A. D. Griffiths, and D. A. Weitz, Ultrahigh-throughput screening in drop-based microfluidics for directed evolution, *Proc. Natl. Acad. Sci. U.S.A.* **107**, 4004 (2010).
- [6] T. Kong, Z. Liu, Y. Song, L. Wang, and H. C. Shum, Engineering polymeric composite particles by emulsion-templating: Thermodynamics versus kinetics, *Soft Matter* **9**, 9780 (2013).
- [7] R. K. Shah, J.-W. Kim, J. J. Agresti, D. A. Weitz, and L.-Y. Chu, Fabrication of monodisperse thermosensitive microgels and gel capsules in microfluidic devices, *Soft Matter* **4**, 2303 (2008).
- [8] C. J. Beverung, C. J. Radke, and H. W. Blanch, Protein adsorption at the oil/water interface: Characterization of adsorption kinetics by dynamic interfacial tension measurements, *Biophys. Chem.* **81**, 59 (1999).
- [9] S. Leptihn, O. K. Castell, B. Cronin, E.-H. Lee, L. C. M. Gross, D. P. Marshall, J. R. Thompson, M. Holden, and M. I. Wallace, Constructing droplet interface bilayers from the contact of aqueous droplets in oil, *Nat. Protoc.* **8**, 1048 (2013).
- [10] S. Kutuzov, J. He, R. Tangirala, T. Emrick, T. P. Russell, and A. Böker, On the kinetics of nanoparticle self-assembly at liquid/liquid interfaces, *Phys. Chem. Chem. Phys.* **9**, 6351 (2007).
- [11] M. He, J. S. Kuo, and D. T. Chiu, Effects of ultrasmall orifices on the electrogeneration of femtoliter-volume aqueous droplets, *Langmuir* **22**, 6408 (2006).
- [12] A. Bransky, N. Korin, M. Khoury, and S. Levenberg, A microfluidic droplet generator based on a piezoelectric actuator, *Lab Chip* **9**, 516 (2009).
- [13] J.-C. Galas, D. Bartolo, and V. Studer, Active connectors for microfluidic drops on demand, *New J. Phys.* **11**, 075027 (2009).
- [14] T.-H. Wu, Y. Chen, S.-Y. Park, J. Hong, T. Teslaa, J. F. Zhong, D. Di Carlo, M. A. Teitell, and P.-Y. Chiou, Pulsed laser triggered high speed microfluidic fluorescence activated cell sorter, *Lab Chip* **12**, 1378 (2012).
- [15] G. Villar, A. D. Graham, and H. Bayley, A tissue-like printed material, *Science* **340**, 48 (2013).
- [16] M. Booth, V.R. Schild, F. Downs, and H. Bayley, Functional aqueous droplet networks, *Mol. Biosyst.* **13**, 1658 (2017).
- [17] A. G. Kanellopoulos and M. J. Owen, Adsorption of sodium dodecyl sulphate at the silicone fluid/water interface, *Trans. Faraday Soc.* **67**, 3127 (1971).
- [18] T. Tate, On the magnitude of a drop of liquid formed under different circumstances, *The London, Edinburgh, and Dublin Philosophical Magazine and Journal of Science* **27**, 176 (1864).
- [19] A. H. Cortés-Estrada, L. A. Ibarra-Bracamontes, A. Aguilar-Corona, G. Viramontes-Gamboa, and G. Carbajal-De la Torre, in *Experimental and Computational Fluid Mechanics*, edited by J. Klapp and A. Medina, Environmental Science and Engineering (Springer International Publishing, Cham, Switzerland, 2014), p. 219.
- [20] P. B. Umbanhowar, V. Prasad, and D. A. Weitz, Monodisperse emulsion generation via drop break off in a coflowing stream, *Langmuir* **16**, 347 (2000).
- [21] L. Yobas, S. Martens, W.-L. Ong, and N. Ranganathan, High-performance flow-focusing geometry for spontaneous generation of monodispersed droplets, *Lab Chip* **6**, 1073 (2006).
- [22] A. S. Utada, A. Fernandez-Nieves, H. A. Stone, and D. A. Weitz, Dripping to Jetting Transitions in Coflowing Liquid Streams, *Phys. Rev. Lett.* **99**, 094502 (2007).
- [23] M. Zagnoni and J. M. Cooper, A microdroplet-based shift register, *Lab Chip* **10**, 3069 (2010).
- [24] We checked numerically to ensure that these approximations have no effect on the model predictions.
- [25] M. Xu, W. Zhang, X. Pei, J. Jiang, Z. Cui, and B. P. Binks, CO₂/N₂ triggered switchable pickering emulsions stabilized by alumina nanoparticles in combination with a conventional anionic surfactant, *RSC Adv.* **7**, 29742 (2017).
- [26] Samples of an ARDUINO code to monitor the driver can be found at <https://learn.sparkfun.com/tutorials/easy-driver-hook-up-guide>.

Diffusion through nanopores in connected lipid bilayer networks

M. Valet,¹ L.-L. Pontani,¹ R. Voituriez,^{1,2} E. Wandersman,^{1,*} and A. M. Prevost^{1,†}

¹Laboratoire Jean Perrin CNRS UMR 8237, Sorbonne Université, 4 place Jussieu, 75005 Paris, France

²Laboratoire de Physique Théorique de la Matière Condensée,

CNRS UMR 7600, Sorbonne Université, 4 place Jussieu, 75005 Paris, France

(Dated: July 9, 2019)

A biomimetic model of cell-cell communication was developed to probe the passive molecular transport across ion channels inserted in synthetic lipid bilayers formed between contacting droplets arranged in a linear array. Diffusion of a fluorescent probe across the array was measured for different pore concentrations. The diffusion characteristic time scale is found to vary non-linearly with the pore concentration. Our measurements are successfully modeled by a continuous time random walk description, whose waiting time is the first exit time from a droplet through a cluster of pores. The size of the cluster of pores is found to increase with their concentration. Our results provide a direct link between the mesoscopic permeation properties and the microscopic characteristics of the pores such as their number, size and spatial arrangement.

In multicellular organisms, cell-cell communication is essential for morphogenesis, cell growth and differentiation as well as cell homeostasis [1]. Cells have thus developed various mechanisms to communicate with each other, such as the release of solutes/vesicles in their environment, electrical signals and direct cell-cell contacts. Within direct cell-cell contacts, communication through molecular exchange is made possible with protein gates that create nanopores spanning between apposed cytoplasmic cell membranes. Plants and fungi for instance, use respectively the so-called plasmodesmata and septal pores. In animals, two kinds of pores, gap junction channels and tunneling nanotubes have also been identified and are very similar in their structure and function to their plants and fungi counterparts. Gap junctions in particular, consist of juxtaposed protein based hemichannels that can assemble into clustered structures of typical size a few hundreds of nanometers [2]. They enable a passive diffusion-based transport of small hydrophilic molecules between connected cells, whose properties are mostly measured for cells *in vitro* with dye transfer techniques [3], such as gap-FRAP [4] for instance, allowing to determine the permeability of the gap junction.

In recent years, the use of well controlled artificial multicellular systems to design complex reaction-diffusion processes within the framework of bottom-up synthetic biology has considerably increased. In particular, synthetic membranes such as Droplet Interface Bilayers (DIBs) [5], that are obtained by putting in contact aqueous droplets bathing in an oil-lipid mixture, have allowed the study of molecular transport through both passive ion channels [6, 7] and active transporters [8], using fluorescence imaging. Very recently, networks of DIBs connected by passive staphylococcal α -hemolysin pores (α HL), were used to probe genetically engineered reaction-diffusion based processes [9]. In all these experiments, both for cells *in vitro* and for artificial systems, diffusion processes across either gap junctions or DIBs decorated with nanopores, are usually modeled with a

Fick's law combined with a phenomenological permeation law through a membrane, yielding a large scale effective diffusion coefficient. The microscopic mechanisms that underly the permeation law and therefore control the value of this effective diffusion coefficient are however poorly described. In particular, its dependence with the concentration of the nanopores in the membrane and their spatial arrangement has never been evidenced experimentally, nor modeled theoretically.

In this Letter, we report a thorough study of the diffusion of molecular probes through linear networks of aqueous droplets connected by DIBs decorated with α HL pores at different concentrations. We model the diffusion from one droplet to its neighbors with a continuous time random walk model whose waiting time is the first exit time from a droplet, either through independent pores or through clusters of pores. Our experimental measurements strongly suggest that the diffusion law is controlled by the clustering of the nanopores, and provide estimates of the clusters size as a function of α HL's concentration.

Monomers of α HL (Sigma Aldrich) were diluted in an aqueous buffer (HEPES 10 mM, KCl 100 mM, Sigma Aldrich, pH 7.4) at concentrations c ranging from 150 to 300 μ g/mL. DPhPC lipids in chloroform (4ME 16:0 PC/1,2-diphytanoyl-*sn*-glycero-3-phosphocholine, Avanti) were evaporated under nitrogen and resuspended at a concentration of 6.5 mg/mL in a mixture (50:50 vol:vol) of hexadecane and silicone oil AR20 (Sigma Aldrich).

Droplets of the α HL solution were produced inside a Plexiglas pool containing the oil/lipid solution and mounted on an XY translation stage, using a Droplet-On-Demand technique [10] (Fig. 1a). Briefly, the aqueous phase was flown through a glass capillary (inner diameter 20 μ m) periodically extracted through the oil/lipid-air interface. The frequency of this extraction, together with the size of the capillary and the flow rate, control the radius R of the produced droplets. Linear arrays were obtained by depositing droplets of typical $R \approx 75 \mu$ m in

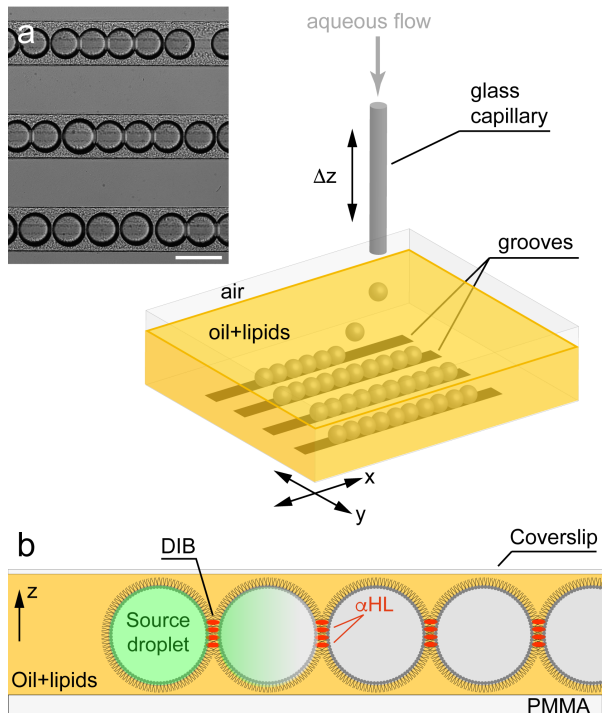


FIG. 1. (a) Sketch of the experimental setup. The aqueous solution is injected through a glass capillary pulled out periodically across the oil/lipid-air interface. The detached droplets sediment in a Plexiglas pool decorated with parallel grooves and form a DIB network. Lateral positioning of the droplets is achieved by moving the pool with a motorized translation stage. Eventually, a source droplet seeded with fluorophores is deposited. Diffusion of fluorophores is imaged in epifluorescence microscopy. Inset: Image of three typical DIB networks. The white bar is $200 \mu\text{m}$ long. (b) Sketch of the diffusion process of fluorophores across DIBs decorated with α HL protein pores.

micromilled grooves (width $200 \mu\text{m}$, depth $100 \mu\text{m}$) at the bottom of the pool (Fig. 1a). Since each droplet is stabilized with a lipid monolayer, a bilayer was formed at each droplet-droplet contact, thus forming linear arrays of DIBs in which α HL monomers can heptamerize to form nanopores (Fig. 1b). The adhesion area appearing between neighboring droplets was a signature of a DIB formation (see the pairs of white segments at each contact on Fig. 2a). In practice, the resulting networks had 3 up to 10 droplets (see Supplemental Material).

Source droplets containing a solution of fluorophores (5-carboxyfluorescein from Sigma $20 \mu\text{M}$ in HEPES 10 mM , KCl 100 mM) were then added either at the end (Fig. 2a) or in the middle of a DIB array (see Supplemental Material). To limit evaporation of the aqueous droplets, a coverslip was placed on the oil/lipid pool (Fig. 1b). Diffusion of fluorophores from the source droplet to its neighbors through the nanopores was imaged in epifluorescence microscopy overnight (typically

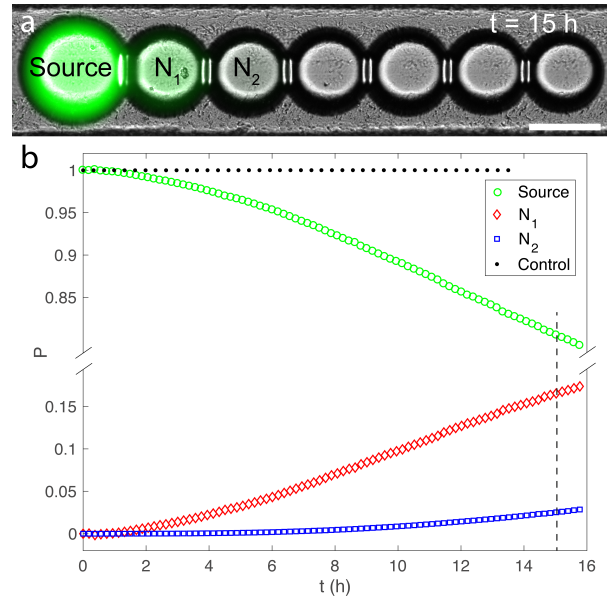


FIG. 2. (a) Composite image from bright field (grey) and fluorescence (green) microscopy, of a typical diffusion process of carboxyfluorescein across a DIB network ($c = 200 \mu\text{g}/\text{mL}$) at $t = 15 \text{ h}$. The white bar is $100 \mu\text{m}$ long. (b) Occupancy probability P of carboxyfluorescein as a function of time, for the network of (a). From top to bottom, the different curves correspond respectively to the source droplet S (green circles), the first N_1 (red diamonds) and second N_2 (blue squares) neighboring droplets. The black disks show $P_s(t)$ for the source droplet in a typical control experiment, *i.e.* without any pores. The dashed line corresponds to $t = 15 \text{ h}$.

for 15 hours, every 11 minutes). A typical diffusion process over 16 hours is shown in Fig. 2. Control experiments (see Supplemental Material) in the absence of α HL nanopores were also performed, and no significant increase of the fluorescence intensity in the neighboring droplets was measured in 90% of the cases. However, in some cases, an osmotic shock could occur, create transient pores in the DIB, and lead to a rapid increase of the fluorescence signal in immediate neighbors over short time scales (typically less than 1 hour). Such fast kinetics events can be easily identified and have also been excluded from our analysis.

To quantify the diffusion process, image analysis was performed on bright field images in order to find the radii and center coordinates of each droplet using a homemade Matlab routine. The fluorescence intensity $I_i(t)$ inside each droplet N_i was measured by taking the average intensity inside a disk that measures half the total droplet size. We checked however that the value of $I_i(t)$ does not change with the disk size. Furthermore, we have verified that the measured fluorescence intensity is proportional to the concentration of fluorophores in the explored concentration range. The occupancy probability P_i inside a droplet (except for the source droplet) was

then defined as

$$P_i(t) = \frac{I_i(t) - I_i(t_0)}{I_s(t) + \sum_{j \neq s} (I_j(t) - I_j(t_0))} \quad (1)$$

where $I_i(t_0)$ is the average intensity at the beginning of the experiment, $I_s(t)$ the intensity of the source droplet and where the summation runs over all droplets in the network but the source. For the source droplet, the numerator of Eq. 1 is taken as $I_s(t)$, so that $P_s(t_0) = 1$. Therefore, $P_s(t)$ decreases with t as fluorophores diffuse from the source to its neighbors, while $P_i(t)$ of the neighboring droplets $N_{i,i \neq s}$ increases (Fig. 2b). Note that two possible artefacts can affect the time evolution of the fluorescence intensities $I_s(t)$ and $I_i(t)$. On the one hand, a size decrease of the droplets due to evaporation can cause an increase of the fluorophore concentration and thus of the fluorescence intensity. Photobleaching on the other hand can cause a decrease of the measured fluorescence intensity. To quantify these combined effects, we measured on control experiments (without any pores, thus without any diffusion away from the source) the time variation of $I_s(t)$. We found that the source intensity increases moderately over time (about 10% of relative increase in 13 hours, not shown). We can conclude that evaporation effects dominate over photobleaching. We further checked that the definition of $P_s(t)$ was efficient in correcting this artefact. For the control experiment (Fig. 2b, black disks) the value of P is indeed equal to unity over the whole time course of the experiment. Last, considering experiments with pores, we excluded from our analysis the rare experiments for which the evaporation rate was anomalously high and dominant over diffusion, yielding an increase of the source intensity I_s over time.

We studied the diffusion kinetics by specifically focusing on the source and first neighbor droplets and using different networks with different α HL monomer concentrations. The introduced monomers α HL_m are first adsorbed and then diffuse within the bilayer to form a heptamer α HL. Since the heptamerization process is fast [11], we describe this chemical sequence as a single step equilibrium 7α HL_m \leftrightarrow α HL, which implies that the number of pores adsorbed inside the bilayer scales with the monomer concentration c as c^7 .

Figure 3a shows the occupancy probability P_1 for the first neighbor as a function of time t for increasing α HL monomer concentrations $c=150; 200; 250; 300 \mu\text{g/mL}$. Each curve is an average over several experimental realizations. All curves can be separated within experimental error bars and the diffusion dynamics are faster as the pore concentration increases.

Theoretically, for an infinite array of connected compartments, one can model the time evolution of P_i using a continuous time random walk approach [12]. Each probe

molecule is described as a random walker jumping to the adjacent site with a time-dependent probability. The corresponding waiting time is defined as the first exit time of a molecule from a droplet. For 3D brownian diffusion, the latter is known to be exponentially distributed with a mean value that we denote τ [13]. Since diffusion within a droplet occurs on time scales much shorter (~ 10 s, with a diffusion coefficient of carboxyfluorescein in water $D = 4.10^{-10} \text{m}^2/\text{s}$ [14]) than the typical diffusion time from one droplet to its neighbors (~ 1 h), one can assume that the fluorophore concentration is uniform within the droplets, and therefore model the droplets network with a set of discrete connected sites. Within this framework, one can derive using standard tools [12] the occupancy probability within the first neighbor P_1^{th}

$$P_1^{th}(t) = e^{-t/\tau} \mathcal{I}_1(t/\tau) \quad (2)$$

where \mathcal{I}_1 is the modified Bessel function of the first kind. In our experiments, droplet arrays have a finite size. Thus, Eq. 2 cannot model our data at long times. However, in the short time limit ($t/\tau \ll 1$), Eq. 2 yields to first order $P_1^{th} \sim \lambda t$ with $\lambda = 2/\tau$, independently of the total number and position of the droplets.

Experimentally, at very short times, our data shows a small deviation from linearity (Fig. 3a) that we interpret as the combined result of both DIBs equilibration and proteins adsorption kinetics at the lipid bilayer. Past this regime, one observes that $P_1(t)$ is approximately linear. For the highest concentration of nanopores, $P_1(t)$ eventually reaches a steady state. For all experimental curves used to compute the average, we have identified this linear regime and chosen to fit it to extract λ . This was done by testing for the existence of an inflection point at $t = t_{in}$ and extracting the slope λ in its vicinity. In case the inflection point was inexistent, we fitted the last 3 hours of the data. Whatever the method used, we checked that the values of λ were equally distributed within experimental error bars. For the purpose of illustration, we have performed linear fits on the averaged $P_1(t)$, as shown with the dashed lines on Fig. 3a. We also linearly fitted every single curve to extract λ as a function of the nanopore concentration. Resulting λ 's are shown in Fig. 3b on a log-log plot, and are consistent with a power-law dependence with c . Fitting this data with a power law yields $\lambda \sim c^{3 \pm 1}$. The value of this exponent will be discussed further down theoretically. The inset of Fig. 3b shows the occupancy probability as a function of the rescaled time $\langle \lambda \rangle t$, where $\langle \lambda \rangle$ is the average value plotted on the main panel. All curves at different c collapse on the same master curve, indicating that λ^{-1} is the only time scale that governs the diffusion kinetics.

In recent years, DIBs have increasingly been used [9, 15] to study both passive and active transport of molecules using fluorescence based measurements [6, 7, 9]. All these studies assume that diffusion of a molecular

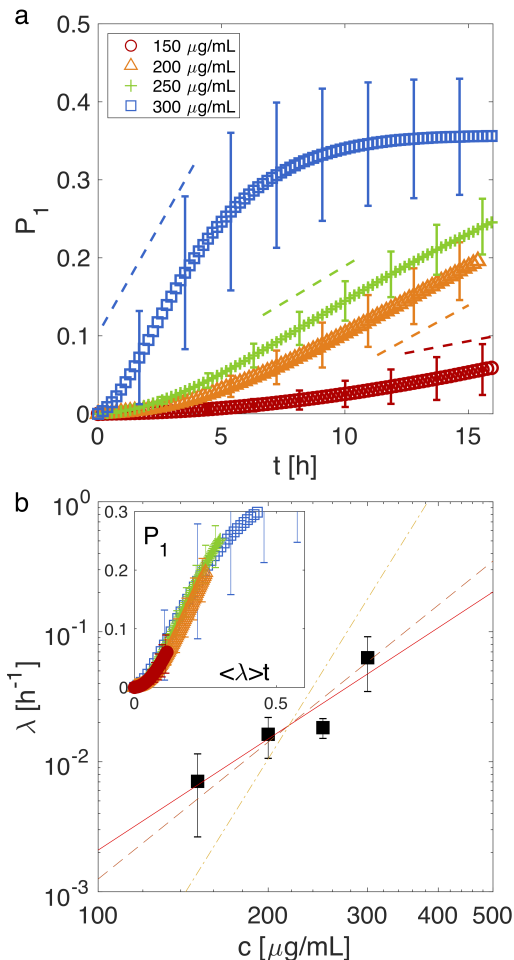


FIG. 3. (a) Occupancy probability P_1 as a function of time t for 4 different αHL monomer concentrations, $c=150; 200; 250; 300 \mu\text{g/mL}$, with $N = 18; 25; 8; 10$ respectively. Error bars are standard deviation of the data. The dashed lines are linear fits used to extract the characteristic rate λ (see main text). They are shifted vertically to ease visualization. (b) Characteristic rate λ as a function of c . The solid line is a power law fit of exponent 3 ± 1 . The dashed line is a fit using an exponent of $7/2$. The dashed dotted line is a fit using an exponent of 7. Inset: Occupancy probability as a function of the rescaled time $\langle \lambda \rangle t$.

probe across a membrane can be described with a phenomenological permeation law, from which an effective large scale permeation coefficient is deduced. However, the microscopic origins that set its value have not been explored. Within the theoretical description presented above (see Eq. 2), we propose that the molecular transport from one droplet to another is fully characterized by the mean waiting time τ in a droplet. This time is the average time necessary for a chemical messenger to reach any single pore of diameter a within the cell, *i.e.* the first exit time [16, 17]. For a confining domain of volume V and a single pore, this time has been obtained

theoretically [16–18] and writes in the large V limit

$$\langle T_1 \rangle = \frac{V}{2Da} \quad (3)$$

For a spherical domain of radius R , this time is much larger – by a factor R/a ($\sim 10^5$) – than the typical time needed for a probe to explore *in bulk* a typical length R . Importantly, this result was shown to be independent of the shape of the confining volume. In addition, it has been shown for 3D diffusion in [19, 20] that in the case where $d \gg a$, where d is the distance between targets, pores can be considered as independent. As a result, the first passage time $\langle T_n \rangle$ simply writes $\langle T_n \rangle = \langle T_1 \rangle / n$ independently of both the shape of the confinement domain and the spatial organization of targets. When $d \sim a$, T_n is still independent of the shape of the confining domain, but screening effects [19, 20] between targets have to be taken into account. In the limit of a close-packed configuration, *i.e.* if n pores are clustered, they can be considered as a single pore of area na^2 , with a typical size $a^* = \sqrt{na}$, and thus $\langle T_n \rangle = \langle T_1 \rangle / \sqrt{n}$.

Since αHL is a heptamer, we expect for both cases the characteristic diffusion rate λ to scale either as c^7 if pores are considered independent, or as $c^{7/2}$ if pores are clustered. Shown in Fig. 3b (dashed line) is a power law fit of $\lambda(c)$ with an exponent $7/2$, in reasonable agreement with the data. On the contrary, a power law with an exponent 7 is far from providing a quantitative agreement. It suggests that the diffusion kinetics are controlled by clustered rather than independent nanopores. This non-linearity of the diffusion characteristic time contrasts with previously used phenomenological models [9]. Using expressions of $\langle T_n \rangle$, one can also deduce the typical cluster sizes $\sqrt{na} \approx \lambda \langle T_1 \rangle a$. Taking $R = 75 \mu\text{m}$, $D = 4.10^{-10} \text{m}^2/\text{s}$, and $a = 1.4 \text{nm}$ [21] gives sizes of clusters that range from about 10 nm ($n \approx 100$) at the lowest concentration to about 100 nm ($n \approx 10^4$) at the highest concentration. This clustering should also depend on membrane composition, which might explain the discrepancies in the reported αHL pore concentrations between different lipid mixtures [22]. Interestingly, it has recently been shown theoretically in [23] that stochastic variations of transmittance between compartments lead to anomalous diffusion in networks of compartments. In our experiments, the distribution of sizes of the nanopore clusters could induce randomness of the transmittance and explain the variability of our data.

We have used DIBs decorated with αHL passive ion channels to mimic the passive molecular transport through biological cells. Using fluorescence imaging, we have quantified the effect of the pore concentration on the diffusion kinetics of a molecule from one cell to its neighbors. We have found that the diffusion kinetics are efficiently captured by a continuous time random walk model. We also found that the characteristic diffusion

time scale varies as the inverse square root of the number of pores within the lipid bilayer, suggesting a pore clustering scenario. Such clustering has been evidenced numerically for transmembrane proteins [24]. Taking into account this clustering for nanopores is thus likely to be relevant for molecular transport in real biological systems.

The authors deeply thank J. Mathé, J.-C. Galas, A. Estevez-Torres and A. Senoussi for sharing experimental details, T. Bertrand for fruitful theoretical discussions and acknowledge financial support from ANR (BOAT, ANR-17-CE30-0001).

* elie.wandersman@sorbonne-universite.fr

† alexis.prevost@sorbonne-universite.fr

- [1] S. Bloemendal and U. Kück, *Naturwissenschaften* **100**, 3 (2013).
- [2] J.-C. Hervé and M. Derangeon, *Cell and Tissue Research* **352**, 21 (2013).
- [3] M. Abbaci, M. Barberi-Heyob, W. Blondel, F. Guillemin, and J. Didelon, *Biotechniques* **45**, 33 (2008).
- [4] M. Wade, J. Trosko, and M. Schindler, *Science* **232**, 525 (1986).
- [5] S. Leptihn, O. K. Castell, B. Cronin, E.-H. Lee, L. C. M. Gross, D. P. Marshall, J. R. Thompson, M. Holden, and M. I. Wallace, *Nature Protocols* **8**, 1048 (2013).
- [6] A. J. Heron, J. R. Thompson, B. Cronin, H. Bayley, and M. I. Wallace, *Journal of the American Chemical Society* **131**, 1652 (2009).
- [7] E. Walsh, A. Feuerborn, and P. R. Cook, *Scientific Reports* **6**, 34355 (2016).
- [8] H. E. Findlay, N. J. Harris, P. J. Booth, X. Liu, and P. J. Booth, *Scientific Reports* **6**, 39349 (2016).
- [9] A. Dupin and F. C. Simmel, *Nature Chemistry* **11**, 32 (2019).
- [10] M. Valet, L.-L. Pontani, A. M. Prevost, and E. Wandersman, *Physical Review Applied* **9**, 014002 (2018).
- [11] J. R. Thompson, B. Cronin, H. Bayley, and M. I. Wallace, *Biophysical Journal* **101**, 2679 (2011).
- [12] B. D. Hughes, *Random walks and random environments* (Clarendon Press Oxford, New York, 1995).
- [13] O. Bénichou, C. Chevalier, J. Klafter, B. Meyer, and R. Voituriez, *Nature Chemistry* **2**, 472 (2010).
- [14] T. Casalini, M. Salvalaglio, G. Perale, M. Masi, and C. Cavallotti, *The Journal of Physical Chemistry B* **115**, 12896 (2011).
- [15] M. J. Booth, V. R. Schild, F. G. Downs, and H. Bayley, *Molecular BioSystems* **13**, 1658 (2017).
- [16] Z. Schuss, A. Singer, and D. Holcman, *Proceedings of the National Academy of Sciences of the United States of America* **104**, 16098 (2007).
- [17] I. V. Grigoriev, Y. A. Makhnovskii, A. M. Berezhkovskii, and V. Y. Zitserman, *The Journal of Chemical Physics* **116**, 9574 (2002).
- [18] O. Bénichou and R. Voituriez, *Physical Review Letters* **100**, 168105 (2008).
- [19] A. Cheviakov, M. Ward, and R. Straube, *Multiscale Modeling & Simulation* **8**, 836 (2010).
- [20] C. Chevalier, O. Bénichou, B. Meyer, and R. Voituriez, *Journal of Physics A: Mathematical and Theoretical* **44**, 025002 (2011).
- [21] L. Song, M. R. Hobaugh, C. Shustak, S. Cheley, H. Bayley, and J. E. Gouaux, *Science* **274**, 1859 (1996).
- [22] J. Lemièrre, K. Guevorkian, C. Campillo, C. Sykes, and T. Betz, *Soft Matter* **9**, 3181 (2013).
- [23] G. Muñoz-Gil, M. A. Garcia-March, C. Manzo, A. Celi, and M. Lewenstein, *Frontiers in Physics* **7**, 31 (2019).
- [24] U. Schmidt, G. Guigas, and M. Weiss, *Physical Review Letters* **101**, 128104 (2008).

BIBLIOGRAPHY

- [1] Jean-Louis Rigaud and Daniel Lévy. Reconstitution of Membrane Proteins into Liposomes. *Methods in Enzymology*, 372:65–86, 2003.
- [2] Hagan Bayley, Brid Cronin, Andrew Heron, Matthew A Holden, William Hwag, Ruhma Syeda, James Thompson, and Mark Wallace. Droplet Interface Bilayers. *Mol. Biosyst.*, 4(12):1191–1208, 2009.
- [3] L. M. Tsofina, E. A. Liberman, and A. V. Babakov. Production of Bimolecular Protein-Lipid Membranes in Aqueous Solution. *Nature*, 212(5063):681–683, 1966.
- [4] Michael J Booth, Vanessa Restrepo Schild, Florence Downs, and Hagan Bayley. Functional aqueous droplet networks, 2017.
- [5] Sebastian Leptihn, Oliver K Castell, Brid Cronin, En-Hsin Lee, Linda C M Gross, David P Marshall, James R Thompson, Matthew Holden, and Mark I Wallace. Constructing droplet interface bilayers from the contact of aqueous droplets in oil. *Nature protocols*, 8(6):1048–1057, 2013.
- [6] Jason T. Sengel and Mark I. Wallace. Imaging the individual dynamics of electropores. *Proc Natl Acad Sci*, 113(19):5281–6, 2016.
- [7] James R. R Thompson, Bríd Cronin, Hagan Bayley, and Mark I. I Wallace. Rapid assembly of a multimeric membrane protein pore. *Biophysical journal*, 101(11):2679–83, 2011.
- [8] Guru A. Venkatesan, Joonho Lee, Amir Barati Farimani, Mohammad Heiranian, C. Patrick Collier, Narayana R. Aluru, and Stephen A. Sarles. Adsorption Kinetics Dictate Monolayer Self-Assembly for Both Lipid-In and Lipid-Out Approaches to Droplet Interface Bilayer Formation. *Langmuir*, 31(47):12883–12893, 2015.
- [9] M. Valet, L.-L. Pontani, A.M. Prevost, and E. Wandersman. Quasistatic Microdroplet Production in a Capillary Trap. *Physical Review Applied*, 9(1):014002, 2018.
- [10] Jerome Bibette. *Emulsion science : basic principles : an overview*. Springer, 2002, page 140. ISBN: 9783540708209.
- [11] C Charcosset, I Limayem, and H Fessi. The membrane emulsification process—a review. *Journal of Chemical Technology & Biotechnology*, 79(3):209–218, 2004.
- [12] Tobias Wauer, Holger Gerlach, Shiksha Mantri, Jamie Hill, Hagan Bayley, and K. Tanuj Sapra. Construction and Manipulation of Functional Three-Dimensional Droplet Networks. *ACS Nano*, 8(1):771–779, 2014.
- [13] Gabriel Villar, Alexander D Graham, and Hagan Bayley. A Tissue Like Printed Material. *Science*, 48(April):48–53, 2013.
- [14] Shenglong Liao, Yonglin He, Dingguan Wang, Libing Dong, Wenbin Du, and Yapei Wang. Dynamic Interfacial Printing for Monodisperse Droplets and Polymeric Microparticles. *Advanced Materials Technologies*, 1(1):1600021, 2016.

- [15] A. G. Kanellopoulos and M. J. Owen. Adsorption of sodium dodecyl sulphate at the silicone fluid/water interface. *Transactions of the Faraday Society*, 67(0):3127, 1971.
- [16] Joseph Alouf, Daniel Ladant, Michel R. Popoff, Gilles Prévost, Mira Y. Tawk, Gaëlle Zimmermann-Meisse, and Emmanuel Jover. The staphylococcal alpha-toxin and leukotoxins. *The Comprehensive Sourcebook of Bacterial Protein Toxins*:739–772, 2015.
- [17] Langzhou Song, Michael R Hobaugh, Christopher Shustak, Stephen Cheley, Hagan Bayley, and J Eric Gouaux. Structure of Staphylococcal α -Hemolysin, a Heptameric Transmembrane Pore. *Source: Science, New Series J. Biol. Chem. Science J. Exp. Med. Science J. Biol. Chem. Biochem. J.*, 274(8443):1859–1866, 1996.
- [18] Bryan J. Berube and Juliane Bubeck Wardenburg. Staphylococcus aureus α -toxin: Nearly a century of intrigue. *Toxins*, 5(6):1140–1166, 2013.
- [19] Eric Gouaux. Channel-forming toxins: tales of transformation. *Current Opinion in Structural Biology*, 7(4):566–573, 1997.
- [20] Bernard Diu. *Elements de physique statistique*. Hermann, 1989. ISBN: 2705660658.
- [21] Aurore Dupin and Friedrich C. Simmel. Signalling and differentiation in emulsion-based multi-compartmentalized in vitro gene circuits. *Nature Chemistry*, 11(1):32–39, 2019.
- [22] D. Holcman and Z. Schuss. The Narrow Escape Problem. *SIAM Review*, 56(2):213–257, 2014.
- [23] Sidney Redner. *A Guide To First-Passage Processes*. Cambridge University Press, Cambridge, 2001. ISBN: 9780511606014.
- [24] Alexei Cheviakov, Michael J. Ward, and Ronny Straube. An Asymptotic Analysis of the Mean First Passage Time for Narrow Escape Problems: Part II: The Sphere. *Multiscale Modeling & Simulation*, 8:836–870, 2010.
- [25] C Chevalier, O Bénichou, B Meyer, and R Voituriez. First-passage quantities of Brownian motion in a bounded domain with multiple targets: a unified approach. *Journal of Physics A: Mathematical and Theoretical*, 44(2):025002, 2011.
- [26] B. D. (Barry D.) Hughes. *Random walks and random environments*. Clarendon Press, 1995. ISBN: 0198537883.
- [27] Z. Schuss, A. Singer, and D. Holcman. The narrow escape problem for diffusion in cellular microdomains. *Proceedings of the National Academy of Sciences*, 104(41):16098–16103, 2007.
- [28] Tommaso Casalini, Matteo Salvalaglio, Giuseppe Perale, Maurizio Masi, and Carlo Cavallotti. Diffusion and Aggregation of Sodium Fluorescein in Aqueous Solutions. *The Journal of Physical Chemistry B*, 115(44):12896–12904, 2011.
- [29] Erik D. Carlson, Rui Gan, C. Eric Hodgman, and Michael C. Jewett. Cell-free protein synthesis: Applications come of age. *Biotechnology Advances*, 30(5):1185–1194, 2012.
- [30] Yoshihiro Shimizu, Akio Inoue, Yukihide Tomari, Tsutomu Suzuki, Takashi Yokogawa, Kazuya Nishikawa, and Takuya Ueda. Cell-free translation reconstituted with purified components. *Nature Biotechnology*, 19(8):751–755, 2001.

- [31] Michael C Jewett, Kara A Calhoun, Alexei Voloshin, Jessica J Wu, and James R Swartz. An integrated cell-free metabolic platform for protein production and synthetic biology. *Molecular Systems Biology*, 4(1):220, 2008.
- [32] Jonathan Garamella, Ryan Marshall, Mark Rustad, and Vincent Noireaux. The All E. coli TX-TL Toolbox 2.0: A Platform for Cell-Free Synthetic Biology. *ACS Synthetic Biology*, 5(4):344–355, 2016.
- [33] Birgit Schneider, Friederike Junge, Vladimir A. Shirokov, Florian Durst, Daniel Schwarz, Volker Dötsch, and Frank Bernhard. Membrane Protein Expression in Cell-Free Systems. In pages 165–186. Humana Press, 2010.
- [34] Tatiana Trantidou, Mark Friddin, Yuval Elani, Nicholas J. Brooks, Robert V. Law, John M. Seddon, and Oscar Ces. Engineering Compartmentalized Biomimetic Micro- and Nanocontainers. *ACS Nano*, 11(7):6549–6565, 2017.
- [35] Sagardip Majumder, Jonathan Garamella, Ying-Lin Wang, Maxwell DeNies, Vincent Noireaux, and Allen P. Liu. Cell-sized mechanosensitive and biosensing compartment programmed with DNA. *Chemical Communications*, 53(53):7349–7352, 2017.
- [36] Dirk van Swaay and Andrew DeMello. Microfluidic methods for forming liposomes. *Lab on a Chip*, 13(5):752, 2013.
- [37] S. Pautot, B. J. Frisken, and D. A. Weitz. Engineering asymmetric vesicles. *Proceedings of the National Academy of Sciences*, 100(19):10718–10721, 2003.
- [38] Vincent Noireaux and Albert Libchaber. A vesicle bioreactor as a step toward an artificial cell assembly. *Proceedings of the National Academy of Sciences of the United States of America*, 101(51):17669–17674, 2004.
- [39] Kadla R. Rosholm, Matthew A. B. Baker, Pietro Ridone, Yoshitaka Nakayama, Paul R. Rohde, Luis G. Cuello, Lawrence K. Lee, and Boris Martinac. Activation of the mechanosensitive ion channel MscL by mechanical stimulation of supported Droplet-Hydrogel bilayers. *Scientific Reports*, 7(1):45180, 2017.
- [40] Ruhma Syeda, Jose S. Santos, Mauricio Montal, and Hagan Bayley. Tetrameric assembly of KvLm K⁺ channels with defined numbers of voltage sensors. *Proceedings of the National Academy of Sciences of the United States of America*, 109(42):16917, 2012.
- [41] Mark S Friddin, Hywel Morgan, and Maurits R R de Planque. Cell-free protein expression systems in microdroplets: Stabilization of interdroplet bilayers. *Biomicrofluidics*, 7(1):14108, 2013.
- [42] Heather E. Findlay, Nicola J. Harris, Paula J. Booth, X. Liu, and Paula J. Booth. No Title. 6(1):39349, 2016.
- [43] Maie A. Elfaramawy, Satoshi Fujii, Atsuko Uyeda, Toshihisa Osaki, Shoji Takeuchi, Yasuhiko Kato, Hajime Watanabe, and Tomoaki Matsuura. Quantitative analysis of cell-free synthesized membrane proteins at the stabilized droplet interface bilayer. *Chemical Communications*, 54(86):12226–12229, 2018.
- [44] Masayuki Iwamoto, Maie A. Elfaramawy, Mariko Yamatake, Tomoaki Matsuura, and Shigetoshi Oiki. Concurrent *In Vitro* Synthesis and Functional Detection of Nascent Activity of the KcsA Channel under a Membrane Potential. *ACS Synthetic Biology*, 7(4):1004–1011, 2018.

- [45] Ruhma Syeda, Matthew A. Holden, William L. Hwang, and Hagan Bayley. Screening Blockers Against a Potassium Channel with a Droplet Interface Bilayer Array. *Journal of the American Chemical Society*, 130(46):15543–15548, 2008.
- [46] Massimo Scanziani and Michael Häusser. Electrophysiology in the age of light. *Nature*, 461(7266):930–939, 2009.
- [47] H.T. Tien and A.L. Ottova. Supported planar lipid bilayers (s-BLMs) as electrochemical biosensors. *Electrochimica Acta*, 43(23):3587–3610, 1998.
- [48] Lars D. Mosgaard, Karis A. Zecchi, Thomas Heimburg, and Rima Budvytyte. The Effect of the Nonlinearity of the Response of Lipid Membranes to Voltage Perturbations on the Interpretation of Their Electrical Properties. A New Theoretical Description. *Membranes*, 5(4):495–512, 2015.
- [49] M Montal and P Mueller. Formation of Bimolecular Membranes from Lipid Monolayers and a Study of Their Electrical Properties (membrane structure/membrane reconstitution/asymmetric membranes/lipid bilayers). 69(12):3561–3566, 1972.
- [50] L Q Gu and H Bayley. Interaction of the noncovalent molecular adapter, beta-cyclodextrin, with the staphylococcal alpha-hemolysin pore. *Biophysical Journal*, 79(4):1967, 2000.
- [51] Manuela Pastoriza-Gallego, Ghani Oukhaled, Jérôme Mathé, Bénédicte Thiebot, Jean-Michel Betton, Loïc Auvray, and Juan Pelta. Urea denaturation of α -hemolysin pore inserted in planar lipid bilayer detected by single nanopore recording: Loss of structural asymmetry. *FEBS Letters*, 581(18):3371–3376, 2007.
- [52] Jonghyeon Shin and Vincent Noireaux. Efficient cell-free expression with the endogenous E.coli RNA polymerase and sigma factor 70. *Journal of Biological Engineering*, 4(8):8, 2010.
- [53] Jonghyeon Shin and Vincent Noireaux. An E. coli Cell-Free Expression Toolbox: Application to Synthetic Gene Circuits and Artificial Cells. *ACS Synthetic Biology*, 1(1):29–41, 2012.
- [54] Filippo Caschera and Vincent Noireaux. Synthesis of 2.3 mg/ml of protein with an all Escherichia coli cell-free transcription-translation system. *Biochimie*, 99(1):162–168, 2014.
- [55] G Menestrina. Ionic channels formed by Staphylococcus aureus alpha-toxin: voltage-dependent inhibition by divalent and trivalent cations. *The Journal of membrane biology*, 90(2):177–90, 1986.
- [56] I Daubechies. *Ten Lectures on Wavelets*. CBMS-NSF Regional Conference Series in Applied Mathematics. Society for Industrial and Applied Mathematics (SIAM, 3600 Market Street, Floor 6, Philadelphia, PA 19104), 1992. ISBN: 9781611970104.
- [57] Maximilian Weitz, Jongmin Kim, Korbinian Kapsner, Erik Winfree, Elisa Franco, and Friedrich C. Simmel. Diversity in the dynamical behaviour of a compartmentalized programmable biochemical oscillator. *Nature Chemistry*, 6(4):295–302, 2014.
- [58] Scott T Retterer and Michael L Simpson. Microscale and nanoscale compartments for biotechnology. *Current Opinion in Biotechnology*, 23(4):522–528, 2012.

- [59] Vincent Noireaux, Yusuke T. Maeda, and Albert Libchaber. Development of an artificial cell, from self-organization to computation and self-reproduction. *Proceedings of the National Academy of Sciences*, 108(9):3473–3480, 2011.
- [60] Michael B. Elowitz and Stanislas Leibler. A synthetic oscillatory network of transcriptional regulators. *Nature*, 403(6767):335–338, 2000.
- [61] Jeff Hasty, David McMillen, and J. J. Collins. Engineered gene circuits. *Nature*, 420(6912):224–230, 2002.
- [62] Timothy S. Gardner, Charles R. Cantor, and James J. Collins. Construction of a genetic toggle switch in *Escherichia coli*. *Nature*, 403(6767):339–342, 2000.
- [63] Priscilla E. M. Purnick and Ron Weiss. The second wave of synthetic biology: from modules to systems. *Nature Reviews Molecular Cell Biology*, 10(6):410–422, 2009.
- [64] George M. Whitesides and Bartosz Grzybowski. Self-Assembly at All Scales. *Science*, 295(5564):2418–2421, 2002.
- [65] Huan-Xiang Zhou, Germán Rivas, and Allen P Minton. Macromolecular crowding and confinement: biochemical, biophysical, and potential physiological consequences. *Annual review of biophysics*, 37:375–97, 2008.
- [66] Anna H. Chen and Pamela A. Silver. Designing biological compartmentalization. *Trends in Cell Biology*, 22(12):662–670, 2012.
- [67] Hanson Lee, William C. DeLoache, and John E. Dueber. Spatial organization of enzymes for metabolic engineering. *Metabolic Engineering*, 14(3):242–251, 2012.
- [68] Ting F Zhu and Jack W Szostak. Coupled growth and division of model protocell membranes. *Journal of the American Chemical Society*, 131(15):5705–13, 2009.
- [69] Jerome Chalmeau, Nadezda Monina, Jonghyeon Shin, Christophe Vieu, and Vincent Noireaux. alpha-Hemolysin pore formation into a supported phospholipid bilayer using cell-free expression. *Biochimica et Biophysica Acta - Biomembranes*, 1808(1):271–278, 2011.
- [70] Lisa Sercombe, Tejaswi Veerati, Fatemeh Moheimani, Sherry Y. Wu, Anil K. Sood, and Susan Hua. Advances and Challenges of Liposome Assisted Drug Delivery. *Frontiers in Pharmacology*, 6:286, 2015.
- [71] Hadis Daraee, Ali Etemadi, Mohammad Kouhi, Samira Alimirzalu, and Abolfazl Akbarzadeh. Application of liposomes in medicine and drug delivery. *Artificial Cells, Nanomedicine, and Biotechnology*, 44(1):381–391, 2016.
- [72] Alexander D. Graham, Sam N. Olof, Madeline J. Burke, James P. K. Armstrong, Ellina A. Mikhailova, James G. Nicholson, Stuart J. Box, Francis G. Szele, Adam W. Perriman, and Hagan Bayley. High-Resolution Patterned Cellular Constructs by Droplet-Based 3D Printing. *Scientific Reports*, 7(1):7004, 2017.
- [73] Maxwell Allen-Benton, Heather E Findlay, and Paula J Booth. Probing membrane protein properties using droplet interface bilayers. *Experimental Biology and Medicine*:153537021984793, 2019.
- [74] Jacob N Israechvili. *Intermolecular and Surface Forces (2nd edition)*. Academic Press, 1991.

- [75] Rob Phillips, Jane Kondev, Julie Theriot, and Hernan G. Garcia. *Physical Biology of the Cell*. Garland Science.
- [76] Annela M. Seddon, Paul Curnow, and Paula J. Booth. Membrane proteins, lipids and detergents: not just a soap opera. *Biochimica et Biophysica Acta (BBA) - Biomembranes*, 1666(1-2):105–117, 2004.
- [77] C Miller. Ion Channels in Liposomes. *Annual Review of Physiology*, 46(1):549–558, 1984.
- [78] Nan-Nan Deng, Maaruthy Yelleswarapu, and Wilhelm T. S. Huck. Monodisperse Uni- and Multicompartment Liposomes. *Journal of the American Chemical Society*, 138(24):7584–7591, 2016.
- [79] W.R. Redwood, F.R. Pfeiffer, J.A. Weisbach, and T.E. Thompson. Physical properties of bilayer membranes formed from a synthetic saturated phospholipid in n-decane. *Biochimica et Biophysica Acta (BBA) - Biomembranes*, 233(1):1–6, 1971.
- [80] Paul Mueller, Donald O. Rudin, H. Ti Tien, and William C. Wescott. Reconstitution of Cell Membrane Structure in vitro and its Transformation into an Excitable System. *Nature*, 194(4832):979–980, 1962.
- [81] M Montal and P Mueller. Formation of Bimolecular Membranes from Lipid Monolayers and a Study of Their Electrical Properties. *Proceedings of the National Academy of Sciences*, 69(12):3561–3566, 1972.
- [82] Andrew J Heron, James R Thompson, Bríd Cronin, Hagan Bayley, and Mark I. Simultaneous measurement of ion current and fluorescence from single protein pores. *Biophysics*:1–8, 2009.
- [83] Oskar B. Jagers, Pietro Ridone, Boris Martinac, and Matthew A. B. Baker. Fluorescence microscopy of piezo1 in droplet hydrogel bilayers. *Channels*, 13(1):102–109, 2019.
- [84] E C Freeman, J S Najem, S Sukharev, M K Philen, and D J Leo. Soft Matter The mechano-electrical response of droplet interface bilayer membranes. *Soft Matter*, 12:3021–3031, 2016.
- [85] Stephen A Sarles and Donald J Leo. Membrane-based biomolecular smart materials. *Smart Materials and Structures*, 20(9):094018, 2011.
- [86] Mark S Friddin, Guido Bolognesi, Yuval Elani, Nicholas J Brooks, Robert V Law, John M Seddon, Mark A A Neil, and Oscar Ces. Optically assembled droplet interface bilayer (OptiDIB) networks from cell-sized microdroplets. *Soft Matter*, 12(37):7731–7734, 2016.
- [87] Linda C M Gross, Andrew J. Heron, Sylvan C. Baca, and Mark I. Wallace. Determining membrane capacitance by dynamic control of droplet interface bilayer area. *Langmuir*, 27(23):14335–14342, 2011.
- [88] William L. Hwang, Min Chen, Brid Cronin, Matthew A. Holden, and Hagan Bayley. Asymmetric Droplet Interface Bilayers. *Journal of the American Chemical Society*, 130(18):5878–5879, 2008.
- [89] Robert A. Fletcher, Jacquelyn A. Brazin, Matthew E. Staymates, Bruce A. Benner, and J. Greg Gillen. Fabrication of polymer microsphere particle standards containing trace explosives using an oil/water emulsion solvent extraction piezoelectric printing process. *Talanta*, 76(4):949–955, 2008.

- [90] Shelley L. Anna, Nathalie Bontoux, and Howard A. Stone. Formation of dispersions using "flow focusing" in microchannels. *Applied Physics Letters*, 82(3):364–366, 2003.
- [91] Todd Thorsen, Richard W. Roberts, Frances H. Arnold, and Stephen R. Quake. Dynamic Pattern Formation in a Vesicle-Generating Microfluidic Device. *Physical Review Letters*, 86(18):4163–4166, 2001.
- [92] Shashi Thutupalli, Stephan Herminghaus, and Ralf Seemann. Bilayer membranes in micro-fluidics: from gel emulsions to soft functional devices. *Soft Matter*, 7(4):1312–1320, 2011.
- [93] Rémi Dangla, Etienne Fradet, Yonatan Lopez, and Charles N Baroud. The physical mechanisms of step emulsification. *Journal of Physics D: Applied Physics*, 46(11):114003, 2013.
- [94] Yuval Elani, Andrew J. DeMello, Xize Niu, and Oscar Ces. Novel technologies for the formation of 2-D and 3-D droplet interface bilayer networks. *Lab on a Chip*, 12(18):3514, 2012.
- [95] Takasi Nisisako et al. Microfluidic passive permeability assay using nanoliter droplet interface lipid bilayers. *The Analyst*, 138(22):6793, 2013.
- [96] Mary-Anne Nguyen, Bernadeta Srijanto, C. Patrick Collier, Scott T. Retterer, and Stephen A. Sarles. Hydrodynamic trapping for rapid assembly and in situ electrical characterization of droplet interface bilayer arrays. *Lab on a Chip*, 16(18):3576–3588, 2016.
- [97] Bárbara Schlicht and Michele Zagnoni. Droplet-interface-bilayer assays in microfluidic passive networks. *Scientific Reports*, 5:9951, 2015.
- [98] David F. James. The meniscus on the outside of a small circular cylinder. *Journal of Fluid Mechanics*, 63(4):657–664, 1974.
- [99] Yanfei Tang and Shengfeng Cheng. The meniscus on the outside of a circular cylinder: From microscopic to macroscopic scales. *Journal of Colloid and Interface Science*, 533:401–408, 2019.
- [100] William H. Press, Saul A. Teukolsky, William T. Vetterling, Brian P. Flannery, and Cambridge University Press. *Numerical recipes : the art of scientific computing*, page 1235. ISBN: 0521880688.
- [101] Manon Valet, Léa-Laetitia Pontani, Raphaël Voituriez, Elie Wandersman, and Alexis M. Prevost. Diffusion through nanopores in connected lipid bilayer networks, 2019. arXiv: [1902.04912](https://arxiv.org/abs/1902.04912).
- [102] Daniel L. Parton, Jochen W. Klingelhoefer, and Mark S.P. Sansom. Aggregation of Model Membrane Proteins, Modulated by Hydrophobic Mismatch, Membrane Curvature, and Protein Class. *Biophysical Journal*, 101(3):691–699, 2011.
- [103] Christian Meesters, Antje Brack, Nadja Hellmann, and Heinz Decker. Structural characterization of the α -hemolysin monomer from *Staphylococcus aureus*. *Proteins: Structure, Function, and Bioinformatics*, 75(1):118–126, 2009.
- [104] Paul Cassidy and Sidney Harshman. Studies on the binding of staphylococcal 125I-labeled α -toxin to rabbit erythrocytes. *Biochemistry*, 15(11):2348–2355, 1976.
- [105] S Bhakdi and J Tranum-Jensen. Alpha-toxin of *Staphylococcus aureus*. *Microbiological reviews*, 55(4):733–51, 1991.

- [106] A Hildebrand, M Pohl, and S Bhakdi. Staphylococcus aureus alpha-toxin. Dual mechanism of binding to target cells. eng. *The Journal of biological chemistry*, 266(26):17195–17200, 1991.
- [107] Georgia A Wilke and Juliane Bubeck Wardenburg. Role of a disintegrin and metalloprotease 10 in Staphylococcus aureus alpha-hemolysin-mediated cellular injury. *Proceedings of the National Academy of Sciences of the United States of America*, 107(30):13473–8, 2010.
- [108] Stefania Galdiero and Eric Gouaux. High resolution crystallographic studies of alpha-hemolysin-phospholipid complexes define heptamer-lipid head group interactions: implication for understanding protein-lipid interactions. *Protein science : a publication of the Protein Society*, 13(6):1503–11, 2004.
- [109] J H Freer, J P Arbuthnott, and A W Bernheimer. Interaction of staphylococcal alpha-toxin with artificial and natural membranes. *Journal of bacteriology*, 95(3):1153–68, 1968.
- [110] Matthew A. Holden, David Needham, and Hagan Bayley. Functional Bionetworks from Nanoliter Water Droplets. *Journal of the American Chemical Society*, 129(27):8650–8655, 2007.
- [111] Rikiya Watanabe et al. Arrayed lipid bilayer chambers allow single-molecule analysis of membrane transporter activity. *Nature Communications*, 5(1):4519, 2014.
- [112] Sidney Redner. *A guide to first-passage processes*. Cambridge University Press, 2001, page 312. ISBN: 0521652480.
- [113] Elliott W. Montroll and George H. Weiss. Random Walks on Lattices. II. *Journal of Mathematical Physics*, 6(2):167–181, 1965.
- [114] Shoon Kyung Kim. Mean First Passage Time for a Random Walker and Its Application to Chemical Kinetics. *The Journal of Chemical Physics*, 28(6):1057–1067, 1958.
- [115] Zhonghan Hu, Liwen Cheng, and B. J. Berne. First passage time distribution in stochastic processes with moving and static absorbing boundaries with application to biological rupture experiments. *The Journal of Chemical Physics*, 133(3):034105, 2010.
- [116] Joseph S. Lucas, Yaojun Zhang, Olga K. Dudko, and Cornelis Murre. 3D Trajectories Adopted by Coding and Regulatory DNA Elements: First-Passage Times for Genomic Interactions. *Cell*, 158(2):339–352, 2014.
- [117] Thibaut Calandre. Optimisation d’observables de premier passage pour des processus de diffusion intermittents confinés, 2014.
- [118] Alexander M. Berezhkovskii, Vladimir Yu. Zitserman, and Stanislav Y. Shvartsman. Diffusivity in periodic arrays of spherical cavities. *The Journal of Chemical Physics*, 118(15):7146–7147, 2003.
- [119] Alexander M. Berezhkovskii, Vladimir Yu. Zitserman, and Stanislav Y. Shvartsman. Effective diffusivity in periodic porous materials. *The Journal of Chemical Physics*, 119(14):6991–6993, 2003.
- [120] J. Illingworth and J. Kittler. A survey of the hough transform. *Computer Vision, Graphics, and Image Processing*, 44(1):87–116, 1988.

- [121] Richard O. Duda and Peter E. Hart. Use of the Hough transformation to detect lines and curves in pictures. *Communications of the ACM*, 15(1):11–15, 1972.
- [122] L Song, M R Hobough, C Shustak, S Cheley, H Bayley, and J E Gouaux. Structure of staphylococcal alpha-hemolysin, a heptameric transmembrane pore. *Science*, 5294(274):1859–1866, 1996.
- [123] Hai-Chau Chang and Lih-Chung Wang. A Simple Proof of Thue’s Theorem on Circle Packing, 2010. arXiv: [1009.4322](https://arxiv.org/abs/1009.4322).
- [124] G. Belmonte, L. Cescatti, B. Ferrari, T. Nicolussi, M. Ropele, and G. Menestrina. Pore formation by *Staphylococcus aureus* alpha-toxin in lipid bilayers. *European Biophysics Journal*, 14(6):349–358, 1987.
- [125] Jochen J Sieber et al. Anatomy and Dynamics of a Supramolecular Membrane Protein Cluster. *Science*, 317(5841):1072 LP –1076, 2007.
- [126] Robijn Bruinsma and Philip Pincus. Protein aggregation in membranes. *Current Opinion in Solid State and Materials Science*, 1(3):401–406, 1996.
- [127] S. Chandrasekhar. Stochastic Problems in Physics and Astronomy. *Reviews of Modern Physics*, 15(1):1–89, 1943.
- [128] C. R. Heathcote and J. E. Moyal. The Random Walk [In Continuous Time] and Its Application to the Theory of Queues. *Biometrika*, 46(3/4):400, 1959.
- [129] R. A. Robinson and C. L. Chia. The Diffusion Coefficient of Calcium Chloride in Aqueous Solution at 25°. *Journal of the American Chemical Society*, 74(11):2776–2777, 1952.
- [130] Martin Bock, Amit Kumar Tyagi, Jan-Ulrich Kreft, and Wolfgang Alt. Generalized Voronoi Tessellation as a Model of Two-dimensional Cell Tissue Dynamics. *Bulletin of Mathematical Biology*, 72(7):1696–1731, 2010.
- [131] Alexander G. Fletcher, Miriam Osterfield, Ruth E. Baker, and Stanislav Y. Shvartsman. Vertex Models of Epithelial Morphogenesis. *Biophysical Journal*, 106(11):2291, 2014.
- [132] Dapeng Bi, Xingbo Yang, M. Cristina Marchetti, and M. Lisa Manning. Motility-Driven Glass and Jamming Transitions in Biological Tissues. *Physical Review X*, 6(2):021011, 2016.
- [133] M W Nirenberg and J H Matthaei. The dependence of cell-free protein synthesis in *E. coli* upon naturally occurring or synthetic polyribonucleotides. *Proceedings of the National Academy of Sciences of the United States of America*, 47(10):1588–602, 1961.
- [134] Ryan Marshall et al. Rapid and Scalable Characterization of CRISPR Technologies Using an *E. coli* Cell-Free Transcription-Translation System. *Molecular Cell*, 69(1):146–157.e3, 2018.
- [135] D E Nevin and J M Pratt. A coupled in vitro transcription-translation system for the exclusive synthesis of polypeptides expressed from the T7 promoter. *FEBS letters*, 291(2):259–63, 1991.
- [136] A. S Spirin, V. I Baranov, L. A Ryabova, S. Y Ovodov, and Y. B Alakhov. A continuous cell-free translation system capable of producing polypeptides in high yield. *Science*, 242(4882), 1988.

- [137] James U Bowie. Stabilizing membrane proteins. *Current Opinion in Structural Biology*, 11(4):397–402, 2001.
- [138] T.K. Ritchie, Y.V. Grinkova, T.H. Bayburt, I.G. Denisov, J.K. Zolnerciks, W.M. Atkins, and S.G. Sligar. Reconstitution of Membrane Proteins in Phospholipid Bilayer Nanodiscs. *Methods in Enzymology*, 464:211–231, 2009.
- [139] Sergei I Sukharev, Paul Blount, Boris Martinac, Kung, Ching, Kung, and Ching. Mechanosensitive Channels of Escherichia coli :The MscL Gene, Protein, and Activities. *Annual Review of Physiology*, 59(1):633–657, 1997.
- [140] S Sukharev, S R Durell, and H R Guy. Structural models of the MscL gating mechanism. *Biophysical journal*, 81(2):917–36, 2001.
- [141] Enrico Schleiff and Jürgen Soll. Membrane protein insertion: mixing eukaryotic and prokaryotic concepts. *EMBO reports*, 6(11):1023–7, 2005.
- [142] Rita Sachse, Srujan K. Dondapati, Susanne F. Fenz, Thomas Schmidt, and Stefan Kubick. Membrane protein synthesis in cell-free systems: From biomimetic systems to bio-membranes. *FEBS Letters*, 588(17):2774–2781, 2014.
- [143] Miranda L Jacobs, Margrethe A Boyd, and Neha P Kamat. Diblock copolymers enhance folding of a mechanosensitive membrane protein during cell-free expression. *Proceedings of the National Academy of Sciences of the United States of America*, 116(10):4031–4036, 2019.
- [144] Rob Phillips. Membranes by the Numbers, 2017. arXiv: [1703.02066](https://arxiv.org/abs/1703.02066).
- [145] K S Cole. Rectification and inductance in the squid giant axon. *The Journal of general physiology*, 25(1):29–51, 1941.
- [146] Ron Milo. What is the total number of protein molecules per cell volume? A call to rethink some published values. *BioEssays : news and reviews in molecular, cellular and developmental biology*, 35(12):1050–5, 2013.
- [147] Eyal Karzbrun, Jonghyeon Shin, Roy H. Bar-Ziv, and Vincent Noireaux. Coarse-Grained Dynamics of Protein Synthesis in a Cell-Free System. *Physical Review Letters*, 106(4):048104, 2011.
- [148] Ulla Vogel, Michael Sørensen, Steen Pedersen, Kaj Frank Jensen, and Mogens Kilstrop. Decreasing transcription elongation rate in Escherichia Coli exposed to amino acid starvation. *Molecular Microbiology*, 6(15):2191–2200, 1992.
- [149] Alfred Goldberg. Magnesium binding by Escherichia coli ribosomes. *Journal of Molecular Biology*, 15(2):663–673, 1966.
- [150] Dong-Yeon D Lee, Leticia Galera-Laporta, Maja Bialecka-Fornal, Eun Chae Moon, Zhouxin Shen, Steven P Briggs, Jordi Garcia-Ojalvo, and Gürol M Süel. Magnesium Flux Modulates Ribosomes to Increase Bacterial Survival. *Cell*, 177(2):352–360.e13, 2019.
- [151] Joseph Sambrook and W Russel, D. Molecular cloning : a laboratory manual (3rd. ed), 2000.
- [152] Andrey Feklistov, Brian D. Sharon, Seth A. Darst, and Carol A. Gross. Bacterial Sigma Factors: A Historical, Structural, and Genomic Perspective. *Annual Review of Microbiology*, 68(1):357–376, 2014.
- [153] Timothy D. Craggs. Green fluorescent protein: structure, folding and chromophore maturation. *Chemical Society Reviews*, 38(10):2865, 2009.

- [154] Ryota Sakamoto, Vincent Noireaux, and Yusuke T. Maeda. Anomalous Scaling of Gene Expression in Confined Cell-Free Reactions. *Scientific Reports*, 8(1):7364, 2018.
- [155] O Alvarez and R Latorre. Voltage-dependent capacitance in lipid bilayers made from monolayers. *Biophysical journal*, 21(1):1–17, 1978.
- [156] Thomas Heimburg. The Capacitance and Electromechanical Coupling of Lipid Membranes Close to Transitions: The Effect of Electrostriction. *Biophysical Journal*, 103(5):918, 2012.
- [157] Lars D. Mosgaard, Karis A. Zecchi, and Thomas Heimburg. Mechano-capacitive properties of polarized membranes. *Soft Matter*, 11(40):7899–7910, 2015.
- [158] Katrine R. Laub, Katja Witschas, Andreas Blicher, Søren B. Madsen, Andreas Lückhoff, and Thomas Heimburg. Comparing ion conductance recordings of synthetic lipid bilayers with cell membranes containing TRP channels. *Biochimica et Biophysica Acta (BBA) - Biomembranes*, 1818(5):1123–1134, 2012.
- [159] Andreas Blicher and Thomas Heimburg. Voltage-Gated Lipid Ion Channels. *PLoS ONE*, 8(6):e65707, 2013. Zoya Leonenko, editor.